Fall 2015

Kinetic processes in reconnection: Impact of magnetospheric hot O+ and cold ions in magnetopause reconnection and electron heating in magnetotail reconnection

Shan Wang
University of New Hampshire, Durham

Kinetic processes in reconnection: Impact of magnetospheric hot O^+ and cold ions in magnetopause reconnection and electron heating in magnetotail reconnection

BY

SHAN WANG

B.S. in Space Physics, Peking University, China, 2012

DISSERTATION

Submitted to the University of New Hampshire
in partial fulfillment of
the requirements for the degree of

Doctor of Philosophy

in

Physics

September, 2015

This dissertation has been examined and approved in partial fulfillment of the requirements for the degree of Doctor of Philosophy in Physics by:

Dissertation Director, Lynn M. Kistler
Professor of Physics, Director of Space Science Center (EOS)

Li-Jen Chen
Affiliate Research Associate Professor, University of New Hampshire,
Associate Research Scientist, NASA Goddard Space Flight Center and
Department of Astronomy, University of Maryland at College Park

Roy B. Torbert
Professor of Physics

Kai Germaschewski
Associate Professor of Physics

David M. Mattingly
Assistant Professor of Physics

On July 22, 2015

Original approval signatures are on file with the University of New Hampshire Graduate School.

Dedication

To my mother Yan Song, and my father Jun Wang.

Acknowledgments

I express my great thanks to my advisor, Prof. Lynn M. Kistler. She has been helping me to steer my research direction at every critical point, and always encouraging me with her unique friendly smile. It was a long time before I could understand how she could keep peaceful with data that looked so disappointing, simply said "nothing is easy", and continued with the careful analysis. This is an attitude and an ability I learnt from her, with great respect. I am grateful to Christopher G. Mouikis as my mentor. I was inspired with ideas every time we had detailed discussions, and I learnt what it means to "exhaust the data analysis" from him. It was so kind of him to have patience listening to my feeling during frustrated times, and helping me build up confidence to get out of depression. I am thankful to Li-Jen Chen as my other mentor. I appreciate that she would like to trust me in work, tolerant my weakness and cultivate me with much care. I was always motivated by her endless encouragements and enthusiasm. I am also grateful to Roy B. Torbert, Kai Germascheski, and David M. Mattingly as my thesis committee members, for their help in my dissertation.

I give my gratitude to Yanhua Liu, Ruilong Guo and Naoki Bessho, who shared with me their knowledge and significantly helped me in research. I acknowledge Jason R. Shuster, Matthew R. Argall, Guanlai Li and Fathima M. Muzamil for many helpful discussions. I want to thank all professors I took classes with, particularly Prof. Martin Lee and Prof. Eberhard Möbius, from whom I see the great personalities of life-long curiosity and rigorousness that define them to be great senior scientists. Thanks Steven Petrinec for producing Figure 4-11. Thanks William Daughton, Homa Karimabadi, and Vadim Roytershteyn for providing simulation data. The work in this thesis is supported by NASA grants

NNX12AD16G, NNX13AK31G, and NSF grant AGS-1202537.

In addition, I am grateful to my other friends for their accompany and help, particularly Xiaoyan Chong, Christian P. Ferradas, Jichun Zhang, Anthony A. Salkin, Shujie Li, Wenyuan Yu, Junhong Chen, and Liang Wang in UNH, and my old friends Hong Zhao, Chao Yue, Yiming Jiang, Li Lin, and Xiaotong Zhu. At last, I thank my parents, who provide me unconditional support, though bearing the loneliness of not having me around.

I appreciate the experience of my graduate life, which is full of doubts and confusions. I doubted my ability, my persistence, the value of my work, and even the meaning of my life. I still don't get answers to them all. However, I have convinced myself that I am able to make valuable contribution with my work when I really try my best, and at least for now, I am determined to dedicate in the space physics research. The graduate life is a process for me to know about the limitations of myself and of the work, and to learn how to maximize the outcome with the imperfect reality. It helps me build up enough confidence to proceed, and at the same time learn to always keep humble.

Even a few years ago, I used to attribute most of my progress to my own hard work. Now I realize that every piece of my progress is based on numerous help and support from my advisors, parents and friends, which lift me up to a new level of the platform. The only thing I can do and I should do is to spare no effort to grasp the opportunity on the platform, and give it a nice shot. Thanks everyone, and thanks my graduate life!

Table of Contents

List of Tables

List of Figures

ABSTRACT

Kinetic processes in reconnection: Impact of magnetospheric hot O^+ and cold ions in magnetopause reconnection and electron heating in magnetotail reconnection

by

Shan Wang

University of New Hampshire, September, 2015

We investigate three aspects of magnetic reconnection where kinetic processes play a strong role: hot O^+ and cold ion behaviors in magnetopause reconnection, their effect on the reconnection rate, and electron heating during magnetotail reconnection. At the magnetopause, we analyze observed velocity distribution functions (VDFs) and find that hot O^+, despite its large gyroradius, almost fully participates in the reconnection outflow with a demagnetization-pickup process. Finite Larmor radius effects are apparent, controlling how far the ions extend to the magnetosheath side. For cold ions, if entering the central diffusion region, they behave like hot ions; otherwise, they convect with the magnetic field adiabatically. How these species behave determines their effect on the reconnection rate. We compare the observed reconnection rate with predictions of the fluid-based Cassak-Shay formula for 8 events. The measured rate does correlate with the predictions when all magnetospheric and magnetosheath populations are included, but the correlation is better when just magnetosheath populations are used. This indicates possible deviations from the Cassak-Shay theory caused by the kinetic effects of the different populations. The diffusion region aspect ratio does not show a clear dependence on the O^+ abundance, density asymmetry or guide field. To understand the electron heating, using a particle-in-cell simulation,

we divide the reconnection exhaust into four sub-regions based on electron temperatures and VDFs. The same defining distributions are found in observations. The associated acceleration mechanisms are determined by tracing particles through the simulation fields. Electrons obtain initial energization from the electron diffusion region (EDR) electromagnetic fields and the parallel potential, and pitch angle scattering isotropizes the distribution. Further downstream, electrons with initial high $v_{\parallel}$ ($v_{\perp}$) are mainly accelerated with the curvature (gradient-B) drift opposite to the out-of-plane electric field, generating distinct populations in VDFs. We estimate the heating coefficient, $r_h = k_B \Delta T_e / m_i v_{Ai}^2$, using a simple model of the outflowing EDR distribution. The electron heating in 11 magnetotail reconnections shows $r_h \sim$1.5%-2.6% with considerable variations caused by the magnetotail pressure unloading, in reasonable agreement with the simulation results. Thus, both for heavy ions and electrons, we find the key to understanding the reconnection dynamics is in interpreting the individual particle behavior.

Chapter 1

Introduction

Magnetic reconnection is a process associated with changes of the magnetic field topology, that transfers energies from the electromagnetic fields to the plasmas. The concept of magnetic reconnection was first introduced by *Giovanelli* [1946], and many theoretical models to explain the reconnection process have been developed ever since [e.g., *Parker*, 1957; *Sweet*, 1958; *Petschek*, 1964; *Vasyliunas*, 1975; *Priest and Titov*, 1996]. Magnetic reconnection successfully explains observational signatures in different regimes: Earth's magnetopause [*Paschmann et al.*, 1979], Earth's magnetotail [*Nagai et al.*, 1998], Sun's atmosphere [*Longcope et al.*, 2005], and laboratory experiments [*Yamada*, 1999], and therefore its existence has been widely accepted. Because of its role to energize plasmas, reconnection has become a very important problem in plasma physics that has not been fully resolved yet.

In the reconnection study, how single particles behave in the reconnection electromagnetic field structure is the most fundamental question to answer. In particular, at the Earth's magnetopause, plasmas from the two sides (magnetosphere and magnetosheath) have asymmetries in densities and temperatures. The ion plasmas from the magnetosphere can also have variations in composition, with the presence of hot O^+ and/or cold ions in addition to the hot H^+ ions. These additional populations with different characteristic Larmor radii might behave differently, which needs to be investigated. After understanding the single particle motions, we can further study how reconnection produces the bulk

acceleration and heating of plasmas as a fluid. The efficiency of reconnection is measured by the reconnection rate. How it depends on local plasma and magnetic field conditions, and whether the kinetic effects due to the different behaviors of different species have impact on the reconnection rate, are next questions. In this thesis, we will discuss the above topics. In the rest of this chapter, we will briefly review the basic theoretical background and observational progress of reconnection studies.

1.1 Fundamental concepts of magnetic reconnection

The most general definition of magnetic reconnection is the localized breakdown of the *frozen-in* condition that leads to a change in the magnetic field connectivity of plasmas [*Axford*, 1984; *Schindler et al.*, 1988; *Hesse and Schindler*, 1988; *Birn and Priest*, 2007]. Ideal plasmas follow the frozen-in condition:

$$\vec{E} + \vec{v} \times \vec{B} = 0 \tag{1.1}$$

where $\vec{v}$ is the flow velocity. Thus, a pair of plasma elements that are originally connected by a field line will always maintain the connectivity. Faraday's law shows

$$\frac{\partial \vec{B}}{\partial t} = -\nabla \times \vec{E} \tag{1.2}$$

For plasmas enclosed in a surface S bounded by a loop C, applying $\nabla \cdot \vec{B} = 0$, Faraday's law leads to

$$\frac{d}{dt} \iint_S \vec{B} \cdot \hat{n} da = \iint_S \left[\frac{\partial \vec{B}}{\partial t} - \nabla \times \left(\vec{v} \times \vec{B} \right) \right] \cdot \hat{n} da = - \oint_C \left(\vec{E} + \vec{v} \times \vec{B} \right) \cdot d\vec{l} \tag{1.3}$$

Therefore, the frozen-in condition means that eq. (1.3) is equal to zero, and the magnetic flux within the same amount of the plasmas is also conserved. In some non-ideal regions, there can be a non-zero term R on the right-hand side of eq.(1.1). If it has a form of

$$\vec{R} = \nabla\Phi + \vec{u} \times \vec{B} \tag{1.4}$$

we can still find a frame moving with $\vec{u}$ where eq.(1.3) equal to zero holds. It means that the magnetic flux conservation cannot be violated by a simple loss of the magnetic connectivity between plasma elements, but a change in the magnetic topology associated with the energy dissipation is required [*Hesse and Schindler*, 1988; *Birn and Priest*, 2007]. The latter is the reconnection we are interested in, and the region where eq.(1.3) is non-zero is called the *diffusion region*, since the magnetic fields are diffused in this region. It is clear that a mechanism to break down the frozen-in condition and provide a term R with a non-zero curl is a necessary condition for reconnection to occur.

The 2-dimensional (2D) reconnection structure with an assumption of translational symmetry in the third dimension is depicted in Figure 1-1. Our discussions in this thesis will be restricted to the 2D assumption. Magnetic field lines with opposite orientations and the frozen-in plasmas from the inflow regions above and below approach together. According to Ampere's law:

$$\mu_0 \vec{J} = \nabla \times \vec{B} \tag{1.5}$$

a current sheet forms at the mid-plane. The L direction is along the inflow magnetic field, N is normal to the current sheet, and M is into the plane to finish the right-handed coordinate system. Reconnection occurs in the central diffusion region marked by the green box, changing the reconnecting magnetic field components along L to the reconnected components along N. The diffusion region has a width of δ and a length of l, and δ/l is

called the *aspect ratio*. There is a magnetic null point at the diffusion region center, and its extension in the M direction forms an X-line. Downstream of the diffusion region, plasmas are remagnetized into the reconnected magnetic fields and convect away as the outflow.

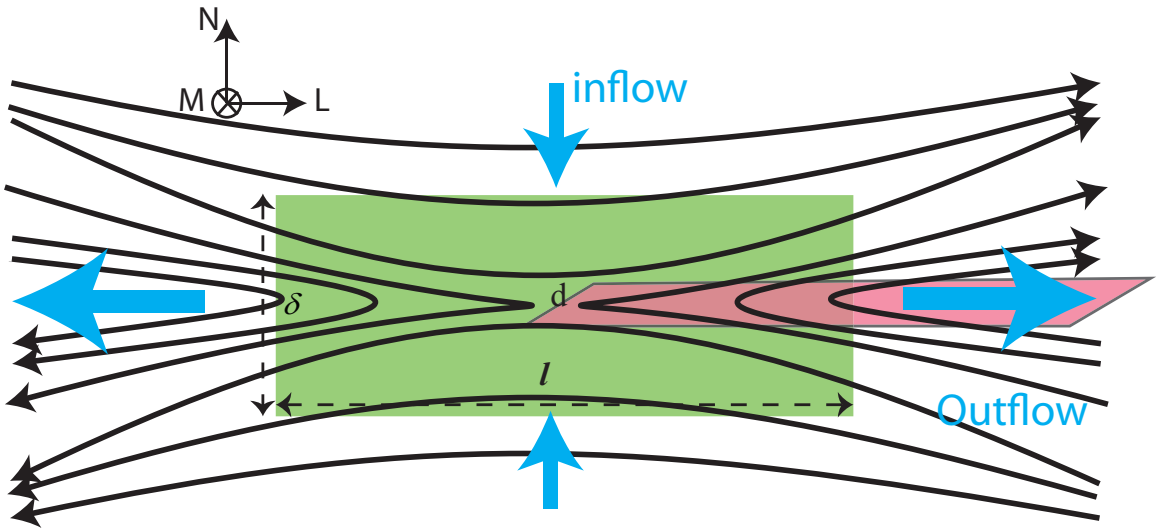

Figure 1-1: Illustration of the reconnection structure.

The *reconnection rate* measures the magnetic flux reconnected per unit time:

$$\frac{d\Phi}{dt} = -\oint (\vec{E} + \vec{v} \times \vec{B}) \cdot dl = E_{X,M} d \tag{1.6}$$

where $E_{X,M}$ is the M component of the electric field along the X-line, the integral path is along the boundaries in the $L - M$ plane as indicated by the magenta region in Figure 1-1, and d is the length of the X-line. The rightmost equality in eq.(1.6) is valid under the assumption that reconnection is a 2D structure and is uniform in the M direction. Thus, the local reconnection rate R, i.e., the reconnection rate per unit length, is equal to $E_{X,M}$. In general, there can be a magnetic field component along the X-line, which acts as a guide field in the 2D reconnection model, and the local R becomes the electric field parallel to the magnetic field ($E_{\parallel}$) at the X-line.

In steady-state reconnection, with a spatially uniform E_M, $E_{X,M}$ at the X-line is equal

to the convective E_M in the inflow and outflow regions, i.e.,

$$R = v_{in}B_{in} = v_{out}B_{out} \tag{1.7}$$

where v_{in} is the inflow velocity in the N direction, B_{in} is the magnetic field in the inflow region along the L direction, v_{out} is the outflow velocity in L, and B_{out} is the outflow magnetic field in N. Normalizing R by $v_A B_{in}$, where $v_A = B_{in}/\sqrt{\mu_0 \rho}$ is the upstream Alfvén speed and ρ is the mass density, we can use the inflow Alfvén Mach number $M_A = v_{in}/v_A$ to represent the reconnection rate of the system, independent of the variations of the upstream conditions.

1.2 Theoretical reconnection models

The first theoretical model for the *collisional* Magnetohydrodynamics (MHD) reconnection was the *Sweet-Parker* model [*Parker*, 1957; *Sweet*, 1958]. It describes a 2D steady-state incompressible reconnection. In collisional reconnection, the frozen-in condition is broken down by resistivity as shown in Ohm's law:

$$\vec{E} + \vec{v} \times \vec{B} = \eta \vec{J} \tag{1.8}$$

In the Sweet-Parker model, the diffusion region has a length of l determined by the global scale of the current sheet, so that $l \gg \delta$; η is uniform inside the diffusion region. Mass conservation shows

$$v_{in} l = v_{out} \delta \tag{1.9}$$

which results in $v_{in} \ll v_{out}$. Assuming that the upstream electromagnetic energy is all converted to the kinetic energy of the plasmas without thermalization, the momentum and

energy conservations give

$$|S| = \frac{v_{in} B_{in}^2}{\mu_0} = \frac{1}{2} \rho v_{in} v_{out}^2 \tag{1.10}$$

where S is the upstream Poynting flux, and ρ is the plasma mass density. From eq.(1.10) we get $v_{out} = \sqrt{2} v_A \sim v_A$ [*Hughes*, 1995].

The conclusion that v_{out} is of order v_A is one of the most important scaling laws in reconnection. It was predicted by different theoretical models independent of the diffusion mechanism, and was later confirmed by simulations [*Shay et al.*, 1999] and observations [*Sonnerup et al.*, 1981]. Another intuitive way to understand $v_{out} \sim v_A$ is to treat the reconnection structure as a standing Alfvén wave [*Birn and Priest*, 2007; *Drake et al.*, 2008]. The reconnected outflow magnetic field line forms a half wavelength of the wave, the phase velocity of the wave is $v_p = v_{Ao}$, where v_{Ao} is the Alfvén speed according to the reconnected magnetic field B_{out}, the outflow speed in the L direction follows

$$\tilde{v}_{out} = v_p \frac{\tilde{B}_{in}}{B_{out}} \cos(kz) \sin(k v_p t) \tag{1.11}$$

where z is the distance from the mid-plane in the N direction, and hence v_{out} has an amplitude of v_A [*Birn and Priest*, 2007].

With $v_{out} \sim v_A$, the reconnection rate for the system becomes

$$M_A = \frac{v_{in}}{v_A} \sim \frac{v_{in}}{v_{out}} = \frac{\delta}{l} \tag{1.12}$$

This means that the geometric aspect ratio of the diffusion region represents the reconnection rate.

In the Sweet-Parker model, M_A is $\sim S^{-1/2}$, where $S = \mu_0 l v_A / \eta$ is the Lundquist number. Sweet-Parker reconnection was confirmed by simulations [*Biskamp*, 1986; *Cassak et al.*, 2005], however, it predicted a reconnection rate that was too slow for the space environ-

ment where the resistivity is small and the global scale is large, e.g., the solar corona. Later *Petschek* [1964] developed another MHD reconnection model, which included two slow shocks at the separatrix and reduced the diffusion region length. In this way, Petschek's model can predict a faster system reconnection rate $M_A \sim \pi/(8 \ln S)$, which can be up to ~ 0.1 with the realistic parameters in the space environment, agreeing with the observations. However, Petschek's model requires a non-uniform resistivity, which makes it not generally valid and difficult to find evidence in simulations and observations [*Birn and Priest*, 2007].

In space plasmas, resistivity is usually negligible, which motivated people to develop *collisionless* reconnection models, which incorporate the kinetic effects of plasmas. The violation of the frozen-in condition is now governed by the generalized Ohm's law:

$$\vec{E} + \vec{v} \times \vec{B} = \eta \vec{J} + \frac{\vec{J} \times \vec{B}}{ne} - \frac{1}{ne} \nabla \cdot \overleftrightarrow{P_e} + \frac{m_e}{ne^2} \left[\frac{\partial \vec{J}}{\partial t} + \nabla \cdot \left(\vec{J}\vec{v} + \vec{v}\vec{J} - \frac{\vec{J}\vec{J}}{ne} \right) \right] \tag{1.13}$$

where $\overleftrightarrow{P_e}$ is the electron pressure tensor in the electron rest frame, and the terms of the order of m_e/m_i are neglected [*Vasyliunas*, 1975; *Birn and Priest*, 2007]. From the right-hand side of the generalized Ohm's law, we can learn which terms contribute to breaking down the frozen-in condition, and at which scale each term may dominate. The first term is the resistivity term, the same as in the collisional reconnection model, but is negligible for collisionless reconnection. The second term is the *Hall term*, which results from the decoupling of the ion and electron motions. The third term is related to the electron pressure tensor, and the last term is called the electron inertial term. Note that the Hall term and the diagonal terms in the electron pressure tensor term satisfy eq.(1.4), i.e., they are curl-free or can be removed by changing frames, so that they cannot break down magnetic flux conservation. It is the non-gyrotropic electron pressure tensor and electron inertial terms that cause reconnection to proceed.

The dominant scale sizes can be evaluated by comparing the amplitude of each term

with the $|\vec{v} \times \vec{B}| \sim v_A B$ term [*Vasyliunas*, 1975; *Birn and Priest*, 2007]. If we take into account the ion's finite temperature, the ions cannot keep their guiding center motion at a scale smaller than their Larmor radii, i.e., ions are demagnetized. On the contrary, electrons are still frozen-in, and the different motions between ions and electrons start to generate the Hall term at the scale of the ion Larmor radii. If the thermal velocity of the ions is negligible, with Ampere's law eq.(1.5), we obtain $|J| \sim B|/(\mu_0 \delta)$. Comparing $|\vec{J} \times \vec{B}|/ne$ with $v_A B$, the Hall term becomes important at a scale of $\delta < d_i$, where $d_i = c/\omega_{pi}$ is the ion inertial length. Similarly, the electron inertial term becomes large at the scale of the electron inertial length d_e. The characteristic scale of the electron pressure term is related to d_e and the electron Larmor radius, depending on the electron temperature. With the inclusion of kinetic effects, the diffusion region scales are no longer merely dependent on the global MHD scale as in the Sweet-Parker model. It was found that the diffusion region length was around $l \sim 10 d_i$, which produces a fast reconnection rate ~ 0.1 [*Shay et al.*, 1999].

As mentioned above, the Hall term comes from the decoupling of the ion and electron motions. The collisionless reconnection structure showing such decoupling effect is illustrated in Figure 1-2. Ions are demagnetized in a larger scale of the ion diffusion region (blue region), while electrons get access to the region closer to the X-line before being demagnetized in the electron diffusion region (EDR) (green region). The ion-electron decoupling forms an in-plane Hall current (red), and results in quadrupolar Hall magnetic fields in the M direction. The current sheet current in the M direction and the in-plane Hall current together produce a $\vec{J} \times \vec{B}$ Hall electric field (blue arrows), with an N component pointing towards the mid-plane, and an L component pointing from the X-line to the exhaust.

The Hall field signature is consistent with the standing whistler wave: it drives elec-

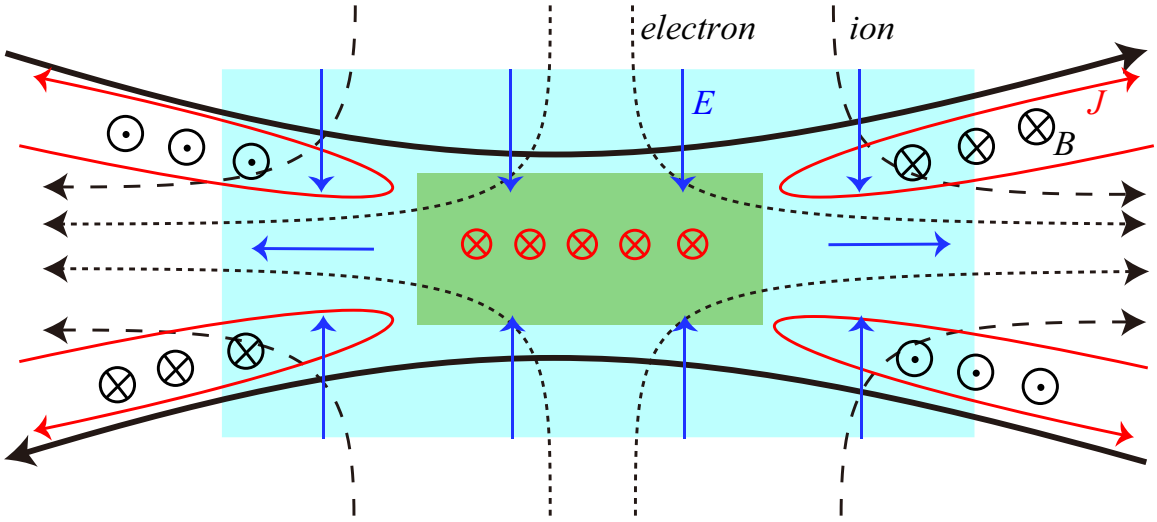

Figure 1-2: Illustration of the collisionless reconnection structure showing the decoupling of ion and electron motions.

trons to move out of the plane together with the magnetic field they are tied to, creating the quadrupolar B_M structure [*Mandt et al.*, 1994; *Birn and Priest*, 2007; *Drake et al.*, 2008]. Therefore, inside the ion diffusion region, the standing Alfvén wave no longer governs the reconnection structure and dynamics, but the whistler wave takes over. With similar analysis to the Alfvén wave, we can deduce the electron outflow velocity which is on the order of the electron Alfvén speed (v_{Ae}) based on the inflow magnetic field and density. On the other hand, the whistler wave phase velocity is proportional to the wave number k and inversely proportional to the EDR width, so is the electron outflow speed. The consequence from this dispersive property of the whistler wave is that $nm\delta v_L$, the electron momentum flux in the outflow direction, is independent of the EDR width.

During the *GEM* Reconnection Challenge, it was shown using different numerical simulation models (MHD, Hall MHD, hybrid and particle-in-cell (PIC)) that the fast reconnection rate of $M_A \sim 0.1$ can be achieved as long as the Hall term was included [*Birn et al.*, 2001]. This means that the reconnection rate only depends on the aspect ratio in the ion diffusion region scale, independent of the mechanism that breaks down the magnetic flux

conservation at smaller scales. This result is also consistent with the dispersive property of the whistler wave. The $\vec{E} \times \vec{B}$ drift from the Hall electric field E_N and the Hall magnetic field B_M is related to the outflow velocity v_L. Therefore, although the structure of the innermost part of the diffusion region might be different according to specific mechanisms that demagnetize electrons, the Hall structure can adjust the electron flow speed and width within the ion diffusion region, and the invariance of the electron flux ensures that the reconnection rate is only determined by the ion-scale diffusion region aspect ratio [*Drake et al.*, 2008]. The aspect ratio of 0.1 is another important but not fully understood scaling factor in reconnection studies.

1.3 Single-particle acceleration

The above models describe the fluid structures of magnetic reconnection. In order to understand how reconnection occurs inside the diffusion region where the fluid description is not valid, and how the energy is transferred from the electromagnetic field to plasmas, we need to discuss the single particle motions and accelerations in reconnection.

The particle motions in a current sheet with a normal component of the magnetic field was first studied by *Speiser* [1965]. When particles arrive at the current sheet mid-plane, they perform the meandering motion as shown in Figure 1-3. Here the x, y, and z directions correspond to L, M, and N, respectively. Particles bounce in the z direction and typically have a net motion in y. At the same time, particles also gyrate around the normal component of the magnetic field, turning from the y direction to the x direction. After finishing about half a period of turning, particles are ejected. The detailed trajectory and how many times the particles bounce before the ejection depend on the particles' energy and gyro-phase when they arrive at the mid-plane; however, they generally end up with a net displacement in y. When there is an electric field along y, which is the case in reconnection, particles

are accelerated. This is the basic acceleration mechanism for particles in the reconnection diffusion region.

Outside of their own diffusion region, ions and electrons are re-magnetized to the magnetic field, convect with and move along the field lines. In the ion diffusion region scale of the realistic reconnection structure, the Hall electric field in z pointing towards the mid-plane (Figure 1-2) helps trap ions near the mid-plane, and the electric field in x pointing towards the outflow direction (Figure 1-2) contributes to accelerating ions as they move downstream [*Wygant et al.*, 2005; *Liu et al.*, 2015].

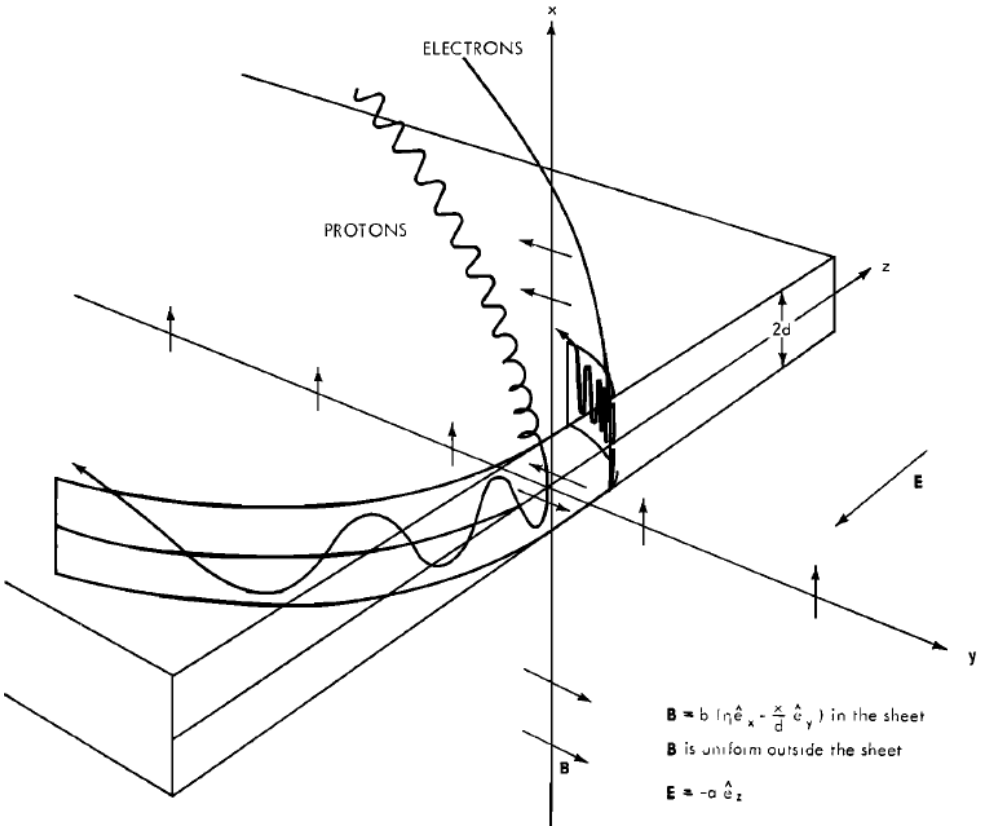

Figure 1-3: Illustration of the Speiser motion particles in a current sheet with a magnetic field component normal to the current sheet. Adapted from *Speiser* [1965].

Near the separatrix, large scales of the electric field parallel to the magnetic field ($E_{\|}$), which has a large component in x, can develop. It is mostly balanced by the electron

pressure gradient according to the generalized Ohm's law [*Le et al.*, 2009]. From PIC simulation results, such an $E_{\parallel}$ structure can extend to a large distance in the exhaust [*Le et al.*, 2009; *Egedal et al.*, 2012]. $E_{\parallel}$ can have localized bipolar or unipolar structures [*Drake et al.*, 2003; *Wang et al.*, 2014], but the large-scale $E_{\parallel}$ generally points away from the X-line. Therefore, electrons with energies below the potential of $E_{\parallel}$ can be trapped and bounce along the field lines [*Egedal et al.*, 2012], while ions obtain further acceleration and are repulsed to escape [*Liu et al.*, 2015].

Further downstream, the magnetic fields gradually pile up. Thus, particles can have curvature and gradient-B drifts in the M direction, especially close to the mid-plane where the magnetic field curvature and gradient are large. In this way, particles can be further accelerated by E_M [*Hoshino et al.*, 2001a; *Drake et al.*, 2006].

1.4 Magnetic reconnection in the Earth's magnetosphere

Magnetic reconnection in the Earth's magnetosphere was first investigated by *Dungey* [1961], who proposed the Dungey cycle model for the plasma convection in the magnetosphere. Figure 1-4 shows Dungey's original schematic plot for the southward Interplanetary Magnetic Field (IMF) condition. Reconnection first happens at the dayside magnetopause between the draped IMF in the magnetosheath and the magnetic field in the magnetosphere. When IMF has a different orientation, it is found that reconnection always occurs but the reconnection site at the magnetopause changes [*Fuselier et al.*, 2002]. Depending on the IMF orientation, reconnection at the dayside magnetopause can be either antiparallel reconnection, where the shear angle of the magnetic fields on two sides of the magnetopause is $\sim 180°$, or component reconnection, where the shear angle is much smaller. The reconnected field lines have only one end connecting to the Earth, and convect towards the magnetotail. Thus, magnetic flux is added to the lobes which builds up the magnetotail

pressure. As a consequence, the magnetotail current sheet turns thin, and the thickness can be comparable to the ion Larmor radius. The generation of a thin current sheet is a critical condition to destabilize the current sheet structure and to initialize reconnection in the magnetotail, though the exact mechanism for the reconnection onset is still unclear [*Birn and Priest*, 2007]. Reconnected field lines on the Earthward side of the magnetotail reconnection site return to the Earth, finishing the Dungey cycle.

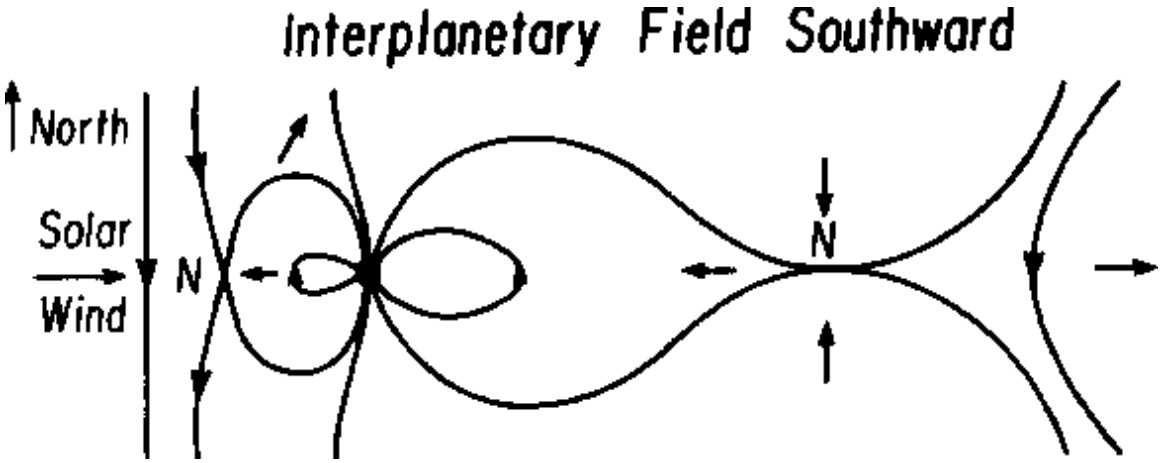

Figure 1-4: Illustration of the Dungey cycle with southward IMF. Reconnection occurs at both dayside magnetopause and magnetotail marked by the null point N. Adapted from *Dungey* [1963].

There has been direct observational evidence of reconnection in the magnetosphere. The clearest signature is the ion velocity jet along the L direction correlated with the magnetic field rotations, which have been observed in both magnetopause and magnetotail [e.g., *Paschmann et al.*, 1979; *Runov et al.*, 2005]. Besides, the Hall electric and magnetic field signatures have been observed supporting the detection of the reconnection ion diffusion region [*Mozer et al.*, 2002; *Vaivads et al.*, 2004].

More convincing evidence was also provided with detailed analysis of the spacecraft measurements. As discussed above, the reconnection structure can be regarded as a standing Alfvén wave, i.e., a rotational discontinuity. Therefore, it is possible to transform to a

deHoffmann-Teller (HT) frame, where the electric field vanishes [*deHoffmann and Teller*, 1950]. In the HT frame, plasmas flow along the magnetic field with the local Alfvén speed, which is the result of tangential pressure balance. A test for the field-aligned Afvénic flow in the HT frame is called the *Walén test* [*Walén*, 1944], and it has been successfully applied to the magnetopause observations to prove the existence of reconnection [*Sonnerup et al.*, 1987]. Figures 1-5a-1-5b show an example where the the observed plasma velocity agrees with the prediction from the Walén test for more than half an hour of observations, indicating a continuous reconnection [*Phan et al.*, 2004].

In addition, the velocity distribution functions (VDFs) are useful tools to analyze the behaviors of plasmas. When a spacecraft is located downstream of the diffusion region, ions must have velocities at least as high as the magnetic field convection velocity, i.e., deHoffmann-Teller velocity (v_{HT}), to be detected. Consequently, the VDF may exhibit a D-shaped signature with a lower cutoff velocity [*Cowley*, 1982], as shown in Figure 1-5c [*Phan et al.*, 2003]. The D-shaped VDF also acts as evidence for reconnection. The electron VDFs have been reported to be highly structured from inflow to outflow regions in both magnetotail observations and simulations [e.g. *Hoshino et al.*, 2001b; *Asano et al.*, 2008], which indicate the electron energization in reconnection.

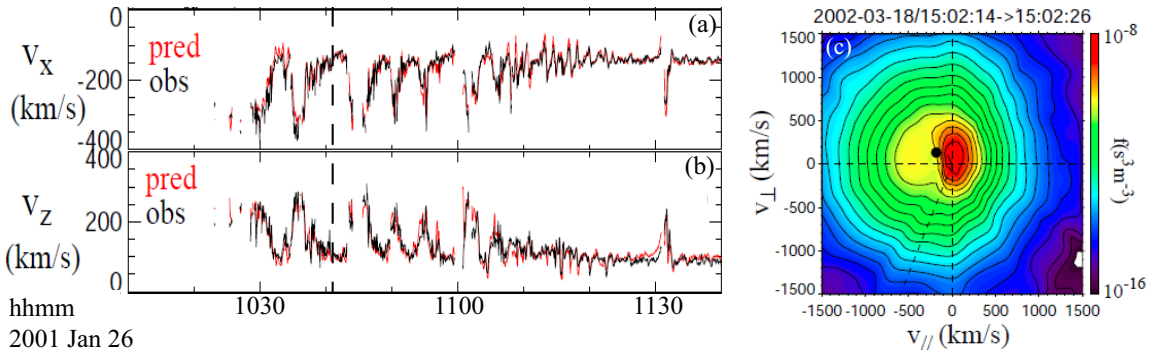

Figure 1-5: Observational evidence for the magnetopause reconnection. (a)-(b) Ion flows agree with the Walén test prediction. (c) D-shaped ion VDF with a lower velocity cutoff at v_{HT} in the parallel direction. Adapted from *Phan et al.* [2003, 2004].

1.5 Scope of this study

The overall goal of this study is to resolve a few outstanding problems in reconnection using a kinetic approach. One long outstanding problem is, "what effect do heavy ions or an enhanced cold population have on magnetic reconnection?" Both of these increase the mass density, but because of the different Larmor radius scales they introduce to the reconnection region, kinetic processes likely play an important role. The second problem is, "how are electrons heated in the reconnection region?" Because the predominant heating occurs in the electron diffusion region, where the electrons have become demagnetized, this problem also benefits from examining single particle behavior.

1.5.1 Magnetospheric hot O^+ and cold ions in the dayside magnetopause reconnection

One important feature for the dayside magnetopause reconnection is the asymmetric upstream conditions from two sides of the magnetopause. Typically the magnetosheath consists of denser ($n \sim 10\ cm^{-3}$) and colder (ion temperature $T_i \sim$ a few hundred eV) plasmas than the magnetosphere, where $n \sim 1\ cm^{-3}$ and $T_i \sim$ a few keV. The magnetic fields on the two sides can also be different. The different plasma populations may have different behaviors in the reconnection region. Understanding their behaviors is important, since it determines how these populations affect the reconnection structure. In addition, the reconnection rate R depends on the upstream conditions on both sides. *Cassak and Shay* [2007] showed that, theoretically, R in asymmetric reconnection follows

$$R_{cs} = \frac{\delta}{l} v_{A,asym} B_{asym} = 2\frac{\delta}{l}(B_{ph}B_{sh})^{3/2}(\mu_0\rho_{ph}B_{sh} + \mu_0\rho_{sh}B_{ph})^{-1/2}(B_{ph} + B_{sh})^{-1/2} \tag{1.14}$$

where ρ is the mass density, the subscripts of 'ph' and 'sh' indicate the magnetospheric and magnetosheath sides,

$$v_{A,asym} = \sqrt{\frac{B_{ph}B_{sh}}{\mu_0}}\sqrt{\frac{B_{ph}+B_{sh}}{\rho_{sh}B_{ph}+\rho_{ph}B_{sh}}} \tag{1.15}$$

is the hybrid asymmetric Alfvén speed, and

$$B_{asym} = \frac{2B_{ph}B_{sh}}{B_{ph}+B_{sh}} \tag{1.16}$$

is the hybrid asymmetric magnetic field.

During active times, the plasma sheet can contain significant amounts of O^+ [*Mouikis et al.*, 2010], and this population can drift to the magnetopause. A statistical study by [*Bouhram et al.*, 2005] of the ion composition at the dayside magnetopause showed that O^+ could be dominant in mass density in the magnetospheric boundary layer (MSPBL) on the dusk-side 30% of the time, while it is only dominant about 3% of the time on the dawn-side. They also showed that the O^+ population in the magnetosheath boundary layer (MSHBL) has a mean energy three times higher than that in the MSPBL, indicating that energetic ions escape more easily than lower energy ions. On the magnetospheric side, in addition to the hot plasma, there are also cold ions from drainage plumes or ionospheric outflow convecting to the magnetopause [e.g., *Borovsky et al.*, 2013; *Su et al.*, 2000]. If these O^+ and cold ions participate in the magnetopause reconnection, they may contribute more mass loading.

The Cassak-Shay theory has been tested in simulations. Using global MHD simulations, *Borovsky et al.* [2008, 2013] showed that the local reconnection rate, assuming the aspect ratio to be 0.1, is controlled by the upstream parameters on both the magnetosheath side and the magnetospheric side, rather than only by the magnetosheath parameters di-

rectly determined by the solar wind electric field. When plasmaspheric plumes produced in their simulations impacted the magnetopause, the magnetospheric inflow mass density was increased, and the local reconnection rate was shown to decrease as suggested by R_{cs} [*Borovsky et al.*, 2008, 2013; *Borovsky and Birn*, 2014].

However, the contribution to the reconnection by hot O^+ and cold ions may be different from the simple mass loading because of their possible kinetic effects. O^+ may interact with the magnetopause and directly leak out without being affected by the reconnection electromagnetic fields [*Eastman and Frank*, 1982]. If O^+ ions indeed participate in the reconnection process, they may form a larger scale of the diffusion region because of their larger Larmor radii compared with H^+ ions with the same gyro-velocity, and hence change the reconnection structure. Simulation results suggested that O^+ might increase the aspect ratio, which tends to cancel its effect of decreasing the reconnection rate by the larger mass density [*Shay and Swisdak*, 2004; *Karimabadi et al.*, 2011]. The overall effect of O^+ on the reconnection rate has not been tested in observations.

On the contrary, cold ions with smaller Larmor radii are more difficult to demagnetize, especially when there is a guide field, which is often the case at the dayside magnetopause. If the cold ions crossing the separatrix remain magnetized, they may maintain their adiabatic motion and be swept away by the magnetic field before reaching deep into the magnetosheath [*Drake et al.*, 2009a]. Thus their dynamics needs to be examined with observations.

Direct comparison of the Cassak-Shay theory with observations is still missing, particularly the consideration of possible effects from magnetospheric hot O^+ and cold ions. We will discuss the motions of these ion populations in the magnetopause reconnection (Chapter 3), and test the Cassak-Shay formulas to examine how the magnetopause reconnection rate depends on the local conditions (Chapter 4).

1.5.2 Electron heating in the magnetotail reconnection

It has been accepted that ions and electrons can be significantly energized in reconnection, however, the bulk thermal heating of plasmas has not been fully understood. Using the increase of the temperature scalar from inflow to outflow regions (ΔT_e) to represent the bulk heating, it measures how much electromagnetic energy is converted to the particles' average thermal energy. *Phan et al.* [2013] showed that in the asymmetric reconnection at dayside magnetopause, the bulk heating of the magnetosheath electrons scales with the upstream ions' Alfvén speed (v_{Ai}). The electron heating coefficient

$$r_h = k_B \Delta T_e / m_i v_{Ai}^2 \tag{1.17}$$

is about 1.7%, where k_B is the Boltzmann constant, and m_i is the ion mass. *Shay et al.* [2014] using a systematic simulation study showed that the electron bulk heating coefficient in symmetric reconnection with negligible guide field is around 3.3%. These studies suggested the heating coefficient with respect to $m_i v_{Ai}^2$ as another important scaling in reconnection to be resolved.

We will use both PIC simulations and magnetotail observations to study the electron bulk heating in reconnection with negligible guide field. We will first examine the electron temperature profile and the associated VDFs in the reconnection exhaust, and understand their features with single particle acceleration mechanisms (Chapter 5). Then we will propose a simplified VDF model to obtain the electron heating coefficient and present a statistical study of the electron bulk heating in the magnetotail observations (Chapter 6).

Chapter 2

Instrumentation and simulation

2.1 Cluster mission

The Cluster mission led by ESA/NASA consists of four identical spacecraft. Two pairs of the spacecraft were launched on 16 July and 9 August 2000, to a polar orbit with a perigee of 4 Earth radii (R_E) and an apogee of 19 R_E. The main goal for the Cluster mission is to study the small and medium scales of the plasma structures (100 km to 2-3 R_E) during the interaction between the solar wind and the Earth's magnetosphere [*Escoubet et al.*, 2001]. The separation between four spacecraft varies between 20 and 36,000 km, allowing for instantaneous multi-point measurements to study the three-dimensional structure [*Escoubet et al.*, 2013]. Each year, Cluster has a dayside season between November and June, when the spacecraft cross the dayside magnetopause and the cusp (between magnetospheric magnetic field lines going sunward and tailward), and they can provide observations for the dayside magnetopause reconnection. During the tail season between July and October, the spacecraft has an apogee in the magnetotail and can provide measurements for the reconnection there. Each Cluster spacecraft carries 11 instruments, and those from which the data are used in this study are briefly introduced as follows.

CIS: The Cluster Ion Spectrometry (CIS) package onboard Cluster spacecraft measures the full, 3D ion distributions in the magnetosphere [*Rème et al.*, 2001]. It consists of two

instruments. The COmposition and DIstribution Function analyser (CODIF) gives the ion composition, distinguishing H^+, He^+, He^{++}, and O^+ ions with different mass per charge values. It has a medium angular resolution of 22.5°, and has an energy range of 40-40,000 eV/e. The Hot Ion Analyzer (HIA) instrument does not distinguish the ion species, but has a higher angular resolution of 5.6° and an energy range of 5-32,000 eV/e. The time resolution for the ions' full 3D distribution ranges between 4 and 16 s.

RAPID: The Research with Adaptive Particle Imaging Detectors (RAPID) instrument measures 3D energetic ion and electrons fluxes in energies above ∼30 keV [*Wilken et al.*, 1997]. For the ion measurements, it also distinguishes H^+, He^+, and O^+ ions. It has 8 energy channels and 9 pitch angle bins for each species. The ion 3D data, which are used in this study, have a nominal time resolution of 8 spins (32 s).

PEACE: The Plasma Electron And Current Experiment (PEACE) measures the electron distributions [*Johnstone et al.*, 1997]. It has two sensors: HEEA (High Energy Electron Analyser) and LEEA (Low Energy Electron Analyser), which are mounted opposite to each other. PEACE has 88 energy channels in the range of [0.6 eV, 26 keV], and energy range in usage is adjusted mainly according to the spacecraft potential. In the magnetotail, LEEA typically has an energy range of [5 eV, 2.5 keV], and that for HEEA is [30 eV, 2.6 keV]. Each sensor has 12 angular bins. Combining the observations from two sensors, PEACE obtains full pitch angle range measurements in half a spin, and it takes one spin to take the full 3D measurements. The moments data (density, velocity, etc.) are produced from the 3D data. Due to the limitation in the telemetry transmission, the 3D and moments data have a typical resolution of 40 spins under the normal mode. There are higher resolutions on C2 up to one spin after 25 November 2001 and C4 up to 3 spins after 21 March 2002, due to the donating telemetry from other failed instruments on these spacecraft [*Fazakerley*, 2014].

FGM: The FluxGate Magnetometer (FGM) instrument provides the magnetic field measurements [*Balogh et al.*, 2001]. It has 6 ranges and resolutions according to the magnetic field features where the spacecraft are located. The best resolution is 7.8×10^{-3} nT with the measurement range of [-64, 63.97] nT, and the largest measurement range is [-65,536, 65,536] nT with a resolution of 8 nT. The full-resolution magnetic field data have time resolutions of 22 Hz and 67 Hz in the normal and burst modes, respectively.

EFW: The Electric Field and Waves (EFW) instrument measures the electric field with four spherical probes on two pairs of long wire booms, which are orthogonal to each other with 88 m tip-tip [*Gustafsson et al.*, 1997]. It measures the 2D electric fields in the spin plane, and the field in the third dimension can be deduced with an assumption of $\vec{E} \cdot \vec{B} = 0$, which is true most of the time. The full resolution of the electric field data have a resolution of 25 Hz or 450 Hz depending on the telemetry mode. It also provides the spacecraft potential data, which is the potential difference between the spacecraft and the probe, with a full resolution of 5 Hz.

WHISPER: The Waves of High frequency and Sounder for Probing of Electron density by Relaxation (WHISPER) instrument measures the electric field wave spectra with a frequency range of [2, 82] kHz [*Décréau et al.*, 1997]. It has two operation modes. In the natural mode, the transmitter stands by and receives the wave signals, which produces a NATURAL spectrum. In the sounding mode, the transmitter sends a wave train during a short time interval and receives the signals afterwards, which produces an ACTIVE spectrum. According to the wave spectra features, WHISPER also provides the electron density product.

2.2 CODIF O^+ contamination and H^+ flux saturation in the magnetosheath

There are two limitations in the CODIF measurements that are related to the study in this thesis and will be addressed here. The first one is the O^+ contamination by the high-flux magnetosheath H^+ at the dayside magnetopause boundary layer. CODIF uses a combination of electrostatic and time-of-flight (TOF) analysis techniques [*Möbius et al.*, 1998]. The ElectroStatic Analyzer (ESA) of CODIF discriminates ions depending on their energy per charge (E/q). Particles accepted by the ESA will undergo a post-acceleration of 15 kV. The TOF analyzer deduces the velocity of the accepted ion by measuring 'start' and 'stop' times as the particle traverses a known distance. In this way, it accumulates the counts of particles with different times of flight, generating the TOF spectrum. For a given energy per charge, a separation by time of flight is equivalent to a separation by mass per charge.

Normally, there is a low level of false 'start'-'stop' coincidences, which leads to a low level of background that affects all species. This background level increases with the incident particle rate. For the peak magnetosheath flow, about 1% of the H^+ rate extends to the O^+ channels, and is observed as background in O^+. Because the O^+ flux is normally low compared with the intense magnetosheath flux, this low background percentage still constitutes a significant background for the O^+. However, the background only affects the limited energy and angle range where the H^+ flux is intense. Figure 2-1 shows an example of the issue. The top panel shows the H^+ energy spectrogram during a time when there are multiple traversals between the magnetosphere (Msph) and the magnetosheath (Msh) across the magnetopause (MP). In the Msph, the H^+ energy flux is predominantly at high energies. In the Msh, there is a much more intense flow of H^+ around 1 keV/e. The second panel shows the O^+ spectrum. A significant "ghost spectrum" of O^+ is clearly seen at

the same energies as the intense H^+ flux. This part of the spectrum, circled in red, is the background. However, at higher energies there is a separate population. This is real O^+, not background. At these higher energies, away from the Msh bulk proton energy, the instrument properly distinguishes the different species.

The key point, that makes this distinction possible, is that if H^+ and O^+ have the same velocity, the O^+ energy will be a factor of 16 (the mass ratio) higher. Thus any O^+ ion moving at the same MSH velocity as H^+ will be at $\sim$16 keV, not at $\sim$1 keV. Since the instrument measures each energy per charge at a different time, the 16 keV O^+ does not suffer contamination from the high rate at 1 keV. In addition, the majority of the O^+ detected close to the magnetopause originates in the magnetosphere. As can be seen in the O^+ energy spectrum plot (Figure 2-1b), the majority of the O^+ counts in the MSPH are at energies above 5 keV. Again, these "real" O^+ measurements are not affected by the H^+ background around 1 keV, and it is easy to observe O^+ with the same bulk flow as H^+ and to examine the distribution functions for magnetospheric ions crossing the magnetopause. Figure 2-1c shows the number density of H^+ (black) and O^+ (red) above 5 keV excluding the contamination. Figures 2-1d-2-1g show comparisons of the H^+ (black) and O^+ (red) velocity components and the total velocity during this time period, where only O^+ above 5 keV has been included in the calculation. The H^+ and O^+ velocities agree, in significant detail, most of the time. This would not have been the case if the background were included in the calculation, as that would have added a component at a significantly different velocity. This shows that while the CODIF moment data cannot be blindly used in these regions, by choosing the uncontaminated range of the O^+ distribution, the important parameters can be derived. In addition, the dominant magnetospheric population is located at the higher energies where there is no contamination. Therefore the CODIF data can be used to test for finite Larmor radius effects that may lead to transport of this population across the

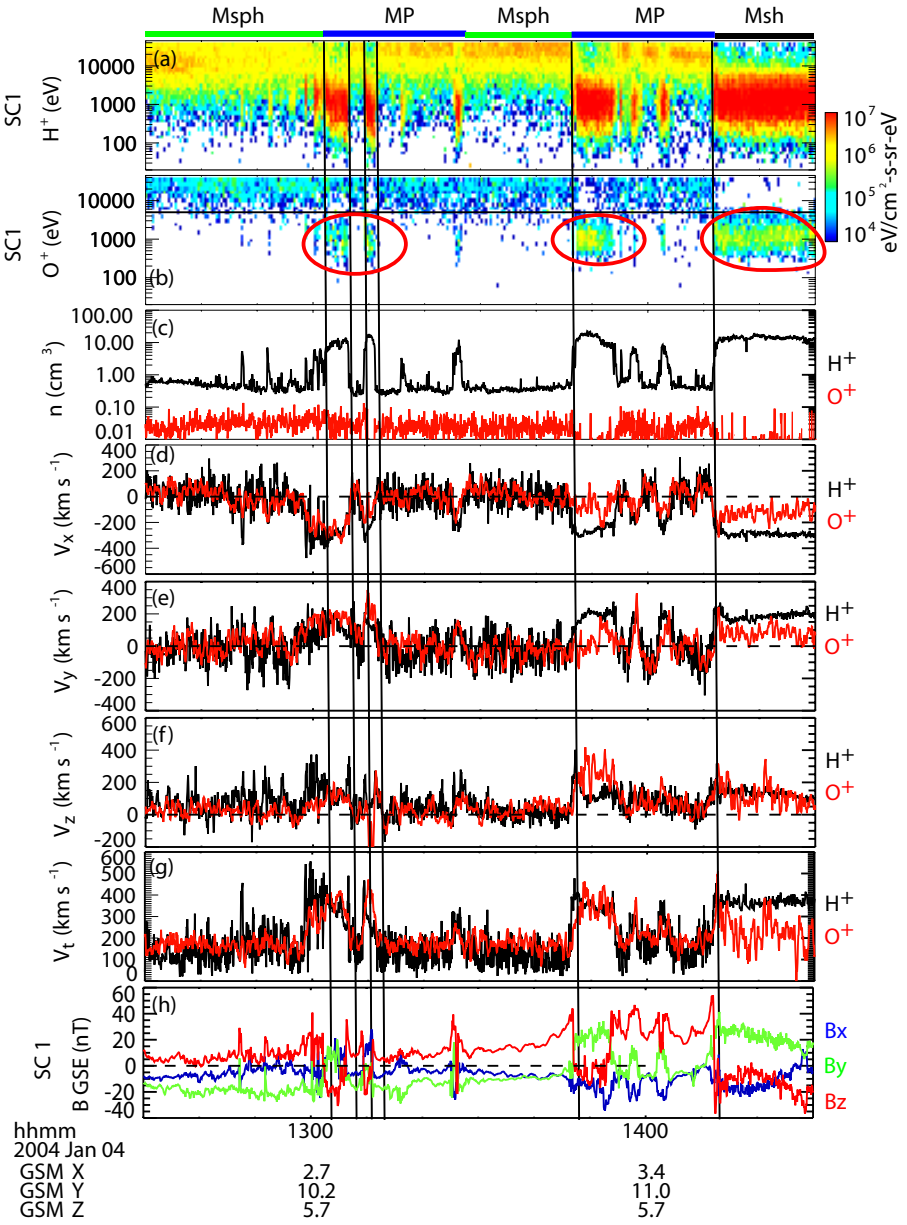

Figure 2-1: Cluster/CODIF data showing the comparison between H^+ velocities and O^+ velocities calculated using energies >5 keV to avoid the contamination from H^+. (a) H^+ energy flux; (b) O^+ energy flux; (c) H^+ (black) and O^+ (red) number density; (d)-(f) H^+ (black) and O^+ (red) velocity components in GSE; (g) H^+ (black) and O^+ (red) total velocity; (h) magnetic field in GSE. The number density and velocities of O^+ are calculated with energy channels above 5 keV (black line in panel (b)) and are box-car averaged using a window of 20 s. The red circles in (b) show the contamination of H^+ in O^+.

magnetopause. In summary, despite the background contamination, with the CODIF data set we are able to determine when O^+ participates fully in the reconnection, flowing with H^+ in the outflow jets, and test for kinetic effects by examining the distribution functions of the more energetic population.

The second problem is the underestimate of the particle density in regions with large plasma flux, such as in the magnetosheath. In such regions, the TOF electronics in the CODIF instrument cannot measure the full rate due to electronic dead-time effects. However, the CODIF instrument has a second set of electronics (position electronics), which are capable of measuring a much higher maximum count rate than the TOF electronics. Thus, by monitoring the count rates of the two sets of electronics it is possible to: (a) identify times when the TOF electronics suffers from significant dead-time effects and (b) account for the missing counts during such times, by scaling up the TOF measurements to match those measured by the position electronics, and distributing the total missing counts into different angular bins in a reasonable way.

Figure 2-2a shows the H^+ energy flux from CODIF. Figures 2-2b-2-2c show CODIF density measurements (black line) before and after the high-rates correction is applied. Density measurements from HIA are shown in red. The deduced total electron density from the WHISPER wave instrument is shown in blue. These measurements are used to cross-calibrate CODIF and to confirm the accuracy of the high-rates correction. Note that in Figure 2-2b during each encounter with the high-flux, low energy, magnetosheath plasma, the CODIF-measured density (black) is much lower than that of the other two instruments. During the entire interval shown in Figure 2-2c when WHISPER density data is available, the corrected CODIF H^+ and WHISPER deduced e^- densities are in almost perfect agreement [*Genestreti*, 2012]. This cross-calibration effort has given us confidence in the CODIF H^+ measurements taken in the magnetosheath. Such high-rate correction is

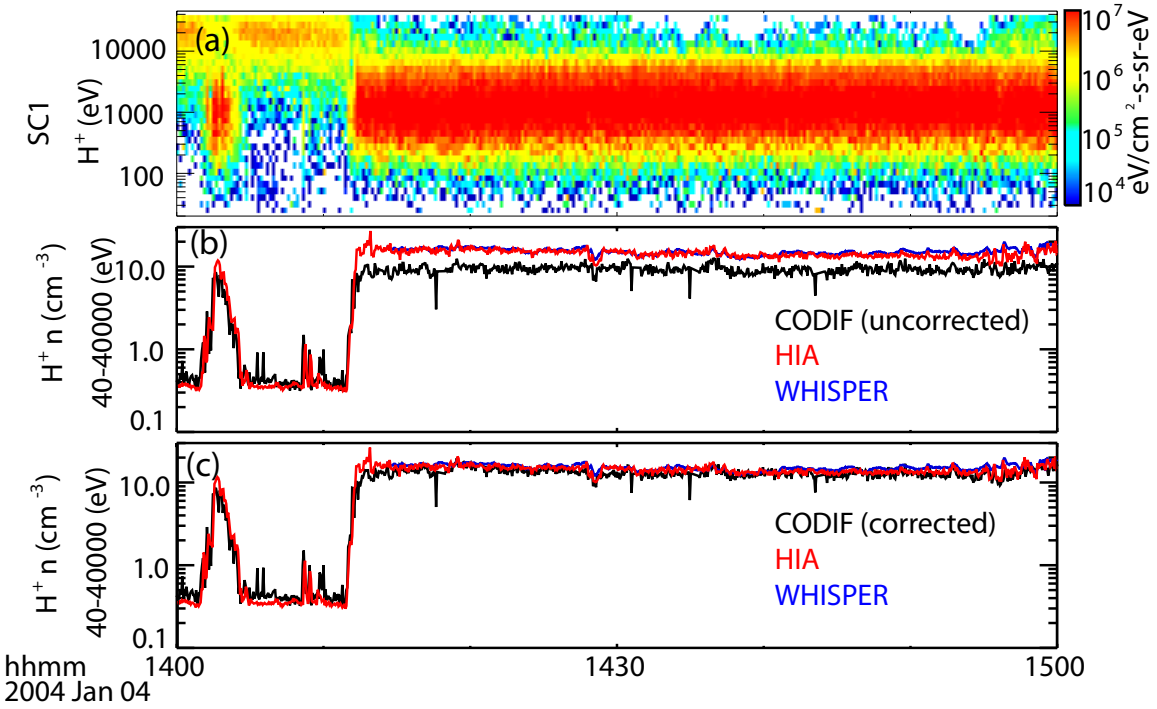

Figure 2-2: Illustration of the high rate correction of the CODIF density. (a) H^+ energy flux; (b) CODIF uncorrected H^+ density compared with HIA and WHISPER data; (c) CODIF H^+ density with high rate correction compared with HIA and WHISPER data.

applied for the events in this study.

2.3 Estimate of the magnetospheric cold ion densities near the magnetopause

Cold ions of plasmaspheric or ionospheric origin may appear on the magnetospheric side of the magnetopause, whose density needs to be carefully estimated. Far from the magnetopause in the magnetosphere, they have typical energies around 1 eV and cannot be measured by most ion instruments due to their lower energy limit. As the cold ions convect to the magnetopause, they obtain an $\vec{E} \times \vec{B}$ drift velocity and their apparent energies are increased. Therefore, the cold ion population, or a fraction of this population, can be measured by HIA or CODIF. In Figure 2-3a, the H^+ spectrum exhibits a separate low-energy

population close to 50 eV around 23:15:40 UT (marked by the red dashed line), indicating the existence of cold ions near the magnetopause. However, it is not certain that the whole population is observed by CODIF/HIA in order to accurately deduce the density.

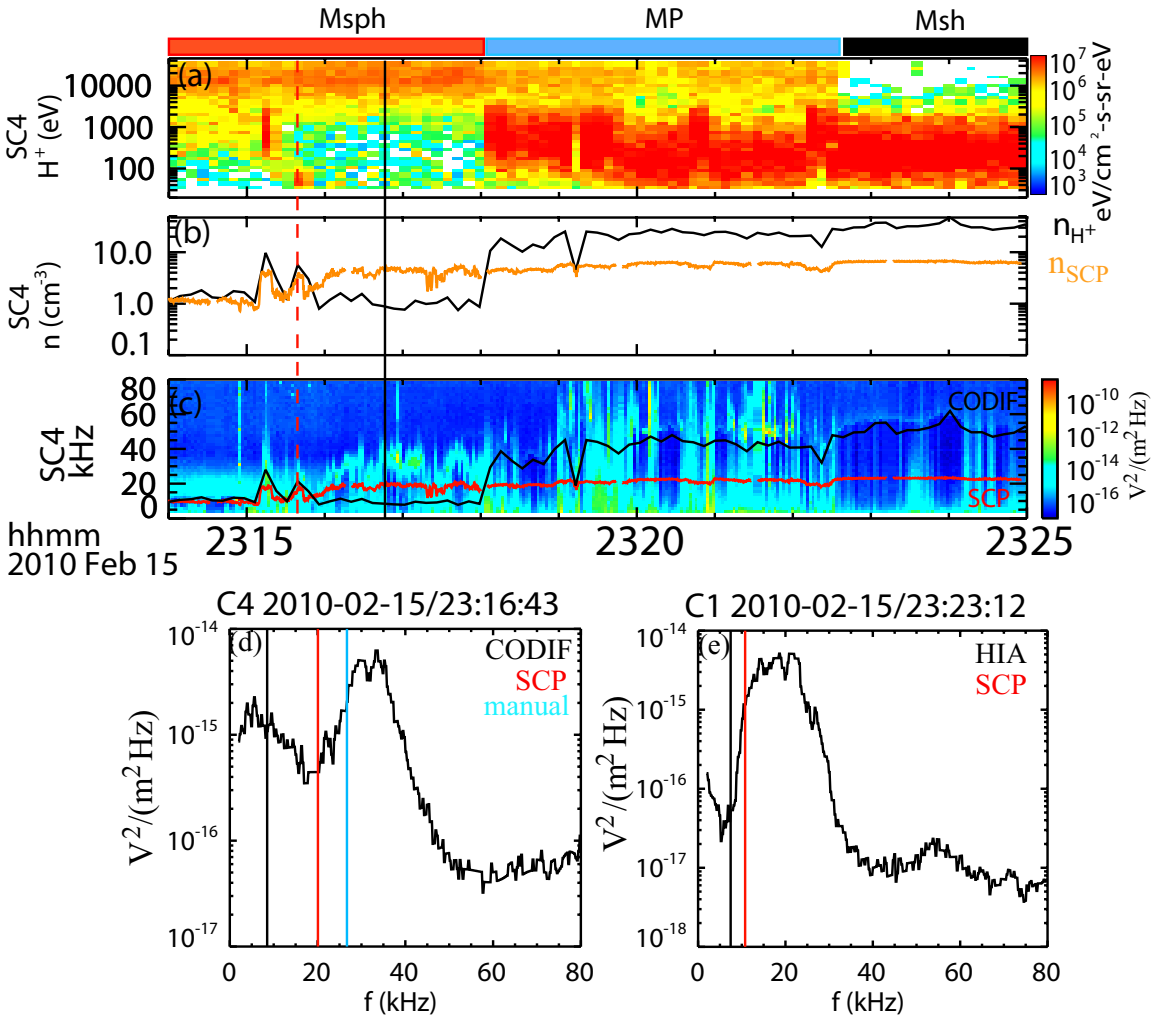

Figure 2-3: Plasma density estimate when the cold ions are present. (a) H^+ energy spectrum; (b) H^+ density (black), and the total e^- density derived from spacecraft potential (SCP) (orange); (c) Natural mode wave spectrum from WHISPER superimposed with plasma frequencies (f_{pe}) derived from $n_{H^+,CODIF}$ and n_{SCP}; (d)-(e) 1D WHISPER wave spectra for C4 and C1. Vertical lines mark the f_{pe} derived from the density with ion measurements (black) and SCP (red). f_{pe} from SCP well matches the cutoff frequency for C1, but underestimates that for C4. The blue line in (d) is the cutoff frequency manually selected.

One indirect way to obtain the density measurement is using the spacecraft potential (SCP). Empirical formulas have been built up to deduce the electron density from the SCP,

which are based on the current balance between the ambient electrons going towards the spacecraft and the photoelectrons emitted from the spacecraft [*Lybekk et al.*, 2012]. The density (n_{SCP}) calculated from these formulas for the interval shown in Figure 2-3 is plotted as the orange line in panel b. n_{SCP} is close to n_{H^+} (black) at the beginning of the interval in the magnetosphere, increases to higher values around 23:16 where n_{H^+} still maintains the same density level with earlier intervals, and is lower than n_{H^+} when the magnetosheath population becomes dominant. The discrepancy in the magnetosheath should be attributed to the limitation of the empirical formula between SCP and n_{SCP}. This formula depends on the density range [*Lybekk et al.*, 2012] and is optimized for estimating the density of tenuous plasmas where the Debye length was considerably larger than the spacecraft scale [*Pedersen et al.*, 2008]. Therefore it does not work well in the magnetosheath where the density is high. However, the n_{H^+} increase when the spacecraft is still in the magnetosphere is likely real, indicating the existence of the cold ions where CODIF cannot measure them. Note that the O^+ density is much smaller than the difference between n_{H^+} and n_{SCP} (not shown), so that it cannot explain the discrepancy.

Finally, another way to determine the plasma density is using the natural mode wave measured by WHISPER, where its cutoff frequency corresponds to the electron plasma frequency ($f_{pe} = \sqrt{ne^2/\epsilon_0 m_e}/2\pi$), where n is the plasma density and m_e is the electron mass [*Décréau et al.*, 1997; *André and Cully*, 2012]. WHISPER has an electron density product with more rigorous calibrations, however, close to the boundary layers like that shown in Figure 2-3, the electron density data are usually not available, so we need to determine it directly from the wave spectra.

We employ all three methods (CODIDF/HIA measurements, SCP formula and wave cutoff frequencies) to estimate the plasma density. In Figure 2-3c, at the beginning of the interval (in the magnetosphere), the cutoff frequency observed by WHISPER agrees

well with the cutoff derived from n_{H^+} (black) and n_{SCP} (red), indicating that all three methods provide reliable densities. Around 23:16-23:18 UT, the measured cutoff frequency is higher than the derived ones from both methods, which might indicate that both methods underestimated the plasma density. Figure 2-3d shows the one-dimensional (1D) cut of the wave spectrum within this interval (at the time marked by the black vertical line in (a)-(c)), which indicates the difference between the real and the derived cutoff frequencies more clearly. We manually determine the cutoff frequency for each point with a clear cutoff during the interval of interest. The selected frequency is in the middle of the spectrum slope. In Figure 2-3d, the slope is selected to be between 23.5 Hz and 30 Hz, which also acts as the uncertainty of such a method. Thus, the cutoff frequency is 26.75±3.25 Hz, corresponding to a density of 8.83 cm^{-3} with an uncertainty range of 6.82 cm^{-3} to 11.11 cm^{-3}. The uncertainty of the density is about 25%.

Figure 2-3e shows another example of the WHISPER spectrum from C1 on the magnetospheric side of the magnetopause close to C4. At this time, n_{SCP} was higher than n_{HIA}, so that the cutoff frequency derived from n_{SCP} (red) was higher than that from n_{HIA} (black). In this case, the cutoff frequency from n_{SCP} agrees well with the real one at the spectrum sharp slope. Therefore, for C1 in this case, n_{SCP} does represent the plasma density, and we do not need to manually select the WHISPER cutoff frequency. The consistency of n_{SCP} and/or n_{HIA} with the density derived from the WHISPER cutoff frequency gives more confidence to the density estimate, and reduces its uncertainty.

Using the above procedure, where we mainly use the wave cutoff frequency as a reference when it is clear, we determine the total plasma density. By subtracting the hot H^+ and O^+ densities observed by CODIF (above 100 eV) from the total density, we can get the cold ion density.

2.4 Obtaining electron temperature data with the PEACE pitch angle distributions

As mentioned above, the PEACE moments data often have low time resolutions down to $\sim$ 160 s. In this study, we need the electron temperature data with higher resolutions in the reconnection exhaust region. Therefore, we use the pitch angle distributions to estimate the electron temperature at spin resolution (4 s). We apply two methods for the estimate: direct integration and Maxwellian fitting.

The direct integration method is as follows. By definition, the temperature tensor is the integration of the 3D PSD (f_{3D}):

$$\mathbf{T} = \frac{m \iiint (\vec{v} - \vec{v}_0)(\vec{v} - \vec{v}_0) f_{3D} d^3v}{k_B \iiint f_{3D} d^3v} \tag{2.1}$$

where $\vec{v}$ is the velocity, $\vec{v}_0$ is the bulk velocity, m is the mass and k_B is the Boltzmann constant. For the electron distributions in the reconnection region, which is what we are interested in, its bulk speed is much smaller than its thermal velocity, and the calculation with and without the subtraction of the bulk velocity show negligible difference. Therefore, we assume $\vec{v}_0$ to be zero. Assuming the electron distribution to be gyro-tropic, and the $\mathbf{T}$ tensor is diagonal in the field-aligned coordinate, we can get $T_{e\parallel}$ and $T_{e\perp}$ as

$$T_{e\parallel} = \frac{m \iiint v_\parallel^2 f_{3D} d^3v}{k_B \iiint f_{3D} d^3v} \tag{2.2}$$

$$T_{e\perp} = \frac{m \iiint v_\perp^2 f_{3D} d^3v}{2k_B \iiint f_{3D} d^3v} \tag{2.3}$$

and $T_{et} = (T_{e\parallel} + 2T_{e\perp})/3$. With pitch angle distributions of PSD (f), eq. (2.2) and (2.3)

become

$$T_{e\parallel} = \frac{m \sum\limits_{v_\parallel, v_\perp} v_\parallel^2 2\pi f v_\perp \Delta v_\parallel \Delta v_\perp}{k_B \sum\limits_{v_\parallel, v_\perp} 2\pi f v_\perp \Delta v_\parallel \Delta v_\perp} = \frac{\sum\limits_{E,\theta} 4\sqrt{2}\pi f E^{3/2} \cos^2\theta \sin\theta \Delta E \Delta\theta}{k_B \sum\limits_{E,\theta} 2\sqrt{2}\pi f E^{1/2} \sin\theta \Delta E \Delta\theta} \tag{2.4}$$

$$T_{e\perp} = \frac{m \sum\limits_{v_\parallel, v_\perp} v_\perp^2 2\pi f v_\perp \Delta v_\parallel \Delta v_\perp}{2k_B \sum\limits_{v_\parallel, v_\perp} 2\pi f v_\perp \Delta v_\parallel \Delta v_\perp} = \frac{\sum\limits_{E,\theta} 2\sqrt{2}\pi f E^{3/2} \sin^3\theta \Delta E \Delta\theta}{k_B \sum\limits_{E,\theta} 2\sqrt{2}\pi f E^{1/2} \sin\theta \Delta E \Delta\theta} \tag{2.5}$$

where $E = 1/2m(v_\parallel^2 + v_\perp^2)$ is the energy, and θ is the pitch angle.

The data used for the integration are selected according to the following rationale. LEEA measurements almost covered the energy range for the distributions in the inflow (point 1) and separatrix regions (point 2), but not for those in the outflow region. Therefore, for the outflow points (3-8) we used distributions at consecutive two points from HEEA together, which covered the full pitch angle range, to calculate the temperatures. In addition, the low-energy distributions were contaminated by photo-electrons. Therefore, we need to choose a lower limit of the energy for integration ($E_{l,int}$). We chose $E_{l,int}$ where the distribution deviated from the sharp decrease at low energies (usually around 200-400 eV), and tried to make it relatively consistent between different points.

Figure 2-4 shows the comparison between the integrated electron total temperature ($T_{e,int}$) and that from the PEACE moments data ($T_{e,mom}$). During the shown interval, C2 has a high time resolution (4s), and $T_{e,int}$ (blue) agrees well with $T_{e,mom}$ (blue) (Figure 2-4a), especially for high-temperature intervals (above ~2000 eV). On the other hand, it significantly improves the time resolution for the C1 measurements (Figure 2-4b). Figure 2-4c shows a 1D distribution example, which is the pitch angle averaged PSD from HEEA in two half-spin frames. The blue vertical line marks the $E_{l,int}$.

In addition to the direct integration, we also used Maxwellian fitting to estimate the

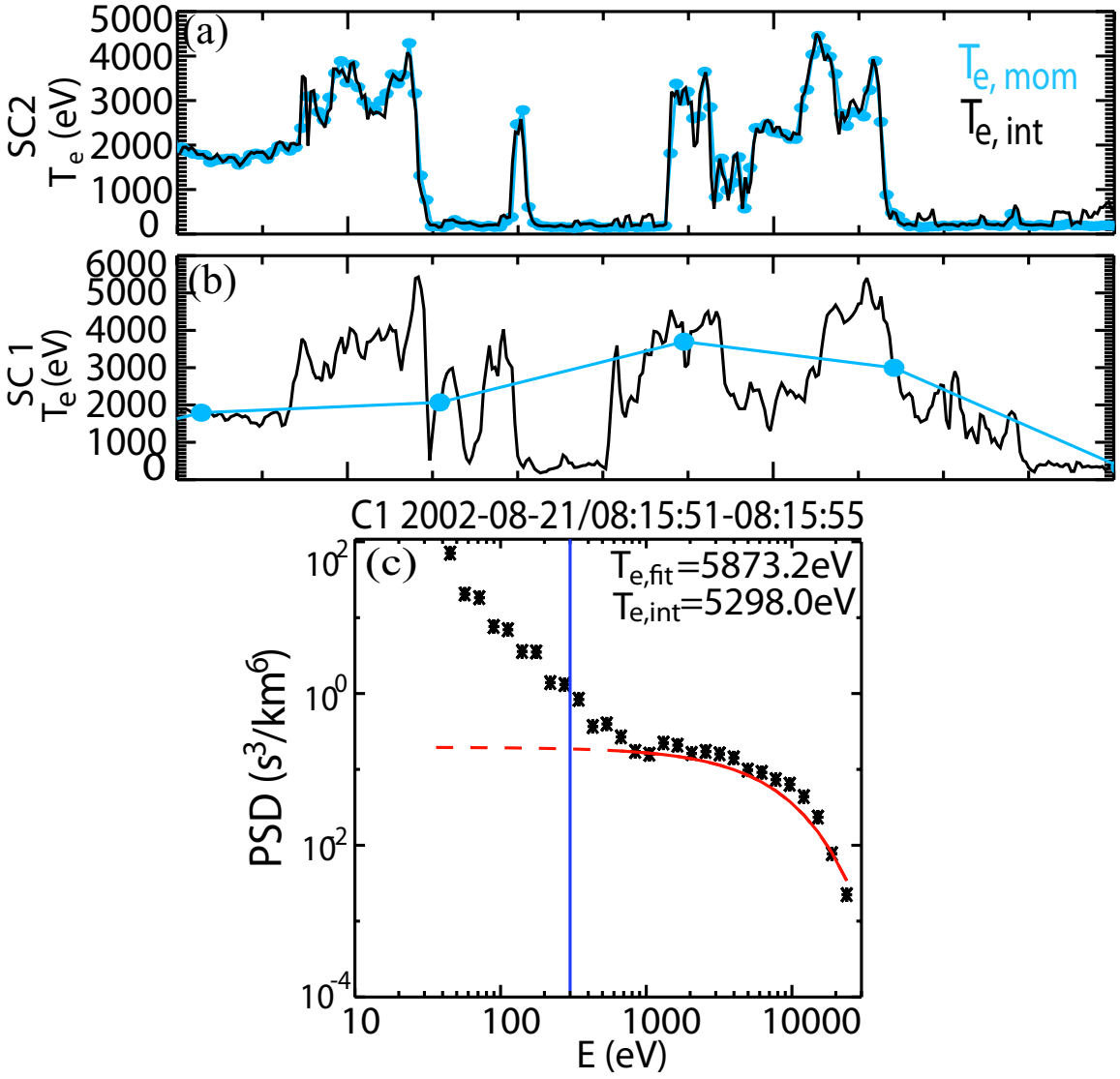

Figure 2-4: Electron temperature estimates from the pitch angle distributions. (a)-(b) comparisons between the electron total temperature integrated from the pitch angle distributions ($T_{e,int}$, black) and that from the PEACE moments data ($T_{e,mom}$, blue) for C2 and C1 data. (c) an example 1D pitch-angle averaged PSD from C1. The black points are the PSD data, the blue vertical line marks the lower energy limit to perform the temperature integration, and the red curve is the Maxwellian fitting results with the energy range overlaid by the solid part (above 400 eV).

temperatures, where the reduced 1D PSD (f) follows

$$f = n\left(\frac{m}{2\pi k_B T}\right)^{3/2} \exp\left(-\frac{E}{k_B T}\right) \tag{2.6}$$

We took the average PSD over all pitch angles as shown in Figure 2-4c, and estimated the temperature from the best fitting results. For the example spectrum in Figure 2-4c, the red curve is the Maxwellian fitting result, where the black points in the energy range overlaid with the solid red fitting curve (above 400 eV) are used in fitting. The resulting temperature $T_{e,fit}$ is around 5900 eV, with a difference of $\sim$ 10 $\%T_e$ with $T_{e,int}$. Thus we use two methods and the comparison with the available moments data to confirm that our temperature estimates with the pitch angle distribution are reliable.

Since it is more robust to perform the integration for long intervals than using the fitting method, we apply both methods to analyze the temperature for individual data points of interest, but only use $T_{e,int}$ for statistics.

2.5 Ion pressure calculation with the combination of CODIF and RAPID measurements

In this study, we need to combine the CODIF and RAPID H^+ and O^+ measurements in the plasma sheet to calculate the total ion pressure, and add it with the magnetic pressure to obtain a total pressure. However, there is an energy gap between the available CODIF and RAPID energy channels, which can have a considerable contribution for the pressure calculation. Therefore, we perform an interpolation to fill in the data gap. The interpolation uses the pitch-angle averaged ion spectra, and we assume that the pitch angle distribution for the interpolated energy channels are the same as that for the RAPID channel used for the interpolation. For H^+, the measurement in the lowest energy channel of RAPID is not reliable, and there is an energy gap between the first and second energy channels [*Kronberg and Daly*, 2015]. Therefore, we interpolate two data points for the H^+ spectra between the highest CODIF channel at $\sim$35 keV and the second RAPID channel at $\sim$80 keV. For O^+, the lowest energy channel often does not have valid data since it was found

to be mainly contaminated by H^+, and there is an energy gap between the first and second energy channels [*Kronberg and Daly*, 2015]. Thus, the interpolation is between the highest CODIF channel at $\sim$ 30 keV and the second RAPID channel at $\sim$300 keV. Since the energy gap for O^+ is large, we interpolate five data points in this energy range. With more than five data points, the improvement of the spectrum interpolation for the pressure calculation is negligible.

Figure 2-5 shows an example of the interpolation in the energies between CODIF and RAPID energy ranges for H^+, with the original (a) and interpolated (b) energy spectrograms, pitch angle distribution for the RAPID energy channel used for the interpolation (c), and the H^+ total pressure calculation. The 1D PSD at the time marked by the vertical line is shown in Figure 2-5.

We apply two methods to interpolate the PSD for the lowest two RAPID energy channels between the two horizontal lines in Figures 2-5a and 2-5b. The ion spectrum in the plasma sheet at a distance of $R > 12R_E$ follows the κ distribution

$$f = n\left(\frac{m}{2\pi\kappa W_0}\right)^{3/2}\frac{\Gamma(\kappa+1)}{\Gamma(\kappa-1/2)}\left(1+\frac{E}{\kappa W_0}\right)^{(-\kappa+1)} \tag{2.7}$$

where W_0 is the energy at the peak differential particle flux and $W_0 = k_B T(1-3/2\kappa)$ [e.g., *Christon et al.*, 1989]. The statistical κ value is $\sim 4-8$ [*Christon et al.*, 1989]. Therefore, we perform a κ fitting for the combined CODIF and RAPID spectra. In Figure 2-5e, the dashed line is the fitting result with $\kappa = 6.0$, and the red points are at the interpolation energies. The PSDs of the two interpolated points are 109.5 s^3/km^6 with a 95% confidence interval of [96.8, 124.2] s^3/km^6 and 17.9 s^3/km^6 with a 95% confidence interval of [15.2, 21.3] s^3/km^6. The fitting agrees with the general trend of the combined spectrum, so that the interpolated points are considered reliable.

We also tried a simpler method assuming a power-law distribution between the two

points used for the interpolation (marked by arrows in Figure 2-5e), i.e., a linear interpolation between the two points in the $log - log$ scale. The interpolated data are shown in blue, which are close to the κ fitting results. The energy spectrogram after the linear interpolation looks smooth in the transition energies between CODIF and RAPID (Figure 2-5b).

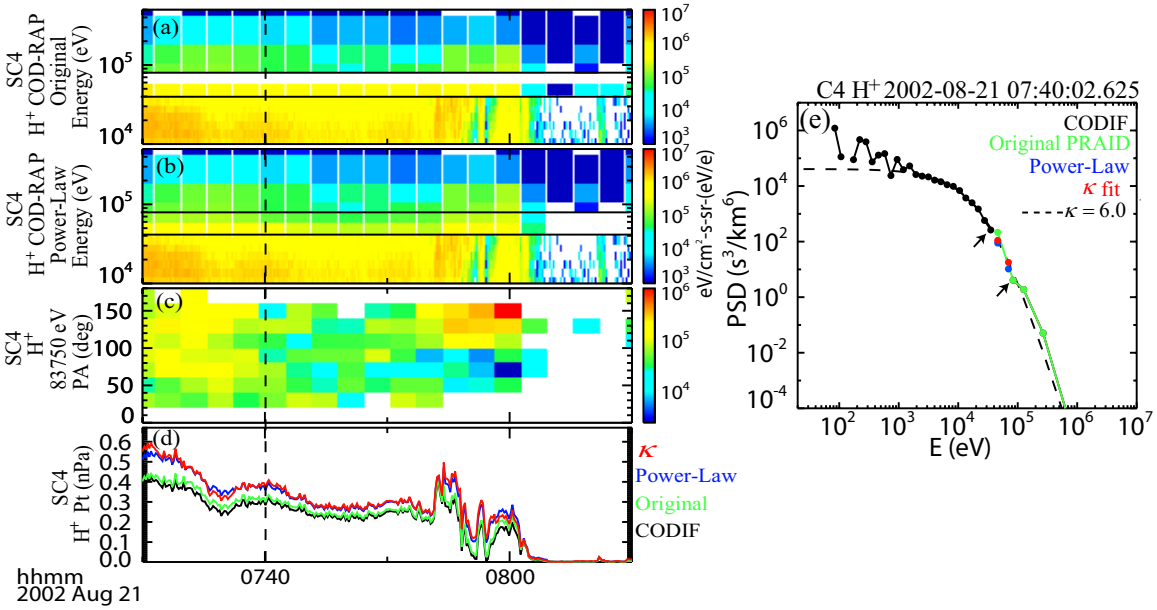

Figure 2-5: Pressure calculation with combined CODIF and RAPID data. (a)-(b) combined H^+ energy spectrogram from CODIF and RAPID measurements, where the original RAPID data are used in (a), and those with the power-law interpolation at the lowest two energy channels of RAPID (between two horizontal lines) are presented in (b). (c) H^+ pitch angle distribution at the RAPID energy channel that is used for the interpolation (right above the upper horizontal line in (a) and (b). (d) total H^+ pressure using only CODIF data (black) and combined CODIF-RAPID data with the lowest two energy channels of RAPID missing (green), power-law interpolated (blue) and fitted with a κ distribution (red). (e) 1D pitch-angle averaged PSD at the time marked by the vertical lines in (a)-(d) showing the interpolated RAPID data points as indicated by the legend. The two points used for the interpolation are marked by the black arrows.

With the pitch angle distribution in the RAPID energy channel that is used for the interpolation (Figure 2-5c), the pressure can be calculated with the new ion distribution as shown in Figure 2-5d. The pressure with the original RAPID data excluding the measurement at the lowest channel (green) is close to that with only CODIF measurements,

indicating that the contribution from energies higher than the third RAPID energy channel is small. However, there is a clear increase in pressure calculated from the interpolated spectrograms with κ fitting (red) and the power-law distribution (blue), which can account for $10\% - 30\%$ of the total pressure. In particular, the perpendicular pressure with the κ fitting interpolation at the time shown in Figure 2-5e is 0.385 nPa with a 95% confidence intervals of [0.375, 0.394] nPa, and the uncertainty determined by the confidence interval is about 2.4%. On the other hand, the pressure obtained by the power-law interpolation is 0.369 nPa, with a 4.1% of the pressure difference from that using the κ interpolation. The obtained ion pressure will be added with the magnetic pressure to calculate the total pressure, so that the difference caused by the different interpolation methods is more negligible. Since it is easier and more robust to get continuously reliable interpolations with the power-law assumption than with κ fitting, we use the power-law interpolation for H^+ and O^+ spectra in the data used in this study.

2.6 Solar Wind Data

The solar wind data we use are from the OMNI website (http://omniweb.gsfc.nasa.gov), which combine the measurements from multiple spacecraft (WIND and ACE, etc) at the L1 point. The 1-min resolution solar wind data are shifted to the position of the Earth's bow shock, so that they can be compared with the in situ observations in the magnetosphere more easily.

2.7 Particle-in-cell simulation

In this thesis, we also analyze particle-in-cell (PIC) simulations of reconnection. The PIC method is a numerical way to solve the Vlasov equation for the particle distribution $f_s(\vec{x}, \vec{p}, t)$, where s represents the species [*Birdsall and Langdon*, 1991; *Bowers et al.*,

2008; *Germaschewski et al.*, 2013]:

$$\frac{\partial f_s}{\partial t} + \vec{v} \cdot \frac{\partial f_s}{\partial \vec{x}} + q_s \left(\vec{E} + \vec{v} \times \vec{B} \right) \cdot \frac{\partial f_s}{\partial \vec{p}} = 0 \tag{2.8}$$

In the PIC method, the distribution function is approximated using quasi-particles with finite spatial sizes. Instead of directly solving eq. (2.8), the PIC code calculates the motions for quasi-particles, which are governed by equations

$$\frac{dN_i^s}{dt} = 0, \frac{d\vec{x}_i^s}{dt} = \vec{v}_i^s, \frac{d\vec{p}_i^s}{dt} = q_s \left(\vec{E}_i + \vec{v}_i^s \times \vec{B}_i \right) \tag{2.9}$$

where i represents the i_{th} quasi-particle. The moments of quasi-particles are integrated from the distribution functions using area weighting [*Daughton et al.*, 2006; *Germaschewski et al.*, 2013]. The size of the quasi-particles resolves the Debye length, so that the simulation is modeling the collective behavior of plasmas, instead of the strong interactions between individual particles. Thus, the simulation can be considered collisionless.

For the PIC simulations used in this thesis study, the electromagnetic fields are calculated with scalar and vector potentials [*Daughton et al.*, 2006]

$$\vec{B} = \nabla \times \vec{A} \tag{2.10}$$

$$\vec{E} = -\nabla\phi - \frac{1}{c}\frac{\partial \vec{A}}{\partial t} \tag{2.11}$$

which follow the Maxwell's equations, and require the input of the charge density and the current density calculated from the particle data. The fields are advanced with an explicit algorithm [*Morse and Nielson*, 1971], and the particles are advanced using the leapfrog method. The simulations apply open boundary conditions, the details of which are described in *Daughton et al.* [2006].

Run NO.	m_i/m_e	B_g/B_0	n_b/n_0	T_b/T_0	v_{Ai0}/c
1	400	0	0.05	0.33	0.025
2	400	0.03	0.05	0.33	0.025
3	1836	0	0.23	0.76	0.012
4	1836	0.05	0.23	0.76	0.012

Table 2.1: Parameters for the PIC simulations used in this study. B_g is the guide field, B_0 is the asymptotic magnetic field of Harris current sheet, n_b is the background plasma density, n_0 is the Harris sheet density, T_b is the background plasma temperature, T_0 is the current sheet temperature, and v_{Ai0} is the ion Alfvén speed based on B_0 and n_0.

We analyze four PIC simulations of symmetric magnetic reconnection with zero or weak guide field, where the reconnection is initiated by a perturbation in the magnetic field [*Daughton et al.*, 2006]. All simulations are 2.5-dimensional, but are different in the ion-to-electron mass ratio (m_i/m_e) and guide field strength. The simulations start from an equilibrium Harris current sheet with $B_x = B_0 \tanh(z/L)$ and $n = n_0 \,\mathrm{sech}^2(z/L) + n_b$, where x is along the current sheet, z is perpendicular to the current sheet, $L/d_i = 0.5$, $d_i = c/\omega_{pi}$ is the ion inertial length, ω_{pi} is the ion plasma frequency based on the peak density at the current sheet center n_0, and n_b is the background lobe density. For all simulations, the initial ion and electron temperature ratio is T_i/T_e=5, and $\omega_{pe}/\omega_{ce} = 2$, where ω_{pe} is the electron plasma frequency based on n_0, and ω_{ce} is the electron gyro-frequency based on B_0. Other simulation parameters are listed in Table 2.1. The simulation domain size is $L_x \times L_z = 80d_i \times 20d_i$ for runs 1 and 2, and $20d_i \times 20d_i$ for runs 3 and 4.

Chapter 3

Magnetospheric hot O^+ and cold ion behaviors in magnetopause reconnection

3.1 Introduction

We first discuss the behavior of the magnetospheric ions at the dayside magnetopause: whether they directly leak out to the magnetosheath with the finite Larmor radius effect, participate into the reconnection undergoing a non-adiabatic demagnetization process, or are involved in reconnection adiabatically without being demagnetized. There have been observations of particles escaping from the magnetosphere into the magnetosheath, and the velocity characteristics were used to discuss the escape mechanisms. *Sibeck et al.* [1987], using data from the CCE satellite, showed that the reason that ions appear on the magnetosheath-side magnetopause is due to the finite Larmor radius effect at low latitudes, and they gradually escape to the magnetosheath at higher latitudes. More recently, [*Marcucci et al.*, 2004] reported a case study in which O^+ formed a boundary layer on the magnetosheath side of the magnetopause at mid latitudes. The finite Larmor radius effects lead to a measured bulk velocity that is higher than the actual bulk motion [e.g., *Zong*

and Wilken, 1998, 1999]. Furthermore, *Zong et al.* [2001] reported a case where O^+ at the magnetopause was observed by Geotail and interpreted it as escape along the magnetic field during steady reconnection. *Kasahara et al.* [2008] showed a case where the high-energy O^+ escaped along the field lines under northward IMF condition with reconnection at high latitudes. *Phan et al.* [2004] also showed that O^+ appeared during every outflow jet in a series of Flux Transfer Events (FTE) observed during a reconnection event that lasted for about two hours, indicating its involvement in reconnection.

Borovsky et al. [2013] and *Walsh et al.* [2014] used simulation results and THEMIS observations to show that cold ions from the drainage plumes can become the main contributor of the plasmas density at the magnetopause, and therefore that the outflow speed is decreased accordingly. *Lee et al.* [2014] analyzed a case of antiparallel reconnection at the magnetopause where cold ions were observed, and showed that the cold ions mainly move with the $\vec{E} \times \vec{B}$ drift velocity. They interpreted the motion of the cold ions to be adiabatic.

Until now, there has not been a study that analyzes the distribution functions of hot magnetospheric O^+ in dayside magnetopause reconnection events or those of cold ions in reconnection with a guide field. In this chapter, we compare simple models of the motion of magnetospheric energetic H^+ and O^+, as well as cold ions in dayside magnetopause reconnection events, with the velocity distribution functions (VDFs) observed in the data, to distinguish the mechanisms for the formation of each population in the distribution. In this way we attempt to elucidate whether and how the energetic heavy ions and cold ions are involved in reconnection.

3.2 Models for ion velocity distribution functions

With different types of motions, ions exhibit different signatures in VDFs. In this section we provide simplified VDF models, which identify the observable signatures of Finite Larmor

Radius (FLR) effects and reconnection outflow in VDFs.

3.2.1 Finite Larmor Radius effect

Figure 3-1a shows the schematic trajectories of particles in an equilibrium current sheet in the $M - N$ plane, with the magnetosphere (Msph) below and the magnetosheath (Msh) above the current sheet. The gyration of the ions is always left-handed (looking along the magnetic field), so that a magnetospheric particle from below the current sheet with a Larmor radius larger than half of the current sheet thickness performs a meandering motion, i.e., it gyrates up and down but usually has a net velocity in the M direction, shown as the trajectory on the right of Figure 3-1a. The distance that a magnetospheric particle reaches on the magnetosheath side (above) of the current sheet depends on the gyro-phase at which the particle reaches the current sheet center. The particle that moves almost tangential to the current sheet center can reach the furthest point, which is about two Larmor radii from the current sheet center (Figure 3-1a).

The origin of the coordinate system, shown with dashed lines in Figure 3-1a, is at the center of the outermost gyration circle shown, with a radius of r. If a spacecraft is located at a distance $h > r$ from the current sheet center, represented by the blue line, it can only detect ions that can gyrate above the spacecraft location. Therefore, only parts of the particle gyro-phases can be observed. Consider the ions with a Larmor radius of r and a gyro-velocity of v. For the ion that can gyrate furthest away from the current sheet center, i.e., its guiding center is at r, when it arrives at the distance of h, $v_M = v \sin\theta$, and $v_N = \pm v \cos\theta$, where θ represents the gyro-phase when the particle arrives at the distance of h (Figure 3-1a). The guiding centers of other particles with the same gyro-velocity are lower than r. If they can arrive at the distance of h to be observed, they will have $v_M > v \sin\theta$ at h. Therefore, the observed v_N is positive when gyrating up and negative

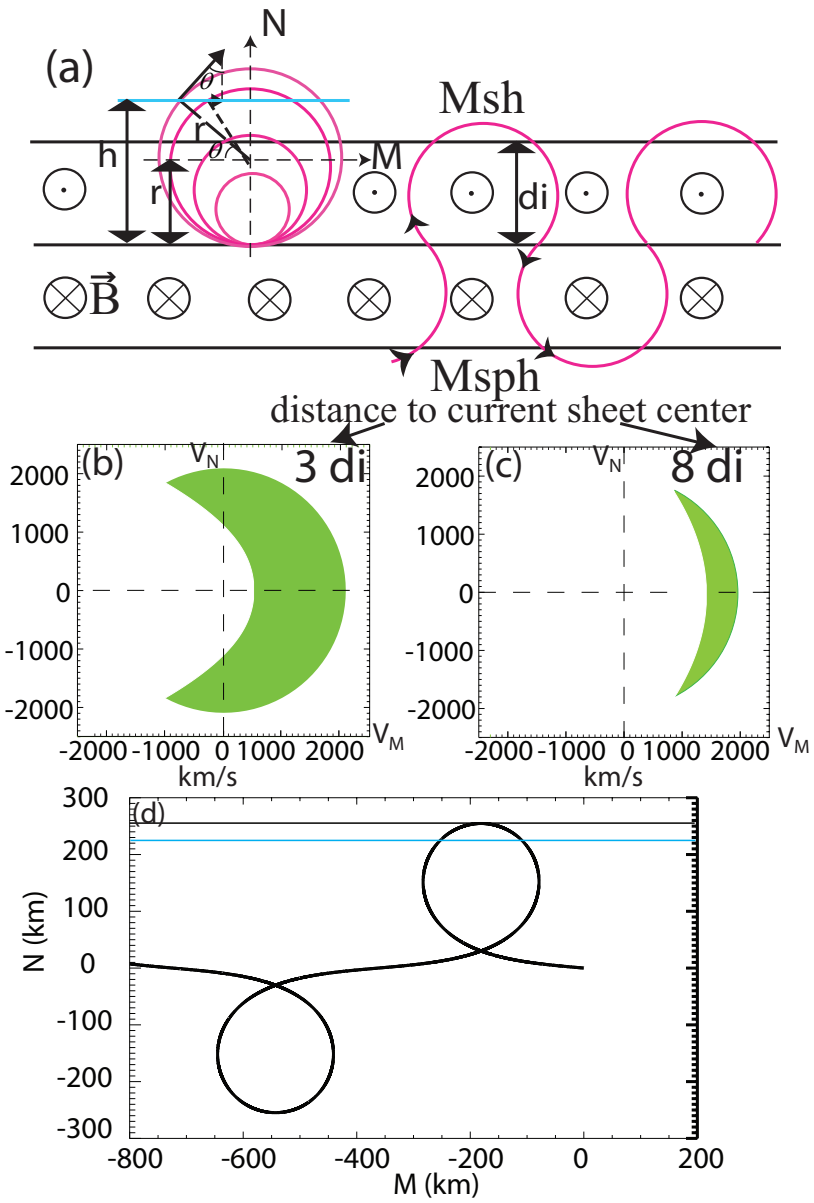

Figure 3-1: Models of ion motion for magnetospheric hot ions showing the finite Larmor radius effect (a)-(d) and reconnection with a guide field (e)-(g). (a) Trajectories of ions in the equilibrium current sheet. (b) and (c) Expected ion velocity distribution functions (VDFs) in the $v_M - v_N$ plane. (d) Comparison between the calculation and the test-particle tracing of the finite Larmor radius effect. (e) Trajectories of ions and electrons in reconnection with a guide field. (f) and(g) expected ion VDFs model in the MSHBL side of the current sheet center.

when gyrating down. The observed v_M can only be positive, and its minimum value is $v \sin\theta$. The cutoff velocity of the particles with the gyro-velocity of v at the distance of

h is $v_M = v\sin\theta,\ v_N = \pm v\cos\theta$. Since v is arbitrary, we can derive the cutoff velocity $v_c = v\sin\theta$ for all v at a fixed h to get the approximate VDF. Such cutoff velocity signatures in the VDF are called the finite Larmor radius effect (FLR).

We assume that the magnetic field follows the Harris current sheet

$$B = B_0 tanh\left(\frac{z}{L}\right) \tag{3.1}$$

where z is in the N direction, B_0 is the asymptotic magnetic field away from the current sheet and L is the half width of the current sheet. We further assume that L is the same as the ion inertial length (d_i). As the particle gyrates, the magnetic field at the particle location changes continuously. We approximate the average motion to be the gyration around a uniform magnetic field with the magnetic field strength (B_r) at one Larmor radius $r = mv/eB_r$ above the current sheet center:

$$B_r = B_0 tanh\left(\frac{r}{d_i}\right) \tag{3.2}$$

so that

$$v = \frac{eB_r r}{m} = \frac{eB_0 tanh\left(\frac{r}{d_i}\right) r}{m} \tag{3.3}$$

θ can be expressed as

$$\sin\theta = \frac{h-r}{r} \tag{3.4}$$

Therefore, the v_M cutoff can be expressed as

$$v_c = v\sin\theta = \frac{eB_0 tanh\left(\frac{r}{d_i}\right)(h-r)}{m} \tag{3.5}$$

With this relation, we can calculate the cutoff velocity for particles with the guiding

centers located at different r, i.e., with different gyro-velocity amplitudes. We take the parameters from the Cluster data on 25 February, 2005, when there was an observed reconnection event discussed below, in order to approximate the observed current sheet. We take B_0 as the magnetosheath magnetic field, around 50 nT, and the half width of the current sheet as the ion inertial length, which is around 75 km for this event.

Figures 3-1b and 3-1c show the resulting VDFs in the $v_M - v_N$ plane, at distances h from the current sheet center of 3 d_i and 8 d_i, respectively. The distribution functions show a higher velocity cutoff at larger distances from the current sheet center, as expected.

In the above analysis, we use the assumption that the gyro-motion is approximately the gyration around a uniform magnetic field with the strength at the guiding center, so that the furthest location where the particle can arrive is two Larmor radii above the current sheet center based on the magnetic field at the guiding center. We use a test-particle technique to test this assumption. The magnetic field is set to be the Harris current sheet used above, and the current sheet center is at $N = 0$. Figure 3-1d shows a trajectory for an ion with a gyro-velocity of 487 km/s starting at the current sheet center with an initial gyro-phase (θ) of 5° relative to the M direction. A smaller θ corresponds to a farther distance from the current sheet. Since the particle with $\theta = 0$ moves in the $-M$ direction for a long time before gyrating up, we only test particles with θ larger than 5°. The furthest location for the $\theta = 5°$ particle is 254 km (black horizontal line in Figure 3-1d). The gyro-velocity of 487 km/s is the v_M cutoff with $v_N = 0$ at 3 d_i as shown in Figure 3-1b, so that the estimated furthest location for the particle with this gyro-velocity is $3d_i = 225km$, represented by the blue line in Figure 3-1d. It is close to the test-particle result in the Harris current sheet of 254 km, and the difference between the two is about 11%. We tested the trajectories of particles with gyro-velocities between 300 and 3000 km/s, which cover the range of hot magnetospheric H^+ velocities detected by Cluster. The difference between the simplified

calculation and the test-particle result ranges between 4% and 15%, with smaller differences at larger gyro-velocities.

Therefore, we can use our simplified method to analyze the ion's gyro-motion in the presence of a current sheet, where Figures 3-1b and 3-1c are expected to represent its velocity distribution with FLR. In addition, if the plasma has a bulk velocity, the whole distribution will shift with the bulk velocity, since only the gyro-motion causes the velocity cutoff.

3.2.2 Reconnection outflow distribution functions

Figure 3-2a illustrates the magnetic field configuration at the dayside magnetopause reconnection region. In addition to the reversal B_L in the current sheet center, there is also a guide field pointing into the plane. The ion and electron reconnection outflow (blue and green arrows, respectively) points away from the X-line. In the magnetosphere boundary layer (MSPBL), which is on the magnetospheric side of the B_L reversal, the field lines connect with the ionosphere. The outflow electrons that have a very fast speed along the field lines can be quickly reflected back from the ionosphere, so that the high energy electrons appear in both parallel and antiparallel directions in this region [*Fuselier et al.*, 2011]. These bi-directional electrons are indicated with the double green arrows in Figure 3-2a. In the magnetosheath boundary layer (MSHBL) and the magnetosheath (Msh), plasmas can have a bulk background flow velocity along the current sheet, especially in the high latitudes. The gray arrows in Figure 3-2a indicate the Msh flow direction in the event discussed below.

D-shaped VDFs in the outflow region are good indicators of reconnection, although they are not always observed [*Cowley*, 1982; *Phan et al.*, 2004]. The magnetic field lines convect with the deHoffmann-Teller velocity (V_{HT}), so that only the population with a velocity higher than V_{HT} can be detected. The velocity cutoff at V_{HT} in the outflow direction

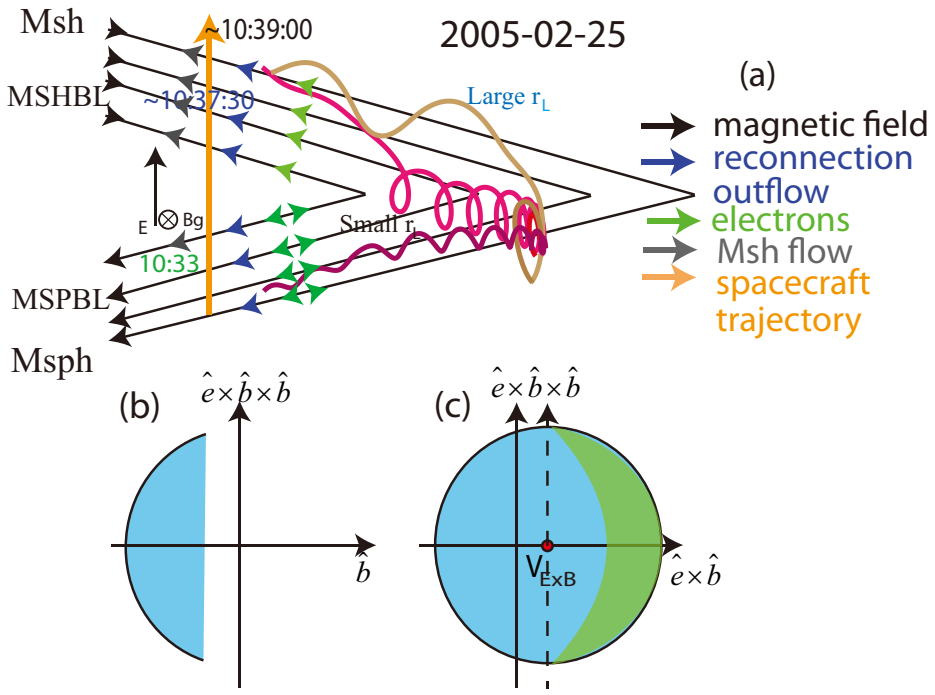

Figure 3-2: Models of ion motion for magnetospheric hot ions in reconnection (a) Trajectories of ions and electrons in reconnection with a guide field. (b) and (c) expected ion VDFs model in the MSHBL side of the current sheet center.

results in the D-shaped distribution [*Cowley*, 1982]. Furthermore, the velocity cutoff in the distribution depends on the location of the spacecraft due to the time-of-flight (TOF) effect. Closer to the separatrix, the detected particles come from the newly reconnected magnetic field lines closer to the X point, so they must travel in a shorter time from where they are accelerated to the spacecraft location, than those observed in the current sheet center with the same distance from the X-line in the L direction. Therefore, the cutoff velocity of the D-shaped distribution function increases from the field reversal region to the separatrix [*Fuselier et al.*, 2005].

According to *Drake et al.* [2009a,b], when there is negligible guide field or the particles have large Larmor radii when there is a strong guide field, ions exhibit non-adiabatic motions after entering the exhaust region. The ions are then picked up by the magnetic field lines with a perpendicular velocity comparable to the initial value they have when they enter the

exhaust after crossing the separatrix region [*Drake et al.*, 2009b]. In this way, for an ion away from the current sheet center, its parallel velocity (mainly along B_L) is reflected in the exhaust frame, since there is no electric field in this frame to accelerate the particle. In the rest frame, the ion would gain a parallel velocity that is twice the parallel component of V_{HT}, and gain a perpendicular velocity equal to the $\vec{E} \times \vec{B}$ drift speed. This provides a microphysical explanation for the D-shaped distribution with the cutoff velocity at V_{HT} along the parallel direction, as shown in Figure 3-2b. Thus the velocity cutoff is caused by both the reflection of the parallel velocity in the deHoffmann-Teller frame and the TOF effect, where the TOF effect makes the cutoff velocity vary in different sub-regions: lower in the field reversal region and higher close to the separatrix.

In the presence of a guide field, particles with small Larmor radii are taken away adiabatically by the magnetic field, with an $\vec{E} \times \vec{B}$ drift velocity, right after they cross the separatrix boundary layer to the exhaust region [*Drake et al.*, 2009a]. At the same time, they flow along the guide field with their initial velocities from the inflow region. The purple curve in Figure 3-2a illustrates the trajectory of such an ion. The ions with large Larmor radii become non-adiabatic when crossing from the inflow to the exhaust regions and can travel deeper towards the other side of the current sheet center. They don't move along the guide field; instead, they gyrate around it. Unless B_L is negligible compared with the guide field strength, the ions with large Larmor radii still have a parallel component along B_L of the velocity in the exhaust. The magenta and brown curves in Figure 3-2a, which go further towards the magnetosheath side than the purple curve, illustrate their trajectories. The VDFs in the parallel direction should still have D-shaped velocity cutoffs as in the anti-parallel case in Figure 3-2b, but ions with small/large Larmor radii may be distinguished by whether the motion is adiabatic, according to [*Drake et al.*, 2009a].

The ion VDFs in the perpendicular plane should have a shift in the bulk velocity at

the local $\vec{E} \times \vec{B}$ drift velocity (Figure 3-2c). The particles gyrate around the magnetic field as they move in the outflow direction, so that the finite Larmor radius effect may also be observed in this region. Therefore, there should be perpendicular velocity cutoffs due to the FLR effect on top of the distribution in the perpendicular plane. This is shown by the green shading in Figure 3-2c.

In summary, during reconnection at the magnetopause, we expect to observe D-shaped distributions in the outflow region away from the current sheet center with a parallel cutoff velocity, and velocity cutoffs from finite Larmor radius effects in the perpendicular direction close to and outside of the magnetosheath separatrix. All these velocity cutoffs are expected to occur at lower velocities near the field reversal region and at higher velocities close to the separatrix. In reality, because of the complexity of the magnetic field topology, the acceleration directions may be difficult to compare with the simplified model. However, one possible way to determine whether the ion undergoes a non-adiabatic process is to compare the velocity directions as it crosses the current sheet. If the process is adiabatic, the velocity direction in the magnetic field coordinates in the exhaust frame will be maintained. If the process is non-adiabatic, the velocity direction in geographic coordinates in the exhaust frame will be maintained, while there are changes in the magnetic field coordinates because of the magnetic field reversal.

3.3 Observations of the reconnection event on 25 February, 2005

3.3.1 Overview

Figure 3-3 shows the overview of a reconnection event that occurred on 25 February, 2005 as observed by Cluster S/C 4. The Cluster spacecraft crossed the dayside mid-latitude

magnetopause (Figures 3-3a-3-3b) around 10:00 UT. The spacecraft stayed in the boundary layer for about 1 hour before they fully entered the magnetosheath. From 10:15 to 10:45 UT, the IMF was southward for over 30 minutes (Figure 3-3c) and there was ongoing reconnection. This event was previously reported by *Dunlop et al.* [2009] and *Fuselier et al.* [2011]. The transition from high-energy plasmas to low energy plasmas (Figures 3-3d-3-3f) indicates the crossing from the magnetosphere (Msph) to the magnetosheath (Msh). The intermediate interval, where the mixture of the plasmas from both sides was observed, contains the boundary layers at the magnetopause (MP). Figure 3-3g shows the H^+ number density (black), 16 times the O^+ density calculated over the full CODIF energy range (blue) and 16 times the O^+ density for energies from 5 keV to 40 keV (red). The O^+ density is multiplied by 16 to show its relationship with H^+ in mass density. It can be seen that on the magnetosphere side, the mass density of H^+ and O^+ are comparable. The intervals with low values of the above 5 keV O^+ density (red), indicate the regions closer to the magnetosheath side.

Figure 3-3h shows the magnetic field in the LMN coordinates determined by Minimum Variance Analysis [*Sonnerup and Cahill Jr.*, 1967] between 10:28:46 and 10:36:11 UT. The relationship between the LMN and GSM coordinates is: L=[-0.437, -0.534, 0.723] GSM; M= [0.209, -0.843, -0.497] GSM; N=[0.875, -0.066, 0.480] GSM. Therefore, the L direction has a large component in the Z_{GSM} direction, and the M direction is mainly in the $-Y_{GSM}$ direction.

Figures 3-3i-3-3k show the comparison of the H^+ and O^+ velocities in LMN. The velocities for the above 5 keV O^+ are smoothed with a time window of 20 s because of the large fluctuations due to the low density. In the Msph, the O^+ velocity calculated over the full energy range is essentially identical to the O^+ velocity calculated above 5 keV. The O^+ and the H^+ velocities follow the same trend except for some spikes in the H^+ velocities, as

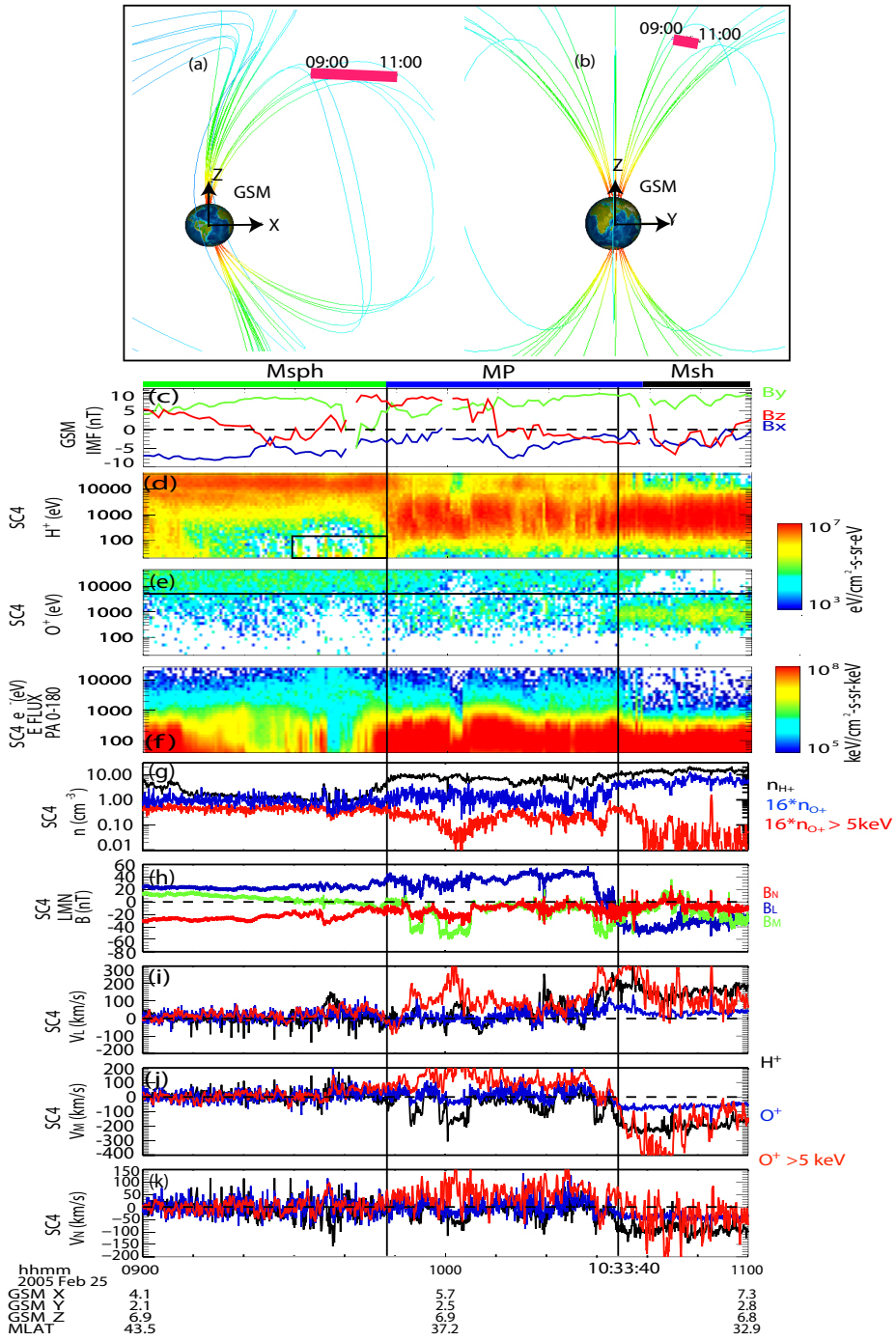

Figure 3-3: Overview of the reconnection event on 25 February, 2005. (a)-(b) Cluster orbits; (c) 1-min resolution IMF in GSM; (d)-(f) H^+, O^+ and e^- energy spectra; (g) H^+ number density (black), 16 times the O^+ number density for the full energy range (blue), and 16 times the O^+ number density for the energies above 5 keV (red); (h) magnetic field in LMN coordinates; (i)-(k) H^+ (black), O^+ with full energy range (blue) and O^+ with energies above 5 keV (red) velocities in L, M, N directions.

expected. Therefore, we can trust that the velocities of the above 5 keV O^+ do represent the motion of O^+ and consequently can also be used in the intervals where the O^+ spectra are contaminated at low energies. Close to the field reversal region around 10:33:40 UT, high-energy O^+ has a very similar velocity to that of H^+ with a clear increase in v_L, which indicates that both species follow the reconnection outflow. Further to the magnetosheath side, the O^+ velocity shows a significant increase in the M direction. As shown in Figure 3-3e, the O^+ spectra show an energy dispersion, with the high-energy ions extending further into the magnetosheath. This causes the velocity increase observed in Figure 3-3j. As will be discussed in the following sections, this indicates the presence of the finite Larmor radius effect.

Figure 3-4 shows the time period close to the main crossing, from 10:28 to 10:41 UT. The main crossing around 10:33 UT and the brief crossing around 10:37-10:38 UT have been used to determine the local reconnection structure [*Dunlop et al.*, 2009; *Fuselier et al.*, 2011]. *Fuselier et al.* [2011] analyzed C3 data to show that the high-energy electron flux changed from bi-directional in the MSPBL to unidirectional in the MSHBL. They also compared the spacecraft location with the predictions of anti-parallel reconnection and maximum shear angle component reconnection models to argue that the local reconnection is consistent with component reconnection, and that the spacecraft was located northward of the X line [*Fuselier et al.*, 2011]. The orange arrow in Figure 3-2a illustrates the spacecraft trajectory for this event. The large B_M in the boundary layer (Figure 3-4e) also supports the conclusion that it is a component reconnection.

In the present study we also use the electron flux directions to determine the observed sub-regions. At the magnetopause, before the main crossing around 10:33 UT, the spacecraft was mainly located in the MSPBL as shown in Figure 3-4. After the main crossing, the spacecraft transitioned back and forth between the MSPBL, MSHBL and Msh, which can

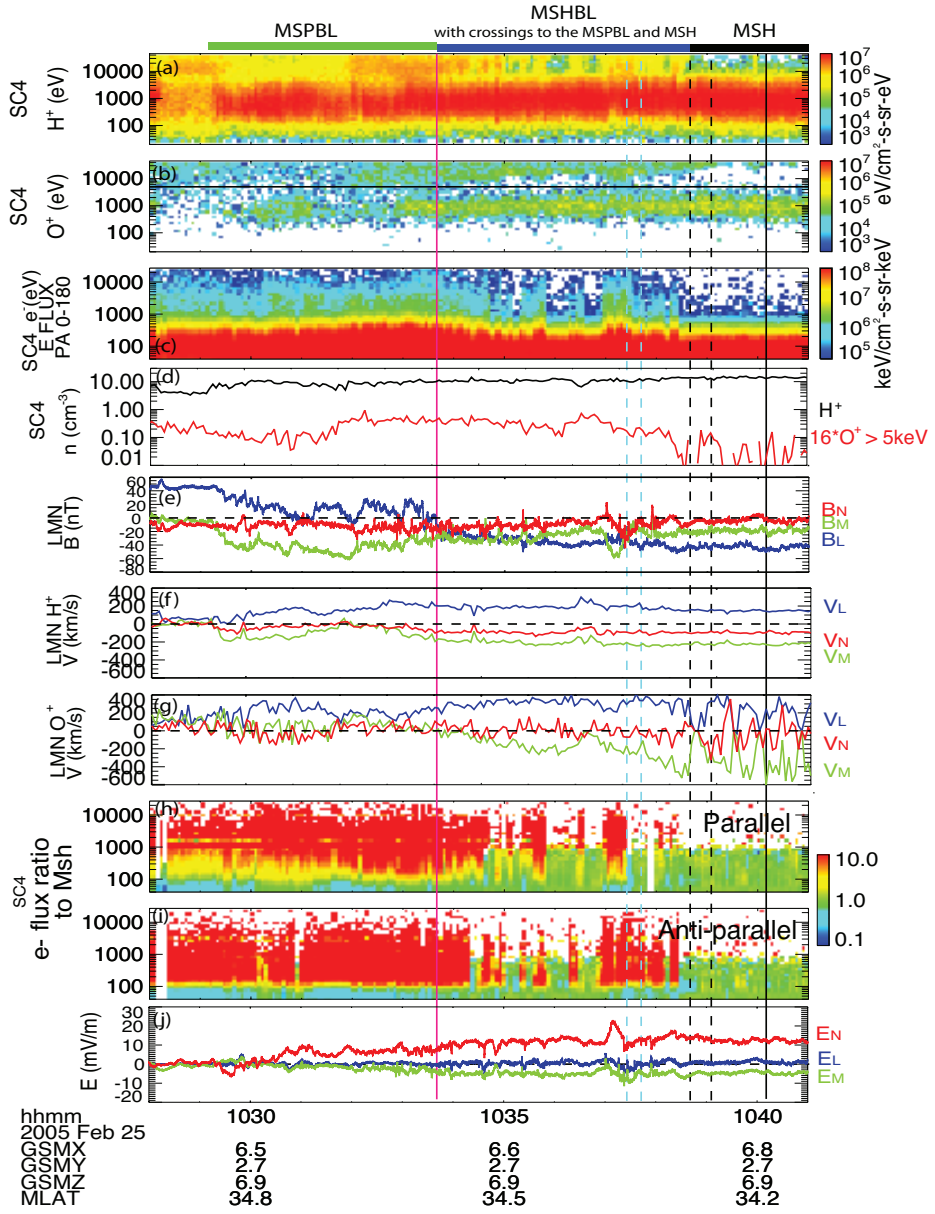

Figure 3-4: Overview of the brief crossing around 10:38 UT. Formats in (a)-(e) are the same as in Figures 3-3d-3-3h; (f) H^+ velocity in LMN; (g) O^+ above 5 keV velocity in LMN; (h)-(i) parallel and antiparallel electron flux ratio between the local value and the magnetosheath level. (j) convective electric field calculated from the magnetic field and H^+ velocity in LMN. The vertical lines represent the main crossing (magenta), MSHBL (blue) and Msh (black) intervals.

be distinguished from the electrons' pitch angle distributions. Figures 3-4h and 3-4i show the ratios of the local value of the electron energy flux to the magnetosheath value in the parallel and antiparallel directions, respectively. The magnetosheath value used is the

average in the interval of 10:40:10-10:41:00 UT (indicated by the black solid line). The flux in the high-energy channels in the magnetosheath interval, which do not have valid values, are set to be 1.0 keV/cm^2-s-sr-keV in order to emphasize the high flux in the boundary layer. In the MSPBL, the electron flux is enhanced at high energies in both parallel and antiparallel directions, representing the reconnection outflow and the reflected electrons from the ionosphere, respectively. The interval within the blue dashed vertical lines shows high-energy flux only in the antiparallel direction, indicating that it is in the MSHBL. The interval represented with black dashed lines without high-energy flux in any direction is in the Msh. Figure 3-4j shows the convective electric field calculated from the magnetic field and H^+ velocity, since the electric field data from EFW have many gaps during this interval. Comparing the electric field data from EFW with that calculated from the magnetic field and H^+ velocity (not shown), the average values match well in the intervals when EFW data are available, while the EFW data show large fluctuations indicating the presence of waves. Therefore, the convective electric field with the condition of $\vec{E} \cdot \vec{B} = 0$ is still valid on average. Shortly before the main crossing ($\sim$ 10:29:30 UT) and while in the MSPBL, E_N is negative, which may prevent the demagnetized magnetospheric ions from coming into the reconnection region [*Malakit et al.*, 2013]. However in the later intervals, deeper in the magnetosheath side, E_N is positive, which can further pull the magnetospheric populations towards the magnetosheath side.

3.3.2 Magnetospheric origin hot ions transport across the reconnection region

Ion VDFs for this event were shown by *Fuselier et al.* [2011] to assist in determining the sub-regions. They focused on the behavior of the magnetosheath origin populations. In this subsection, we use the behavior of magnetosheath origin H^+ as a reference and discuss the

hot ion (H^+ and O^+) signatures to understand their transport from the magnetosphere to the magnetosheath side through the reconnection region.

Figure 3-5 shows the ion VDFs in the magnetic field-aligned coordinates (FAC). The first two columns are in the $v_{\parallel} - v_{\perp 2}$ plane, and the last two columns are in the $v_{\perp 1} - v_{\perp 2}$ plane, where $v_{\perp 1}$ is in the direction of $-(\vec{v} \times \vec{B}) \times \vec{B}$ and $v_{\perp 2}$ is the other perpendicular direction. The first and the third columns show the VDFs of H^+ using the full energy range and the second and fourth columns are the VDFs of O^+ using energies higher than 5 keV to avoid the contamination from H^+. The velocity range depicted is different for the two species.

From Figures 3-5a to 3-5f we show the observed VDFs ranging from the MSPBL to the Msh. While the counts levels are low for these high time resolution VDFs, the features observed are well above the background level for the instrument, and the features that we identify are observed consistently in multiple events. The VDFs in the MSPBL are stable and therefore we are able to average the distribution functions over 30 s (10:32:45-10:33:17 UT). The following three frames are the subsequent frames of VDFs in the MSHBL, at the spin resolution (4 s), for the brief re-crossing around 10:37:30 UT (indicated by the blue dashed lines in Figure 3-4) where only antiparallel high-energy electron flux enhancements are observed. Figures 3-5e-3-5f show the VDFs in the magnetosheath after this crossing when no high-energy electrons are observed in any direction, within the time period represented by the black dashed lines in Figure 3-4.

In the MSPBL (Figure 3-5a1), the H^+ VDF shows two main populations: (1) a high-flux population (red and yellow) with a clear shift in the $v_{\parallel}$ direction, which is the accelerated Msh H^+ in the reconnection outflow; (2) an isotropic hot population from the Msph (blue). In the perpendicular plane (Figure 3-5a3), all populations follow a positive $\vec{E} \times \vec{B}$ drift velocity in the positive $v_{\perp 1}$ direction. There is no O^+ originating from the Msh, but the hot

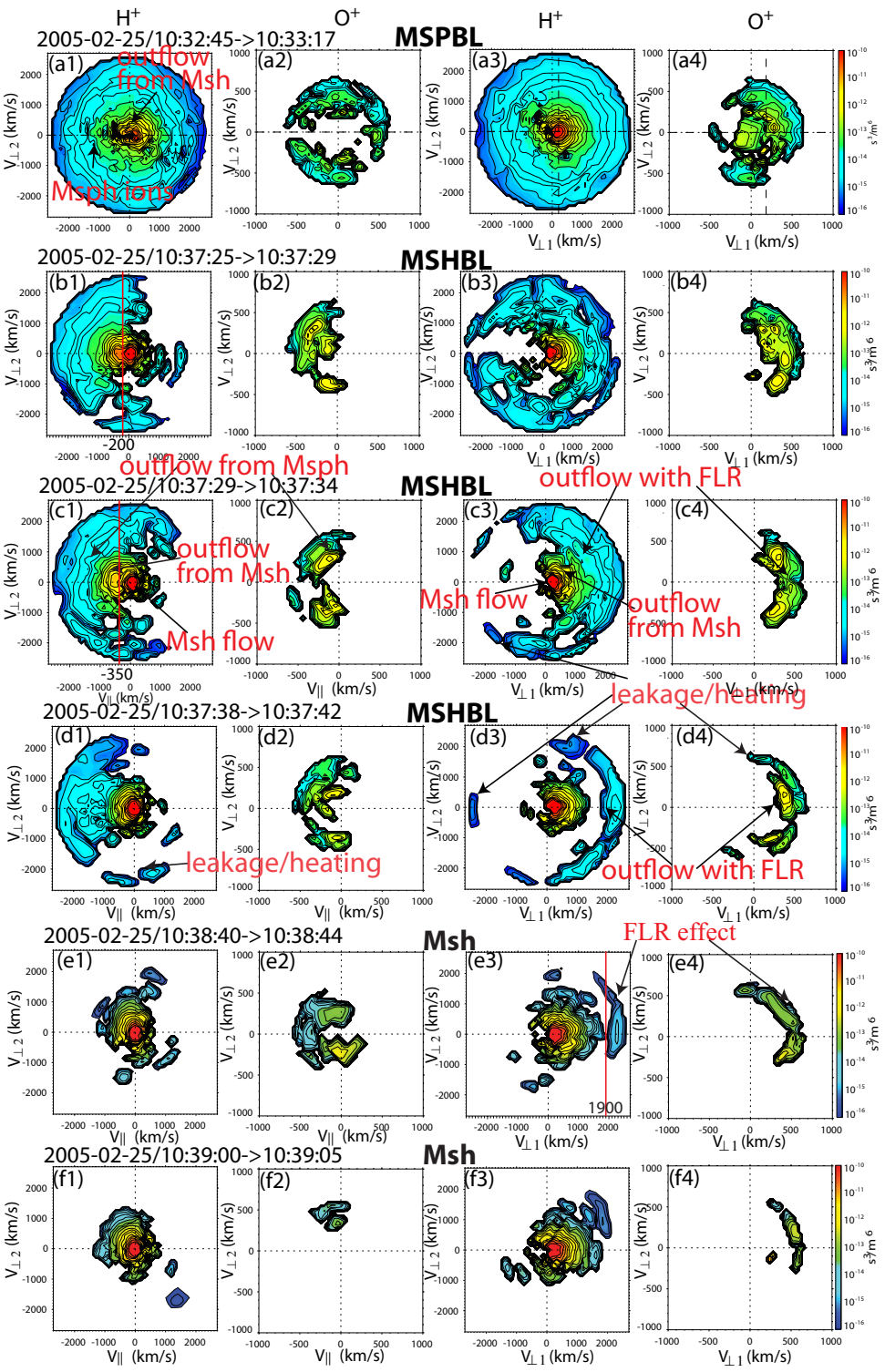

Figure 3-5: H^+ and O^+ velocity distribution functions (VDFs) in the magnetic field coordinates (FACs) on 25 February, 2005. $v_{\perp 1}$ is in the $\vec{E} \times \vec{B}$ direction, and $v_{\perp 2}$ is in the other perpendicular direction. See text for details.

magnetospheric O^+ population (Figure 3-5a2) shows the same isotropic distribution as the H^+ with the same bulk drift velocity around 200 km/s in the $v_{\perp 1}$ direction (Figure 3-5a4).

In the MSHBL (Figures 3-5b-3-5d), there are three main populations for H^+: (1) a cold core population (red) with a near-zero parallel velocity, which is the Msh flow; (2) a population with a higher velocity in the antiparallel direction, which is the reflected Msh particles in the outflow that have been accelerated during reconnection; (3) the hot ions from the Msph. As analyzed in the model in section 3.2.2, the reconnection outflow from the Msh (population 2) does show a D-shaped distribution with a velocity cutoff in the antiparallel direction, and the cutoff velocity increases from the field reversal region towards the magnetosheath-side separatrix, i.e., around -200 km/s in Figure 3-5b1 and around -350 km/s in Figure 3-5c1. Hot ions from the Msph (population 3) also flow in the antiparallel direction, and have velocity cutoffs in the anti-parallel direction (Figures 3-5b1, 3-5c1 and 3-5d1). As the spacecraft moves closer to the separatrix on the Msh side, this hot magnetospheric population and the magnetosheath origin outflow are more and more focused in the antiparallel direction. O^+ shows similar signatures, with the velocity deviated to the antiparallel direction above a cutoff velocity, although the increase of the cutoff velocity is not so clear. The consistency of the distribution functions of the magnetospheric hot ions (H^+ and O^+) and the magnetosheath origin reconnection outflow implies that these magnetospheric origin H^+ and O^+ are also involved in the reconnection process.

In the $v_{\perp 1} - v_{\perp 2}$ plane cut at the bulk parallel velocity, the whole distribution shifts with a bulk velocity in the $v_{\perp 1}$ direction. The magnetospheric hot ions (both H^+ and O^+) show the velocity cutoff increasing from the field reversal region to the magnetosheath-side separatrix in the $v_{\perp 1}$ direction: from Figures 3-5b3 - 3-5d3, there are fewer and fewer ions from the hot H^+ populations in the negative $v_{\perp 1}$ direction, and from Figures 3-5b4 - 3-5d4,

the O^+ distributions gradually shift further to the positive $v_{\perp 1}$ direction. This is consistent with the signatures in the VDF model discussed in section 3.2.2: ions gyrate around both the reconnected and the guide field with different velocities, causing the finite Larmor radius effect to generate an increasing velocity cutoff in the gyro-direction from the field reversal region to the separatrix.

We also plot the VDFs in the LMN coordinates (Figure 3-6) for the same time period as those in Figures 3-5d. The dashed lines in each panel represent the bulk velocity, and the solid line represents the magnetic field direction. For this time, the guide field B_M is only about 1/5 of the reconnected field B_L. It is clear that both H^+ and O^+ shift to the positive L direction, corresponding to the outflow velocity. Since the gyration of ions is left-handed relative to the magnetic field, the gyro-direction on the magnetosheath side is close to the negative M direction. Thus, the perpendicular velocity cutoff (Figures 3-5d3 and 3-5d4), if it is due to the finite Larmor radius effect, is supposed to be close to the negative M direction. This is consistent with the VDFs in Figures 3-6a, 3-6b, 3-6e and 3-6f.

However, the high-energy population is more gyrotropic than the low-energy populations (Figures 3-5b3, c3, d3, d4). The population that is the most energetic and most gyrotropic has a very low velocity in the parallel direction and in the L direction, and it may even have a negative v_L (Figures 3-6a-3-6d). The gyrotropy of the hot population cannot be well explained by the FLR effect, since FLR would lead to more non-gyrotropy.

Figures 3-5e - 3-5f show the distributions in the Msh right after the crossing, which are represented by the black dashed lines in Figure 3-4. The main distribution comes from the Msh flow, while the Msph populations gradually disappear. In the $v_{\perp 1}$ direction, the hot ions show the increasing cutoff velocities as the spacecraft transition deeper into the Msh, indicating the FLR effect. Note that although the hot populations appear in the Msh outside of the reconnection separatrix, their guiding centers are still within the separatrix,

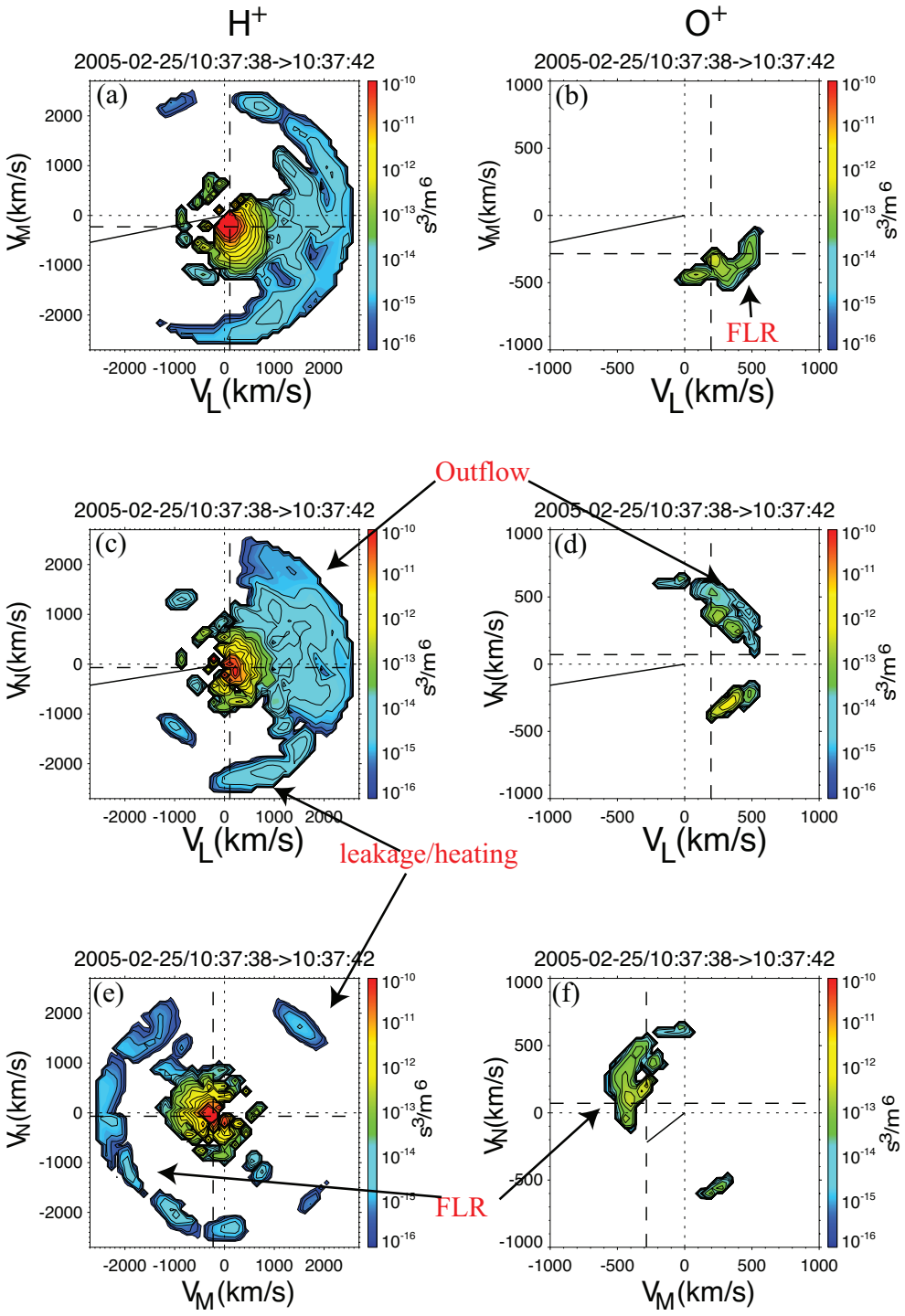

Figure 3-6: H^+ and O^+ VDFs in the LMN coordinates for the time shown in Figures 3-5d. In each panel, the dashed lines represent the bulk velocities, and the solid lines show the magnetic field directions.

so that these ions still follow the reconnection outflow instead of freely escaping to the Msh.

3.3.3 Magnetospheric origin cold ions in reconnection

It can be seen from Figure 3-3d that close to the magnetospheric side boundary of the magnetopause, there are cold ions with energies increasing towards the magnetopause (represented by the black box). Although IMF conditions are variable in this interval, it is likely that these cold ions from the magnetosphere are entrained in the reconnection, and we perform more detailed analysis in this section.

Figure 3-7 shows the overview plot close to the field reversal region observed by C1. The energy flux from C1 shows more clear evidence of the cold ions than C4, with an energy of about 100 eV in the MSPBL around 10:33:30 UT (indicated by the first dashed line in Figure 3-7a). Figure 3-7b is the magnetic field in LMN, where the corresponding directions in GSE are as follows. L=[-0.423, -0.470, 0.775] GSE; M=[0.314, -0.879, -0.361] GSE; N=[0.850, 0.090, 0.519] GSE. Figure 3-7c is the ion velocity in LMN. Figure 3-7d shows the $\vec{E} \times \vec{B}$ drift velocities calculated by $-(\vec{v} \times \vec{B}) \times \vec{B}/|B|^2$. It is clear that the drift velocity changes significantly along with the magnetic field reversal, especially in the M direction; however, in most of the interval, the drift velocity maintains a strong L component, which is the same as the exhaust direction. Note that the ion velocity (Figure 3-7c) differs from the $\vec{E} \times \vec{B}$ drift velocity (Figure 3-7d) as the ion velocity has a component parallel to the magnetic field.

Columns 1, 3 and 4 of Figure 3-8 show the VDFs in FAC for velocities lower than 1000 km/s. The vertical axis is the magnitude of $v_\perp$, and the horizontal axis is $v_\parallel$. The flux is the average over all perpendicular directions. Column 3 shows the flux only for particles with positive GSE v_y, while column 4 shows the flux for negative GSE v_y. Column 2 is a cut of the VDF in the GSE $v_y - v_z$ plane at zero velocity of v_x with the same velocity range.

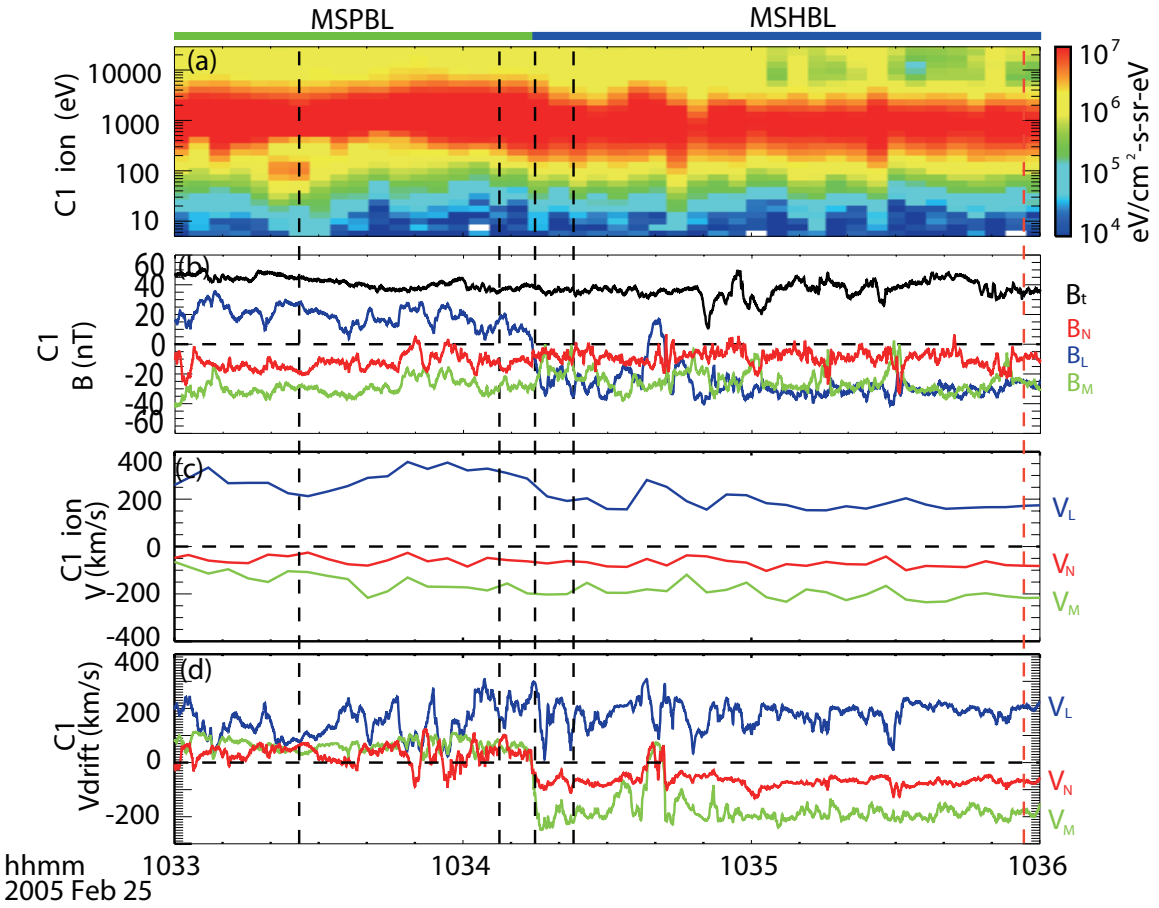

Figure 3-7: Overview around the field reversal region for C1. (a) ion energy flux spectra; (b) magnetic field in LMN; (c) ion velocity in LMN; (d) $\vec{E} \times \vec{B}$ drift velocity calculated with the velocity and magnetic field data. It can be clearly seen that there are cold ions ($\sim$100 eV) in the MSPBL in the energy flux. The black dashed lines represent the intervals for the distribution functions shown in Figure 3-8. The red dashed line represents the time for the magnetosheath distribution function in Figure 3-10b.

In order to better distinguish between the different populations, the VDFs are plotted in units of the energy flux. Figure 3-9 illustrates the motion of the ion populations observed in Figure 3-8, and the letters 'a'-'d' represent the locations of the spacecraft for Figures 3-8a - 3-8d.

Figures 3-8a are in the MSPBL far from the field reversal region, represented by the first black dashed line in Figure 3-7. There are two populations with the high flux (black in color) in Figure 3-8a1. The bulk shift of the two populations in the perpendicular direction

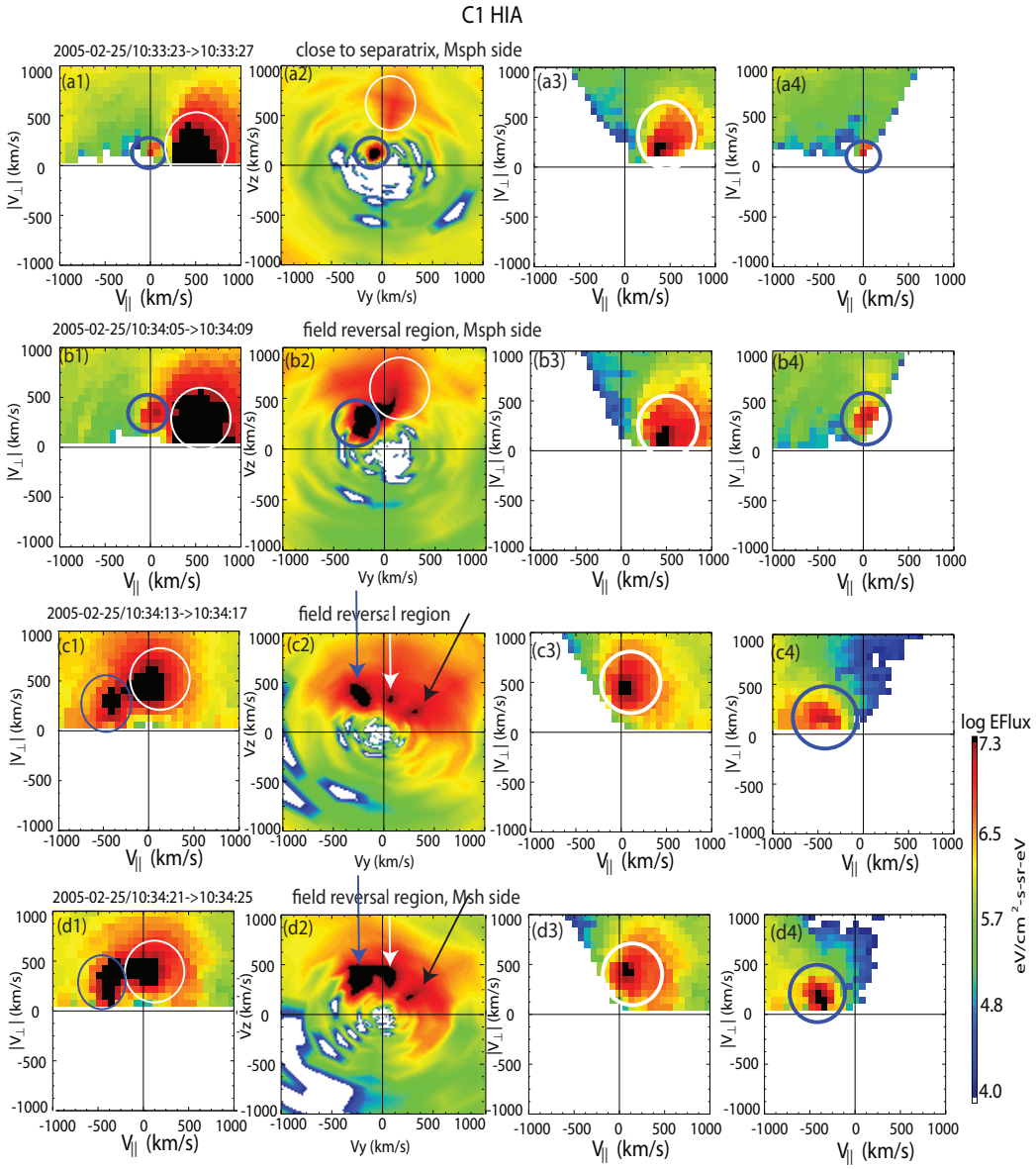

Figure 3-8: Ion VDFs in unit of the energy flux in FAC and GSE coordinates. Column 1: in the $v_{\parallel} - |v_{\perp}|$ plane with the flux averaged over all perpendicular directions; column 2: GSE $v_y - v_z$ plane cut at $v_x = 0$; column 3: same format as column 1 but only contains the flux in the positive GSE v_y direction; column 4: same format as column 3 but only contains the flux in the negative GSE v_y direction. The two high-count populations are the magnetosheath origin H^+ (marked by white circles or arrows) and the cold ions from the magnetosphere (marked by blue circles or arrows). The black arrows in (c2) and (d2) mark the magnetosheath H^+ that directly crosses the separatrix to the exhaust. See text for more details.

is in the direction of $v_{\perp 1}$, i.e., $\vec{E} \times \vec{B}$ drift direction. This is shown more clearly in Figure 3-10a, which displays the distribution for the same time periods as Figure 3-8a, but in the

$v_{\parallel} - v_{\perp 1}$ plane. Both populations have the same perpendicular drift velocity of about 200 km/s. The denser and hotter population with a positive $v_{\parallel}$ (indicated by the white circle in 3-8a) is the accelerated magnetosheath H^+ transmitted to the magnetospheric side. Figure 3-10 shows that it has the D-shaped distribution with a parallel velocity cutoff around 250 km/s, represented by the blue line. The dark blue curve numbered as '3' in Figure 3-9 shows the trajectory for this population. It goes through the ion diffusion region (blue region in Figure 3-9) as it crosses the field reversal region. The distribution indicated by the blue circle, that has very little thermal spread and near-zero parallel velocity, is the cold population from the magnetosphere. The orange curve numbered as '1' in Figure 3-9 shows the trajectory of this cold population. In GSE, the accelerated magnetosheath H^+ is mainly in the $-X$ (not shown) and $+Z$ directions. The two populations seen in the FAC plot in Figure 3-8a1 correspond to the two populations in the GSE $v_y - v_z$ plane (Figure 3-8a2): a hotter one with positive v_y (indicated by the white circle) and a colder one with negative v_y (indicated by the blue circle). This can be further demonstrated by the VDFs with the $+v_y$ and $-v_y$ parts separately plotted in FAC in Figures 3-8a3 - 3-8a4. Comparing Figures 3-8a3 - 3-8a4 with the VDF in FAC for all flux in Figure 3-8a1, we can see that exactly the population with $+v_y$ is the accelerated magnetosheath population (Figure 3-8a3) and the one with $-v_y$ is the magnetospheric cold ions (Figure 3-8a4).

The following three rows show the VDFs near the field reversal region, represented by the following three black dashed lines in Figure 3-7. For all the VDFs in FAC (Figures 3-8b1, 3-8c1 and 3-8d1), there are clearly two populations rotating towards the antiparallel direction as the magnetic field rotates (Figure 3-7b). Meanwhile, the thermal spread of the colder population increases as it rotates. It is possible that this population is also the cold magnetospheric population, but it could also be a population from the magnetosheath.

In the MSHBL, there are often two populations observed, both of which correspond

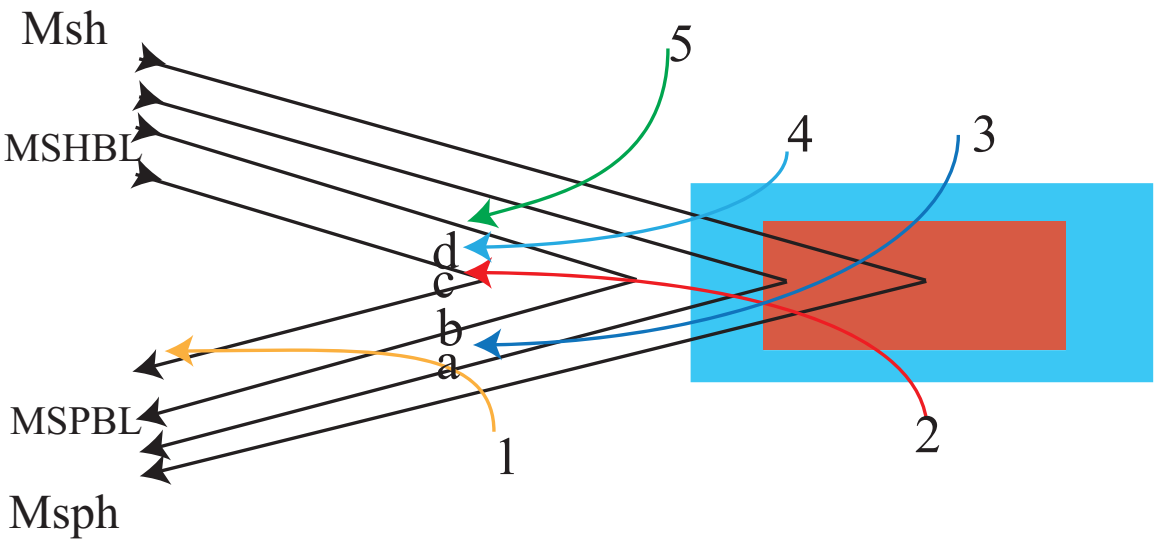

Figure 3-9: Illustration of the spacecraft locations and the ion trajectories of the magnetospheric cold ions and the magnetosheath origin ions shown in the VDFs of Figure 3-8. (a)-(d) indicate the spacecraft locations at the same time as Figures 3-8a-3-8d. The trajectories 1-2 are for the magnetospheric cold ions. The trajectories 3-4 are for the accelerated magnetosheath H^+. Trajectory 5 is for the magnetosheath H^+ that directly crosses the separatrix to the exhaust region. The blue rectangular region indicates the ion diffusion region where the magnetosheath origin H^+ and magnetospheric hot ions are demagnetized. The red region is where the cold ions from the magnetosphere can be demagnetized.

to the magnetosheath origin H^+: a population that goes through the ion diffusion region (blue region in Figure 3-9) and is accelerated by reconnection as a part of the outflow jet (line 4 in Figure 3-9), and a population that follows the background magnetosheath flow and crosses the separatrix directly (line 5 in Figure 3-9). If the magnetosheath flow goes towards the X-line, the directly crossing population will show opposite velocity directions with the outflow jet. However, in this event, the background magnetosheath has the same velocity direction in the L direction with the outflow jet, so the difference between the two populations is small.

We first check whether the colder population in Figures 3-8b1, 3-8c1 and 3-8d1 is the cold ion population from the magnetosphere or the magnetosheath population that directly crosses the sepatratrix. Comparing Figures 3-8b2, 3-8c2 and 3-8d2, we can see that there

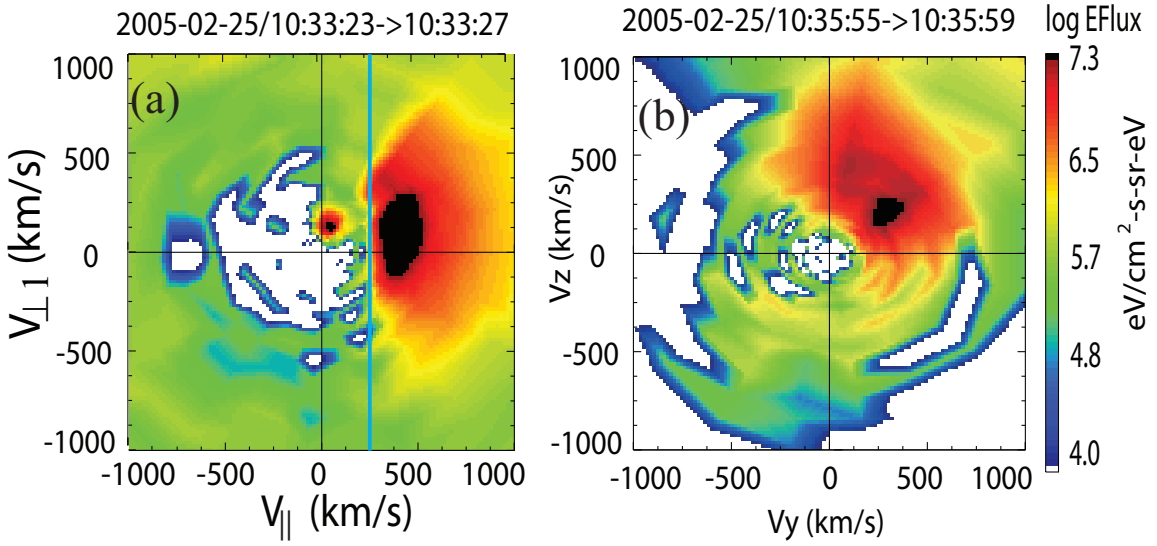

Figure 3-10: Supplementary ion VDFs from HIA on C1. (a) VDF in the $v_{||} - v_{\perp 1}$ plane close to the magnetospheric side of the separatrix at the same time as the first row in Figure 3-8. The blue line indicates the cutoff velocity of the magnetosheath origin population. The cold ions mainly move along $v_{\perp 1}$ direction, which is the $\vec{E} \times \vec{B}$ drift direction. (b) magnetosheath ion VDF in the GSE $v_y - v_z$ plane at the time marked by the red dashed line in Figure 3-7.

are always two populations, one with $-v_y$ (represented by the blue arrow) and one with small $+v_y$ (represented by the white arrow), respectively, which are the same populations with those in Figure 3-8a2. In addition, in Figures 3-8c2-3-8d2, there is an additional population with larger $+v_y$ (represented by the black arrow). Therefore, it is probable that this third population is the magnetosheath H^+ crossing the separatrix to the exhaust region without going through the diffusion region, which is different from the other two populations. Figure 3-10b shows the VDF (GSE $v_y - v_z$ plane) for the magnetosheath H^+ at the time marked by the red dashed line in Figure 3-7. It exhibits a $+v_y$ and a $+v_z$, similar to the population in Figures 3-8c2 and 3-8d2 marked by black arrows. This demonstrates that the third population is the incoming magnetosheath H^+ directly crossing the separatrix without acceleration in the diffusion region. In Figure 3-9, the three curves pointing to the locations of 'c' and 'd' indicate the trajectories of the three populations: cold ions from the magnetosphere ('2', red), accelerated magnetosheath H^+ ('4', light blue)

and the H^+ following the magnetosheath flow to directly cross the separatrix ('5', green).

The L direction has a significant component in Z_{GSE}, and the M direction is mainly in $-Y_{GSE}$. Therefore, both the cold magnetospheric ions and the accelerated magnetosheath ions move towards the L direction, but have different velocities in M. In the MSPBL, E_N is positive during most of the interval (Figure 3-4j), and the calculated $\vec{E} \times \vec{B}$ drift velocity has a positive v_M (Figure 3-7d before 10:34 UT). Therefore, the magnetospheric cold ions obtained a $+v_M$ ($-v_y$) by the $\vec{E} \times \vec{B}$ drift. The magnetosheath ions have a $-v_M$ ($+v_y$) when they are in the magnetosheath (Figure 3-7c after ~10:35 UT). Inside the reconnection region, their v_y changes, but the sign of v_y still keeps positive, so that we can observe two populations with different $+v_y$ in Figures 3-8c2 and 3-8d2. Note that they also follow the $\vec{E} \times \vec{B}$ drift velocity as shown in Figure 3-10, and the difference in v_M is mainly due to the different $v_{\|}$ along the guide field.

The VDFs for particles with $+v_y$ in FAC (Figures 3-8b3, 3-8c3 and 3-8d3) confirm that the population with small $+v_y$ in Figures 3-8b2, 3-8c2 and 3-8d2 correspond to the population rotating from parallel to perpendicular in FAC, which is the accelerated magnetosheath population. The VDFs for particles with $-v_y$ in FAC (Figures 3-8b4, 3-8c4 and 3-8d4) confirm that the population with $-v_y$ in Figures 3-8b2, 3-8c2 and 3-8d2 correspond to the population rotating from perpendicular to antiparallel in FAC, which is the cold ion population. The magnetosheath H^+ directly crossing the separatrix and those accelerated through the diffusion region have similar velocity directions, so that they are not distinguishable in FAC. At later times where the guide field decreases, the magnetosheath population goes towards the antiparallel direction as shown in Figure 3-5, and it is no longer possible to distinguish it from the magnetospheric cold ions.

As the magnetic field rotates, the cold magnetospheric ions do not change their velocity direction ($-v_y$), which means that they are not always going along the field line. The $\vec{E} \times \vec{B}$

drift helps them to follow the reconnection outflow jet. In addition, during the interval from Figures 3-8a to Figure 3-8d, i.e., from close to the magnetospheric separatrix to the field reversal region, the magnetic field magnitude shows small decreases (Figure 3-7b), but the thermal spread of the magnetospheric cold ions increases. This indicates that the magnetic moment of the cold population, which can be characterized by $T_\perp/B$, is increased and hence, not conserved. These signatures imply that they are not moving in an adiabatic way.

3.4 Discussion

We have analyzed the observed distribution functions of a reconnection event at the dayside magnetopause in the presence of a strong guide field. The fluid structure of the reconnection region is mainly determined by the magnetosheath origin population because it has the highest density. The analysis above shows that the different populations evident in the distribution functions: the magnetosheath origin H^+, the magnetospheric origin hot H^+ and O^+, and the magnetospheric origin cold ions, all generally move along with the reconnection outflow. However, they still show different signatures in detail. In this section we further discuss these signatures and indications of their motions.

3.4.1 Quantitative determination of the FLR effect

In the VDFs from the MSHBL and Msh, we see the velocity cutoff in the perpendicular direction, which increases from the field reversal region to the Msh. This is likely to be the FLR effect.

In order to confirm this, we estimate the cutoff velocities for H^+ and O^+. Figure 3-11a shows the antiparallel electron flux ratio, indicating the MSHBL (red in high energies) and the Msh (lack of high-energy electrons) intervals. The following 5 panels show O^+ pitch angle distributions from the highest five energy channels. They show that the O^+

pitch angle distribution is peaked in the perpendicular direction with the higher energy populations extending deeper into the Msh. The cutoff velocity should be the sum of the gyro-velocity and the drift velocity. The drift velocity is the same for H^+ and O^+, while, with the same Larmor radius, the gyro-velocity is different by a factor of 16. Around 10:38:40 UT, O^+ in the 13.4 keV energy channel showed a cut off. This corresponded to a velocity of 400 km/s. The drift velocity measured by EFW in this case was 300 km/s (Figure 3-11g), so the gyration velocity was 100 km/s. An H^+ ion with the same Larmor radius would have a gyro-velocity of 1600 km/s. The drift velocity was the same, so the H^+ cutoff velocity should be 1900 km/s. Figure 3-5e3 shows the H^+ VDF for this time. It shows that indeed, the H^+ cutoff was at $\sim$1900 km/s in the perpendicular direction, which matches our estimation. At a later time (10:39:00 UT), using the same method, the estimated H^+ cutoff velocity was around 2700 km/s, close to the upper limit of CODIF instrument, so that we cannot observe it in the VDF. The consistency between the H^+ and O^+ cutoffs with this analysis confirms that the cutoffs are due to the finite Larmor radius effect.

3.4.2 Explanation for the isotropic high-energy population detected in the magnetosheath boundary layer

In the MSHBL, a small portion of the high-energy magnetospheric ions show gyrotropic signatures and have small or even opposite velocities in the outflow direction (Figures 3-5c - 3-5d,3-6c - 3-6d). This cannot be well explained by the FLR effect, since the velocity cutoff by the FLR effect would make it less gyrotropic.

It indicates that the guiding centers of the most energetic gyrotropic population are closer to the Msh side than those of lower-energy populations. This is consistent with the discussion above that with the presence of the guide field, ions with larger Larmor radii can

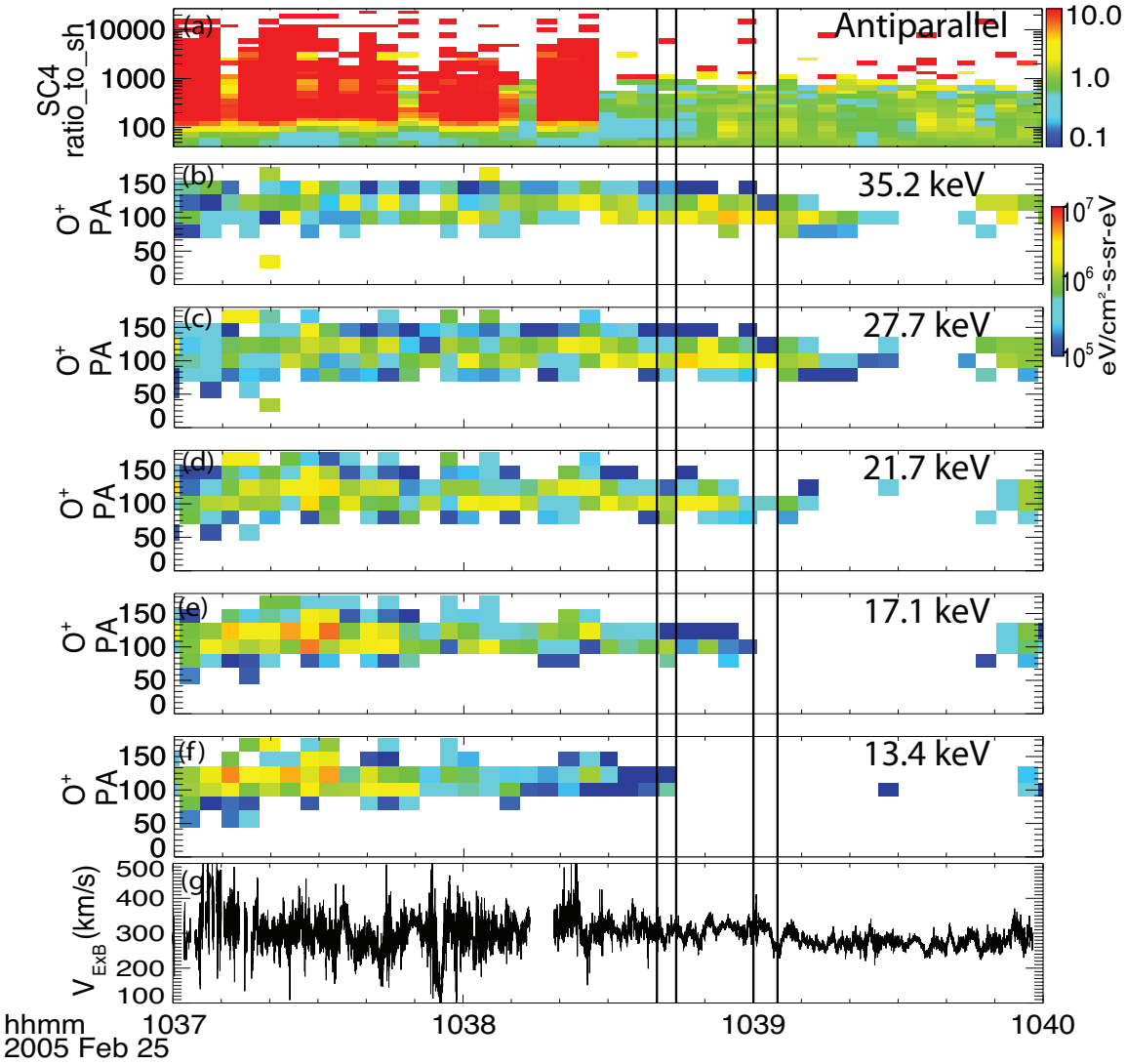

Figure 3-11: (a) antiparallel electron flux ratio to indicate the sub-regions in reconnection; (b)-(f) O^+ pitch angle distribution in the highest five energy channels; (g) $\vec{E} \times \vec{B}$ drift velocity provided by EFW.

go deeper to the Msh side, since the ions with lower energies are easier to directly convect with the magnetic field towards downstream.

In addition, it might be an indication of the direct leakage for energetic particles to the Msh. The low velocity in the outflow direction may not be caused by certain gyro-phase in the gyration around B_M and B_N, but may be because the ions are not or have not been accelerated to a high velocity. It is possible that these ions, with very large Larmor radii,

gyrated deeper towards the magnetosheath side of the boundary layer, and changed their guiding center locations either through interacting with the magnetopause or due to the sudden motion of the magnetopause. In this way, they might escape the magnetopause to the magnetosheath through direct leakage without being significantly accelerated in reconnection.

3.4.3 The motions of heavy ions (O^+)

In this study, for the first time we show that the hot magnetospheric heavy ions have a clear shift in the VDFs along the outflow direction. This demonstrates their pick-up motion and participation in the reconnection outflow.

They show signatures of the FLR effect in the magnetosheath boundary layer and the magnetosheath, but this does not directly cause their escape through leakage, because it is the guiding center motion that determines their trajectory. If there are no further interactions with the magnetopause boundaries, such as sudden magnetopause motion or wave scattering, they should move with the reconnection outflow and escape the magnetopause further downstream.

Since most of the O^+ population participates in the reconnection, it is possible that it forms a larger scale of the diffusion region that changes the fluid structure of the reconnection, though there is no direct evidence of this from the observations in this event. The event shown here has low O^+ density ($\sim 0.035\ cm^{-3}$) compared to the magnetosheath H^+ ($14.35\ cm^{-3}$). Thus the participation of heavy ions does not require a high density of the heavy ions. The asymmetric hybrid Alfvén speed (eq. 1.15) is decreased by O^+ from 221 km/s to 217 km/s in this case, which is too small a decrease to confirm observationally.

3.4.4 The motions of cold ions

In this reconnection event, Cluster also observed cold ions in the reconnection region. For the distribution closer to the magnetospheric side separatrix, i.e., away from the field reversal region, the cold population mainly has the $\vec{E} \times \vec{B}$ drift velocity and has near zero parallel velocity (e.g., Figure 3-8a). The magnetosheath origin population shows a D-shaped signature in the parallel direction at about 250 km/s (Figure 3-10), which indicates that the ions coming from the diffusion region need to have a larger parallel velocity than this cutoff to be detected. Therefore, the cold population observed in this time frame does not come from the diffusion region, but moves across the separatrix locally. Therefore, this cold population is probably convected away by the magnetic field with only an adiabatic process after entering the current sheet, as indicated by trajectory '1' in Figure 3-9. The small parallel velocity, if not negligible, may be obtained due to magnetic moment conservation in the exhaust frame. This matches the prediction of the model in [*Drake et al.*, 2009a].

However, the cold ions are also detected in the field reversal region, even on the magnetosheath side. Since they move in both the outflow direction and the direction towards the magnetosheath, the deeper into the magnetosheath they can be detected downstream, the closer to the X-line they enter the reconnection region, as illustrated by lines 1 and 2 in Figure 3-9. Because of their smaller Larmor radii, the cold ions might remain magnetized close to the edge of the ion diffusion region where the hotter ions are already demagnetized (blue region in Figure 3-9). However, closer to the X-line, there should be a region with a smaller scale than the hot ion diffusion region, where the cold ions are demagnetized and accelerated (red region in Figure 3-9). This brings the cold ions to a similar velocity as the magnetosheath population so that they are able to reach the magnetosheath side, as indicated by the trajectory '2' in Figure 3-9. When they are detected downstream, they are already re-magnetized, but the adiabatic invariant is likely to be changed, as shown

in 3.3.3. In this way, the cold ions can behave as pick-up ions starting out demagnetized close to the diffusion region, and then becoming magnetized and getting "picked up" in the outflow region.

The pick-up cold ions may merge with the accelerated magnetosheath population and go deeper into the magnetosheath, which may explain why we cannot distinguish the cold ions when they are closer to the separatrix on the magnetosheath side. Considering the *Lee et al.* [2014] result for antiparallel reconnection, there might also be a possibility that close to the field reversal region, the cold ions come from the diffusion region and merge with the accelerated magnetosheath population so that they cannot be distinguished.

3.5 Conclusions

In this study, we use observed ion velocity distribution functions to analyze the motion of different populations in dayside magnetopause reconnection with a strong guide field, focusing on the behavior of the magnetospheric hot heavy ions (O^+) and cold ions.

(1) A clear velocity shift is observed in the outflow direction for the majority of the magnetospheric hot H^+ and O^+. This demonstrates that they are picked up and follow the reconnection outflow.

(2) The hot H^+ and O^+ show signatures of the finite Larmor radius effect. The gyrotropic distribution for a small portion of the highest-energy ions in the magnetosheath boundary layer may indicate their direct leakage to the magnetosheath.

(3) The motion of the cold ions depends on the location where they enter the reconnection region. When there is a significant guide field, the $\vec{E} \times \vec{B}$ drift velocity helps the cold ions to catch up with the outflow in L. If they enter from the separatrix region downstream of the diffusion region, they are taken away by the magnetic field in an adiabatic way. However, if they enter the reconnection region close to the X point, they can be demagnetized

and picked up. This allows the cold ions to escape deeper into the magnetosheath side.

Similar signatures are also observed in other events. In every event that we have carefully examined (around 10 events) the magnetospheric hot H^+ and O^+ show both the acceleration in the outflow direction and the finite Larmor radius effect velocity cutoff in the perpendicular direction. In most other cases, there is no strong guide field. Cold ions behave adiabatically near the magnetospheric side separatrix, and exhibited non-adiabatic thermalization closer to the current sheet center, i.e., they have experienced a non-adiabatic demagnetization process inside the diffusion region.

Chapter 4

Dependence of the dayside magnetopause reconnection rate on local conditions

4.1 Introduction

We have shown in the previous chapter that both the hot O^+ and the cold magnetospheric ions do participate in the reconnection, ending up in the outflow jet, so their mass densities need to be taken into account when determining the reconnection rate. As introduced in Chapter 1, the theoretical symmetric reconnection rate is

$$R = v_{in} B_{in} = \frac{\delta}{l} v_A B_{in} \tag{4.1}$$

In asymmetric reconnection, *Cassak and Shay* [2007] deduced a reconnection rate formula 4.2 that takes into account the local parameters from both sides of the magnetopause.

$$R_{cs} = \frac{\delta}{l} v_{A,asym} B_{asym} = 2\frac{\delta}{l} (B_{ph} B_{sh})^{3/2} (\mu_0 \rho_{ph} B_{sh} + \mu_0 \rho_{sh} B_{ph})^{-1/2} (B_{ph} + B_{sh})^{-1/2} \tag{4.2}$$

Note that when the shear angle is less than 180°, there can be a guide field in the M direction, and reconnection occurs between the L components, which is called 'component reconnection'. In component reconnection, the magnetic fields in R_{cs} should only include the B_L component. In this chapter, we will present an observational test of R_{cs} and discuss the contribution of different plasma populations from the two sides of the magnetopause.

Calculating the reconnection rate and the diffusion region aspect ratio for dayside magnetopause reconnection with in situ measurements involves a lot of uncertainties. One straightforward method is to use $R = v_{in}B_{in}$ and $\delta/l = v_{in}/v_A$ [e.g., *Phan et al.*, 2001]. The difficulties of this method are as follows. (1) It requires a good selection of the interval for the inflow region to calculate v_A and v_{in}. The spacecraft may stay in the magnetopause boundary layer, where there is a mixture of plasmas from both the magnetosphere and magnetosheath, for several or tens of minutes, before completely crossing from one side to the other. During this time, the inflow condition might change. The magnetopause motion moving back and forth further complicates such selections. (2) It requires the transformation to the LMN coordinate system. The normal component of the velocity is sensitive to the determination of the normal direction. There are several ways to determine the coordinate transformation, including, the minimum variance of the magnetic field (MVAB) [*Sonnerup and Cahill Jr.*, 1967], the minimization of the Faraday residue (MFR) [*Khrabrov and Sonnerup*, 1998], and the joint variance analysis [*Mozer and Retinò*, 2007]. However, uncertainties still exist with each of these methods. For component reconnection, there is also an additional uncertainty in the determination of the L and M directions. (3) The inflow velocity should be measured in the magnetopause frame, and hence we need to determine the speed of the magnetopause motion (v_{MP}). v_{MP} can be assumed to be close to zero if the spacecraft quickly crosses the magnetopause back and forth for several times during the observation interval [e.g., *Mozer and Retinò*, 2007], or it can be estimated by

timing analysis with data from four spacecraft [e.g., *Phan et al.*, 2001]. In the magnetopause frame, E_M is constant across the magnetopause in steady state reconnection. Therefore, the magnetopause speed can be regarded as reasonably estimated if E_M remains relatively constant [e.g., *Sonnerup et al.*, 1987; *Mozer et al.*, 2002], while the MFR method can determine the normal direction and the magnetopause motion at the same time [*Khrabrov and Sonnerup*, 1998; *Phan et al.*, 2001; *Mozer et al.*, 2002]. The combination of all these error sources leads to considerable uncertainties.

There are other ways to calculate the reconnection rate and the aspect ratio, but they also have large uncertainties and restrictions. The B_N/B_L ratio is one way to calculate the diffusion region aspect ratio. Since B_N is small, it is sensitive to the error of the normal direction. In addition, the B_N/B_L ratio varies with distances from the X-line, so it is difficult to know whether it accurately represents the aspect ratio of the diffusion region. There have been studies using direct measurements of the electric field [*Vaivads et al.*, 2004; *Mozer and Retinò*, 2007]. Usually the 3-dimensional electric field data includes the assumption of $\vec{E} \cdot \vec{B} = 0$ due to the instrument limitations. *Mozer et al.* [2002] estimated that the electric field component parallel to the magnetic field was an order of magnitude smaller than the other components in the ion diffusion region, so that the above assumption is valid in the ion scale. However, all the uncertainties associated with the v_{in}/v_A method also affect this method. There are also less common methods to calculate reconnection rates. *Fuselier et al.* [2005] utilized the velocity cutoffs in the ion velocity distribution function (VDF) with multi-spacecraft measurements. *Rosenqvist et al.* [2008] related the energy conversion rate $Q = \int \vec{J} \times \vec{B} \cdot \vec{v} v_{MP} dt$ with the inflow velocity as $v_{in} = Q\mu_0 / \left(2B_{in}^2\right)$ to calculate the reconnection rate. These methods might work for individual events, but are case sensitive to how the spacecraft cross the reconnection region.

The observed magnetopause reconnection rates that have been reported are usually from

case studies. One exception is *Mozer and Retinò* [2007], which is a statistical study of the aspect ratio using electric field measurements. They studied 11 magnetopause reconnection events, using POLAR spacecraft data, and showed that the aspect ratio varied between 0.02 and 0.16 with an average value of 0.07. Since the dayside magnetopause reconnection is dominated by the magnetosheath plasmas due to their high density, previous reconnection estimations always used the magnetosheath Alfvén speed ($v_{A,sh}$) and magnetic field as the inflow parameters. However, the R_{cs} of the asymmetric reconnection rate and the effects of cold ions and hot O^+ from the magnetosphere have not been tested by in situ observations. *Walsh et al.* [2014] reported an event observed by THEMIS spacecraft, where magnetospheric cold ions were observed in the reconnection outflow by one spacecraft, but not by another. The observed outflow velocity was much smaller when the cold ions were present [*Walsh et al.*, 2014]. This seems to support the argument that the mass loading by the cold ions can reduce the outflow velocity, and therefore the reconnection rate.

In this study, we analyze the Cluster observations of reconnection events during 8 dayside magnetopause crossings, where particular crossings were encountered by multiple Cluster spacecraft. We evaluate the local reconnection rate, comparing the measured reconnection rate $R_m = v_{in}B_{in}$ in the magnetosheath inflow region with the predicted reconnection rates (R_{pre}) by R_{cs}, where inflow parameters from both sides are included in the calculation and by eq. (4.1) where only magnetosheath inflow parameters are used. We will show the uncertainties in calculating the reconnection rate using currently available data, and we will determine the best possible estimates.

4.2 A case study with reconnection rate calculation

In this section, we present a reconnection event at the dayside magnetopause observed by Cluster on 15 February, 2010, and illustrate the procedures used for determining the

reconnection rate for all events.

4.2.1 Event overview

Figure 4-1 shows the overview of this event as observed by C4. During this interval, C4 transitioned from the magnetosphere to the magnetosheath; the peak H^+ flux (Figure 4-1a) changed from high energies (above 1 keV) to low energies (below 1 keV), and the O^+ flux above 5 keV (Figure 4-1b) and the high-energy e^- flux (Figure 4-1c and 4-1d) above 1 keV both decreased. In the middle of the time interval, the plasma energy flux exhibits a mixture of the populations from the two sides, indicating that C4 was in the magnetopause. During this transition, the H^+ density from CODIF (n_{H^+}) (Figure 4-1e, black) increased from $\sim$1 cm^{-3} to $\sim$30 cm^{-3}. The O^+ density above 5 keV decreased (Figure 4-1e, red): the O^+ density was much lower than that of H^+ during this event. The orange line in Figure 4-1e shows the density (n_{SCP}) derived from the spacecraft potential (SCP) [*Lybekk et al.*, 2012]. Figure 4-1f shows the electric field wave power, which exhibits broadband enhancements at the magnetopause. Figures 4-1g and 4-1h give the H^+ velocity and magnetic field in LMN coordinates determined from the Minimum Variance Analysis (MVA) of the magnetic field. Between 23:19 and 23:20 UT, an ion jet in v_L along with the B_L reversal indicates reconnection.

With the parameters shown in Figure 4-1, we can also determine the location of the separatrices. The magnetospheric separatrix (first blue line) is where the magnetosheath plasma first appears and it coincides with the H^+ density gradient [*Lindstedt et al.*, 2009] (Figure 4-1e). The magnetosheath-side separatrix (second blue vertical line) is the outer boundary of the high-energy electrons of magnetospheric origin [*Lindstedt et al.*, 2009; *Fuselier et al.*, 2011]. The determined separatrices also coincide with the boundaries of the wave enhancements (Figure 4-1f), which independently confirm the separatrix locations.

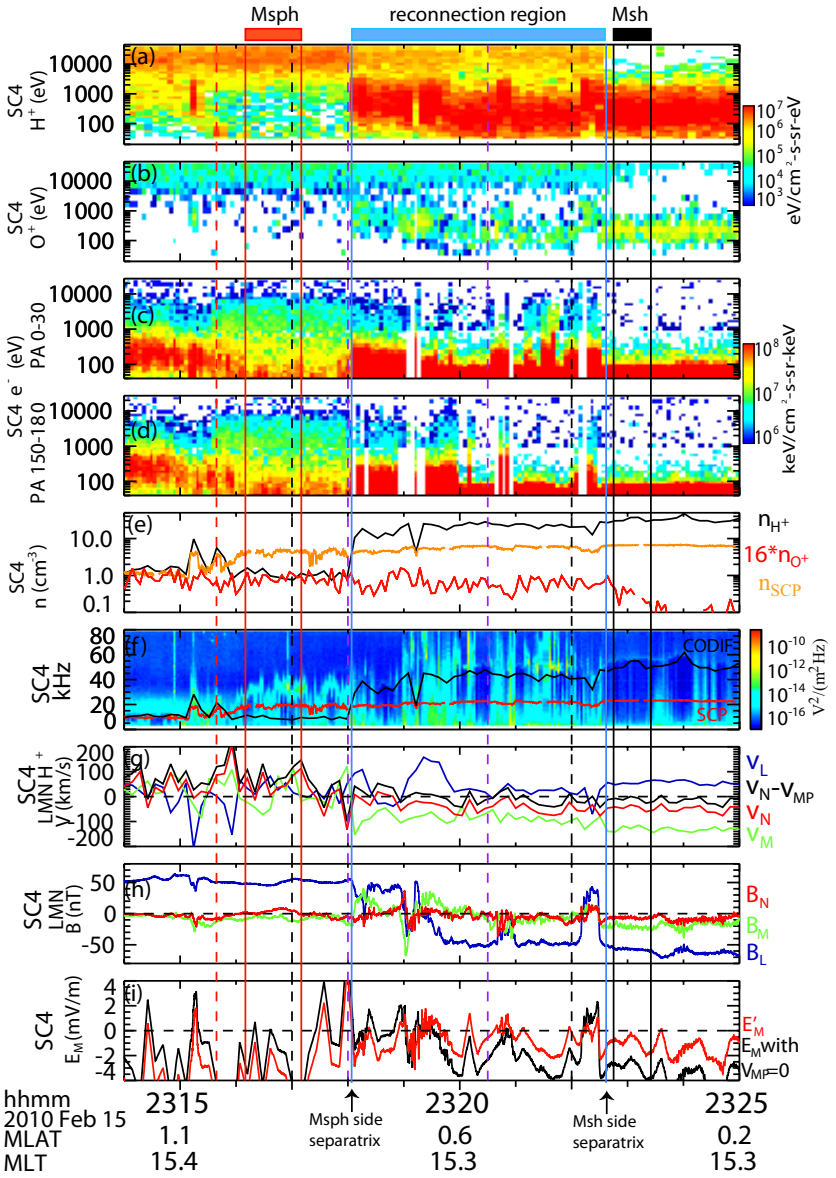

Figure 4-1: Overview of the reconnection event on 15 February, 2010 with the data from C4. (a)-(b) H^+ and O^+ energy spectra; (c)-(d) parallel and anti-parallel e^- energy spectra; (e) n_{H^+} (black), $16n_{O^+}$ (red), and total n_{e^-} derived from spacecraft potential (SCP) (orange); (f) WHISPER wave spectra overplotted with plasma frequencies (f_{pe}) derived from $n_{H+,CODIF}$ and n_{SCP}; (g) H^+ velocity in LMN, and its normal component after subtracting the magnetopause motion (v_{MP} (black); (h) magnetic field in LMN, and the horizontal solid lines mark the e-folding B_L from inflow values; (i) E_M calculated with $-\vec{v}\times\vec{B}$ with (red) and without (black) subtracting v_{MP}. Vertical lines: separatrices (blue); magnetospheric (red) and magnetosheath (black) inflow regions; innermost and outermost intervals used to calculate v_{MP} (purple and black dashed lines). LMN rotation matrix from GSE coordinates determined from MVA: L=[-0.074, 0.478, 0.875]; M=[0.267, -0.836, 0.470]; N=[0.961,0.269, -0.066].

In order to estimate the reconnection rate, we need the upstream parameters in the inflow region. We use the short intervals outside of and close to the separatrices, where the density, velocity and magnetic field parameters are steady, as the inflow regions on the magnetospheric side (red solid vertical lines) and magnetosheath side (black solid vertical lines). In the following, we calculate the reconnection rate using direct measurements of the inflow velocities and the magnetic field and the Cassak-Shay predicted reconnection rate using the observed inflow density and magnetic field; we will compare the two.

4.2.2 Measured reconnection rate

From eq. (4.1), the local reconnection rate can be measured as $R_m = E_M = v_{in}B_{in}$. E_M is constant between the inflow regions on both sides in the magnetopause frame [*Sonnerup et al.*, 1987]. However, the dayside magnetopause moves in the normal direction due to the changes of solar wind pressure, with an amplitude comparable to or larger than the inflow velocity. The measured v_N of ions is a superposition of the magnetopause motion (v_{MP}) and the inflow velocity (v_{in}). Figure 4-1i (black) shows the electric field E_M component calculated from $-\vec{v} \times \vec{B}$ using the H^+ velocity and the magnetic field. Neglecting the large amplitude fluctuations, E_M decreased as B_L reversed from the magnetospheric boundary layer to the magnetosheath boundary layer at 23:18-23:20 UT. Thus, we could estimate the proper v_{MP}, by requiring that EM is constant in the magnetopause frame [e.g., *Mozer and Retinò*, 2007]. We selected the interval across the B_L reversal region and calculated a v_{MP} so that

$$\sum_i^N E'^2_{Mi} = \sum_i^N \Big(-(\vec{v}_i - v_{MP}\hat{n}) \times \vec{B}_i \Big)^2_M \tag{4.3}$$

was minimized, where N is the number of data points and M represents the out-of-plane direction. Thus, we need $\partial\left(\sum E_{Mi}'^2\right)/\partial\left(v_{MP}\right)=0$, and the resulting v_{MP} is

$$v_{MP}=-\frac{\sum_i^N\left(E_{Mi}B_{Li}\right)-\frac{1}{N}\sum_i^N E_{Mi}\sum_i^N B_{Li}}{\sum_i^N B_{Li}^2-\frac{1}{N}\left(\sum_i^N B_{Li}\right)^2} \tag{4.4}$$

where L and M represent minimum variance frame directions, and the electric field is calculated from $-\vec{v}\times\vec{B}$. In eq. (4.4), a negative v_{MP} means the magnetopause moves towards the Earth. This equation is similar to the MFR method except that the normal direction is pre-determined by MVA.

Since the estimation of the magnetopause speed, v_{MP}, is sensitive to the data points used, we used several criteria for the interval selection. (1) The outermost interval includes the approach to the inflow regions on both sides (black dashed lines in Figure 4-1), so that the contribution of inflows from both sides are considered. (2) In the selected interval, points with significant large deviations from the average are removed, e.g., points with large E_M close to 23:18:00 UT. (3) Close to the current sheet center where B_L is small, the frozen-in condition might be invalid, and $v_N B_L$ is not the main contribution to E_M. For these points, the E_M variation of this interval are unlikely to be attributed to the magnetopause motion in the normal direction. Therefore, the sub-interval with $|B_L|<e^{-1}|B_L|_{max}$, where $|B_L|_{max}$ is the maximum $|B_L|$ in the selected interval (representing the asymptotic magnetic field in the inflow region), was removed. The solid black horizontal lines in Figure 4-1h mark the values of $|B_L|=e^{-1}|B_L|_{max}$. (4) The innermost interval (purple dashed lines in Figure 4-1) still includes both sides of the B_L reversal point.

Using different intervals to apply eq. (4.4), we obtained a range of different v_{MP} values. Their average was used as the magnetopause velocity, and their variations were used as the

Interval (mmss)	1700-2200	1710-2150	1720-2140	1730-2130	1740-2120
v_{MP} (km/s)	-26.0	-32.4	-36.1	-36.2	-33.3
Interval (mmss)	1750-2110	1800-2100	1800-2030	1745-2045	1730-2030
v_{MP} (km/s)	-36.3	-34.3	-34.5	-34.0	-33.5

Table 4.1: Intervals and the magnetopause velocities determined by minimizing E_M in these intervals for C4 on 15 February, 2010. The intervals show the minutes and seconds after the hour of 23 UT.

error bar of v_{MP}. For this case with C4 data, the intervals and corresponding v_{MP} are listed in Table 4.1. The first value of -26.0 km/s was eliminated, since it was the trial with the outermost interval deep into the inflow region, and it had a large difference in value from the other intervals. The magnetopause velocity was determined as v_{MP} = -34±2 km/s. The negative value meant that the magnetopause was moving towards the Earth, which was consistent with the crossing from magnetosphere to magnetosheath. The red curve in Figure 4-1i shows $E_M^{'}$ after subtracting v_{MP} = -34 km/s, and it exhibits an average negative value between the inflow regions on two sides. The black curve in Figure 4-1g shows $v_N^{'}$ after subtracting v_{MP}, which is closer to zero on the magnetosheath side of the field reversal region. The average $v_N^{'}$ in the magnetosheath inflow region was -21.2±2 km/s, which was used as v_{in}. We only used the inflow velocity from the magnetosheath side, since the velocity on the magnetospheric side had much larger variations as shown in Figure 4-1g. The average B_L in the magnetosheath inflow region was used as B_{in}. Thus we obtained R_m=1.22±0.12 mV/m with $v_{in}B_{in}$ for the measured reconnection rate.

4.2.3 Predicted reconnection rate from observed local parameters

The asymmetric reconnection rate is predicted by R_{cs} in eq. (4.2). For this calculation, we use LMN coordinates determined from MVA, where B_L is the reconnecting magnetic field and the average B_M across the reconnection regions acts as the guide field. Thus the average B_L in the inflow regions on the two sides are used as B_{ph} and B_{sh} in the reconnection rate

calculation.

On the magnetosheath side, the number density and mass density are dominated by the H^+ ions. The average H^+ density measured by CODIF in the magnetosheath inflow region is used as n_{sh}. The hot magnetospheric plasma close to the magnetopause has a density much smaller than that in the magnetosheath. Its density (n_{ph,H^+}) is the H^+ density above 100 eV measured by CODIF, averaged over the interval when C4 is in the magnetospheric inflow region. Hot magnetospheric O^+, and cold ions from plasmaspheric plumes or ionospheric outflow can increase ρ_{ph}, and hence, decrease the reconnection rate. Therefore, we used the density of O^+ in the magnetopsheric inflow region from CODIF measurements (n_{ph,O^+}) to evaluate the contribution of O^+. The shown interval in Figure 4-1 is the same as that discussed in section 2.3, where we have explained how the cold ion density ($n_{ph,c}$) is determined. In this event, $n_{ph,c}$ is 7.90 cm^{-3} for C4.

Figure 4-2 shows the magnetopause crossing of C1 for the same event. The ion velocity (Figure 4-2d) shows a negative peak around 23:23:30 UT and a positive peak around 23:25:30 UT, along with a B_L reversal (Figure 4-2e). This suggests the crossing from one side of the outflow region to the other, and it is likely that the ion diffusion region is in the middle. Figure 4-3 shows the VDF in the field-aligned coordinate system at the time of the negative velocity jet marked by the red dashed vertical line in Figures 4-2a - 4-2e, which is close to the magnetospheric separatrix. Comparing with the magnetic field direction, the population with negative $v_{\parallel}$ corresponds to the negative v_L jet of the magnetosheath ions. The population with positive $v_{\parallel}$ might be the background magnetosheath ions or those reflected back from the high latitude mirror point. However, another population with zero $v_{\parallel}$ and $+v_{E\times B}$ (marked by the blue circle) is probably the magnetospheric cold ions, since its thermal spread is small and follows the $\vec{E} \times \vec{B}$ drift. Such distinct low-energy populations in VDFs support that cold ions were involved in this reconnection event. Its

density is determined as described in section 2.3, which is 0.50 cm^{-3} for C1.

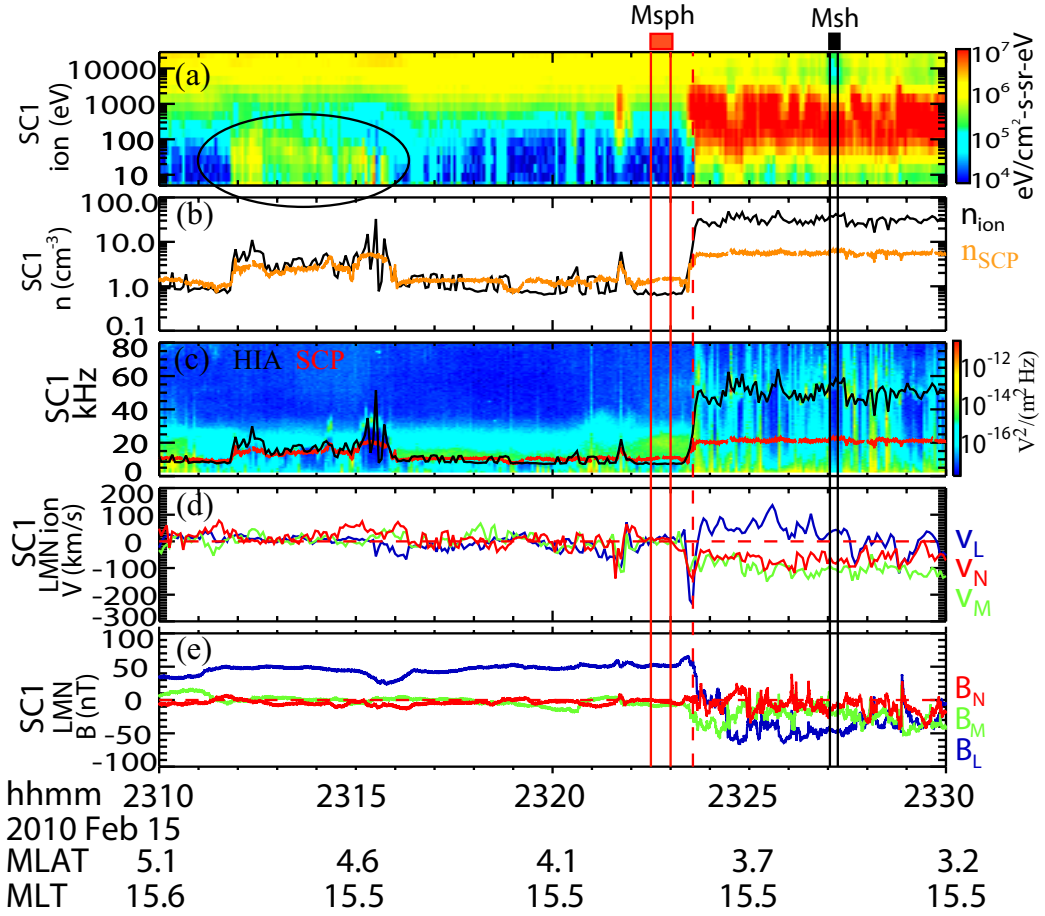

Figure 4-2: Overview of the reconnection event on 15 February, 2010 with the data from C1. (a) Ion energy spectrum from HIA; the black circle suggests the cold ions observed by C4 during the same interval in the magnetospheric inflow region. (b) ion number density from HIA (black) and derived from SCP (orange); (c) Natural mode wave spectrum from WHISPER superimposed with f_{pe} derived from n_{HIA} and n_{SCP}; (d) ion velocity in LMN; (e) magnetic field in LMN. LMN rotation matrix from GSE coordinates: L=[-0.061, 0.481, 0.875]; M=[0.097, -0.869, 0.485]; N=[0.993,0.114, 0.006].

Figure 4-2a shows that the highlighted cold ions are only detected in a limited interval, and Figure 4-2c also shows a decrease of the WHISPER cutoff frequencies at the end of the interval with highlighted cold ions. This indicates that the highlighted cold ion population is only present locally. It is close to and likely does enter the reconnection observed by C4, but might not be involved in the reconnection observed by C1, which was later in time. Although the magnetopause crossings for C1 and C4 were only about 10 min apart, they

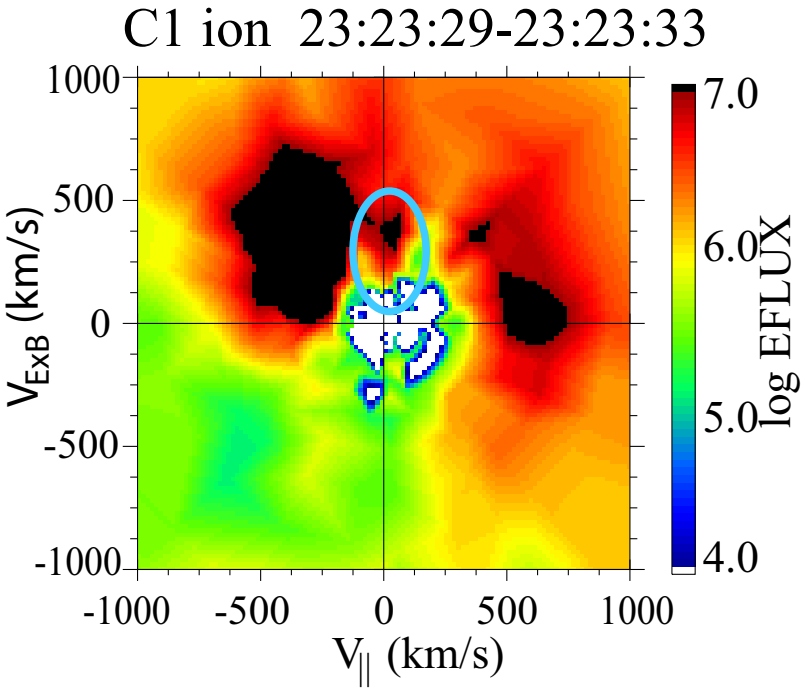

Figure 4-3: Ion VDF flux in the $v_{\parallel} - v_{E\times B}$ plane cut at zero velocity in the third direction for C1 at the time marked by the red dashed vertical lines in Figure 4-2. The blue circle indicates the cold ions from magnetosphere.

might observe the reconnection event with different inflow conditions, e.g., different $n_{ph,c}$.

In order to test whether R_m agrees with the predicted asymmetric reconnection rate (R_{cs}), we first assume that the diffusion region aspect ratio has the typical value of 0.1. We incorporate the mass densities of high-energy ring current H^+, O^+ and cold ions (assumed to be H^+) on the magnetospheric side, and H^+ density in the inflow region on the magnetosheath side, with the inflow magnetic field and the aspect ratio. We find that R_{cs} for this event is 1.33 mV/m for C4, which agrees with R_m (1.22±0.12 mV/m), within the uncertainty.

The Cassak-Shay formula is based on a fluid picture, where the inflows from two sides are well coupled and mixed to become outflows. At the dayside magnetopause, the inflow ions have different populations: magnetosheath H^+, magnetospheric hot plasma H^+, O^+ and magnetospheric cold ions. These ions have different Larmor radii resulting in different

LMN methods	R_{cs}	R_H	$R_{H,high-E}$	R_{sh}	R_m
MVA	1.33	1.35	1.51	1.21	1.22±0.12
Constant B_g	1.35	1.38	1.55	1.31	1.26±0.12
Bisection	1.35	1.38	1.55	1.30	1.32±0.12

Table 4.2: Predicted and measured reconnection rates for the reconnection event observed by C4 on 15 February, 2010, in unit of mV/m.

scales where they become demagnetized, and they may or may not behave in the same way, as discussed in Chapter 3. The kinetic effects might cause the reconnection rate to deviate from the Cassak-Shay formula for the fluid picture. Therefore, we also calculate the predicted reconnection rates without including the contribution of all populations. The results for C4 measurements are listed in the first row of Table 4.2. R_H and $R_{H,high-E}$ follow the form of R_{cs}, incorporating the inflow parameters on both sides. However, R_H excludes the density of O^+, and $R_{H,high-E}$ excludes the densities of both magnetospheric O^+ and cold ions. We also calculate the predicted reconnection rate assuming that it only depends on the magnetosheath parameters:

$$R_{sh} = 0.1 v_{A,sh} B_{sh} \tag{4.5}$$

For the above event, $R_{H,high-E}$ is much higher than R_{cs}. R_H and R_{sh} are closer to R_{cs}, due to the negligible O^+ density, and quasi-symmetric magnetic field and densities on the magnetosphere and magnetosheath sides. For all variations of the predicted rate (R_{pre}), R_{sh} is the closest to R_m. In addition, since all R_{pre} are close to R_m, the approximation of the aspect ratio to be 0.1 seems to be reasonable.

The reconnection rates for C1 in this event are listed in Table 4.5. With some differences in inflow conditions, the determined v_{in} were similar for both C1 and C4, and R_{cs}, R_{sh} and R_m of C1 are consistently lower than those of C4.

4.2.4 X-line orientation

For component reconnection, only B_L contributes to the energy conversion and should be used to calculate the reconnection rate. Previous studies have shown that the X-line might have two preferred orientations [e.g., *Sonnerup*, 1974; *Swisdak and Drake*, 2007]. Figure 4-4 illustrates the magnetic field configuration in the $L-M$ plane. B_{ph} and B_{sh} vectors are the inflow magnetic fields in the $L-M$ plane with an angle of θ in between. The black coordinate system represents the one determined by MVA, where B_L is reversed on two sides, but there is no specific criterion for B_M. *Sonnerup* [1974] suggested that the X-line orientation is such that, the current perpendicular to the X-line vanishes in the reconnection mid-plane, which results in a constant guide field (B_g) across the reconnection region. With such an orientation, there is no net $\vec{J}\times\vec{B}$ force acting on the X-line [*Sonnerup*, 1974]. This constant B_g coordinate ('Const B_g') is shown in red in Figure 4-4, with an angle of α_1 rotated from the MVA coordinate (positive if clockwise). Another possible configuration is to maximize the reconnection outflow speed, which is equivalent to maximizing $v_{A,asym}$ based on B_L on two sides [e.g., *Swisdak and Drake*, 2007]. In the second configuration, the X-line orientation depends on the upstream magnetic field and density, but the orientation where the X-line evenly divides the angle between the magnetic fields on two sides is a good approximation [*Swisdak and Drake*, 2007; *Borovsky et al.*, 2008]. The corresponding coordinate ('Bisection') is shown in blue in Figure 4-4, which has a rotation angle of α_2 from the MVA coordinate.

For the purpose of completeness, we also calculated reconnection rates in the 'Constant B_g' and 'Bisection' coordinates. The normal direction is adopted from the MVA result and the $L-M$ plane is rotated according to the criteria. For the reconnection event on 15 February, 2010 observed by C4, $\alpha_1 = -5.9°$ and $\alpha_2 = -7.1°$. Figure 4-5 compares the magnetic fields in different coordinates. The changes of the coordinates lead to small

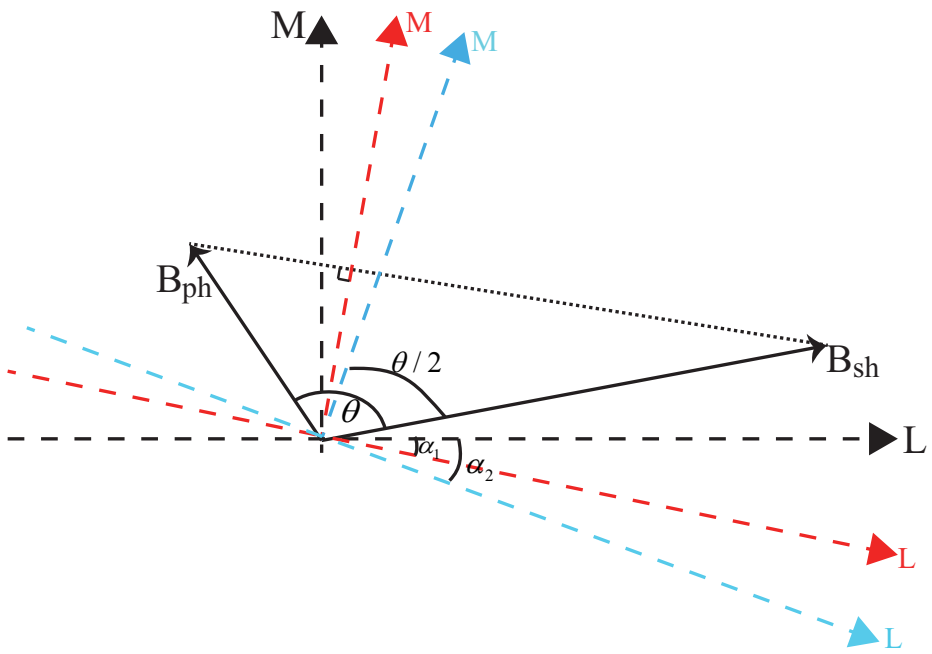

Figure 4-4: Illustration of the X-line orientation and the magnetic field configuration. The black coordinate is determined by MVA, the red coordinate is determined assuming a constant guide field ('Const B_g'), and the blue coordinate is determined assuming the X-line with the same angle between the magnetic fields on two side ('Bisection'). θ is the angle between the inflow magnetic field on two sides, α_1 is the angle rotated from MVA coordinate to the Const. B_g coordinate, and α_2 is the angle rotated from MVA coordinate to the Bisection coordinate.

differences in the magnetic field components. It can be seen that B_M is decreased on the magnetospheric side inflow region and increased on the magnetosheath side after rotation. The rotation of the coordinates results in a small modification in the reconnection rate calculations as shown in Table 4.2. However, the reconnection rate calculation is relatively insensitive to these coordinate changes for this event.

4.3 Statistical result

Using the techniques described above, we successfully analyze 8 dayside magnetopause reconnection events observed by multiple Cluster spacecraft and calculate their reconnection rates. The statistical results are presented in this section.

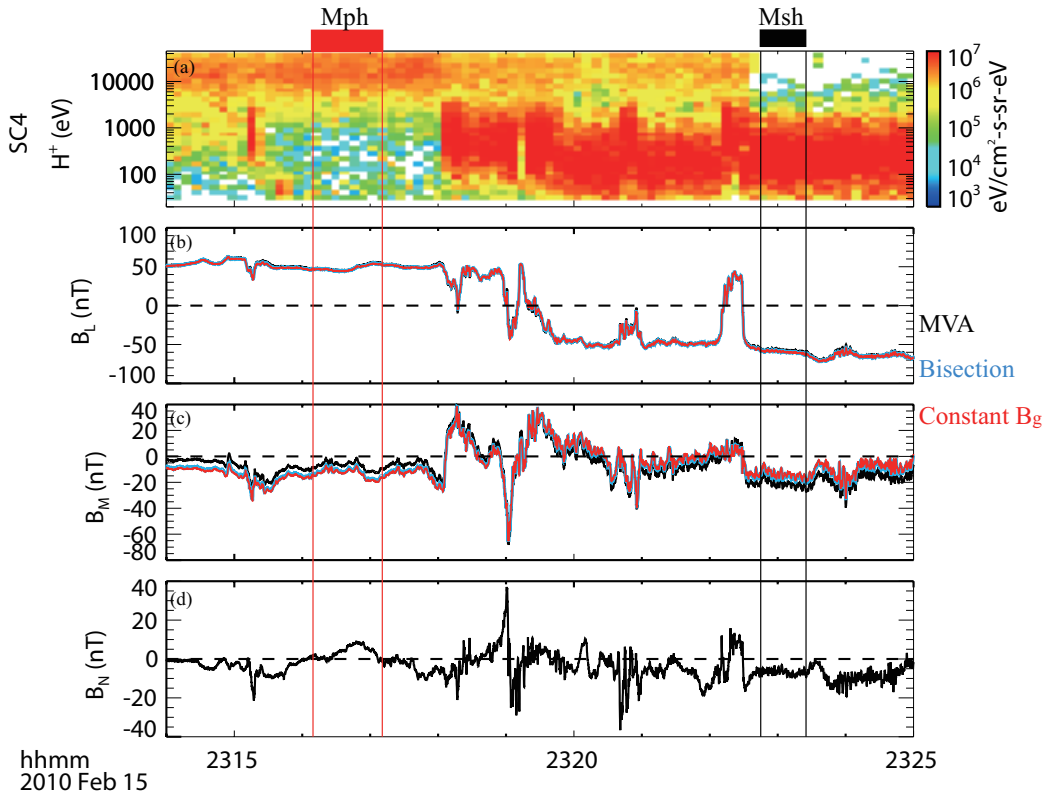

Figure 4-5: Data comparison between coordinates with different assumptions of the X-line orientation for C4 on 15 February, 2010. (a) H^+ energy spectrum; (b)-(c) B_L and B_M in three coordinates; (d) B_N, which is the same for three coordinates. For this event,$\alpha_1 = -5.9°$ and $\alpha_2 = -7.1°$.

4.3.1 Statistical analysis

The ion mass densities in the inflow region were determined in the following way. n_{sh} is the average H^+ density from CODIF, or the average ion density from HIA in the magnetosheath inflow interval. The magnetosheath mass density was $\rho_{sh} = m_{H^+} n_{sh}$. On the magnetospheric side, the density consists of three parts: n_{ph,H^+}, n_{ph,O^+}, and $n_{ph,c}$. n_{ph,H^+} is the average CODIF H^+ density in the magnetospheric side inflow region integrated from energies above 100 eV, and n_{ph,O^+} is the average CODIF O^+ density. For the crossings where CODIF data is not available (C1 after 2004 and C3 after 2005), the quantities from C4 are used, assuming that the magnetospheric hot plasma density and composition do not vary a lot between the crossings of the different spacecraft. The total plasma density in

the magnetospheric inflow region is mainly based on the WHISPER cutoff frequency. If it agrees with any of the derived cutoff frequencies based on HIA, CODIF measurements or SCP formulas, the values in agreement are used; otherwise the cutoff frequency is manually selected. $n_{ph,c}$ is obtained by subtracting the total plasma density in the magnetospheric inflow region by n_{ph,H^+} and n_{ph,O^+}. Then the mass density of the magnetospheric inflow region is $\rho_{ph} = m_{H^+}\left(n_{ph,H^+} + n_{ph,c} + 16n_{ph,O^+}\right)$.

The analyses are performed for C1 and C4 for each event. If the result from one of the spacecraft is not reasonable, e.g., the data is not in good quality or the resulting R_m is negative due to the uncertainty in v_{MP}, only the reasonable result from one spacecraft is used. In addition, there were 2 out of the 8 events where C3 had good data, while C1 and/or C4 data did not provide reasonable results, and hence C3 results were used. The analysis procedures are summarized as follows.

(1) Determine LMN coordinates with MVA of the magnetic field.

(2) Identify the reconnection sub-regions. Separatrices on magnetospheric and magnetosheath sides are identified as the mixture boundaries of the plasmas from the two sides, which can be determined from the plasma flux, density, and the boundary of the electric field wave activity. The inflow regions on the two sides are chosen to be outside and close to the separatrices with steady density, velocity and magnetic field.

(3) Estimate the inflow velocity from the magnetosheath. Apply eq. (4.4) for various intervals across the magnetic field reversal region to estimate the magnetopause motion (v_{MP}), such that the E_M variation is minimized between the inflow regions on two sides. The criteria of the interval selections were described in section 4.2.2. The variation range of v_{MP} as the selected interval changes is used as the error bar of v_{MP}. Inflow velocity from magnetosheath is $v_{in} = v_N - v_{MP}$, where v_N is the average normal component of H^+ velocity in the magnetosheath inflow region. Its error bar is the same as that for v_{MP}.

Date	SC	UT hh:mm	MLAT	MLT	θ_B ($\circ$)	$n_{ph,O+}$ (cm^{-3})	$n_{ph,c}$ (cm^{-3})	n^*_{ph} (cm^{-3})	n_{sh} (cm^{-3})
2003-05-30	1	14:28	42.9	5.9	162	0.026	0.22	1.01	7.82
	4	14:28	39.4	5.9	170	0.051	0.26	1.77	10.76
2004-04-06	1	04:34	31.1	10.2	169	0.110	0.40	2.53	14.63
2005-03-09	3	09:07	26.8	12.3	99	0.052	1.84	2.89	9.22
2007-03-05	1	19:09	35.4	12.9	154	0.010	6.84	7.29	23.25
	3	19:13	29.8	12.6	161	0.010	6.84	7.29	23.50
2008-03-03	1	23:15	3.3	13.2	140	0.060	0.36	1.40	2.64
2008-04-22	1	18:09	23.0	10.2	147	0.004	0.61	0.81	34.21
	4	18:08	17.8	10.2	143	0.004	0.61	0.81	21.90
2010-02-15	1	23:24	3.8	15.5	146	0.094	0.50	2.84	34.41
	4	23:19	0.8	15.4	152	0.094	7.90	10.24	34.98
2012-06-17	1	10:23	-23.7	9.8	152	1.26	0.04	22.20	71.02
	4	10:08	-28.5	9.7	148	1.26	0.04	22.98	43.95

Table 4.3: Measured parameters for reconnection events. θ_B is the shear angle between the inflow magnetic field on two sides. Densities are the average values in the inflow regions and $n^*_{ph} = 16n_{ph,O+} + n_{ph,c} + n_{ph,H+}$. When applying R_{cs}, $\rho_{ph} = m_{H^+}n^*_{ph}$ and $\rho_{sh} = m_{H^+}n_{sh}$.

(4) Calculate the measured reconnection rate. Use the average B_L as B_{in} in the magnetosheath inflow region. $R_m = v_{in}B_{in}$.

(5) Determine plasma densities in the inflow region as discussed above, and the average B_L in the inflow regions as B_{ph} and B_{sh}. Calculate the predicted reconnection rate (R_{pre}) as follows. Assuming the aspect ratio to be 0.1, apply eq. (4.2) to calculate R_{cs} and the other predicted reconnection rates excluding the contributions of O^+ (R_H), of both O^+ and cold ions ($R_{H,high-E}$), and of magnetospheric parameters (R_{sh}).

(6) Rotate the coordinate system according to the 'Constant guide field' and 'Bisection' criteria and calculate the corresponding reconnection rates.

With the above procedures, we get the statistical results listed in Tables 4.3 - 4.5. We analyze these results in the following subsections. We find that the X-line orientations tested in step (6) do not make much difference, and therefore the results shown in the tables and figures are with the LMN coordinates determined by MVA.

Date	SC	$1-M_{O+}^2$	$1-M_c^2$	$1-M_{ph}^2$
2003-05-30	1	0.049	0.026	0.119
	4	0.067	0.021	0.146
2004-04-06	1	0.010	0.023	0.145
2005-03-09	3	0.037	0.082	0.129
2007-03-05	1	0.004	0.182	0.194
	3	0.005	0.194	0.206
2008-03-03	1	0.18	0.066	0.255
2008-04-22	1	0.001	0.012	0.016
	4	0.002	0.019	0.025
2010-02-15	1	0.036	0.012	0.069
	4	0.037	0.196	0.254
2012-06-17	1	0.189	0.0004	0.208
	4	0.353	0.0007	0.402

Table 4.4: Mass fractions $1-M_s^2=\rho_s B_{sh}/\left(\rho_{ph}B_{sh}+\rho_{sh}B_{ph}\right)$ of the population s, where s can be O^+, c (cold ions), and ph (all magnetospheric populations) in reconnection events.

Date	SC	v_{MP} km/s	v_{in} km/s	R_{cs} mV/m	R_{sh} mV/m	R_m mV/m	AP_{cs}	AP_{sh}
2003-05-30	1	-82	35.7±6	3.63	2.83	2.15±0.36	0.06±0.01	0.08±0.01
	4	-30	12.0±2	2.80	2.20	$0.69pm0.11$	0.02±0.01	0.03±0.01
2004-01-04	1	-77	28.2±4	0.22	0.30	0.67±0.09	0.30±0.04	0.22±0.03
	4	-108	19.9±3	0.21	0.30	0.42±0.06	0.20±0.03	0.14±0.02
2004-04-06	1	-4	24.6±3	2.09	1.57	1.29±0.16	0.06±0.01	0.08±0.01
2005-03-09	3	16	24.5±3	0.55	0.25	0.45±0.06	0.08±0.01	0.18±0.02
2007-03-05	1	-24	16.4±5	0.85	0.55	0.57±0.17	0.07±0.02	0.10±0.03
	3	-3	29.4±3	1.17	0.81	1.25±0.13	0.11±0.01	0.15±0.02
2008-03-03	1	-6	21.1±7	0.70	0.42	0.37±0.12	0.05±0.02	0.09±0.03
2008-04-22	1	7	30.7±5	1.21	0.67	1.30±0.11	0.11±0.02	0.19±0.03
	4	-6	26.0±6	1.13	0.62	0.95±0.22	0.08±0.02	0.15±0.04
2010-02-15	1	-51	21.2±7	1.17	0.79	0.98±0.33	0.08±0.03	0.12±0.04
	4	-34	21.2±2	1.33	1.21	1.22±0.12	0.09±0.01	0.10±0.01
2012-06-17	1	-40	14.3±5	2.35	1.65	1.14±0.40	0.05±0.02	0.07±0.02
	4	-37	43.0±3	2.22	2.46	3.72±0.26	0.17±0.01	0.15±0.01

Table 4.5: Calculated parameters for reconnection events. AP_{cs} and AP_{sh} represent 'Aspect Ratios' normalized by R_{cs} and R_{sh}, respectively. The error bars for v_{MP} are the same as those for v_{in} and are only listed with v_{in}.

4.3.2 Magnetospheric O^+ and cold ion abundance

Figure 4-6a shows the relationship between the magnetospheric cold ion density and MLT. For the events with $n_{ph,c}$ greater than 0.3 cm^{-3} (marked by the dashed line), there were distinct cold ion populations present in the energy spectra, identified as a separate population from the hot magnetospheric plasma. For the two events with $n_{ph,c}$ smaller than 0.3 cm^{-3}, there were no clear distinct low-energy populations in the energy spectra or ion VDFs close to the reconnection region. The ion densities from HIA or CODIF in these two events are very close to those from the WHISPER cutoff frequencies. Therefore, they might either have no distinct cold ion populations, or have cold ions with very low densities. We regard them as events with no distinct cold ion populations, and the particles below 100 eV are probably the low-energy tail of the hot plasma population.

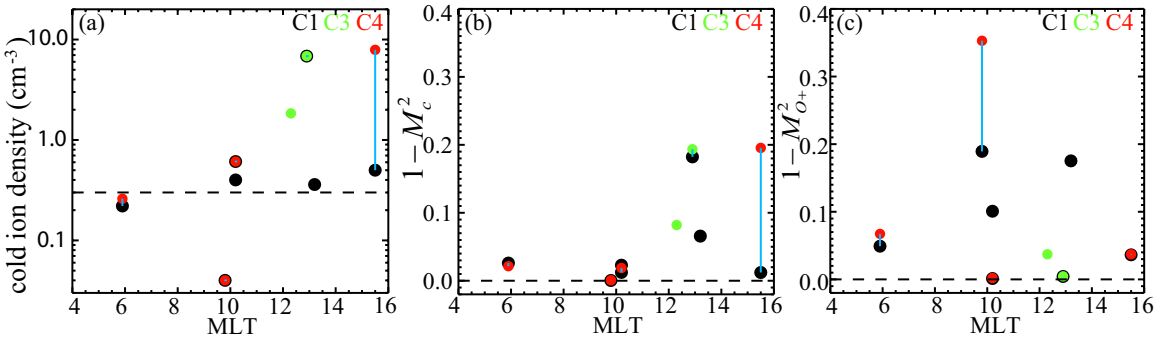

Figure 4-6: Magnetospheric O^+ and cold ion abundance as a function of MLT. Measurements are taken in the magnetospheric inflow regions with different spacecraft marked by different colors. Points connected with blue lines or are overlapped are for the magnetopause crossings of different spacecraft with a short time difference (same for all figures afterwards). (a) cold ion density, where the events with densities below the dashed line do not show clear distinct populations of cold ions, and the low-energy ions are likely to be the low-energy tail of the ring current population. (b)-(c) mass density fractions of cold ions and O^+ in reconnection $1 - M^2_{c/O+} = \rho_{ph,c/O+} B_{sh} / (\rho_{ph} B_{sh} + \rho_{sh} B_{ph})$.

It can be seen that the events with large cold ion densities ($> 1 cm^{-3}$) were in the afternoon sector with MLT between 12 and 16. This is the expected region for cold ions from the plasmaspheric drainage plumes to be observed [*Su et al.*, 2001; *Borovsky et al.*,

2008]. The events with lower densities of cold ions, which were less than 1 cm^{-3}, were closer to the local noon and the morning sector. The low-density plasmaspheric plume might be one possible source for these cold ions. In addition, the ionospheric outflow convecting to dayside magnetopause, with a typical density of a few cm^{-3} at all local times, might be another source of cold ions [*Su et al.*, 2001; *Borovsky et al.*, 2008]. Thus, the similar densities and the MLT distribution of cold ions in these reconnection events might come from the ionospheric outflow. When these cold ions are detected near the reconnection region, they are mainly convecting with the $\vec{E} \times \vec{B}$ drift, so it is difficult to determine their sources.

The statistics show that 6 out of 8 events had cold ions close to the magnetospheric separatrix region, which indicates that the cold ions are a common population close to the reconnection region and therefore might affect the reconnection process. On the other hand, the events where the measurements from different spacecraft show large differences indicate that the cold ion spatial distribution near the magnetopause is not uniform, and this can affect how these cold ions influence the reconnection process.

At the dayside magnetopause, the mass density is usually dominated by the magnetosheath population. If R_{cs} is correct, an increase of the mass density by O^+ or cold ions from the magnetosphere can decrease the reconnection rate. From eq. (4.2), the effect of O^+ and cold ions to the reconnection rate depends on the mass factor

$$M = \sqrt{1 - \frac{\rho_{ph,O^+/c} B_{sh}}{\rho_{ph} B_{sh} + \rho_{sh} B_{ph}}} \tag{4.6}$$

Compared with an event without O^+ or cold ions, the local reconnection rate is decreased to a fraction of M due to these ions [*Borovsky et al.*, 2013], and the mass fraction $1 - M^2_{O^+/c} = \rho_{ph,O^+/c} B_{sh} / (\rho_{ph} B_{sh} + \rho_{sh} B_{ph})$ represents the fractional contribution of O^+ and cold ions compared to other ion populations.

Figures 4-6b and 4-6c show the mass fraction $1 - M^2$ of cold ions and O^+ in our

reconnection events. For the events with high cold ion densities (likely from a plasmaspheric drainage plume), $1 - M^2$ lies around the range of 10% to 20%, and the corresponding multiplicative factor for local reduction of reconnection M is 89% to 95%. *Borovsky et al.* [2013] used empirical solar wind-magnetosphere coupling relations to estimate M due to plasmaspheric drainage plume as 49%-95%, and the corresponding mass fraction $1 - M^2$ is 10%-80%. Our results from in situ measurements of the cold ions at reconnection regions lie within their empirical range of the mass fraction, but we have not found events where cold ions have larger contributions than ∼20%. The low-density cold ions from either the plasmaspheric drainage plume or ionospheric outflow might have a mass fraction of several percent as shown in Figure 4-6b. O^+ typically has a contribution of $1-M^2$ that ranges from a few percent to ∼20% (Figure 4-6c), and there is one extreme case where it contributes up to 35%.

4.3.3 Reconnection rate

In this section, we will present the reconnection rate calculation results. The calculated magnetopause motion, inflow velocity, predicted and measured reconnection rates, and the aspect ratio are listed in Table 4.5.

Figure 4-7 shows the comparison of the predicted Cassak-Shay formula, using observed local parameters, and the corresponding measured reconnection rates, where R_{cs} is calculated with an aspect ratio of 0.1. If R_{cs} is correct, R_m and R_{cs} should have a good positive linear correlation, and the slope between R_m and R_{cs} should be 10 times the aspect ratio. We applied linear fitting between the two parameters in both unweighted and weighted ways, and the weight of each magnetopause crossing is proportional to $1/\Delta R_m^2$, where ΔR_m is the error bar of the measured reconnection rate evaluated by the uncertainty of v_{MP}. Figure 4-7 shows that R_m and R_{cs} indeed exhibit positive correlations, with a linear cor-

relation coefficient of 0.52. The green points in Figure 4-7 are the reconnection rates from an additional event to the 8 events in the list. With the help of the maximum-shear-angle model [*Trattner et al.*, 2007], we concluded that the local measurements for this event are likely to be significantly different from those near the X-line, so that we dropped this event. More details on this will be discussed later.

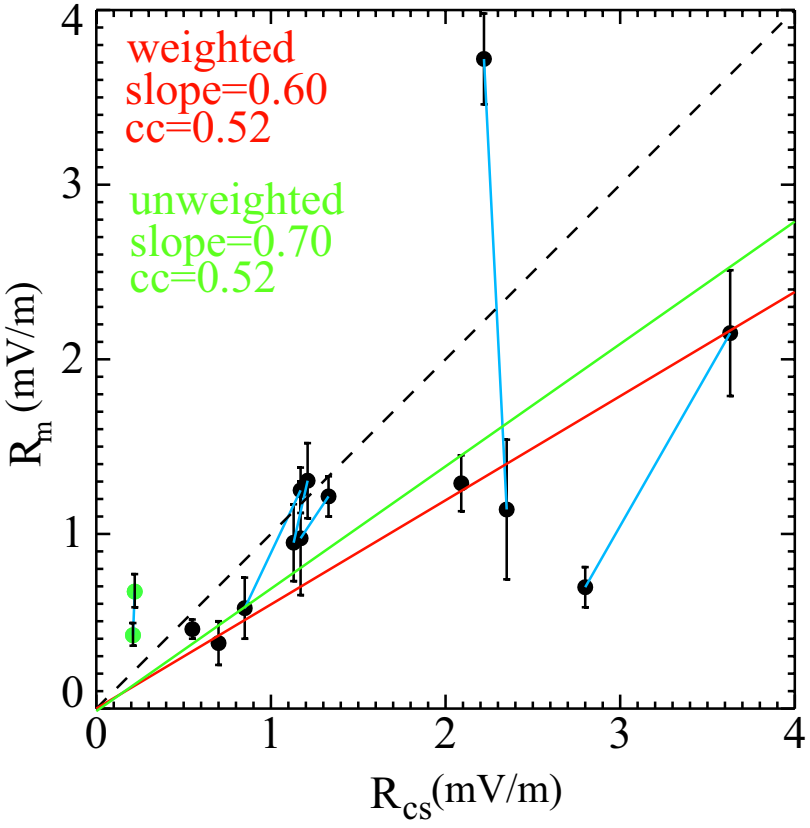

Figure 4-7: Comparison between measured (R_m) and predicted reconnection rates according to the Cassak-Shay formula (R_{cs}) assuming the aspect ratio to be 0.1. The calculation is in the LMN coordinates determined by MVA. Red line: weighted linear fitting between R_m and R_{cs}. Green line: unweighted linear fitting. Dashed line: reference line with a slope of 1. Measurements from different spacecraft are not distinguished with colors. The green points are for a reconnection event not included in the statistics list, which might have large differences between the local parameters and those near the X-line. See text for details.

Figure 4-8 shows the effects of O^+ and cold ions on the reconnection rate. The black points show the R_m vs. R_{cs} correlation, the same as in Figure 4-7. For the other data points, we take out the mass density of O^+ (blue, R_H) or the mass density of both O^+ and

cold ions (red, $R_{H,high-E}$) from R_{cs} in eq.(4.2), while R_m is not changed. Thus, the points with three colors at the same R_m value are for the same reconnection event. The difference between the blue (red) points and the black points indicate the contribution of O^+ (O^+ and cold ions) to the reconnection rate. Excluding O^+ and/or cold ion densities increases R_{pre}. For individual events, the contribution of O^+ and/or cold ions can be considerable. However, the variation of R_{pre} in different events is much larger than the modifications by O^+ and cold ions. Therefore, it is still the magnetosheath parameters which result from the solar wind conditions that dominate the variations in the reconnection rate.

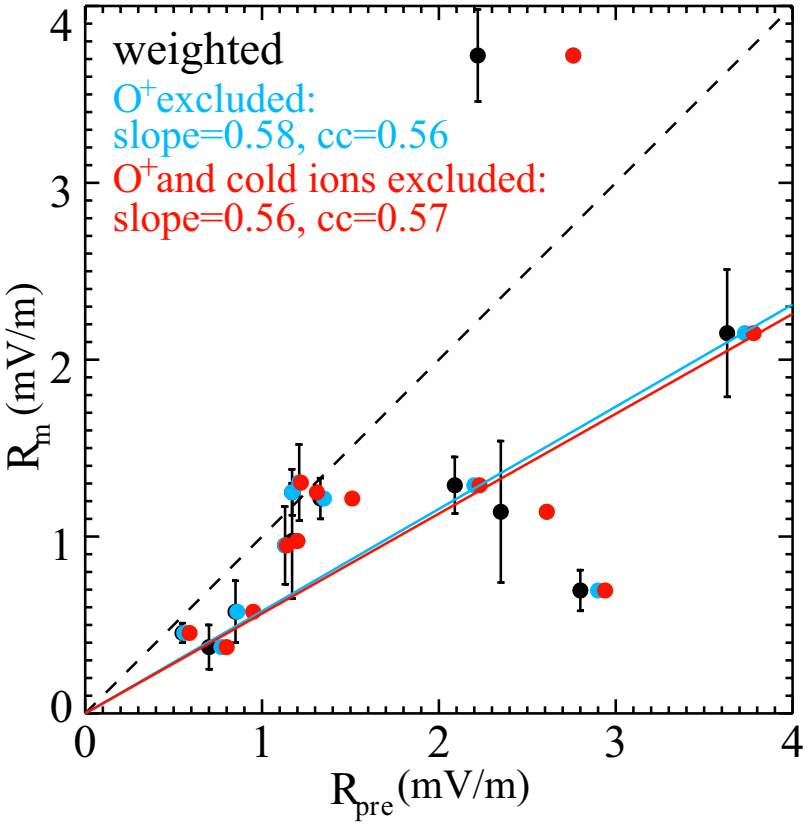

Figure 4-8: Reconnection rates showing the contributions of O^+ and cold ions. Measurements from different spacecraft are not distinguished. Points with the same R_m are for the same event. Black points: R_{pre} from R_{cs}; blue points: R_{pre} with O^+ density excluded; red points: R_{pre} with O^+ and cold ion densities excluded. For individual events, O^+ and cold ions can have large contributions to modify the reconnection rate. However, the magnetosheath parameters dominate the variations of R_{pre}.

As shown in Figure 4-7, the measured reconnection rates generally follow the predicted asymmetric reconnection rate by R_{cs}, converging to an unweighted fitting slope of ~0.7 and a weighted fitting slope of ~0.6. Since the magnetosheath plasmas dominate in dayside magnetopause reconnection, and we have already shown that the variation of the reconnection rate is dominated by the magnetosheath parameter changes, we calculated R_{sh} with only magnetosheath parameters (eq.(4.5)). Keeping R_m unchanged, the reconnection rates are shown in Figure 4-9, with R_{sh} to be the predicted values. Comparing Figure 4-9 with Figure 4-7 for the points with the same R_m values, in most cases, the magnetospheric parameters modify the reconnection rate making it smaller. The linear fit (red line) indicates a correlation with a slope of ~0.9 (unweighted) and ~0.8 (weighted), and the weighted correlation coefficient of 0.62 for R_m with R_{sh} is even slightly better than 0.52 with R_{cs}.

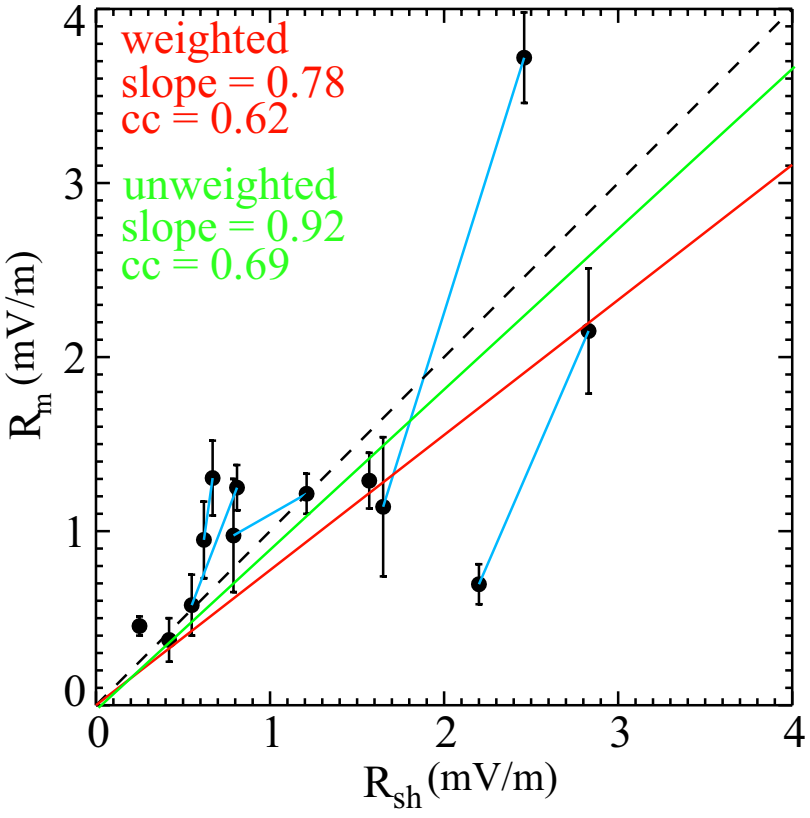

Figure 4-9: Reconnection rates with R_{pre} only including the magnetosheath parameters (R_{sh}). R_m shows a slightly better correlation and larger slope with R_{sh} compared with R_{cs}.

In order to test the significance of the correlation coefficient, we looked up the probability $P_N(r \geq r_0)$, which represents the chance that N measurements of two uncorrelated variables x and y give a coefficient r larger than a particular r_0 [*Taylor*, 1997]. The real correlation between uncorrelated x and y should be zero. Therefore, a larger $P_N(r \geq r_0)$ means that the correlation is less significant, and $P_N(r \geq r_0)$ decreases with increasing N and r_0. In our statistics of the reconnection rate, we have 13 magnetopause crossings from different spacecraft included in the linear fitting. The correlation coefficients in all tests using different R_{pre} are greater than 0.5. With N=13, $P_N(r \geq 0.5)$ is 4.1%. Typically a correlation with $P_N(r \geq r_0) < 0.5$ can be considered as significant [*Taylor*, 1997], and hence, the correlation between R_m and R_{pre} shown above can be considered reliable.

In addition, assuming that the measured samples follow a Gaussian distribution centered at their expected values, we calculated the 95% confident interval for the correlation coefficient of 0.62 between R_m and R_{sh} as [0.10, 0.87] [e.g., *Fisher*, 1921]. The confident interval has a large range due to a limited sample size. The correlation coefficient between R_m and R_{cs} of 0.52 lies in this interval. Therefore, although the apparent correlation coefficient indicates a reliable correlation, there are still large uncertainties in the coefficient. A higher coefficient with R_{sh} might indicate its better performance in predicting the reconnection rate compared with R_{cs}, but it is not statistically significantly better.

4.3.4 Aspect ratio

In the above analysis, the predicted reconnection rates were calculated assuming a fixed aspect ratio of 0.1. The measured and predicted reconnection rates exhibit positive correlations as shown in Figures 4-7 and 4-9. If we assume that v_{in} and v_A are linearly correlated with non-defined ratios between them, the slope between R_m and R_{pre} in Figures 4-7 and 4-9 is ten times of the aspect ratio. From the weighted fitting result, the aspect ratio for

R_m vs. R_{cs} is 0.06-0.07, and that for R_m vs. R_{sh} is 0.08-0.09. Thus, the difference between the two set of values can be interpreted as the correction of the aspect ratio due to the magnetospheric populations.

In addition, the aspect ratio might vary with other parameters, causing the scattering of the slopes for each data point in Figures 4-7 and 4-9. Figure 4-10 shows the aspect ratio normalized by R_{cs}. The correlation between the aspect ratio and the O^+ mass fraction $(1 - M_{O^+}^2)$ (Figure 4-10a) would indicate possible changes of the aspect ratio due to O^+. Previous simulations indicate a positive correlation between the two [*Shay and Swisdak*, 2004; *Karimabadi et al.*, 2011]. The correlation between the aspect ratio and the magnetospheric population mass fraction $(1 - M_{ph}^2)$ (Figure 4-10b) would indicate whether the aspect ratio is changed due to the asymmetry. Previous simulations suggested that the aspect ratio is independent of the asymmetry [*Cassak and Shay*, 2008]. The correlation between the aspect ratio and the magnetic shear angle (Figure 4-10c) would indicate the effect of guide field on the aspect ratio. *Mozer and Retinò* [2007] showed a subtle negative correlation between the aspect ratio and the guide field in observations. On the contrary, *Hesse et al.* [2013] suggested a positive correlation with simulations, inferring that the guide field helps better confine the plasmas in the diffusion region in asymmetric reconnection.

In our results, the aspect ratios are mostly in the range between 0.05 and 0.11. There are two data points outside this range. However, the results from a different spacecraft measuring the same crossings as these two points (connected with blue lines) still lie within this range, indicating that the deviations might be caused by uncertainties in the analysis. The variations of the aspect ratio do not show clear correlations with any of the parameters presented on the horizontal axis of Figures 4-10a-4-10c. We also examined the aspect ratios normalized by R_{sh} (not shown), which exhibits better correlations with R_m. However, other than systematically increasing the aspect ratios from ∼0.06-0.07 to ∼0.08-0.09, there is no

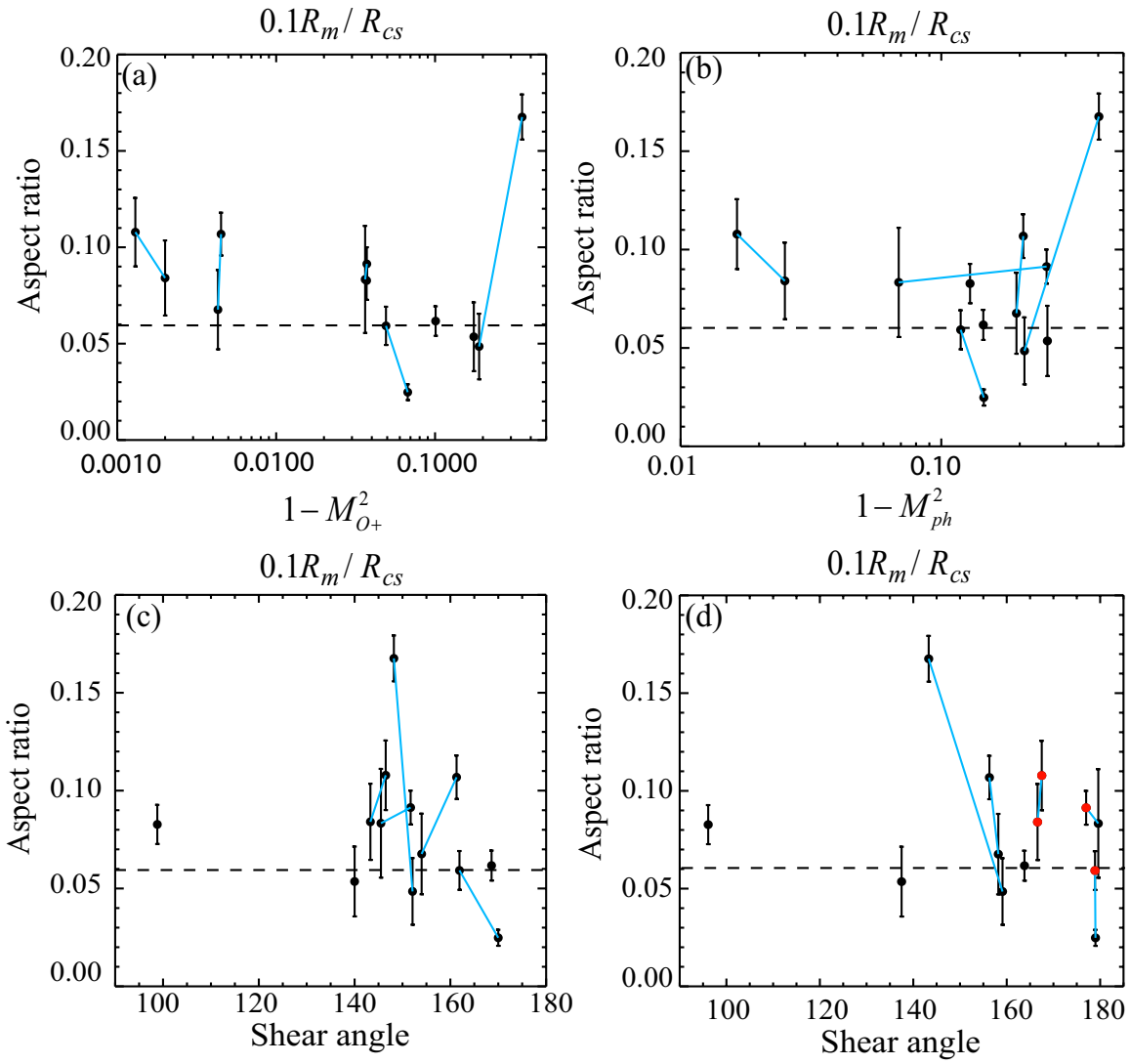

Figure 4-10: Aspect ratio calculated from 0.1 of the slope between R_m and R_{cs} as a function of the O^+ mass fraction (a), magnetospheric populations mass fraction (b), magnetic field shear angle between the field in the inflow region on two sides with Cluster measurements (c) and with the shear angle at the X-line from the maximum-shear angle model. The red points in (d) mark the events where the shear angle at the spacecraft location predicated by the model has a difference greater than 15° with that at the X-line. Larger angles between inflow magnetic fields indicate smaller guide field. The aspect ratio shows no clear dependence on these parameters.

clear dependence with the above parameters.

4.4 Discussion

4.4.1 Effects of the magnetospheric plasmas on the dayside magnetopause reconnection rate

Dayside magnetopause reconnection is mostly dominated by the magnetosheath plasmas, since the reconnection is likely to be driven by the magnetosheath side, and the density is usually higher on that side. We have examined how magnetospheric populations might modify the magnetopause reconnection. They may provide extra mass loading, change the scale of the reconnection region, and cause asymmetry in the reconnection structure. The resulting modifications in the reconnection rate include the changes in the mass density and aspect ratio according to the Cassak-Shay scaling law, and in the scaling law itself.

The Cassak-Shay formula predicts that an increasing density from the magnetosphere by O^+ or cold ions would decrease the reconnection rate. With the data that we have examined, the decrease of the reconnection rate due to O^+ and cold ion mass loading might be up to 10%-20% for individual events. On the other hand, assuming an aspect ratio of the fitting result of 0.06, including their mass density contribution may move the predicted reconnection rates either towards or away from the measured values (Figure 4-8). Therefore, we cannot exclude the possibility that these populations have effects beyond simply providing mass loading.

We did not find a clear correlation between the aspect ratio and the O^+ mass fraction with our results as suggested by previous simulations [*Shay and Swisdak*, 2004]. This might be partially because the O^+ mass fraction is usually small. There are other factors which might have effects on the aspect ratio as well, such as the guide field. Therefore, with a small contribution, an O^+ effect, if there is any, may be hidden. Similar studies should be conducted for magnetotail reconnection events, where O^+ density can be dominant [*Liu*

et al., 2013] and the reconnection is often symmetric and anti-parallel, if the uncertainties in determining magnetotail reconnection rates can be resolved. The effects of O^+ in reconnection should be clearer there.

The asymmetry between the magnetospheric and magnetosheath sides might cause changes in the scaling law itself, e.g., the definitions of $v_{A,asym}$. The Cassak-Shay theory assumes that there is a rectangular diffusion region during reconnection, and that plasmas from two sides of the inflow regions are incompressible and fully coupled in the diffusion region. The deviations from these simplifications by the magnetosphere are the sources of the discrepancy from the Cassak-Shay scaling laws.

Ouellette et al. [2014] examined the asymmetric reconnection outflow parameters with global MHD simulations. They found that the outflow density is usually underestimated by the Cassak-Shay theory. *Birn et al.* [2010] provided a correction factor for compression in the outflow density, which depends on the upstream plasma β on two sides. Another way to understand the underestimate of the outflow density is that it takes a finite time for the plasmas to equilibrate in the reconnected flux tubes [*Ouellette et al.*, 2014]. When the magnetosheath ions have a thermal speed lower than the outflow speed, they might not have enough time to spread along the flux tube. Therefore, the length of the flux tube on the magnetospheric side is shorter, and the outflow density is higher than the Cassak-Shay scaling result [*Ouellette et al.*, 2014]. When the reconnection rate is obtained from observations or simulations, an underestimated outflow density, which is in the denominator of R_{cs}, leads to an underestimate of the aspect ratio.

In addition to the discrepancy that can be understood under the fluid picture, the diffusion region structure might be distorted by asymmetry. The above discussion about the shorter flux tube on the magnetospheric side than the magnetosheath side by *Ouellette et al.* [2014] already indicates this point. MHD simulation results also showed that with

increasing density asymmetry, the outflow further penetrates towards the magnetospheric side of the field reversal region, tilting towards the magnetosphere [*Borovsky and Hesse*, 2007; *Malakit et al.*, 2010]. In asymmetric reconnection, the stagnation point, where the bulk velocity in the normal direction is zero, is on the magnetospheric side of the X point, where B_L changes the sign [*Cassak and Shay*, 2007]. This happens all along the current sheet in the L direction, and forms a stagnation layer, which is the boundary of the tilted outflow.

Such structure changes lead to a question of how plasmas from two sides are coupled. Along the field lines, ions from two sides might spread to different lengths according to their thermal speed [*Ouellette et al.*, 2014]. In the direction perpendicular to the magnetic field, the hot magnetospheric H^+ and O^+ gyrate in a larger scale than the magnetosheath ions. Thus, around the stagnation layer, the magnetosheath ions might be already magnetized, while the magnetospheric hot ions are not. Although observation results show that the magnetospheric hot ions are also deflected and accelerated in reconnection, as discussed in Chapter 3, the fact that ions from two sides behave differently around the stagnation layer still differs from the fully coupled fluid picture. For cold ions, e.g., plasmaspheric plumes, their spatial distributions are not always uniform in MLT and MLAT like that of the ring current. The considerable difference in the cold ion measurements by different spacecraft in the same crossings supports this argument, which is shown in both this study and previous reports [e.g., *Walsh et al.*, 2014]. The cold ions can only be demagnetized in a smaller scale than the ion diffusion region, and they convect with the magnetic field in the regions where they are magnetized (Chapter 3). For the events where the cold ions do not enter the region where they can be demagnetized, they may not affect the reconnection rate as suggested by R_{cs}.

Consequently, the kinetic energy density might not be evenly distributed in plasmas from

the two sides. Taking this into account, *Borovsky and Hesse* [2007] showed that a higher weight for the magnetospheric ions in the outflow density provides better scaling in the reconnection rate in simulation. Therefore, the distortion in the diffusion region structure can change the way ions from two sides are coupled, and in turn deviate the reconnection rate scaling law. A better correction to $v_{A,asym}$ including the effects of imperfect coupling between different plasma populations may be helpful to improve the scaling law.

In this study, we find that the aspect ratio normalized by R_{cs} to be 0.06-0.07, and that normalized by R_{sh} to be 0.08-0.09. The reconnection rate calculated in both methods have reasonable correlations with the local measurements, which means that for practical usage, both methods can be applicable in the reconnection rate estimation. A slightly better correlation for R_m with R_{sh} than with R_{cs} might be caused by the imperfect coupling between different plasma populations, though the different between two correlation coefficients are not statistically significant. Since R_{sh} tends to underestimate v_A by neglecting the magnetospheric parameters, and R_{cs} tends to overestimate v_A with an underestimated outflow density, a better aspect ratio to represent the average geometry of the diffusion region might be between those normalized by R_{sh} and R_{cs}.

In summary, the magnetospheric ions can influence reconnection through adding to the inflow mass density, changing the reconnection diffusion region aspect ratio, and further modifying the reconnection structure with kinetic effects.

4.4.2 Limitations of this study

Our analysis provides reasonable results as shown above. However, there are still limitations in our study. The first limitation is from the data measurement itself. For example, the distance between the spacecraft and the X-line causes uncertainties. The magnetic field configuration and plasma density may vary with distance from the X-line, so that the

parameters on two sides of the magnetopause taken from the local measurements might be different from the inflow conditions at the X-line.

Trattner et al. [2012] reported that anti-parallel reconnection dominates when the IMF is mainly southward. When IMF B_y becomes large, e.g., the clock angle deviates from 180° by more than $\sim 25°$, reconnection might first occur near the sub-solar point as component reconnection, where the magnetosheath and magnetospheric magnetic fields first meet. The X-line extends from this point across the dayside magnetopause towards the cusp or flank regions, where anti-parallel reconnection can happen [*Trattner et al.*, 2012]. Such a model is called the 'maximum shear angle model'. It has been compared with Cluster observations, where the X-line location indicated by the ion spectrum dispersion near the cusp region is consistent with the model results in those examined cases [*Trattner et al.*, 2007, 2012]. Recent studies compared X-line locations between the results in global simulations and models, concluding that the models provide reasonable predictions for southward IMF conditions, however the results are not satisfactory when IMF is northward [*Komar et al.*, 2015].

We examine the likely distance of our observations from the X-line locations using the maximum shear angle model, using as input the solar wind conditions for each event [*Trattner et al.*, 2007, 2012]. The relative location between the spacecraft and the X-line can also be roughly estimated with local measurements. The ion velocity direction and electron pitch-angle distribution can be used to tell which side of the X-line the spacecraft is located on [*Fuselier et al.*, 2011]. The comparison between the ion density gradient and the magnetic field reversal [*Argall et al.*, 2014], and the velocity cutoff in the ion VDFs due to the time-of flight effect [e.g., *Fuselier et al.*, 2005] can be used to tell whether the spacecraft is close to the X-line. Further away from the X-line, the time difference between the density gradient and the magnetic field reversal, and the cutoff velocity in VDF are

larger [*Argall et al.*, 2014; *Fuselier et al.*, 2005].

Figure 4-11a shows an example of an X-line from the maximum shear angle model for the reconnection event on 6 April, 2004 observed by C1. The shear angles are calculated from the magnetic field with T96 model for the magnetosphere and the draping IMF in the magnetosheath. More details of this model are described in *Trattner et al.* [2007, 2012]. In this event, it can be determined from the ion outflow that the spacecraft was above the X-line, and the L direction determined by MVA is in the direction presented by the blue line connecting C1 with the X-line in Figure 4-11a. Its intersection with the X-line is likely to be the X point for this reconnection, and it is close to the point with the minimum distance to C1 on the X-line, which connects with C1 by a black line. The two points are very close. Thus, the model and observation are consistent in determining the X-line location for this event, and the model suggests that the spacecraft was close to the X-line with a distance of $\sim$1 R_E. For this event, the measured parameters on the magnetosphere and magnetosheath sides are likely to be close to those in the inflow regions at X-line. In fact, the magnetic field shear angle is 168.7° in C1 measurements, 162.8° at C1 location in model, and 163.8° at the X point with minimum distance to C1 on the X-line in the model.

On the contrary, Figure 4-11b shows an example where the local measurements are likely to be very different from those near the X-line. First of all, the L direction determined by MVA, which is consistent with the outflow velocity, is marked by the blue line. Its intersection with the X-line determined by the maximum-shear angle model is away from the point closest to the spacecraft. There are multiple magnetopause crossings within 10 min of this event, and there are signatures indicating plasmas coming from multiple X-lines [*Lindstedt et al.*, 2009]. Therefore, it is likely that for this particular crossing, the X-line is not at the closest point to the spacecraft. A most distinct feature is that the spacecraft is located in a region where the magnetic field changes rapidly. According to the model

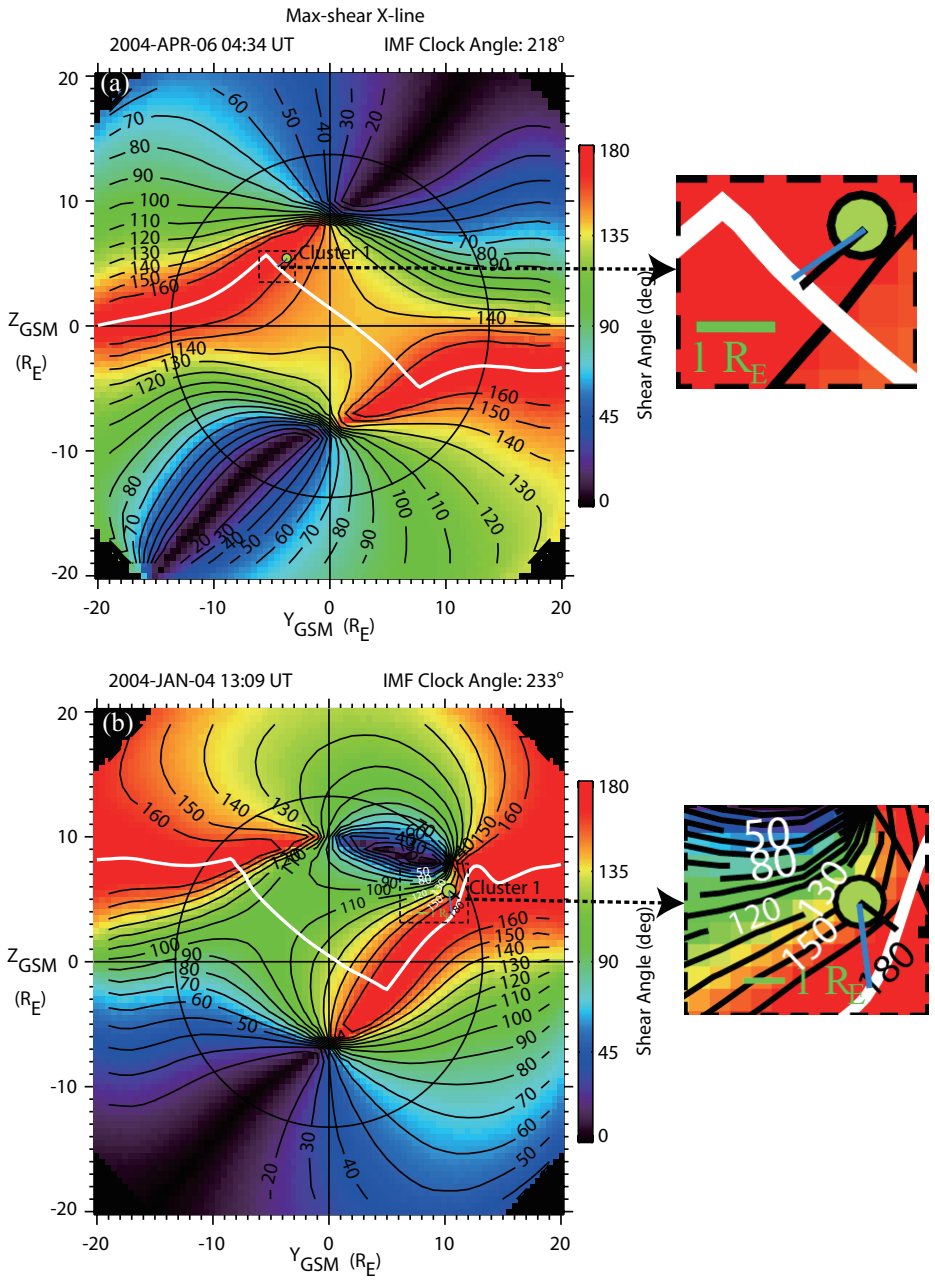

Figure 4-11: X-line information from maximum shear angle model for the reconnection events on 6 April, 2004 (a) and 4 January, 2004 (b). Contours and colors show the magnetic field shear angle. The white line is the X-line predicted by the model. The black circle is the terminator of the magnetopause at X_{GSM}=0. The green circle shows the location of the Cluster spacecraft. A black line connects Cluster with a point on the X-line with the minimum distance from the spacecraft. A blue line connects Cluster with a point on the X-line in the L direction determined by MVA from Cluster measurements. The shear angle difference between the Cluster location and that at the X-line is small in (a) and large in (b). Figure courtesy of Steven Petrinec.

results, the shear angle at the X-line is larger than 165° at the points determined by both minimum distance from Cluster and the L direction from MVA, while it quickly drops to 145° at the spacecraft location. The measured shear angle by Cluster is 115.7°, which has an even larger difference with the shear angle at the X-line. Therefore, it is likely that the local measurements of the magnetic field are very different from those right upstream of the X-line. The reconnection rates of this event are the green points in Figure 4-7. They exhibit a large slope, which means a large aspect ratio around 0.3. However, such results are not reliable, and were not used in the statistics.

For all the events remaining in our statistical study, the differences in the magnetic field shear angle at the X-line, which is the point closest to the spacecraft, and at the spacecraft location, are all smaller than 20°. The differences in the shear angle at the spacecraft location between model and the Cluster measurements are also smaller than 20°. Though there are still inconsistencies in the relative location between the spacecraft and the X-line in about half of the events, the comparison in the shear angle provides some hints about how well the local measurements can represent the real inflow parameters.

In Figure 4-10c, we used the locally measured shear angle to analyze the effect of the guide field on the aspect ratio. Considering the difference in the shear angle between the spacecraft location and the X point, the aspect ratio is shown in Figure 4-10d as a function of the shear angle at the X-line in the model. The red points mark the events where the shear angle difference between the spacecraft location and the X point is larger than 15°. However, the correlation between the aspect ratio and the shear angle is still not strong.

The second limitation is the method for estimating reconnection rates. As is shown in sections 1 and 3, the procedures of interval selections, rotation to the LMN coordinate, and determination of the magnetospause motion, etc., all lead to uncertainties in the reconnection rate calculations. As listed in Table 4.5, the magnetopause motion can be comparable

to or larger than the inflow velocity. This makes the inflow velocity very sensitive to the estimation of the magnetopause motion. Our methods of estimating the magnetopause motion provides reasonable results for the presented events, while the uncertainty can still be up to $\sim$30%.

In addition to the data analysis, the theoretical assumptions may be another error source. Firstly, as listed in Table 4.3, most of these events are at mid-latitudes with MLAT around $20^\circ - 30^\circ$. The magnetosheath flow, which increases with the radial distance from the subsolar point, acts as a shear flow for these events. The shear flow may reduce the reconnection outflow velocity, and hence, reduce the reconnection rate [*Cassak and Otto*, 2011]. With the shear flow larger than the Alfvén speed on either inflow side, reconnection is expected to be suppressed [*Belle-Hamer et al.*, 1995]. The reconnection rate analysis might need modifications under such circumstances. Furthermore, the time evolution of reconnection might cause uncertainties in the reconnection rate analysis. The constant E_M conclusion is valid for steady-state reconnection. If the reconnection event is still developing, this assumption is not valid. *Sonnerup et al.* [2013] applied single-spacecraft analysis methods to simulations with developing reconnections, showing that the temporal development of the reconnection might cause considerable deviation from the analysis results. Moreover, as discussed in section 4.4.1, the density compression, and kinetic effects of plasmas from different origins might require corrections for the Cassak-Shay scaling parameters.

In summary, we have tried reasonable methods to perform the analysis, but it still contains the above mentioned limitations. Better results might be obtained if these limitations can be resolved. However, the sparseness of measurements in space makes it difficult to adequately account for all spatial and temporal variations.

4.5 Conclusions

In this study, we calculate the reconnection rate for 8 dayside magnetopause reconnection events observed by multiple Cluster spacecraft. The measured reconnection rate is calculated as $R_m = v_{in}B_{in}$ in the magnetosheath inflow region, and the predicted reconnection rate is calculated with the Cassak-Shay formula, including all or some of the plasma contributions from two sides of the inflow regions, assuming the aspect ratio to be 0.1. The slope between the measured and predicted reconnection rates gave us an indication of the aspect ratio. The main conclusions are summarized as follows.

(1) The measured reconnection rates (R_m) present clear linear correlations with the Cassak-Shay formula both when including contributions from both inflow regions (R_{cs}), and when including only magnetosheath parameters (R_{sh}). The predictions using only magnetosheath parameters exhibit slightly better correlations than when the inflow parameters on both sides are used. Although the difference between the two is not statistically significant, it may still indicate imperfect coupling between plasmas from two sides of the inflow regions.

(2) Magnetospheric hot O^+ and cold ions appear in the reconnection region. Their mass density fractions are usually a few percent of the total contribution of all ion populations from the two sides of the inflow regions, and are observed to be up to $\sim$30%. If fully coupled in reconnection, they might reduce the reconnection rate by up to $\sim$20%. However, the large scale variations of the reconnection rates are still dominated by the variations of magnetosheath parameters, which come from the solar wind condition variations.

(3) The aspect ratio normalized by R_{cs} is 0.06-0.07, and that normalized by R_{sh} is 0.08-0.09. An aspect ratio between the two is expected to better represent the average geometry of the diffusion region. The fact that both methods show clear correlations between the measured and predicted reconnection rates indicates that both methods are applicable

in estimating magnetopause reconnection rates. However, the outflow density may be underestimated by the Cassak-Shay theory and overestimated by the magnetosheath density. Therefore, if the reconnection rate is known in other ways, e.g., with direct measurements of the inflow speed, the aspect ratio normalized by R_{cs} (R_{sh}) tends to be underestimated (overestimated). On the other hand, if a fixed aspect ratio of 0.1 is used, R_{cs} (R_{sh}) tends to overestimate (underestimate) the reconnection rate.

(4) The aspect ratio does not show a correlation with O^+ density fraction. This may be because the O^+ density is too small to show significant effects. Similar analysis in the magnetotail, where the O^+ can be a dominant contributor, would help to resolve this issue. The aspect ratio does not show a clear correlation with density asymmetry, or guide field, either.

Chapter 5

Understanding of the electron heating process in the exhaust of magnetic reconnection with negligible guide field

5.1 Introduction

In magnetic reconnection, electron heating is an important topic that requires understanding several aspects. The first important aspect is electron bulk heating from the inflow to the exhaust, which represents the amount of magnetic energy that is converted to electron thermal energy.

The concept of bulk heating calculated with the temperature scalar is sufficient to describe the electron thermalization only if the electrons follow a Maxwellian distribution. However, the electron velocity distribution functions (VDFs) in the reconnection exhaust region are found to be highly structured in both observations and simulations. Therefore, an understanding of these VDF structures is necessary to resolve the electron thermalization process.

Types of previously reported VDFs are summarized as follows. Inside the electron diffusion region (EDR), electron VDFs are reported to be triangular in simulations [*Ng et al.*, 2012; *Bessho et al.*, 2014]. Downstream from the EDR, the electron VDF features seem to depend on the distances from the X line and the current sheet mid-plane [*Hoshino et al.*, 2001a; *Asano et al.*, 2008; *Nagai et al.*, 2013; *Shuster et al.*, 2014]. In both simulations and observations, flat-top distributions, where the phase space density (PSD) is constant over a couple decades of the energy range with a steep drop at higher energies, were reported around the ion diffusion region edge in the exhaust with high ion bulk velocities [*Nagai et al.*, 2013], as well as off the mid-plane [*Hoshino et al.*, 2001a; *Asano et al.*, 2008]. The flat-top distributions can be further categorized as isotropic [*Hoshino et al.*, 2001b], or flat-top at low parallel energies with enhanced fluxes at high perpendicular energies [*Smets et al.*, 1998]. In addition, beam structures in VDFs have been observed in simulations and observations. Cold electron beams moving towards the X line (inward) were found close to the separatrix [e.g., *Nagai et al.*, 2001; *Egedal et al.*, 2012]. Inward beams at approximately the 'shoulder energy' (fall-off energy) of the flat-top distributions were reported close to the separatrix and near the locations of flat-top distributions [*Asano et al.*, 2008]. VDFs can also exhibit counter-streaming beams and enhanced fluxes at high perpendicular energies simultaneously close to the magnetic pile-up region, which was reported in simulations [*Shuster et al.*, 2014]. These previous studies suggest associations between the wide variety of reported electron VDF structures and specific regions within reconnection exhausts. Nevertheless, a comprehensive organization and first-principles explanation of these associations are lacking.

Electron heating is essentially related to the energization mechanism of individual particles. Inside the EDR, electrons perform meandering motion and gyrate around the reconnected magnetic fields, where they are accelerated by the reconnection electric field [e.g., *Bessho et al.*, 2014; *Shuster et al.*, 2015]. Such motions were used to explain the VDF fea-

tures in the EDR. Outside the EDR, electrons convect downstream, and those with finite field-aligned velocities also bounce along the magnetic field lines. Three main mechanisms have been used to explain the electron energization outside the EDR. (1) *Egedal et al.* [2010, 2012] used a concept of parallel potential ($e\Phi_{\parallel} = -e\int_{\infty}^{x} \vec{E}_{\parallel} \cdot d\vec{l}$). Electrons are accelerated by the parallel potential as they move along the magnetic field line from near the separatrix region to the mid-plane, and are pitch angle scattered near the mid-plane [*Egedal et al.*, 2012]. They used the parallel potential acceleration to explain the elongation of the VDF in the parallel direction and predict the shoulder energy of the flat-top distribution. (2) *Drake et al.* [2006] attributed the electron acceleration to Fermi acceleration, which is due to the out-of-plane component of the electric field and the electron curvature drift. (3) *Hoshino et al.* [2001b] showed that close to the magnetic pile-up region, the curvature drift for electrons with $\kappa \sim 1$, where κ^2 is the ratio between the magnetic field curvature radius and the electron's Larmor radius, helps to confine the particles close to the mid-plane, while the out-of-plane electric field and the gradient-B drift contribute to the electron acceleration. *Asano et al.* [2008] and *Egedal et al.* [2012] suggested that the pitch angle scattering caused by instabilities near the mid-plane isotropizes the electron VDF, so that the beam structure disappears. On the other hand, *Smets et al.* [1998] pointed out that the pitch angle scattering only affects the high-energy electrons with , so that the parallel elongation remains at low energies. While these studies identify many important electron energization mechanisms, they leave open the questions of how much each mechanism contributes to the energization, and which mechanism dominates at different locations within the exhaust. Also more detailed analysis of how these energization mechanisms form highly structured VDFs is needed.

In order to understand the electron heating process, we need to establish the connection between electron bulk heating, VDF features, and single particle acceleration mechanisms.

Few studies have made efforts on such connections. *Shay et al.* [2014] suggested that the electron temperature (T_e) does not vary much with the distance from the X line; the temperature anisotropy is built up close to the X-line, but the temperature would be isotropized in the far exhaust. However, the highly structured VDFs in different regions, along with the different electron energization processes indicate the existence of more detailed T_e variations and anisotropy characteristics in the exhaust region, which are worthwhile to investigate. *Dahlin et al.* [2014] analyzed simulation moments data and the integrated electron spectrum over the whole simulation domain for reconnection with a large guide field. They concluded that the contributions of Fermi acceleration and the parallel potential to electron heating were comparable. However, their studies did not take into account how the relative contribution of these energization mechanisms depends both on the specific location within the exhaust and the particular populations of the VDFs under consideration. Also, they did not analyze the case of reconnection where the guide field is negligible.

In this study, we use particle-in-cell (PIC) simulations of symmetric reconnection with negligible guide field (i.e., less than 5% of the initial reconnecting component) to study electron heating from all three aspects introduced above: (1) electron bulk heating, (2) VDF structures, and (3) single-particle motions. We compare the simulation results with a magnetotail reconnection event observed by the Cluster spacecraft. Section 5.2 shows the simulation results of T_e spatial variations in the exhaust region and the associated VDFs. The observation results are shown in section 5.3. In section 5.4, we discuss the electron single-particle motion in the exhaust to understand the spatial evolution of VDFs.

5.2 Simulation results

The simulation data we use are introduced in section 2.7. In this chapter, unless otherwise stated, the density is normalized by the initial peak current sheet density n_0, the velocity is

normalized by the ion Alfvén speed v_{Ai0} based on B_0 and n_0, the temperature is normalized by $m_i v_{Ai0}^2$, time is normalized by the inverse of the ion gyro-frequency (ω_{ci}^{-1}) based on B_0, and the length is normalized by the electron inertial length (d_e). Detailed analysis of the T_e profile, electron VDFs and electron motion are carried out for simulation 1 with the mass ratio $m_i/m_e = 400$, background-to-current sheet density ratio $n_b/n_0 = 0.05$ and zero guide field, and the T_e profiles for the other three simulations are examined.

We first analyze the simulation run 1 data to discuss electron temperature characteristics and the related electron VDFs in the reconnection region at $t = 29\omega_{ci}^{-1}$, which is about 11 ω_{ci}^{-1} after the time of peak reconnection rate. At this time, the X line is at [x, z]=[900, 0]. The end of EDR is around x=1090, where the electron outflow jet with high values of the electron velocity in x (u_{ex}) ends (Figure 5-1a), and u_{ex} along $z = 0$ starts to agree with the x component of the $\vec{E} \times \vec{B}$ drift velocity (not shown). The magnetic field pile-up region, where the magnetic field strength (B_t) significantly increases, is around x >1320, which can be seen from the magnetic field line contours (also shown in Figure 5-4a). Thus, EDR and the pile-up region are well separated at this time, allowing for a detailed view.

5.2.1 Temperature profiles

Figures 5-1b-5-1d show the profiles of the electron total temperature (T_{et}), perpendicular temperature ($T_{e\perp}$) and parallel temperature ($T_{e\parallel}$), respectively. The temperature generally increases from the separatrix (marked by the white curves) to the deep exhaust with structured variations. The variations inspire a division of the exhaust into different sub-regions labeled above Figure 5-1a and the boundaries are marked with red dashed lines.

The electron temperature variations along the x direction are better shown by the one-dimensional (1D) cut of the temperature along $z = 0$ presented in Figure 5-2. Quantities are averaged over z=[-2, 2] to avoid large fluctuations. The regions divided according to

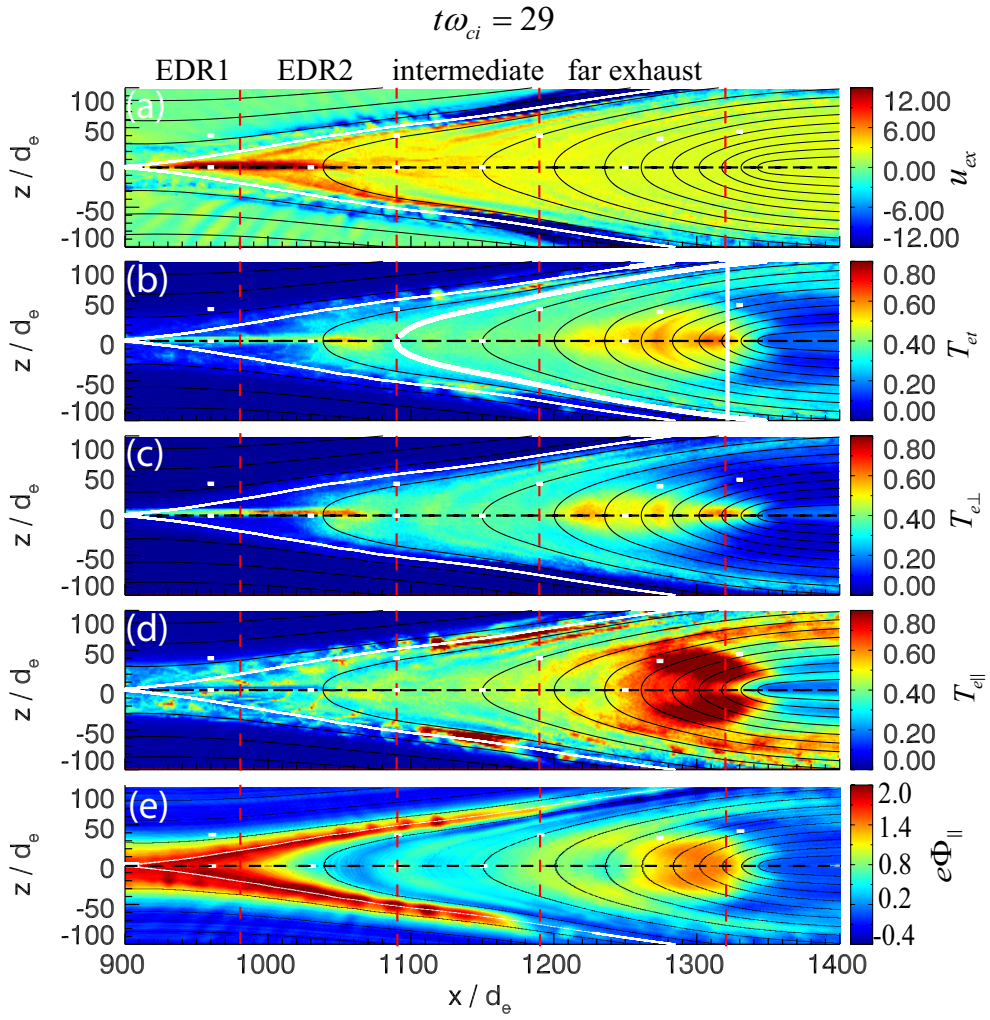

Figure 5-1: Observables relevant to studying electron heating in the open exhaust from the simulation at $t\omega_{ci} = 29$. (a) x component of the electron bulk velocity (u_{ex}) normalized to v_{Ai0}; (b) electron total temperature (T_{et}) normalized to $m_i v_{Ai0}^2$ (c) electron perpendicular temperature ($T_{e\perp}$); (d) electron parallel temperature ($T_{e\parallel}$); (e) electron parallel potential ($e\Phi_{\parallel}$) in unit of $m_i v_{Ai0}^2$. The vertical lines represent the boundaries between regions divided according to the electron temperature characteristics (explained in the text), and the labels for the regions are marked on top of panel (a). The white rectangles in each panel mark the locations of the electron distribution functions in Figure 5-4.

the 1D temperature and electron velocity variations along x are labeled as follows.

EDR1: x=[900, 980], u_{ex} (Figure 5-2a) increases to its peak. $T_{e\parallel}$ (Figure 5-2d) stays low, $T_{e\perp}$ (Figure 5-2d) increases, and T_{et} (Figure 5-2b) increases with $T_{e\perp}$.

EDR2: x=[980, 1090], u_{ex} decreases in this region, and the end of this region corresponds to the end of EDR. EDR2 can be further divided into two parts. In x=[980,1060], u_{ex}

drops fast, and $T_{e\perp}$ and T_{et} increase to a local maximum. In x=[1060,1090], u_{ex} drops more slowly, and $T_{e\perp}$ and T_{et} decrease. $T_{e\parallel}$ increases in this region, especially around the boundary between the two parts.

Intermediate exhaust: x=[1090, 1190], T_e is quasi-isotropic. In addition, $T_{e\parallel}$ and $T_{e\perp}$ roughly stay the same with slight increases.

Far exhaust: x=[1190, 1320], both $T_{e\parallel}$ and $T_{e\perp}$ increase.

In addition to the variations along the x direction, T_e also exhibits different variations along z between the separarix region and the mid-plane at different x locations. Figures 5-1b-5-1d show that the main increase of T_e happens near the separatrix (marked by vertical solid lines). The T_e transition layer for $T_{e\perp}$ is mainly on the outflow side of the separatrix, while for $T_{e\parallel}$ is around the separatrix itself with a lot of localized structures. Figure 5-3 shows the electron temperature profiles in z at three different x locations. The sharp changes in T_e close to the sepatratrix can be clearly seen. Closer to the mid-plane than the transition layer, T_e variations along z depend on x locations. In regions of EDR1 and EDR2 (black curves), $T_{e\perp}$ (Figure 5-3b) has a significant increase close to $z = 0$, and $T_{e\parallel}$ (Figure 5-3c) shows a decrease where $T_{e\perp}$ peaks. T_{et} (Figure 5-3a) exhibits an increase around $z = 0$. In the intermediate exhaust region, neither $T_{e\parallel}$ nor $T_{e\perp}$ has large variations between the mid-plane and the transition layer (blue curves). In the far exhaust region, both $T_{e\parallel}$ and $T_{e\perp}$ generally increase towards $z = 0$ for the shown profile (red curves). However, the peaks of $T_{e\parallel}$ can be bifurcated off mid-plane elsewhere, as shown in Figure 5-1d.

In order to test whether the division of different sub-regions is a universal feature for reconnection, we also examine the T_e profiles at an earlier time when the reconnection rate was at its peak ($t\omega_{ci} = 18$), and in the other three simulation runs listed in Table 2.1. We find that the main features remain in all other tests, with some small differences. The intermediate exhaust region only exists during later times, when the reconnection is well

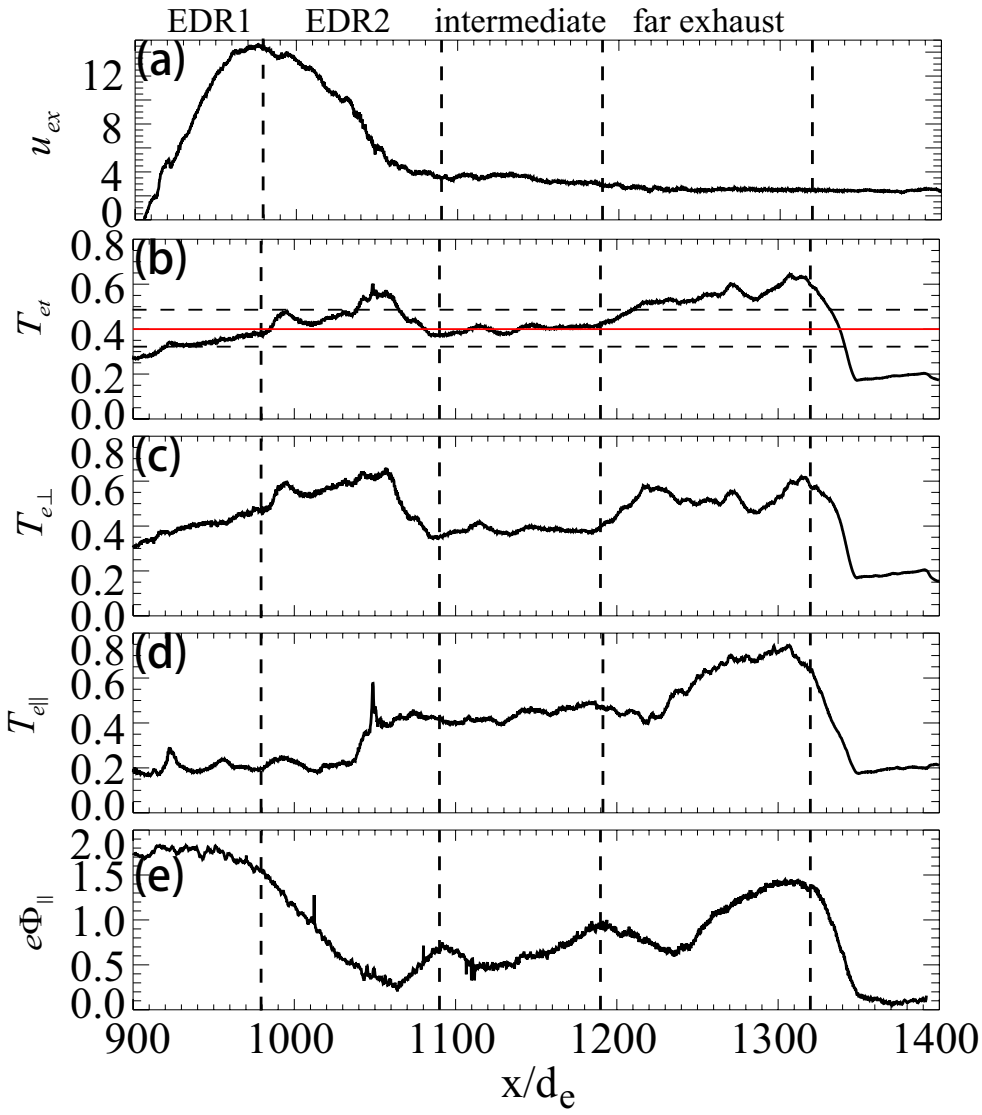

Figure 5-2: One-dimensional cuts along z=0 (averaging over z=[-2, 2]d_e) for the quantities presented in Figure 5-1. (a) u_{ex} shows that the electron outflow jet peaks at the end of the EDR1 region and ends at the boundary of EDR2 and intermediate exhaust regions; (b)-(c) T_{et} and $T_{e\perp}$ maximize in the EDR2 region and near the end of far exhaust; (d) $T_{e\|}$ peaks in far exhaust; (e) $e\Phi_{\|}$ at z=0 peaks near the X line and shows variations in the exhaust. The red horizontal line in (b) marks the average exhaust T_{et}, and the dashed lines above and below mark the values one standard deviation away.

developed. It is identified as a region with $T_{e\|} \sim T_{e\perp}$. Near the peak reconnection rate, when the pile-up region is much closer to the X line ($\sim$60 d_e), this region is missing. For the other runs, there are some differences in the detailed features of the EDR2 region. In those runs, the boundary of the two parts in EDR2 is not always as sharp as that shown

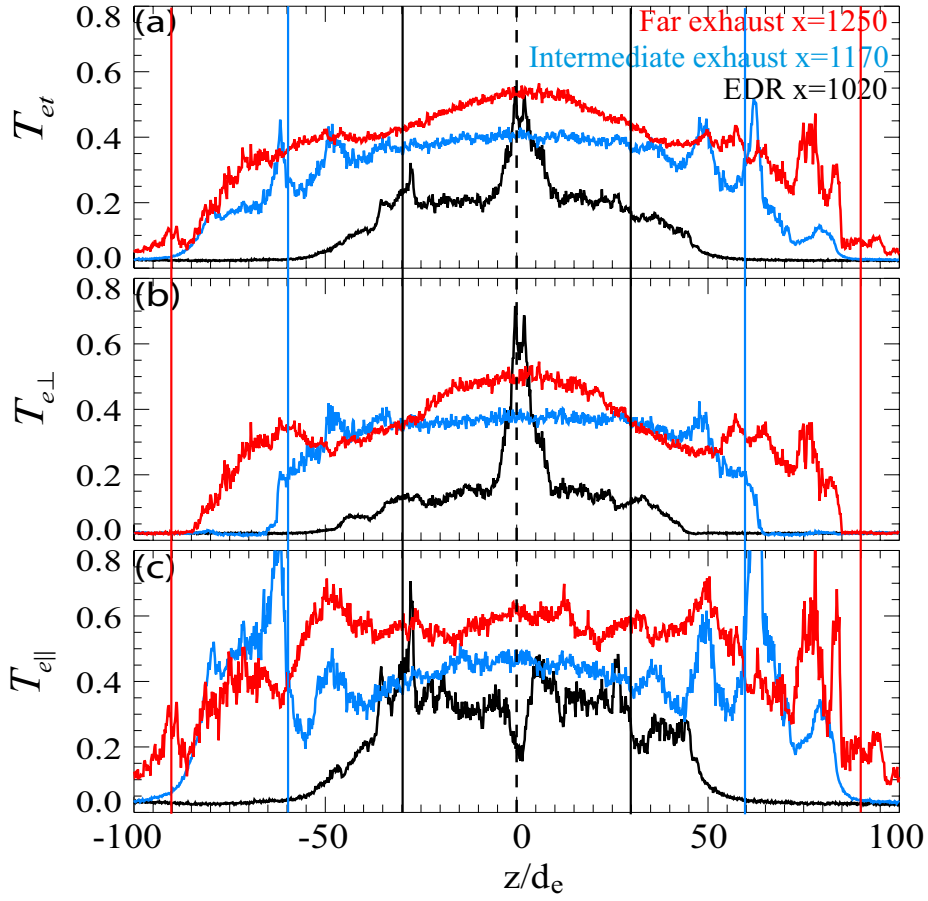

Figure 5-3: Electron temperature variations along z at three x locations in the simulation. (a) T_{et}; (b) $T_{e\perp}$; (c) $T_{e\parallel}$. The temperature enhancements at large z values are near the separatrices, which are marked by solid vertical lines in the same colors with the temperature curves. The temperature shows different variation trends from larger z locations towards z=0 in different regions. See text for details.

in Figure 5-2. The locations of the end of the electron outflow jet, $T_{e\parallel}$ increase, and $T_{e\perp}$ decrease are close, but may not be exactly at the same x position. In run 4, where the guide field is 5% of B_0, there is no clear decrease of $T_{e\perp}$ in EDR2. Except for the above details, the main features of different sub-regions are applicable for all tested simulations.

5.2.2 Electron VDFs resulting in the temperature profiles

In this subsection, we analyze the electron VDFs associated with different T_e sub-regions. We will discuss (1) the features of VDFs, (2) how the changes of VDFs contribute to the

variations in T_e, and (3) possible mechanisms for the VDF variations. The locations of the VDFs discussed below are marked by the white boxes in Figure 5-4a on top of the color coded total magnetic field. Each distribution is taken from a bin with a size of $2d_e \times 2d_e$, while the sizes of the boxes marked in Figure 5-4a are exaggerated.

Point 1 is in the inflow region at [x, z]=[960, 40]. It shows the typical inflow VDF with the thermal spread larger in the parallel direction than in the perpendicular direction [*Egedal et al.*, 2010].

Next we discuss how the VDFs evolve at the mid-plane downstream from the X line and the resulting temperature variations. The VDF in EDR1 (point 2) has a bulk shift in $v_\perp$, and $v_\perp$ extends to high values around 36. On the other hand, the majority of electrons are distributed within $|v_\parallel| < 10$. Thus, it shows a temperature anisotropy of $T_{e\perp} > T_{e\parallel}$. The magnetic field is mainly in the z direction. As elucidated by *Shuster et al.* [2015], the dominant electron acceleration and heating in the EDR is accomplished by the reconnection electric field E_y, and spatially varying B_z. Both processes lead to increases in $T_{e\perp}$, and no significant $T_{e\parallel}$ increase is expected, as can be seen in Figures 5-2c-5-2d.

The heating from the cyclotron turning around the increasing B_z continues to the first part of EDR2 (x=[980, 1060]). $T_{e\perp}$ is increased at an expense of u_{ex} as shown in Figure 5-2a. In the second part of EDR2 (x=[1060, 1090]), $T_{e\perp}$ decreases. Comparing the VDF at the end of EDR2 at [1090, 0] (point 4) with that at [1030, 0] (point 3), we can see that the counts of the most energetic population ($v_\perp > 28$, marked by a red oval in the VDF at point 3) decreases a lot. This indicates that many of the accelerated electrons from the EDR have been ejected along the field lines, which can lead to a decrease of $T_{e\perp}$. Therefore, for the perpendicular electron heating in EDR2, there is a competition between the electron gyration around the increasing B_z, and the loss of the most energetic electrons.

Another T_e profile feature in the second part of EDR2 is the increase of $T_{e\parallel}$. Both

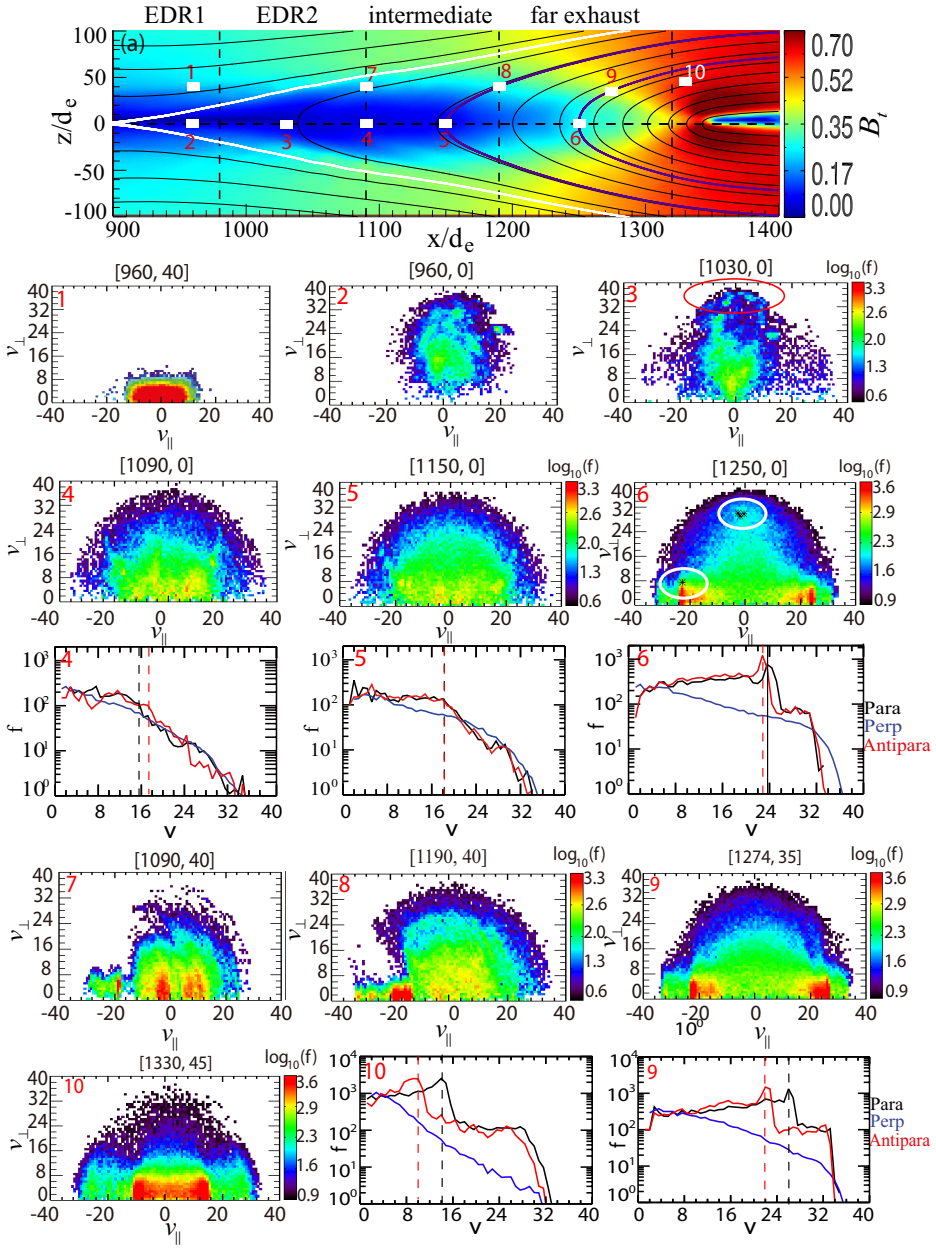

Figure 5-4: Electron velocity distribution functions (VDFs) in the $v_\perp - v_\parallel$ plane from the simulation. Each VDF is constructed from a 2×2 d_e bin. The bin locations are marked with white rectangles in (a) total magnetic field, and the [x, z] coordinates of the bin centers are listed on top of each VDF. For points 4, 5, 6, 9 and 10, 1D cuts of the VDFs in the parallel (PA=[0, 30°], black), perpendicular (PA=[75°, 105°], blue) and anti-parallel (pitch angle (PA)=[150°, 180°], red) directions are shown. The velocities on each axis are normalized to v_{Ai0}. The 2D VDFs of points 1-5, 7 and 8 have the same color scale, and those for points 6, 9 and 10 have the same color scale. The stars inside white ovals marked on the 2D VDF at point 6 are the initial velocities for the backward tracing of test particles presented in Figures 5-9 - 5-11.

VDFs in this region (points 3 and 4) show that the distribution at high energies extends to similar values in $v_{\parallel}$ and $v_{\perp}$. In addition, the low-energy part of the VDF at [1090, 0] is elongated in the parallel direction, similar to that in the inflow region. The magnetic field in this region is still low, so that high-energy electrons can experience efficient pitch angle scattering close to the mid-plane [*Egedal et al.*, 2012]. With pitch angle scattering, the initial perpendicular velocities of EDR electrons can be converted to the parallel directions. With the magnetic field increasing along x, not only can electrons from the X line bounce back and forth along the field lines, those entering the exhaust region through directly crossing the separatrix can also move towards the mid-plane to mix with the EDR electrons. The latter electrons are accelerated in the parallel direction as they travel towards the mid-plane, since the parallel electric field ($E_{\parallel}$) points away from the mid-plane. Pitch angle scattering can also convert their parallel velocities to the perpendicular direction. Thus, the pitch angle scattering makes the high-energy part of the distribution more isotropic. The mixture of electrons crossing the separatrix at different distances downstream of the EDR, together with electrons coming from the EDR and moving along the field lines after pitch angle scattering, forms the parallel elongated part of the distribution. Low-energy electrons are less likely to be demagnetized in this region, so that they are not, or have not been scattered to be isotropic [*Smets et al.*, 1998]. Therefore, the pitch angle scattering of EDR electrons produces more electrons with high , and the mixture of the electrons from EDR and from the separatrix leads to the co-existence of electrons with different . Thus, the parallel velocity spread in the VDF is increased, so is $T_{e\parallel}$.

In the intermediate exhaust (x=[1090, 1190]), the VDF (point 5) characteristics follow that at [1090, 0] with subtle changes: in the high-energy part (with velocities larger than the parallel shoulder velocity around 24 v_{Ai0}), the perpendicular spread becomes slightly larger than the parallel spread, which can be seen from its 1D cuts; in the low energy part, the

parallel shoulder velocities (marked with vertical lines in the 1D cuts of points 4 and 5) are slowly increased. These changes are persistent with increasing x locations. The average $T_{e\parallel}$ and $T_{e\perp}$ are almost the same (Figures 5-2c-5-2d), and the increase of the parallel shoulder velocities gives a slow rise of $T_{e\parallel}$ (Figure 5-2d).

In the far exhaust region (x=[1190, 1320]), which is close to the magnetic field pile-up region, both $T_{e\parallel}$ and $T_{e\perp}$ increase with x. The VDF (point 6) shows three features: (1) further increase of the elongation along $v_\parallel$; (2) counter-streaming beams in high $|v_\parallel|$ with the phase space density (f) peaks around 23 v_{Ai0} and 24 v_{Ai0} in the parallel and anti-parallel directions (marked with vertical lines in 1D cuts of point 6), respectively; (3) a population with higher $v_\perp$ (over 28 v_{Ai0}) than in the intermediate exhaust region (comparing points 5 and 6). Features (1) and (2) lead to an increase in $T_{e\parallel}$, and (3) leads to an increase in $T_{e\perp}$. In the intermediate exhaust, the high-energy part of the VDF is quasi-isotropic. On the contrary, in the far exhaust, two distinct populations coexist, one with high $v_\perp$ and low $v_\parallel$, while the other with high $v_\parallel$ and low $v_\perp$. Besides the counter-streaming beams, the VDFs in the far exhaust are similar with those shown in *Smets et al.* [1998]. The generation of fine structures in high-energy VDFs may be related to the electron acceleration in the exhaust region and the mixture of electrons from different sources, which were not discussed in *Smets et al.* [1998]. We will discuss these mechanisms in detail in section 5.4.

Next we will analyze how the VDFs are associated with the T_e variations along the z direction, and how the z dependence changes at different x locations. We start with the comparison of VDFs between the separarix region and closer to the mid-plane to see how the sharp T_e increase in the separatrix transition layer is formed. Point 7 is at [x, z]=[1090, 40] on the outflow side of the separatrix within the layer of the increasing $T_{e\perp}$. For $v_\parallel > 0$ (outflow direction), the distribution shows significant perpendicular heating. The perpendicular thermal spread of the distribution is much smaller for $v_\parallel < 0$ (towards

the X line). As z decreases and the distance from the separatrix becomes larger, the large perpendicular thermal spread extends further towards the antiparallel direction, and the VDF becomes that at point 4 ([x, z]=[1090, 0]) at the mid-plane. The appearance of the high $v_\perp$ electrons and the extension of this population to the anti-parallel direction leads to the $T_{e\perp}$ increase in the transition layer towards smaller z locations. Detailed interpretation of the separatrix VDFs and their non-gyrotropic features are reported elsewhere [*Guo et al.*, 2014].

Now we discuss T_e and VDFs inside the separatrix transition layer, and compare those off mid-plane and at the mid-plane at different x locations. First we analyze the z dependence of T_e and VDFs in the EDR. VDFs of points 2 and 3 exhibit low $T_{e\parallel}$ and high $T_{e\perp}$. The VDFs at larger z locations are similar with that at point 1 in the inflow with a clear elongation in the parallel direction (not shown). The parallel elongation of the VDF can be indicated by the T_e slices at x=1020 (black in Figure 5-3), where $T_{e\parallel}$ is about 2-3 times of $T_{e\perp}$ for $|z|$ between 10 and 30 d_e. Comparing the VDFs at points 2 and 3 with that at point 1, the dip in $T_{e\parallel}$ and peak in $T_{e\perp}$ shown in Figure 5-3 (black lines) can be understood as a consequence of (1) the parallel direction changes from x to z from off mid-plane to mid-plane, so that the initial VDF elongation in the x direction built up in the inflow region changes from the parallel spread to the perpendicular spread; (2) the electrons in the EDR are energized in the perpendicular direction. *Shay et al.* [2014] showed a T_e profile near the end of EDR, where the increase of $T_{e\perp}$ and the decrease of $T_{e\parallel}$ are almost equal. They concluded that the electron heating was mainly from the parallel potential as electrons moved from the separatrix to the mid-plane, and the temperature was simply exchanged between the parallel and perpendicular directions at the mid-plane. This is equivalent to reason (1) listed above. However, the T_e profile we show here is closer to the X line. The increase of $T_{e\perp}$ is larger than the decrease of $T_{e\parallel}$, so that T_{et} also increases at the mid-plane.

This indicates that the further perpendicular heating in EDR (reason (2)) is also important.

In the intermediate exhaust, though T_e does not show large differences between the mid-plane and large z locations, there are still fine structures in VDFs. Point 8 at [1190, 40] is off mid-plane but at the same field line with the point at [1150, 0] (point 5). There is a clear difference between the VDF at two locations: the VDF off mid-plane has an anti-parallel beam towards the mid-plane, while the VDF at mid-plane does not. This is consistent with the observation results in *Asano et al.* [2008]. However, because of the similarity of these two VDFs, their temperatures do not show significant differences. At [1190, 40], $T_{e\parallel} = 0.360 m_i v_{Ai0}^2$, and $T_{e\perp} = 0.364 m_i m_i v_{Ai0}^2$; at [1150, 0], $T_{e\parallel} = 0.468 m_i v_{Ai0}^2$, and $T_{e\perp} = 0.400 m_i m_i v_{Ai0}^2$. The VDFs and T_e both exhibit gradual changes from $z \sim 40$ to $z = 0$.

In the far exhaust, T_e generally increases at the mid-plane (Figure 5-3, red lines). On the other hand, $T_{e\parallel}$ and $e\Phi_\parallel$ exhibit bifurcated local maximums off mid-plane (Figure 1d). The associated VDF features can be seen through comparing those at point 9 and point 6 connected by the same field line. Point 9 is located inside the bifurcated $T_{e\parallel}$ peak, with a $T_{e\parallel}$ higher than that at point 6 (Figure 1d). The VDF at point 9 also shows counter-streaming beams, however, its peak speeds at 22 v_{Ai0} and 26 v_{Ai0} (vertical lines in 1D cuts of point 9) have a larger parallel spread than that at point 6, which produces a larger $T_{e\parallel}$. The variation of the beam velocity is probably due to the $e\Phi_\parallel$ difference and the mirror force between two points. As will be shown later, the acceleration due to the curvature drift opposite to the electric field near the mid-plane also contributes to changing the beam speeds. We also present a VDF at point 10, which is off mid-plane on the same field line connecting to the mid-plane in the far exhaust, but has a lower $T_{e\parallel}$ than that at the mid-plane. At point 10, the beam speeds (marked with vertical lines in 1D cuts) are around 10 v_{Ai0} and 14 v_{Ai0}, while the VDF at the mid-plane on the same field line with point 10 is similar with the VDF

at point 6, with counter-streaming beams at 25 v_{Ai0} and 26 v_{Ai0} (not shown). Thus, the counter-streaming beam speeds are smaller off mid-plane to produce a lower $T_{e\|}$, which also results from $e\Phi_\|$ and the mirror force between two points. Above all, counter-streaming beams also exist at off mid-plane in the far exhaust. The beam velocities are determined by the $e\Phi_\|$, the mirror force, and the magnetic curvature acceleration that the beam particles experience between the mid-plane and off mid-plane points, and $T_{e\|}$ varies accordingly.

In addition to the changes in the counter-streaming beam velocities, the high $v_\perp$ and low $v_\|$ population presented in the VDF at [1250, 0] disappears in the off mid-plane VDFs at points 9 and 10. The existence of such a population helps increase the perpendicular velocity spread and hence, $T_{e\perp}$. Consequently, $T_{e\perp}$ is higher at the mid-plane. As can be seen from Figure 5-1c, the high $T_{e\perp}$ region is restricted to small z locations in the far exhaust, which corresponds to the locations where the high $v_\perp$ and low $v_\|$ population exists in VDFs.

An additional minor feature is that the bifurcated $T_{e\|}$ peaks are at slightly larger z locations than the bifurcated $e\Phi_\|$ peaks, and are also at larger z than the locations with $T_{e\perp}$ enhancements (Figures 5-1c-5-1e) caused by the existence of the high $v_\perp$ and low $v_\|$ population. The small $v_\|$ of such a population decreases the average parallel thermal spread of the distribution, i.e., decreases $T_{e\|}$, in the $e\Phi_\|$ peak locations, which are closer to the mid-plane than the $T_{e\|}$ peaks. Therefore, it indicates that the difference between the $T_{e\|}$ and $e\Phi_\|$ peak locations is caused by the existence of the high $v_\perp$ and low $v_\|$ population close to the mid-plane.

Asano et al. [2008] and *Egedal et al.* [2012] discussed that the inward beam at large z locations can be pitch angle scattered to form flat-top distributions at the mid-plane, consistent with VDFs in the intermediate exhaust region. However, their explanations are not consistent with the existence of counter-streaming beams at both large and small z

locations, and fine structures in the perpendicular distribution. We will analyze the cause of these features in section 5.4.

In summary, we have discussed the important features of the VDFs in different sub-regions, which paves a foundation to better understand the temperature variations.

5.2.3 Possible applications to observations

The above simulation results show that the T_e profile varies in the reconnection exhaust region, and the variations correspond to different features in the electrons' VDFs. We can apply the known VDF signatures to observations, using them together with other quantities, e.g., magnetic field, ion velocity, etc., to help better organize the observation data into different sub-regions in the reconnection exhaust.

Here we summarize the observable signatures of VDFs to mark the location in the exhaust. Firstly we can distinguish the regions close to and far from the separatrix region. Close to the separatrix region, the VDFs show the transition features between the inflow and outflow VDFs [*Guo et al.*, 2014]. Compared with the inflow distributions, they start to show high energy populations, especially in the perpendicular direction. Compared with the VDFs closer to the mid-plane, they still have high counts in low energies.

Secondly we can tell the relative location between the EDR and the pile-up region near the mid-plane (B_x is small). Inside the EDR (EDR1 and EDR2 in simulation), $T_{e\perp}$ is much higher than $T_{e\parallel}$, with the electrons in VDFs accumulated at small $v_\parallel$ and large $v_\perp$ to form the outflow jet. In the intermediate exhaust, the VDF is the superposition of a flat-top population elongated in the field-aligned directions and a quasi-isotropic high energy population. T_e is quasi-isotropic. Such a region only exists for well-developed reconnections. In the far exhaust, the VDF is likely to have large $v_\parallel$ counter-streaming beams and a population with small $v_\parallel$ - large $v_\perp$ on top of the flat-top distribution.

Thirdly, in regions which are off mid-plane and far from the separatrix as well, we can tell the relative x location between the EDR and the pile-up region. Far from the pile-up region (along the same field lines intersecting the mid-plane in the intermediate exhaust region), there is a field-aligned beam towards the mid-plane. This is the same as those shown in *Asano et al.* [2008] and *Egedal et al.* [2012]. Close to the pile-up region (along the same field lines intersecting the mid-plane in the far exhaust), there are counter-streaming beams. However, the off mid-plane VDFs in the far exhaust do not have a population with small $v_{\parallel}$ - large $v_{\perp}$ like those near the mid-plane in the far exhaust.

5.3 Observations

In this section, we present a reconnection event observed by Cluster spacecraft at the magnetotail on August 21, 2002 with VDFs in different sub-regions.

5.3.1 Event overview

During this event, C1 and C3 encountered the inflow and exhaust regions. Figure 5-5 shows the overview of this reconnection event from C1 ((a)-(c)) and C3 ((d)-(e)), with the electron energy flux, H^+ velocity, and magnetic field in GSM coordinates. At C1, around 08:17:20 UT, electrons were mainly observed at low energies, around hundreds of eV (Figure 5-5a), H^+ velocity was low and B_x was large. Therefore, C1 was likely to be in the inflow region at this time. In the intervals where the electrons' energy flux exhibited enhancements in high energies, e.g., around 08:15 UT, H^+ velocity was also high, which indicates that it is in the outflow region. In the intervals where electrons are in the intermediate energy ranges ($\sim$1 keV) and B_x is still large, e.g., around 08:17:00 UT, C1 could be near the separatrix region.

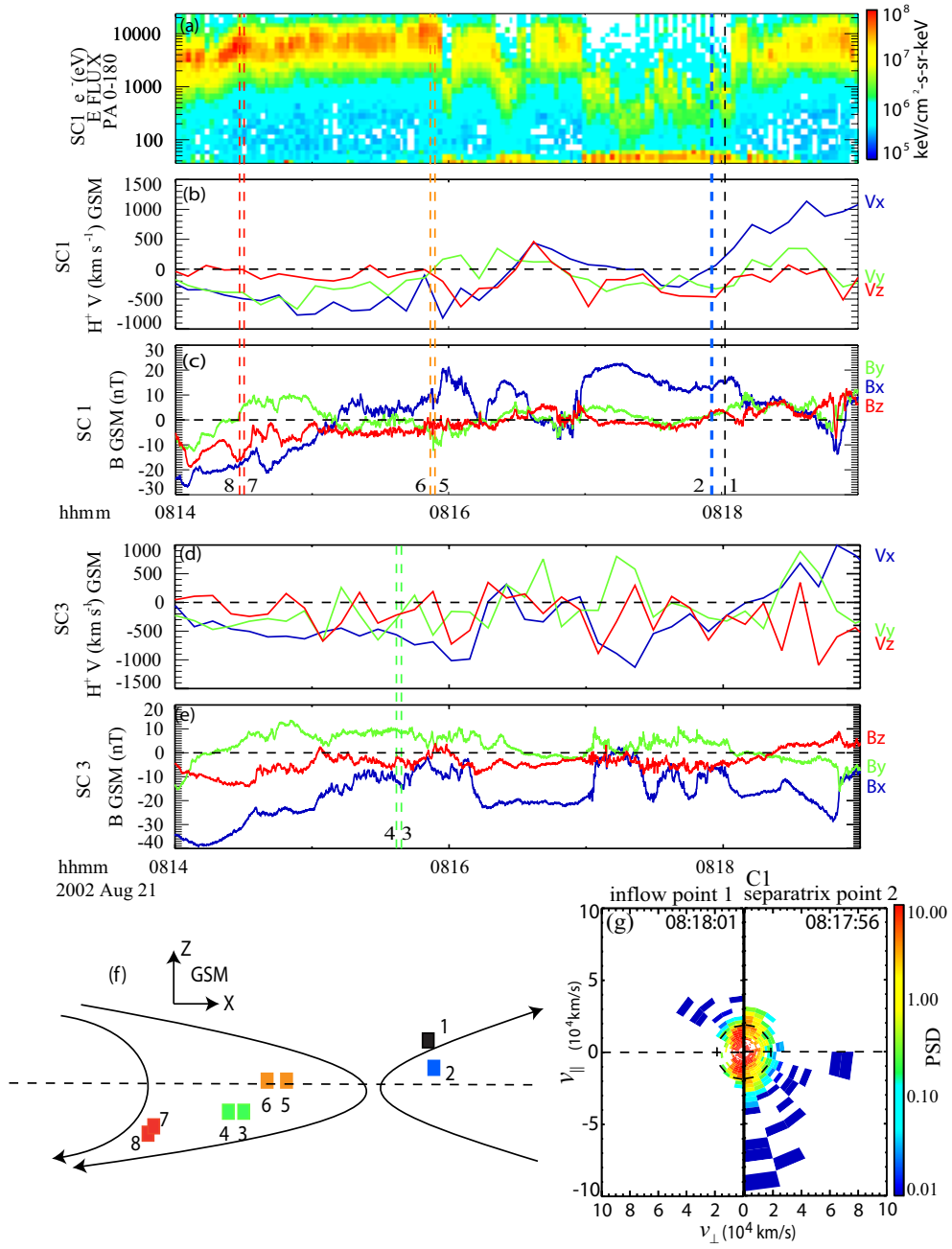

Figure 5-5: Overview of the magnetotail reconnection event observed by Cluster on 21 August, 2002. (a)-(c) are from C1, and (d)-(e) are from C3. (a) electron energy flux; (b),(d) H^+ velocity in GSM; (c), (e) magnetic field in GSM; (f) illustration of the locations of the points represented by the vertical lines in (a)-(e) and the VDFs of these points are shown in (g) and Figures 5-6 - 5-8.

5.3.2 Typical points in different sub-regions

Use of the plasma moments and the magnetic field data can indicate roughly the sub-regions that the spacecraft is in. However, using the simulation results, we can determine

the sub-regions more accurately using the electron VDFs.

Point 1 at 08:18:01 UT (black dashed line in Figure 5-5) is in the inflow region, as determined by the following features. At this point, the electron energy flux is mainly in low energies, the ion velocity is low and B_x is large. Figure 5-5g (left) shows the VDF at this point in the $v_{\parallel} - v_{\perp}$ plane. Clearly this inflow distribution has the elongated flat-top shape in the field-aligned direction with the velocity cutoff around 1.5e4 km/s (∼640 eV), and in the perpendicular direction the flux cuts off at low energies (below 1.0e4 km/s, around 300 eV).

Point 2 at 08:17:56 UT in C1 data (blue dashed line in Figure 5-5) is near the separatrix. At this point, the electron energy flux peaks at higher energies (∼1 keV) than those in the inflow region, but there is no clear difference in H^+ velocity and magnetic field. The right half of Figure 5-5g shows its VDF. Similar to the inflow distribution, it is still elongated in the field-aligned directions, but the shoulder energy increases to $v \sim 2.5e4\ km/s$ (∼1800 eV). At higher energies than the shoulder energy, the distribution extends to about 8.0e4 km/s (over 10 keV) in the perpendicular direction, which is comparable with the velocity extension in the anti-parallel direction. There seems to be a high-energy cutoff in the parallel half of the distribution. However, it is caused by the upper energy limit of LEEA, so that whether the high-energy distribution in the parallel half is the same with the anti-parallel half is unknown for this point. HEEA alternates measuring the parallel and anti-parallel directions in consecutive half-spin frames, so that we can compare the two halves of VDFs between adjacent points. It turns out that there are no clear asymmetries between the parallel and anti-parallel halves, though there is such an asymmetry in the simulation (point 7 in Figure 5-4), and this is a discrepancy between the simulation and observation results. However, the appearance of the flux at high perpendicular velocities above 6e4 km/s indicates that it is in the separatrix region [*Guo et al.*, 2014].

C1 and C3 are most likely in the reconnection exhaust region around 08:14-08:16 UT, where the ion velocity exhibits large negative values (Figures 5-5b and 5-5d). In the sub-interval of around 08:15:10-08:15:50, C1 data show small positive B_x ($\sim$5 nT), and C3 data shows negative Bx with larger amplitudes ($\sim$-10 nT). This indicates that C3 is to the south of the mid-plane, and its distance to the mid-plane is larger than C1 in the same interval. Their locations in the exhaust will be examined more precisely with VDFs.

Points 3 and 4 (green dashed lines in Figure 5-5) are example points between the separatrix and the mid-plane in the intermediate exhaust region defined in the simulation. Figure 5-6 shows the VDFs, which are consecutive frames provided by the PEACE instrument. In the 1D cuts in Figures 5-6-5-8, only HEEA data are shown. In Figures 5-6a and 5-6b, the PSD in the perpendicular direction (blue in 1D cuts) is close to a constant around 0.2 s^3/km^6 in the velocity range of 2.0e4 km/s to 4.0e4 km/s. Around the same energy channel, there is an anti-parallel beam at point 4 (red in Figure 5-6a 1D cuts) with a PSD of about 0.6 s^3/km^6, which is about 2-3 times higher than that in the perpendicular direction. On the contrary, there is no parallel beam at point 3 (Figure 5-6b). It is quasi-flat-top in the velocity range of 2.0e4 km/s to 5.0e4 km/s, with the PSD similar to that in the perpendicular direction. The one-count level of PSD, which shows the level of background noise in the measurements, is over-plotted with the 1D cuts (green dashed lines). The one-count level is more than 2 decades lower than the measured PSD around v=4.0e4 km/s. Thus, the uncertainty in the measurement is negligible, and the differences in PSD among different pitch angles are reliable. HEEA alternately measures the distributions in the parallel and anti-parallel directions. During the whole interval of 08:15:21 UT to 08:15:47 UT, where the magnetic field is similar to that at points 3 and 4, all HEEA measurements show similar distributions, i.e., flat-top without beams in the parallel direction and a beam in the anti-parallel direction. Therefore, the difference in the parallel and anti-parallel directions

between the VDFs at points 3 and 4 is not due to the change of the VDF at different measured locations, but the real difference in the two directions in one type of VDF. At these points, the anti-parallel direction pointed towards the X line, judging from B_x and v_x. Thus, the VDFs at points 3 and 4 agree with those found between the separatrix and the mid-plane in the intermediate exhaust (point 8 in Figure 5-4), as shown in the illustration in Figure 5-5f. This is the same distribution type that *Asano et al.* [2008] reported.

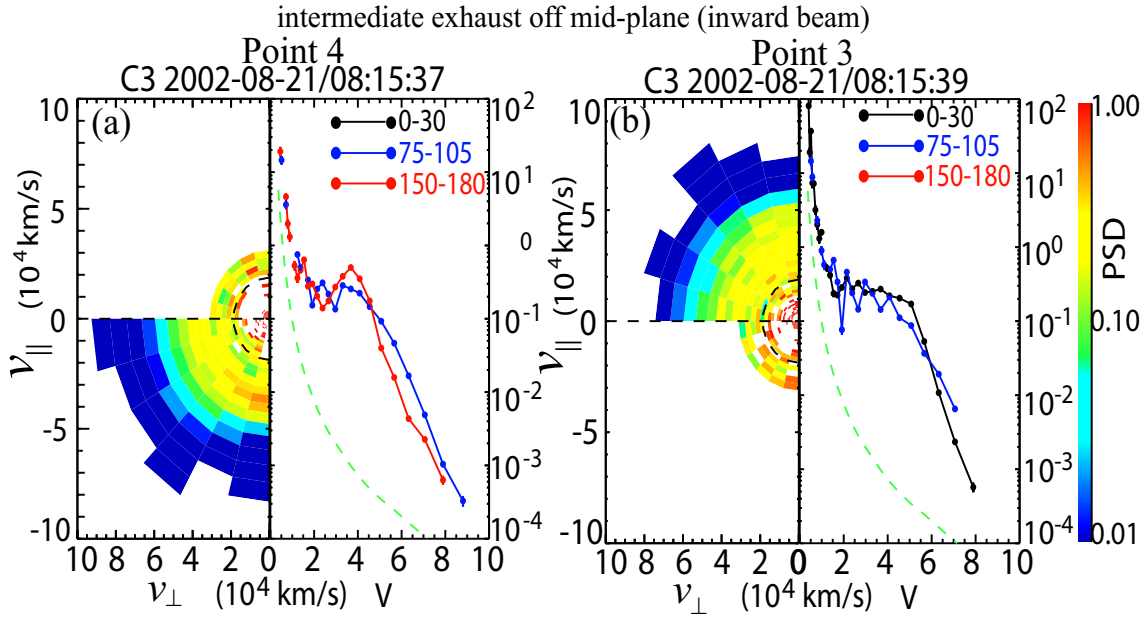

Figure 5-6: Electron VDFs for points 3-4 labeled in Figure 5-5 in the exhaust, with unidirectional inward beams. The left half of each panel is the 2D distribution and the right half is the average 1D cuts for available HEEA detector data, over the pitch angle ranges marked in the legend. The green dashed lines in 1D cuts indicate the one-count level.

Points 5 and 6 around 08:16:00 UT (orange lines in Figure 5-5) are probably in the intermediate exhaust close to the mid-plane, since the magnetic field at these points is smaller than those at points 3 and 4. Figure 5-7 shows the VDFs of points 5 and 6. The distributions in both field-aligned and perpendicular directions at both points exhibit fluxes extending to over 8.0e4 km/s (20 keV) and the shoulder energies are around 10 keV. The VDFs are quasi-isotropic with the parallel flux slightly higher than that in the perpendicular

direction at energies lower than the parallel shoulder energies. In the sense that there are no beams in the field-aligned directions, these VDFs are similar with those in the simulation at [1090, 0] and [1150, 0] in the intermediate exhaust (points 4 and 5 in Figure 5-4). This confirms these points to be located in the intermediate exhaust, close to the mid-plane, as shown in Figure 5-5f, where the pitch angle scattering is efficient enough to generate an isotropic distribution.

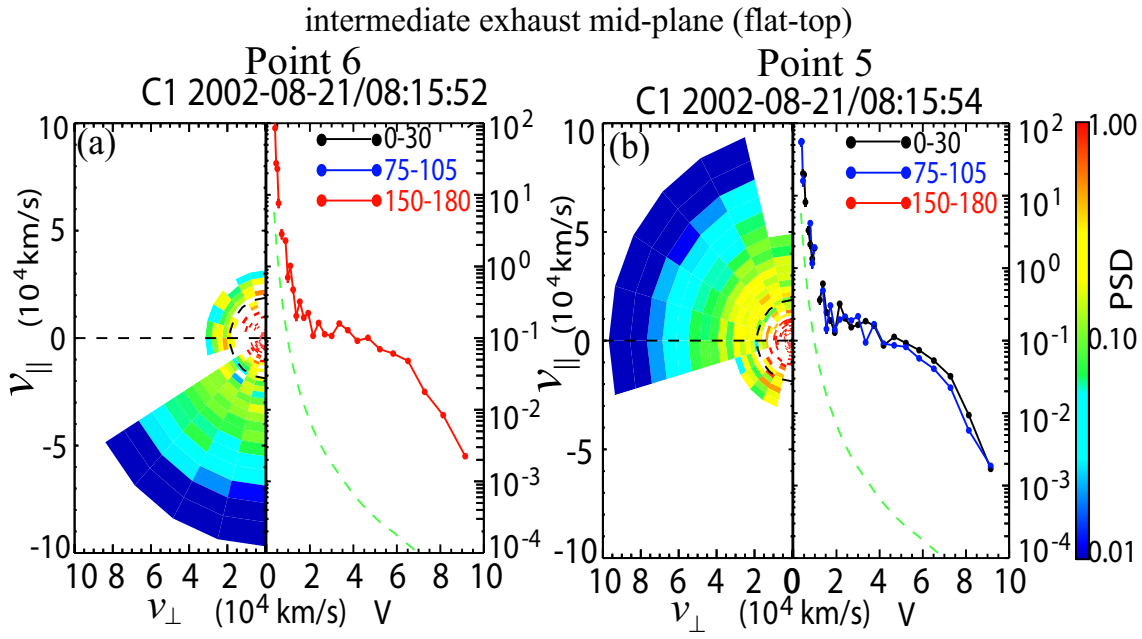

Figure 5-7: Electron VDFs for points 5-6 labeled in Figure 5-5 in the exhaust, with flat-top distributions. The formats are the same as in Figure 5-6.

Points 7 and 8 around 08:14:30 UT (red lines in Figure 5-5) are in the far exhaust close to the pile-up region as determined from the following features. The electrons have high fluxes at high energies, the H^+ velocity still has high -v_x, and B_z has a large negative value. Figure 5-8 shows the VDFs of points 7 and 8, which are from consecutive frames. At high energies, there are counter-streaming beams in the field-aligned directions around 4.5e4 km/s, 6 keV (Figures 5-8a and 5-8b), with a PSD more than twice as high as that in the perpendicular direction. The perpendicular distribution extends to very high energies

over 8.0e4 km/s, 20 keV. This agrees with the simulation results in the far exhaust (point 9 in Figure 5-4), and is consistent with the spacecraft being located close to the pile-up region, as illustrated in Figure 5-5f.

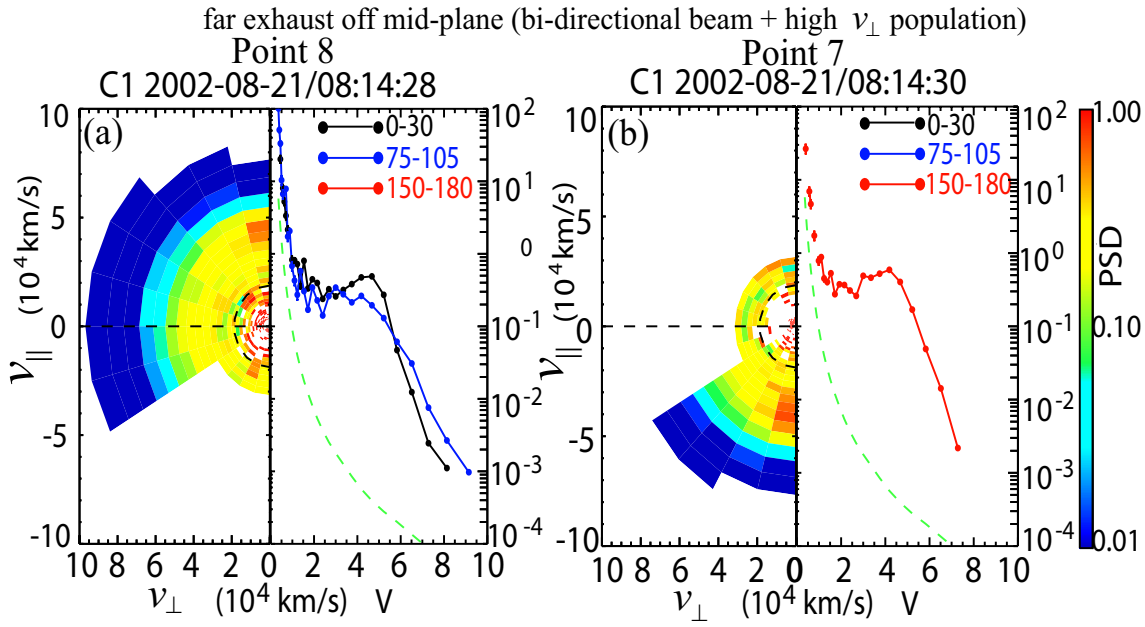

Figure 5-8: Electron VDFs for points 7-8 labeled in Figure 5-5 in the exhaust, with flat-top distributions. The formats are the same as in Figure 5-6.

In summary, the electron VDFs, along with the ion velocity and the magnetic field, accurately determine the sub-regions in the reconnection exhaust. They confirm the simulation results discussed in section 5.2.

5.4 Single-particle motion analysis

In this section, we discuss the mechanisms that generate the distinct types of VDFs presented in sections 5.2 and 5.3. The results are from analyzing the equations governing the single-particle motion and test-particle tracing in PIC fields.

5.4.1 Acceleration mechanisms in the exhaust

We elucidate two aspects of electron energization in the exhaust: the energy source and how the energy is re-distributed between the parallel and perpendicular directions. For simplicity and clearance in the physical meanings of each term, the equations derived in this subsection are non-relativistic.

The energy source can be analyzed with the energy equation of electrons:

$$\frac{dU}{dt} = -e\vec{E} \cdot \vec{v} \tag{5.1}$$

where $U = 1/2mv^2$ is the electron total kinetic energy. Therefore, the electron obtains energy when its velocity $\vec{v}$ has a component opposite to the electric field direction. We can decompose the velocity of an electron as

$$\vec{v} = v_{\parallel}\hat{b} + \vec{v}_{d,E\times B} + \vec{v}_{d,curv} + \vec{v}_{d,gradB} + \Delta\vec{v}_{\perp} \tag{5.2}$$

where $v_{\parallel} = \vec{v}\cdot\hat{b}$ is the velocity component parallel to the magnetic field, and the remaining terms on the right-hand side of eq. (5.2) consist of the perpendicular velocity ($v_{\perp}$) with respect to the magnetic field. For a magnetized electron, which has a well-defined guiding center, the scale of the magnetic field gradient is larger than the electron's Larmor radius, and we apply the guiding center approximation: $\vec{v}_{d,E\times B} = \vec{E} \times \vec{B}/B^2$ is the $\vec{E} \times \vec{B}$ drift velocity, $\vec{v}_{d,curv} = \frac{m|v_{\parallel}|^2}{eB}\left(\hat{b} \cdot \nabla\hat{b}\right) \times \hat{b}$ is the curvature drift velocity, $\vec{v}_{,gradB} = \frac{m|v_{\perp}|^2}{2eB^2}\nabla B \times \hat{b}$ is the gradient-B drift velocity, and $\Delta\vec{v}_{\perp}$ is regarded as the gyro-velocity that is averaged to be zero over a gyro-period. Other higher-order drift velocities, such as the polarization drift, are neglected. For an un-magnetized electron, the guiding center concept is invalid, and the average $\Delta\vec{v}_{\perp}$ over a gyro-period is non-zero. Its gyro-period averaged perpendicular velocity is different from the drift velocity for a magnetized electron; therefore, the middle

three terms in eq. (5.2) do not represent the drift velocity of this particle, and we regard $\Delta\vec{v}_\perp$ as the difference between the total perpendicular velocity (including the gyro-motion) and the guiding center drift velocity for a magnetized electron. Nonetheless, using eq. (5.2), we can discuss an electron that is slightly unmagnetized with its drift motion close to the one for a fully magnetized electron, and we regard $\Delta\vec{v}_\perp$ as a correction of the drift velocity plus a gyro-velocity that might not be constant in amplitude during a gyro-period. Substituting eq. (5.2) into eq. (5.1) and after some derivations (shown in the Appendix), we get

$$\frac{dU}{dt} = -eE_\parallel v_\parallel + \frac{dW_{curv}}{dt} + \frac{dW_{gradB}}{dt} + eB\left(\Delta\vec{v}_\perp \times \vec{v}_{d,E\times B}\right)\cdot\hat{b} \tag{5.3}$$

where

$$\frac{W_{curv}}{dt} = -e\vec{E}\cdot\vec{v}_{d,curv} = eB\left(\vec{v}_{d,curv}\times\vec{v}_{d,E\times B}\right)\cdot\hat{b} \tag{5.4}$$

and

$$\frac{W_{gradB}}{dt} = -e\vec{E}\cdot\vec{v}_{d,gradB} = eB\left(\vec{v}_{d,gradB}\times\vec{v}_{d,E\times B}\right)\cdot\hat{b} \tag{5.5}$$

represent the work done by the electric field with the curvature and gradient-B drift velocities.

In reconnection near the mid-plane, the magnetic curvature and gradient are mainly in the $+x$ direction, producing curvature and gradient-B drift velocities in the out-of-plane direction opposite to the electric field E_y to accelerate electrons. *Hoshino et al.* [2001b] discussed that in the far exhaust close to the mid-plane, the gradient-B drift and curvature drift for $\kappa \sim 1$ particles, where κ^2 is the ratio between the magnetic curvature and the particles' Larmor radius at the mid-plane, contribute to accelerating electrons.

The energy distribution in the parallel and perpendicular directions can be analyzed by

the momentum equation for electrons:

$$m\frac{d\vec{v}}{dt} = -e\left(\vec{E} + \vec{v} \times \vec{B}\right) \tag{5.6}$$

The change of the parallel momentum can be expressed as

$$m\frac{d\left(\vec{v}\cdot\hat{b}\right)}{dt} = m\left(\hat{b}\cdot\frac{d\vec{v}}{dt} + \vec{v}\cdot\frac{d\hat{b}}{dt}\right) \tag{5.7}$$

Multiplying $v_\parallel = \vec{v}\cdot\hat{b}$ on both sides of eq.(5.7), we can obtain the energy equation in the parallel direction as

$$\frac{dU_\parallel}{dt} = v_\parallel m\left(\hat{b}\cdot\frac{d\vec{v}}{dt} + \vec{v}\cdot\frac{d\hat{b}}{dt}\right) \tag{5.8}$$

where $U_\parallel = 1/2mv_\parallel^2$. When the explicit time dependence of $\hat{b}$ is much smaller than the change of $\hat{b}$ experienced by a moving electron, the second term on the right-hand side of eq.(5.8) $m\vec{v}\cdot\frac{d\hat{b}}{dt}$ can be further expressed as

$$m\vec{v}\cdot\frac{d\hat{b}}{dt} = m\vec{v}\cdot\left(\vec{v}_\parallel\cdot\nabla\hat{b} + \vec{v}_\perp\cdot\nabla\hat{b}\right) \tag{5.9}$$

The first term on the right-hand side of eq.(5.9) is equal to $m\left(\vec{v}\cdot\hat{b}\right)\vec{v}\cdot\left(\hat{b}\cdot\nabla\hat{b}\right)$, and will be referred to as the 'curvature force' (F_{curv}) hereafter as it is associated with the magnetic curvature. The second term is referred to as $F_{mirror} = m\vec{v}\cdot\left(\vec{v}_\perp\cdot\nabla\hat{b}\right)$. With the velocity decomposition in eq. (5.2) and some derivations (shown in the Appendix), the parallel energy equation becomes

$$\frac{dU_\parallel}{dt} = -eE_\parallel v_\parallel + \frac{dW_{curv,\parallel}}{dt} + \frac{dW_{mirror,\parallel}}{dt} \tag{5.10}$$

where

$$\begin{aligned}\frac{dW_{curv,\parallel}}{dt} &= F_{curv}\left(\vec{v}\cdot\hat{b}\right)\\ &= eB\left(\vec{v}_{d,curv}\times\vec{v}_{d,E\times B}\right)\cdot\hat{b} - eB\left(\vec{v}_{d,gradB}\times\vec{v}_{d,curv}\right)\cdot\hat{b} - eB\left(\Delta\vec{v}_{\perp}\times\vec{v}_{d,curv}\right)\cdot\hat{b}\end{aligned} \tag{5.11}$$

comes from the F_{curv} term, and

$$\frac{dW_{mirror,\parallel}}{dt} = F_{mirror}\left(\vec{v}\cdot\hat{b}\right) = \frac{mv_{\parallel}}{B}\vec{v}_{\perp}\cdot\left(\vec{v}_{\perp}\cdot\nabla\right)\vec{B} \tag{5.12}$$

comes from the F_{mirror} term. In the limit of zero current ($\nabla\times\vec{B}=0$), $\vec{v}_{d,curv}$ and $\vec{v}_{d,gradB}$ are in the same direction, so that the second term on the right-hand side of eq. (5.11) would vanish. The acceleration by F_{curv} is also referred to as the 'Fermi acceleration', and was suggested to be important to electron acceleration in the reconnection exhaust [*Drake et al.*, 2006; *Dahlin et al.*, 2014].

Subtracting eq. (5.3) with eq. (5.10), we can get the perpendicular energy equation

$$\begin{aligned}\frac{dU_{\perp}}{dt} &= \frac{dU}{dt} - \frac{dU_{\parallel}}{dt}\\ &= eB\left[\vec{v}_{d,gradB}\times\left(\vec{v}_{d,E\times B}+\vec{v}_{d,curv}\right)\right]\cdot\hat{b} + eB\left[\Delta\vec{v}_{\perp}\times\left(\vec{v}_{d,E\times B}+\vec{v}_{d,curv}\right)\right]\cdot\hat{b}\\ &\qquad - \frac{mv_{\parallel}}{B}\vec{v}_{\perp}\cdot\left(\vec{v}_{\perp}\cdot\nabla\right)\vec{B}\end{aligned} \tag{5.13}$$

where $U_{\perp} = 1/2mv_{\perp}^2$. We first analyze eq. (5.13) for a magnetized electron. $v_{d,curv}$, and hence, the second term on the right-hand side of eq. (5.13) are significant when an electron interacts with the region with strong magnetic curvature, e.g., the reconnection mid-plane. For the magnetized electron, its drift velocity can be approximately to be constant over a gyro-period, and its average $\Delta\vec{v}_{\perp}$ over a gyro-period is zero. Therefore, if the interaction lasts for more than a few gyro-periods, the integral of the second term over the interaction

time also becomes zero. Besides, the last term in eq. (5.13) is related to the mirror force, which is $-v_{\parallel}\mu\nabla_{\parallel}B$ averaging over a gyro-period (Appendix), where $\mu = \frac{mv_{\perp}^2}{2B}$ is the magnetic moment. Thus, for a magnetized electron, the energy gain related to $\vec{v}_{d,gradB}$ mainly goes to the perpendicular direction (first term of eq. (5.13)), the energy gain related to $\vec{v}_{d,curv}$ mainly goes to the parallel direction (eq. (5.11)) when $\vec{v}_{d,curv} \times \vec{v}_{d,gradB}$ is small, and the energy converts between the parallel and perpendicular directions by the mirror force.

Eq. (5.13) also suggests that pitch angle scattering can occur for electrons that are not fully magnetized, due to F_{curv} and F_{mirror}. A non-zero $eB\left[\Delta\vec{v}_{\perp} \times (\vec{v}_{d,E\times B} + \vec{v}_{d,curv})\right] \cdot \hat{b}$ in eq. (5.13) is the first candidate term to cause pitch angle scattering, which comes from $F_{curv}\left(\vec{v} \cdot \hat{b}\right)$. In this case, if $|\Delta v_{\perp}|$ varies a lot within a gyro-period, the average $\Delta\vec{v}_{\perp}$ over a gyro-period will be non-zero, which may cause the whole term non-zero as well. In addition, if the interaction of the electron with the strong magnetic curvature region is very rapid, e.g., close to or smaller than one gyro-period, the average $\Delta\vec{v}_{\perp}$ over the interaction time is also non-zero, even if $|\Delta v_{\perp}|$ does not vary a lot. Furthermore, since $\Delta\vec{v}_{\perp} \times \vec{v}_{d,curv}$ accelerates/decelerates $v_{\parallel}$, $\vec{v}_{d,curv}$ continuously varies during the interaction, so that even if the average $\Delta\vec{v}_{\perp}$ itself is zero during the interaction time, the integral of the whole second term on the right-hand side of eq. (5.13) may still be non-zero. The sign of this term depends on the direction of $\Delta\vec{v}_{\perp}$, or the sign of $\Delta\vec{v}_{\perp} \cdot \left(\hat{b} \cdot \nabla\hat{b}\right)$ more specifically (Appendix eq. (3)), when the electron interacts with the region with strong magnetic curvature, i.e., it depends on the electron's gyro-phase. Therefore, its sign is uncertain, so is how the energy is distributed between the parallel and perpendicular directions. Such a stochastic process in the energy distribution between different directions is effectively pitch angle scattering, which comes from the F_{curv} term. Similarly, for an unmagnetized electron, μ is not well defined. The last term in eq. (5.13) cannot reduce to the gyro-period averaged form, and the uncertainty in the dot product between and the magnetic field gradient can also contribute

to pitch angle scattering, which comes from the $F_{mirror}\left(\vec{v}\cdot\hat{b}\right)$ term.

5.4.2 Test-particle results

We trace test-particles in the PIC electromagnetic fields at $t\omega_{ci} = 29$ from simulation 1 to examine the electron energization in the exhaust and to understand the VDF structures. The test particles follow the relativistic momentum equation [*Birdsall and Langdon*, 1991]. Further energization of electrons in the exhaust as they move downstream from the EDR is indicated by the fact that the VDFs in the far exhaust expand to higher $v_{\parallel}$ and $v_{\perp}$ than those in previous regions.

We trace backward in time 200 electrons with high $v_{\parallel}$ and high $v_{\perp}$ in the VDF at [1250, 0] (point 6 in Figure 5-4), respectively. The results of four representative particles, whose initial velocities are marked by stars within white circles in the VDF, will be discussed.

Figure 5-9 shows an electron from the anti-parallel beam of the VDF at [1250, 0], with $v_{\parallel}$ =-22.8 v_{Ai0} and $v_{\perp}$=7.2 v_{Ai0}. This electron will be referred to as the high $v_{\parallel}$ electron hereafter. We use the energy history of the electron along its trajectory and the contribution from $W_{curv,\parallel}$ and $W_{mirror,\parallel}$ to analyze its acceleration. Figure 5-9a shows the trajectory of the electron in the $x-z$ plane, with the color representing $|v_{\parallel}|$. In Figures 5-9b-5-9d, the horizontal axis is the backward tracing time ($\bar{t}$). Figure 5-9b shows how the electron's x position varies with time. A reference point at which the electron's $v_{\parallel}$ is zero is chosen and marked with a black star in panel (a), and the corresponding time is indicated with a vertical line in panels (b)-(d). Figure 5-9c shows the relativistic kinetic energy ($U_t = (\gamma-1)mc^2$) of the electron, and its parallel ($U_{\parallel} = m(\gamma v_{\parallel})^2/(\gamma+1)$) and perpendicular ($U_{\perp} = m(\gamma v_{\perp})^2/(\gamma+1)$) components, where $\gamma = \left(1-v^2/c^2\right)^{-1/2}$ is the Lorentz factor. Such definitions satisfy $U_t = U_{\parallel} + U_{\perp}$, and reduce to the non-relativistic expressions shown in section 5.4.1 when $\gamma = 1$. For the particle shown in Figure 5-9,

$\gamma \sim 1.25$ at $-\bar{t} = 0$. W_{curv} integrated from eq. (5.4) is plotted in Figure 5-9c in green. Figure 5-9d shows the parallel energy gain from $W_{curv,\parallel}$ (red) and $W_{mirror,\parallel}$ (blue), which are the integrations of eq. (5.11) and (5.12) along the electron's trajectory, and the sum of these two terms (green). The black line is $U_\parallel - W_\parallel$, where $W_\parallel$ is the integration of $-e\vec{E}_\parallel \cdot \vec{v}_\parallel$ over time to represent the work done by the parallel electric field. Thus $U_\parallel - W_\parallel$ represents the parallel energy gain originally from the work done by the perpendicular electric field. The difference between the black and green lines is due to the relativistic effect, since the non-relativistic forms of $W_{curv,\parallel}$ and $W_{mirror,\parallel}$ are used and the effect of γ is not taken into account. For this high $v_\parallel$ electron, the relativistic effect is small. For other electrons discussed below, the different may be larger, and the analysis will be mostly qualitative.

For this high $v_\parallel$ electron, we mainly discuss its acceleration in the intermediate and far exhaust regions, after it arrives at the mid-plane for the first time around the boundary between EDR2 and the intermediate exhaust (upper boundary of box 1 in Figure 5-9a, and the right boundary of box 1 in Figures 5-9c and 5-9d). At this time, the electron has an initial $U_\parallel$ of about 0.44 $m_i v_{Ai0}^2$ and a negligible $U_\perp$. This initial $U_\parallel$ is equal to the $e\Phi_\parallel$ difference between the mid-plane and the reference point near the separatrix (the energy conversion by the mirror force is negligible for this electron in this interval). However, the energy was originally obtained from $e\Phi_\parallel$ in the inflow region and from the reconnection E_y, in EDR around x=[900, 970] before the reference point.

We first examine the acceleration for the high $v_\parallel$ electron during its first mid-plane crossing, which is marked by box 1 (yellow box) at $-\bar{t}\omega_{pe} \sim [2300, 2200]$. During this interval, U_t, $U_\parallel$ and $U_\perp$ and W_{curv} in Figure 5-9c, and $W_{curv,\parallel}$ in Figure 5-9d exhibit sharp variations, which suggest that the electron experiences large magnetic curvature, since dW_{curv}/dt is proportional to the magnetic curvature. Hence, this interval is selected to represent the time scale for this mid-plane crossing. It corresponds to the crossing from

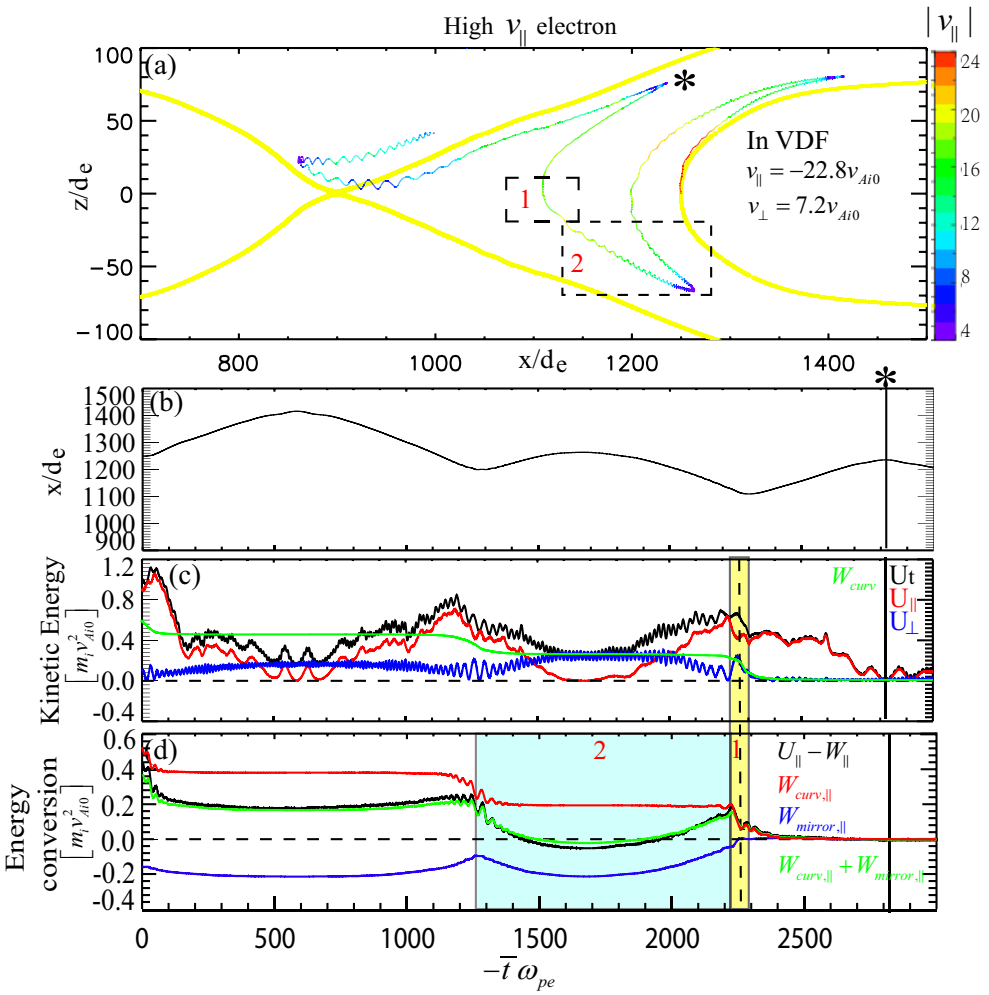

Figure 5-9: Backward test-particle tracing results of the electron with high $v_{||}$ and low $v_{\perp}$ in the VDF at [1250, 0] in the far exhaust. (a) trajectory in the $x - z$ plane; The color on the trajectories represents the local $v_{||}$ amplitude normalized by v_{Ai0}. (b) x locations along the trajectory backward in time; (c) electron total (black), parallel (red) and blue (perpendicular) kinetic energies, and the work from W_{curv} (green). (d) parallel energy gain from the work done by the perpendicular electric field. black: difference between the parallel energy and the work done by the parallel electric field; red: energy contributed by the curvature force; blue: energy contributed by the mirror force; green: sum of the contribution by curvature and mirror forces. The black vertical lines in (b)-(d) indicate a reference point where the energy conversion (d) is set to be zero. It corresponds to the location marked with a star in the trajectory of (a). See text for details.

$z \sim 10$ to $z \sim -20$ as marked in Figure 5-9a. The gyro-period T_g according to the average B_t during this interval is $\sim 60\ \omega_{pe}^{-1}$, so that this crossing takes only about 1.3 gyro-periods.

During this crossing, the increase of U_t mainly comes from W_{curv}, which exhibits an increase

within box 1 (Figure 5-9c, green). During the first half crossing in $-\bar{t}\omega_{pe} \sim [2300, 2280]$ (to the right of the dashed vertical line in box 1), the energy gained from W_{curv} goes to $U_\perp$, since $U_\perp$ increases along with U_t and W_{curv} (Figure 5-9c). During the second half of the crossing in $-\bar{t}\omega_{pe} \sim [2280, 2200]$ (left half of box 1), $U_\parallel$ has a sharp increase, $U_\perp$ decreases, U_t and W_{curv} do not change much, and $W_{curv,\parallel}$ increases. These signatures suggest that $\vec{v}\cdot\left(\hat{b}\cdot\nabla\hat{b}\right)$ is positive, and F_{curv} increases $U_\parallel$ at the expense of $U_\perp$, i.e., pitch angle scattering occurs. Above all, during this first mid-plane crossing, the high $v_\parallel$ electron gains energy from the curvature drift opposite to the electric field. The energy first goes to $U_\perp$, and the pitch angle scattering mainly caused by F_{curv} re-distributes the energy from the perpendicular to the parallel direction.

As the high $v_\parallel$ electron bounces in the intermediate exhaust, F_{mirror} converts $U_\parallel$ to $U_\perp$, and increases the pitch angle as the magnetic field strength increases. When the electron bounces away from $z = 0$ downward and bounces back (marked by box 2 in Figures 5-9a and 5-9d), $W_{mirror,\parallel}$ has a net decrease from $-\bar{t}\omega_{pe} \sim 2220$ to $-\bar{t}\omega_{pe} \sim 1250$.

Next, we discuss the acceleration of the high $v_\parallel$ electron in the far exhaust. When the electron leaves the mid-plane for the first time after pitch angle scattering ($-\bar{t}\omega_{pe} \sim 2220$), it has a $U_\parallel$ of about 0.64 $m_i v_{Ai0}^2$. In the following bounces, $e\Phi_\parallel$ and F_{mirror} make $U_\parallel$ fluctuate with a large amplitude, on the order of $\sim 0.8 m_i v_{Ai0}^2$. The contribution of $e\Phi_\parallel$ can be seen from the difference between the $U_\parallel$ and $U_\parallel - W_\parallel$ curves. At the end of the time ($-\bar{t}\omega_{pe} \sim 0$), $U_\parallel$ is about 0.88 $m_i v_{Ai0}^2$. Compared with $-\bar{t}\omega_{pe} \sim 2220$, the increase of $U_\parallel$ is about 0.24 $m_i v_{Ai0}^2$. During the same interval, Figure 5-9d (black) shows that the parallel energy gain from the sum of F_{curv} and F_{mirror} ($U_\parallel - W_\parallel$) increases from 0.20 $m_i v_{Ai0}^2$ to 0.44 $m_i v_{Ai0}^2$, which accounts for almost all of the total $U_\parallel$ increase. This indicates that most of the net increase of $U_\parallel$ in the far exhaust comes from the work done by $E_\perp$, while $E_\parallel$ has a negligible net contribution in the acceleration in the far exhaust. More specifically, the energy source

is W_{curv} (green line in Figure 5-9c), and F_{mirror} converts a portion of $U_{\parallel}$ to $U_{\perp}$. The high $U_{\parallel}$ the electron has every time when it arrives at the mid-plane leads to a large F_{curv} and $dW_{curv,\parallel}/dt$, which can accelerate the electron more efficiently. In addition, there are no more simultaneous changes of $U_{\parallel}$ and $U_{\perp}$ in opposite directions i.e., one increases and the other decreases, as in the second half of the first mid-plane crossing, which indicates that there is no more efficient pitch angle scattering in the far exhaust. Therefore, the high $v_{\parallel}$ electron in the far exhaust starts with a large initial $v_{\parallel}$ by the end of the pitch angle scattering near the boundary between EDR2 and the intermediate exhaust, and the energy source for further acceleration is W_{curv}.

Figure 5-10 shows the tracing result of an electron taken from the distinct population with low $v_{\parallel} = -1.92v_{Ai0}$ and high $v_{\perp} = 28.8v_{Ai0}$ ($\gamma = 1.44$) in the VDF at [1250, 0]. This electron will be referred to as the high $v_{\perp 1}$ electron hereafter. Figure 5-10a shows its trajectory with the color representing $|v_{\perp}|$. Formats for Figures 5-10b-5-10d are the same as in Figures 5-9b-5-9d. As with the analysis for the high $v_{\parallel}$ electron, the analysis of this high $v_{\perp 1}$ electron is focused on its acceleration starting from the time it first arrives at the mid-plane after the reference point (marked by the star in Figure 5-10a and vertical lines in Figures 5-10b-5-10e). It includes a portion of EDR2 and is mostly in the intermediate and far exhaust regions.

The acceleration of the high $v_{\perp 1}$ electron during its first mid-plane crossing in EDR2 (marked by box 1) is similar with that for the high $v_{\parallel}$ electron. The characteristic time scale of this crossing, where U_t, $U_{\parallel}$, $U_{\perp}$ and $W_{curv,\parallel}$ exhibit sharp changes, is about 100 ω_{pe}^{-1}, corresponding to ∼1.7 gyro-periods. With an initial large $U_{\parallel}$ of $\sim 0.8m_i v_{Ai0}^2$, dW_{curv}/dt and $dW_{curv,\parallel}/dt$ are large in amplitude. U_t increases due to W_{curv} (Figure 5-10c, black), while a part of the energy comes from W_{gradB} (not shown), since $U_{\perp}$ and the gradient-B drift velocity are considerable during this interval. The gained energy directly leads to an

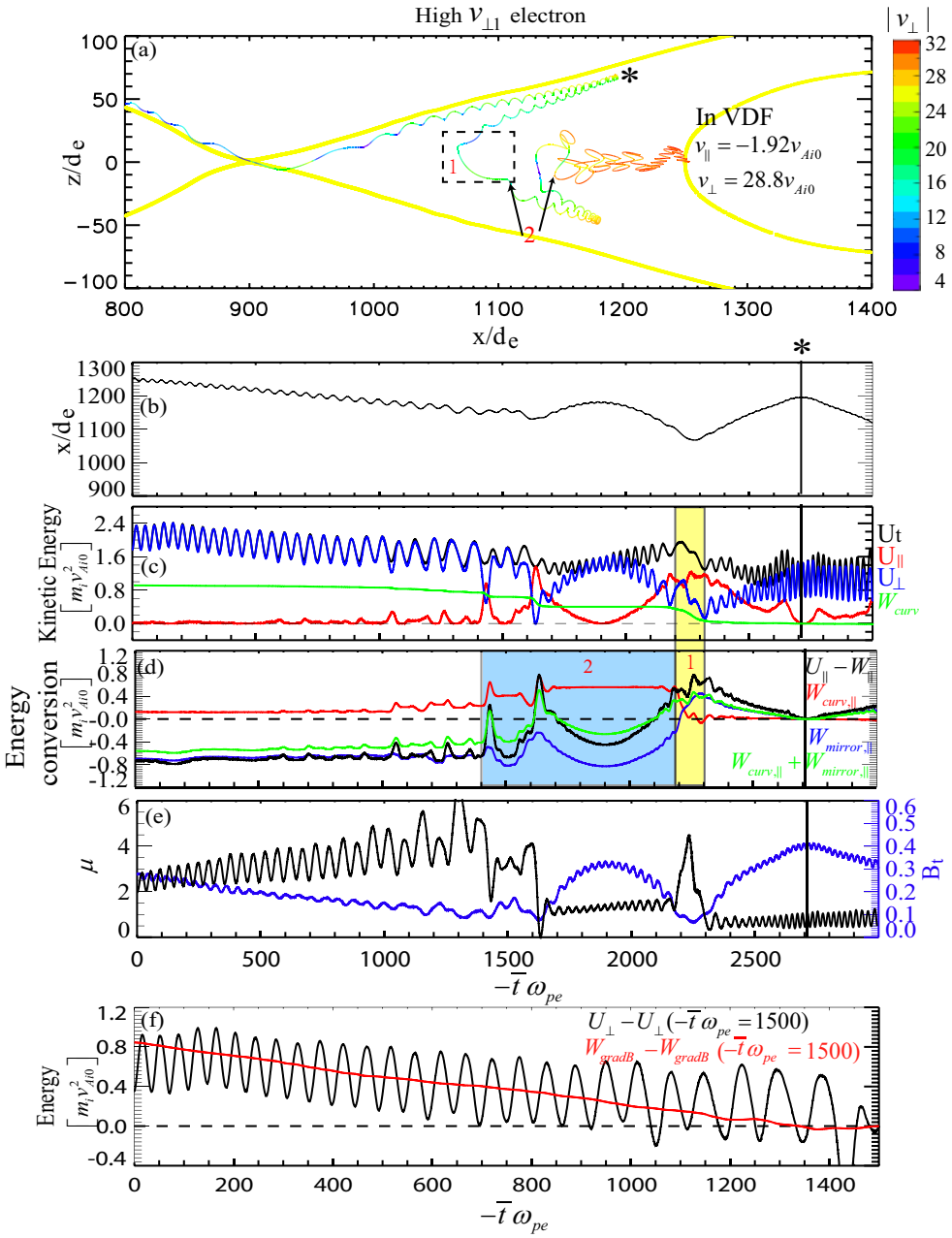

Figure 5-10: Backward test-particle tracing results of an electron with low $v_\parallel$ and high $v_\perp$ in the VDF at [1250, 0]. Panels (a)-(d) have the same formats as in Figure 5-9, except that the color in (a) represents the amplitude of $v_\perp$. (e) magnetic moment (black) and the total magnetic field strength (blue) along the trajectory; (f) perpendicular energy gain (black) and the work from W_{gradB} relative to the reference point at $-\bar{t}\omega_{pe} = 1500$.

increase of $U_\perp$ (Figure 5-10c, blue). It is followed by a small increase of $U_\parallel$ near the left boundary of box 1 (Figure 5-10c, red), along with a simultaneous decrease in $U_\perp$ (Figure

5-10c, blue) and an increase in $W_{curv,\parallel}$ (Figure 5-10d, red). Thus, the acceleration for the high $v_{\perp 1}$ electron during its first mid-plane crossing is from W_{curv} and W_{gradB}, and the pitch angle scattering exists to distribute the energy gain to the parallel direction.

When the high $v_{\perp 1}$ electron bounces in the intermediate exhaust (between arrows in Figure 5-10a and marked by box 2 in Figure 5-10d), its kinetic energy is re-distributed between $U_\parallel$ and $U_\perp$ by both F_{curv} and F_{mirror}, which can be seen from the $W_{curv,\parallel}$ and $W_{mirror,\parallel}$ variations in this interval (Figure 5-10d). By the end of this pitch angle scattering process (left boundary of box 2), $U_\perp$ increases at an expense of $U_\parallel$.

In the far exhaust after pitch angle scattering, the acceleration for the high $v_{\perp 1}$ electron is different from that for the high $v_\parallel$ electron. It starts with an initial high $U_\perp$ and low $U_\parallel$. As the electron travels in the far exhaust ($-\bar{t}\omega_{pe} = [0, 1400]$), its $U_\perp$ is further increased, while $U_\parallel$ remains low (Figure 5-10d). Consequently, its bouncing motion is in a small z range (Figure 5-10a), and its Larmor radius is large with $\kappa \sim 1$. The small $U_\parallel$ leads to a small $dW_{curv,\parallel}/dt$ (Figure 5-10d). As can be seen from its trajectory, its bouncing period is comparable to the gyro-period, so that it feels a large variation of the magnetic field within a gyro-period. This causes the violation of the relativistic $\mu = \gamma^2 m v_\perp^2/2B$ conservation [*Boris*, 2006; *Dahlin et al.*, 2014], which is shown as a non-constant black line in Figure 5-10e during this interval. The magnetic field structure the electron experiences during two quarters of a bouncing period does not change much, so that the energy re-distribution by F_{mirror} is also small (Figure 5-10d). In order to examine the energy source, Figure 5-10f presents $U_\perp$ (black) and W_{gradB} defined in eq. (5.5), both of which are set to be zero at $-\bar{t}\omega_{pe} = 1500$. The two lines follow each other. Therefore, the energy source for the high $v_{\perp 1}$ electron is W_{gradB}. Without much energy redistribution by F_{curv} or F_{mirror}, the obtained energy increases $U_\perp$, and $U_\parallel$ keeps low.

The above mechanism for accelerating the high $v_\perp$ electron requires a small $v_\parallel$ as well.

A larger $v_{\parallel}$ makes electrons bounce in a large $|z|$ range, where the magnetic field gradient is not only in the $+x$ direction, but also has a component in z (Figure 5-4a). Combing with the magnetic field in the x direction, $\vec{v}_{d,gradB}$ can change the sign in the y direction, so that $\vec{E} \cdot \vec{v}_{d,gradB}$ is not always negative throughout the bounces and the electrons cannot be always accelerated. This situation is confirmed with the test-particle analysis for electrons with higher $v_{\parallel}$ in the far exhaust (not shown). Such a mechanism explains why the high $T_{e\perp}$ region in the far exhaust is only restricted close to the mid-plane as mentioned in section 5.2.

Dahlin et al. [2014] suggested that the gradient-B drift has little contribution to the electron heating in reconnection with a strong guide field. However, our analysis shows that with negligible guide field, the gradient-B drift acceleration is important to form a population with large near the mid-plane, and has considerable contribution to the perpendicular heating near the mid-plane in the far exhaust.

With the analysis of the high $v_{\parallel}$ and high $v_{\perp 1}$ electrons, we have seen how these two types of electrons are accelerated in the intermediate and far exhaust regions, forming the two distinct populations in the VDF at the mid-plane of the far exhaust. For completeness, we present the test-particle results for two more electrons (Figure 5-11) mainly to illustrate how they obtain their initial energy before arriving at the mid-plane in the intermediate exhaust.

Figures 5-11a-5-11d show the tracing result of an electron taken from the VDF at [1250, 0] with a low $v_{\parallel} = -0.56 v_{Ai0}$ and a high $v_{\perp} = 29.5 v_{Ai0}$ ($\gamma = 1.48$), in the same formats in Figures 5-10a-5-10d. This electron will be referred to as the high $v_{\perp 2}$ electron hereafter. This high $v_{\perp 2}$ electron is originally accelerated inside EDR in $x \sim$[900, 990], corresponding to the region to the left (right) of the dashed line '0' in Figure 5-11a (Figures 5-11b-5-11d). The electron obtains a high $U_{\perp}$ with the EDR acceleration. At the dashed line '0',

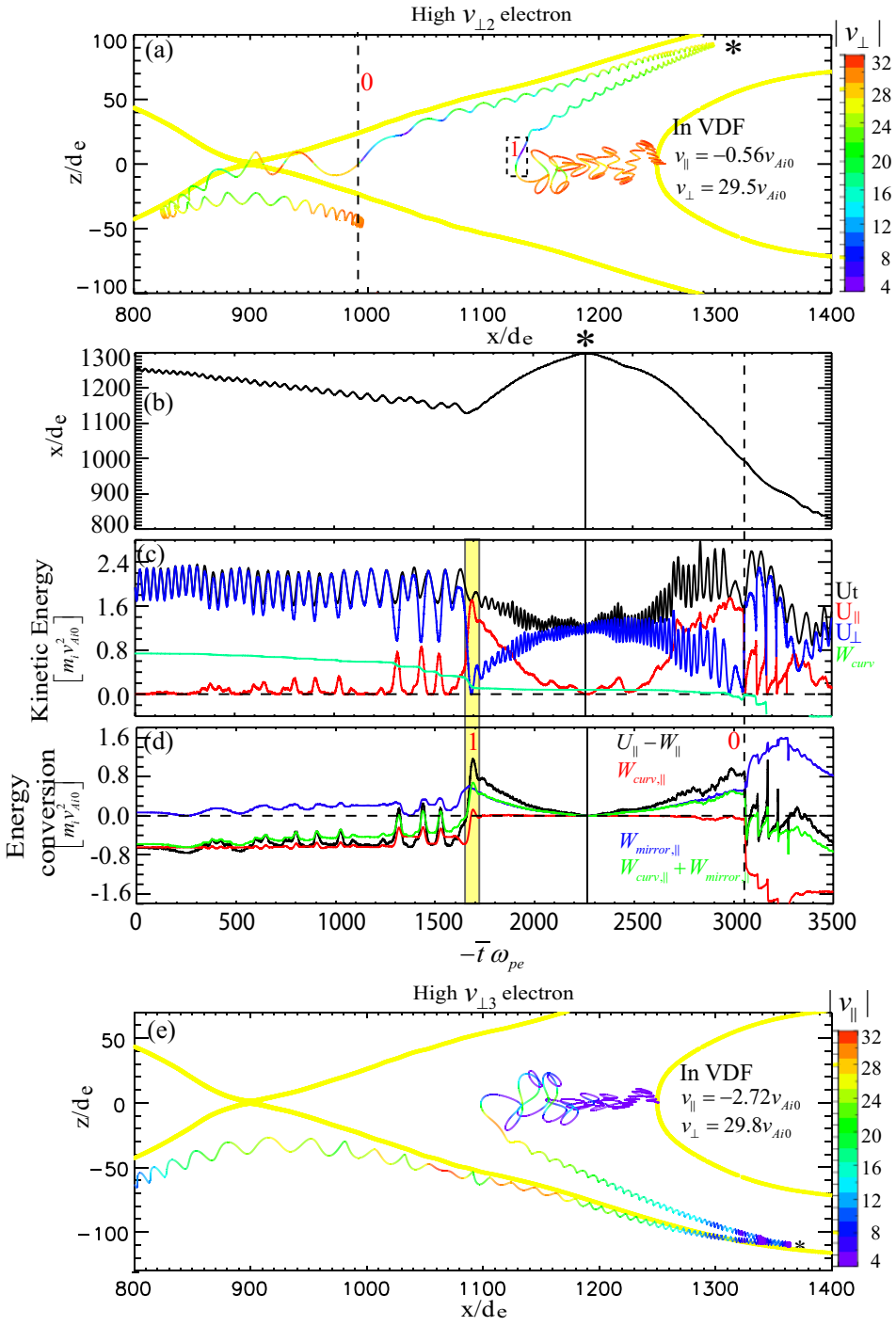

Figure 5-11: Backward test-particle tracing results of two electron with low $v_{\parallel}$ and high $v_{\perp}$ in the VDF at [1250, 0]. (a)-(d) are for one electron crossing EDR with the same formats as in Figures 5-10a - 5-10d. (e) trajectory of another electron directly crossing the downstream separatrix to the exhaust with the color representing the amplitude of $v_{\parallel}$.

pitch angle scattering happens, mainly from F_{curv} (Figure 5-11d, red), which converts its $U_\perp$ to $U_\parallel$ (Figure 5-11c). Then the electron bounces towards the reference point near the separatrix and bounces back to the mid-plane in the intermediate exhaust (marked by box 1). The large amplitude variation in $U_\parallel$ between the mid-plane and the separatrix is due to $e\Phi_\parallel$ and the mirror force. However, U_t (Figure 5-11c, black) has little change between its two crossings at the mid-plane (the right boundary of box 1 and the dashed line '0'), which suggests that the energy of this electron essentially comes from the acceleration in EDR through the meandering motion.

During the first mid-plane crossing in the intermediate exhaust (marked by box 1), this high $v_{\perp 2}$ electron gains energy from W_{curv} and undergoes pitch angle scattering, which is the same as the high $v_\parallel$ and high $v_{\perp 1}$ electrons. However, in this case, $W_{curv,\parallel}$ decreases during the mid-plane crossing (Figure 5-11d, red), and $U_\parallel$ decreases (Figure 5-11c, red) along with a simultaneous increase in $U_\perp$ (Figure 5-11c, blue). Therefore, the pitch angle scattering mainly from F_{curv} converts $U_\parallel$ to $U_\perp$, which is in the opposite direction from that in the first mid-plane crossing for the high $v_\parallel$ and high $v_{\perp 1}$ electrons. This further proves that the pitch angle scattering at the mid-plane due to F_{curv} can happen in both directions, which may lead to an isotropic distribution.

Contrary to the high $v_{\perp 2}$ electron, the high $v_{\perp 3}$ electron shown in Figure 5-11e is not originally accelerated in EDR with the meandering motion. Instead, it directly crosses the separatrix and bounces towards the mid-plane in the intermediate exhaust, on which way it obtains $U_\parallel$ from $e\Phi_\parallel$. After the first mid-plane crossing, its further energization in the intermediate and far exhaust regions are similar with that for the high $v_{\perp 2}$ electron.

5.5 Conclusions

In this study, we use PIC simulations and Cluster magnetotail observations to determine the detailed spatial variations of the electron temperature in the exhaust region of reconnection with negligible guide field, and understand the heating of the electrons by interpreting the electrons' VDFs using simulations of individual particle motion. Our main results are as follows.

(1) We find that the reconnection exhaust can be divided into four distinct regions in the x direction according to the electron velocity and temperature, including their variations along x and z directions, and the anisotropy characteristics. Previously reported highly structured electron VDFs can be identified with particular regions, which are associated with the T_e variations. The main T_e and VDF features in each region are summarized below, and the features can be understood with the above single-particle energization mechanisms.

Inside the EDR (regions EDR1 and EDR2, with differences in the T_e profile along x), $T_{e,\parallel}$ exhibits a local minimum and $T_{e,\perp}$ exhibits a maximum at mid-plane, and the cyclotron motion around increasing B_z dominates the heating process with its signatures presented in VDFs. In the intermediate exhaust region, the electron VDF is a superposition of a slightly parallel elongated flat-top distribution and a quasi-isotropic high-energy distribution near the mid-plane, and with an inward beam off mid-plane. T_e is isotropic with small spatial variations. In the far exhaust close to the pile-up region, T_e generally increases towards the mid-plane and towards the pile-up region, while the $e\Phi_\parallel$ variation might cause fine structures in the profile. VDFs exhibit counter-streaming beams. A distinct population with large $v_\perp$ and small $v_\parallel$ is prominent close to the mid-plane.

(2) By following the electron motion in the reconnection region with test-particles, we have determined the individual contribution of different acceleration mechanisms to the acceleration of electrons in different sub-regions, which are summarized in Figure 5-12.

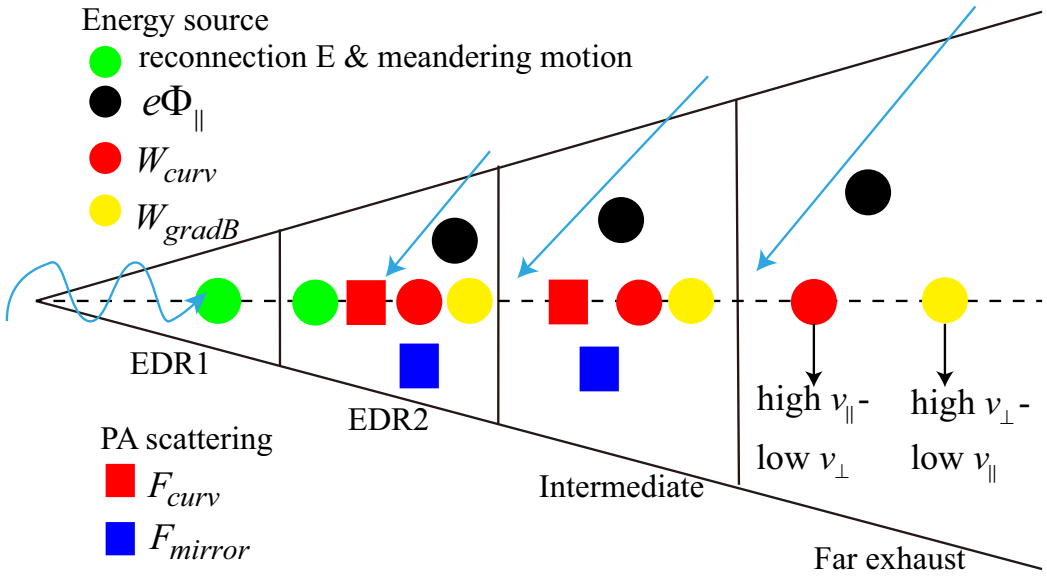

Figure 5-12: Illustration of the dominant electron energization mechanisms in sub-regions of the reconnection exhaust. Light blue lines indicate possible ways for electrons to enter the exhaust. Circles represent the acceleration energy source, and squares represent the pitch angle (PA) scattering mechanisms.

Electrons may enter the exhaust region either through the EDR or by directly crossing the downstream separatrix at different distances from the X line. Electrons in the EDR are accelerated by the reconnection electric field as they perform the meandering motion, while those that directly cross the separatrix obtain the parallel energy from $e\Phi_{\parallel}$ on the way from the separatrix to the mid-plane. The EDR process is dominant in EDR1, and the initial acceleration by $e\Phi_{\parallel}$ is dominant downstream of the EDR. In the EDR2 region, different mechanisms co-exist. After obtaining an initial energy, electrons that start to be re-magnetized can be further accelerated by W_{curv} (Fermi acceleration) and W_{gradB} close to the mid-plane, starting from the end of EDR2 towards downstream. Pitch angle scattering happens mainly in the EDR2 region and in the intermediate exhaust for electrons that are not fully magnetized, and is caused by F_{curv} close to the mid-plane. F_{mirror} also causes changes in pitch angle due to the change of the magnetic field strength downstream and the violation of the μ conservation. In the far exhaust near the mid-plane, where there

is no efficient pitch angle scattering, the high $v_{\parallel}$ -low $v_{\perp}$ and high $v_{\perp}$ -low $v_{\parallel}$ electrons are accelerated mainly from W_{curv} and W_{gradB}, respectively, without exchanging energies between the parallel and perpendicular components.

The analysis of the single-particle acceleration is applied to understand the VDF features. Near the mid-plane in the intermediate exhaust, the flat-top distribution in the parallel direction is due to the mixture of electrons coming from the EDR and bouncing back and force, together with electrons crossing the separatrix with different distances from the X line. The electrons that directly cross the separatrix are accelerated by $e\Phi_{\parallel}$ to different levels: the longer they travel from the separatrix to the mid-plane, the more energy they obtain from $e\Phi_{\parallel}$. The increasing shoulder energy towards downstream is caused by both the mixture with more electrons traveling a longer distance between the separatrix and the mid-plane, and the further electron acceleration by W_{curv} and W_{gradB}.

The beam structures can also be understood. The beam features in the intermediate exhaust were already discussed in previous studies. The beams can be generated close to the separatrix region on the field lines connecting with the mid-plane in the intermediate and far exhaust regions. The beam structure in the VDF might trigger instabilities that cause pitch angle scattering and energy scattering, which can lead to an isotropic flat-top distribution *Asano et al.* [2008]; *Egedal et al.* [2012]. With the analysis in this study, we further emphasize the pitch angle scattering caused by the magnetic field structure at the current sheet mid-plane, which is not due to an instability. In addition, we explain the beam features in the far exhaust. At mid-plane in the far exhaust, without efficient pitch angle scattering, the inward beam structures generated on one side of the mid-plane remain when the beam electrons cross the mid-plane. As the beam electrons keep travelling to the other side of the mid-plane, they mix with the inward beams there in the same VDF. That is why there are counter-streaming beams in this region.

(3) The VDF features associated with each region in the simulation are identified and confirmed by in situ observations in a magnetotail reconnection event.

One limit in this study is that our analysis does not include the effects of waves and instabilities, because we used test-particle analyses where the electromagnetic field values do not evolve. However, the primary electron energization processes are captured. Waves and instabilities are expected to further energize particles and scatter the distributions.

Chapter 6

The electron heating coefficient and effects of unloading in magnetotail reconnection

6.1 Introduction

The electron bulk heating (ΔT_e) in reconnection from inflow to exhaust regions was reported to be proportional to $m_i v_{Ai}^2$, where v_{Ai} is the upstream ion Alfvén speed [*Phan et al.*, 2013]. The heating coefficient, which is defined as

$$r_h = \frac{k_B \Delta T_e}{m_i v_{Ai}^2} \tag{6.1}$$

where k_B is the Boltzmann constant, is reported to be 1.7% in the magnetopause reconnection observations [*Phan et al.*, 2013], and about 3.3% in symmetric reconnection simulations [*Shay et al.*, 2014]. The statistical observational support for the electron bulk heating in symmetric reconnection is still missing, and its temporal evolution has not been discussed.

The reason that r_h is a few percent has not been clear. One attempt to explain this was to analyze the particle motion in the de-Hoffmann Teller frame moving with an outflow

velocity of v_{Ai}, where there is no electric field [*Drake et al.*, 2009b; *Phan et al.*, 2014]. In such a frame, both the incoming and outgoing populations have a velocity around v_{Ai} along the magnetic field, so that they form counter-streaming beams in the velocity distribution functions (VDFs), and the ion (T_i) and electron (T_e) temperatures in the exhaust are expected to be $1/3 m_i v_{Ai}^2$ and $1/3 m_e v_{Ai}^2$, respectively [*Drake et al.*, 2009b; *Phan et al.*, 2014]. Such a model demonstrates the fact that the bulk heating is proportional to $m_i v_{Ai}^2$. However, it predicts an r_h of 33% for ions, which is much higher than the observational results of 13%; it predicts an rh of 0.02% for electrons, which is much lower than 1.7-3.3% from observations and simulations [*Phan et al.*, 2014]. Therefore, a better explanation of the heating coefficient is needed.

In this study, after understanding the electron heating process as discussed in Chapter 5, we will use a simplified electron VDF model of the VDF in the electron diffusion region (EDR) from the particle-in-cell (PIC) simulation to calculate the electron bulk heating coefficient. We will also examine the electron bulk heating and its temporal evolution using the same PIC simulations as those in Chapter 5, and present a statistical result of the electron heating in 13 magnetotail reconnection events observed by the Cluster spacecraft.

6.2 Calculation of r_h with a VDF model in the EDR

The analysis in this section uses the simulation 1 data introduced in Chapter 5 at time $t\omega_{ci} = 26$, which is 8 ω_{ci}^{-1} after the peak reconnection rate. At this time, the magnetic field pile-up region is well separated from the X-line, allowing for detailed examination of the electron temperature (T_e) profile as shown in Figure 6-1a. Figures 6-1b and 6-1c show the 1D slices of the electron temperatures and the x component of the electron bulk velocity (u_{ex}) along the mid-plane, where the region of $x < 1020$ with large u_{ex} indicates the electron diffusion region (EDR). In this Chapter, the velocity in the simulation analysis is normalized

to v_{Ai} based on upstream B_0 and background density n_b, and the temperature is normalized to $m_i v_{Ai}^2$

Our model is based on the electron VDF in the EDR to emphasize the energization in the diffusion region. Studies have shown that electrons are accelerated and thermalized in the EDR as they perform the meandering and cyclotron motion around the reconnected magnetic field normal to the current sheet [e.g., *Bessho et al.*, 2014; *Shuster et al.*, 2015]. The EDR energization mechanism leads to a perpendicular electron heating (Figure 6-1b, red). As analyzed in Chapter 5, the increase of $T_{e\|}$ close to the end of the EDR is due to the pitch angle scattering that converts the perpendicular velocities of the EDR electrons to the parallel direction, and due to the mixture of the EDR electrons with those from the separatrix that are accelerated by the parallel potential. The horizontal line in Figure 6-1b marks the average total temperature ($T_{e,exhaust}$) in the exhaust region enclosed by the white magnetic field contour that intersects with the mid-plane at $x \sim$1035, and the white vertical line at x=1170 in Figure 6-1a. The enclosed region is downstream of EDR, downstream of the separatrix layer where T_e exhibits sharp increases from inflow to exhaust regions, and before the magnetic pile-up region. The obtained average T_{et} is within the range of T_{et} in the EDR between the u_{ex} peak and the end of u_{ex} jet, and the T_{et} variation downstream of the EDR is within a factor of 2. Therefore, the heating coefficient analyzed according to the EDR energization process is representative of the exhaust at least for the four sets of parameters simulated.

The heating coefficient r_h is derived from a simplified electron VDF model based on the real VDF in the PIC simulation. The VDFs at points 1 and 2 (Figures 6-1d and 6-1e) in the v_x-v_y plane, which is almost perpendicular to the magnetic field, are from the simulation at the peak and the end of the electron outflow jet at the mid-plane (marked by the white boxes in Figure 6-1a and vertical lines in Figures 6-1b and 6-1c), respectively. At

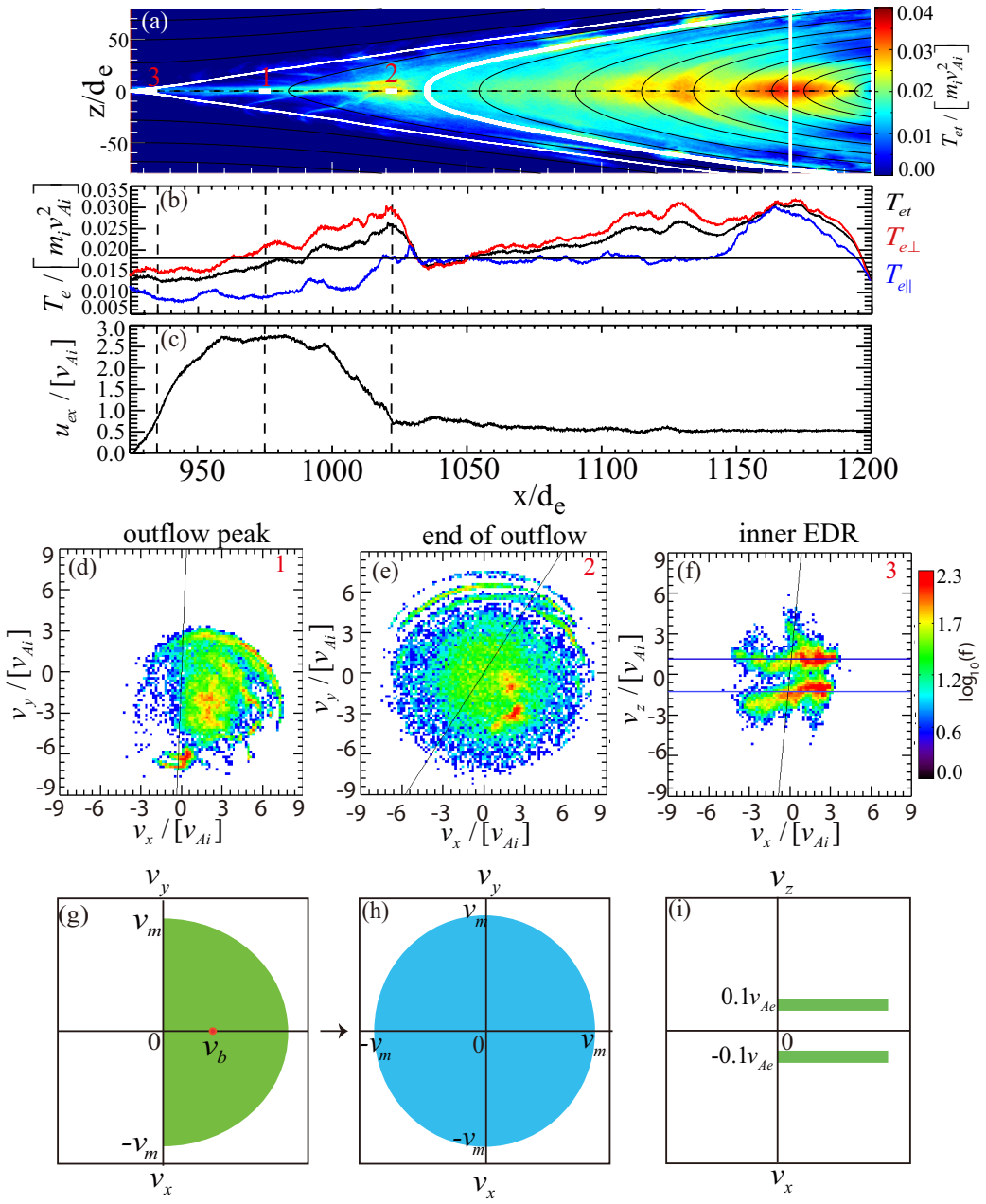

Figure 6-1: Electron VDF model to estimate the electron heating coefficient. (a) Total electron temperature (T_{et}) profile in simulation 1 at time $t\omega_{ci} = 26$. The leftmost white contour marks the separatrix, and the right two white curves enclose the exhaust region where the average T_{et} is taken as $T_{e,exhaust}$. (b)-(c) 1D slices of the x component of the electron bulk velocity (u_{ex}) and temperature components along the mid-plane. (d)-(f) Electron VDFs from the simulation at points 1-3 marked by the white boxes in (a) and vertical lines in (b)-(c). The magnetic fields (black lines in VDFs) are mainly in the z direction. (g)-(i) VDF models representing those in (d)-(f). See text for details.

point 1, most electrons are in the positive v_x half plane, and cyclotron turned towards the negative v_x direction. The distribution is mostly uniform (green in color) with the phase space density (PSD) enhancements at several velocity values (red in color). According to the studies by *Bessho et al.* [2014] and *Shuster et al.* [2015], in such an EDR distribution, the speed at which the PSD shows an enhancement is originated from the acceleration in the y direction when electrons were closer to the X-line. How much an electron can be accelerated depends on how many times it bounces in the z direction when performing the meandering motion [*Bessho et al.*, 2014]. At point 1, the distribution extends in an approximate range of [0, 6] in v_x and [-6, 3] in v_y. Thus, neglecting the localized PSD peaks and the asymmetry in different velocity directions, we use a simplified semi-circle distribution with a uniform PSD in the velocity range of [0, v_m] in all directions in the positive v_x half plane, to model the VDF at point 1 in the v_x-v_y plane, as shown in Figure 6-1g. v_m represents the maximum velocity of the distribution where the PSD abruptly falls off, which is simplified to be the same in all directions in the positive v_x half plane. In the real VDF at point 1, a representative v_m should be around 4.5 to 6. At point 2, the electron thermalization by the cyclotron turning is more complete. The VDF is closer to gyrotropy. We model it as a full circle with a uniform PSD in the same velocity range as shown in Figure 6-1h. In the EDR between the peak and the end of the electron outflow jet, the VDF in the v_x-v_y plane is at an intermediate stage between a semi-circle and a full circle.

The VDF model in the v_x-v_z plane is based on the simulation VDF at point 3 (Figure 6-1f). Inside the EDR before $T_{e\|}$ increases, the electron motion is dominated by the meandering motion, and exhibits peaks at a positive and a negative v_z (Figure 6-1f). It can be modeled as two δ-functions in v_z as shown in Figure 6-1i. At larger x locations around point 1, the PSD peaks in v_z become less clear; however, $T_{e\|}$ has small variations, and it

only changes by 5% from point 3 to point 1. Closer to the end of the EDR where the VDF in the v_x-v_y plane is close to a full circle, more electrons from the separatrix are mixed with those from the X line as $T_{e\|}$ increases, and the VDF is even more scattered in the v_z direction. Thus, $T_{e\|}$ based on the two δ-function VDF in the v_x-v_z plane can be used to represent most of the EDR, but before the VDF becomes a full circle in the v_x-v_y plane. In the model, the PSD only occupies the positive v_x space, since the majority of particles in the EDR are accelerating towards the $+x$ direction as shown in the VDFs at points 1 and 3. In fact, its occupation in the x direction does not affect the $T_{e\|}$ calculation.

T_e can be calculated from the above modeled VDFs. In the v_x-v_y plane, we assume that the change of the VDF from a semi-circle to a full circle is only caused by further gyration around the magnetic field, and the electron density is almost conserved. This assumption is justified by the actual density difference in simulation between points 1 and 2, which is ∼20%. Let the uniform PSD of the semi-circle distribution be f, and that of the full circle be $f/2$. Thus the density is $n = \int_0^{v_m} vdv \int_{-\pi/2}^{\pi/2} fd\theta = \frac{\pi}{2} f v_m^2$, where v_m is the maximum velocity for the distribution. The bulk velocity, which is the maximum electron outflow jet, is $v_b = \frac{1}{n}\int_0^{v_m}\int_{-\pi/2}^{\pi/2} fvcos(\theta)vd\theta dv = \frac{4}{3\pi}v_m$. The corresponding $T_{e\perp}$ is

$$T_{e\perp,semi} = \frac{m_e}{2n}\int_0^{v_m}\int_{-\pi/2}^{\pi/2} f\left[(v\cos\theta - v_b)^2 + v^2\sin^2\theta\right] vd\theta dv \approx 0.89 m_e v_b^2 \tag{6.2}$$

For the full circle distribution, the bulk velocity is zero, and $T_{e\perp}$ is

$$T_{e\perp,full} = \frac{m_e}{2n}\int_0^{v_m}\int_0^{2\pi} \frac{1}{2} f v^3 d\theta dv \approx 1.38 m_e v_b^2 \tag{6.3}$$

In the v_x-v_z plane, we assume that the electron v_z for the meandering motion is its inflow velocity $\sim 0.1 v_{Ae}$, where v_{Ae} is the upstream electron Alfvén speed. In Figure 6-1d, the PSD peaks around $\pm 1.2\ v_{Ai}$ (horizontal blue lines in Figure 6-1f), which corresponds

to $\pm 0.06 v_{Ae}$. The corresponding temperature along z direction is

$$T_{e\parallel} = T_z = m_e \left(0.1 v_{Ae}\right)^2 = 0.01 m_i v_{Ai}^2 \tag{6.4}$$

Thus, the total temperature is $T_e = \left(T_{e\parallel} + 2T_{e\perp}\right)/3$.

In the simulation, the electron outflow jet velocity v_b is $2.7 v_{Ai}$ ($0.135 v_{Ae}$), so that $T_{e\perp,semi}$ = 0.016 $m_i v_{Ai}^2$ and $T_{e\perp,full}$ = 0.025 $m_i v_{Ai}^2$. The simulation moments data show $T_{\perp 1}$ = 0.022 $m_i v_{Ai}^2$ at point 1 and $T_{\perp 2}$ = 0.026 $m_i v_{Ai}^2$ at point 2, which are close to the prediction by the semi-circle and full-circle models. $T_\parallel$ is 0.008 $m_i v_{Ai}^2$ at point 3, with a 20% difference from the predicted 0.01 $m_i v_{Ai}^2$. Such a comparison demonstrates the validity of using our simplified models to represent the real VDFs in the EDR in the PIC simulation for the temperature calculation.

Now that the temperature from the simplified models agrees with the temperature at the same locations in the EDR from the PIC simulation, and as discussed above, the EDR temperature is representative for the whole exhaust, we can use the simplified VDF models to calculate the heating coefficient r_h as

$$r_{h,semi} = \frac{T_{e,semi}}{m_i v_{Ai}^2} = 0.003 + 0.6 \frac{v_b^2}{v_{Ae}^2} \tag{6.5}$$

and

$$r_{h,full} = \frac{T_{e,full}}{m_i v_{Ai}^2} = 0.003 + 0.93 \frac{v_b^2}{v_{Ae}^2} \tag{6.6}$$

The coefficients calculated from the models are $r_{h,semi}$=1.4% and $r_{h,full}$=2.0% according to eq. (6.5) and eq. (6.6). Using the average electron temperature in the whole exhaust in the PIC simulation, we obtain an r_h=1.8%. The r_h derived from the above EDR VDF model is well within the range of the electron heating coefficient for the whole exhaust in the simulation, with the uncertainty of ~20% r_h.

The above model depends on the electron bulk outflow velocity v_b. Theoretically, the electron dynamics is governed by the whistler wave dispersion relation and v_b was predicted to be $\sim v_{Aei}$, where v_{Aei} is the electron Alfvén speed at the edge of the electron inflow region where the electron inflow starts to diverge [*Shay et al.*, 2001; *Drake et al.*, 2008], and v_{Aei} is a fraction of v_{Ae}. Hence, it indicates that the magnetic field profile in the reconnection diffusion region and the electron bulk acceleration are related to the bulk heating coefficient. From the perspective of the single-particle motion, since v_b is related to the maximum velocity of the distribution (v_m), the bulk heating depends on the maximum electron acceleration by the reconnection electric field. According to *Bessho et al.* [2014], it depends on the maximum times an electron can bounce in the z direction when it is trapped in the current sheet to perform the meandering motion.

6.3 Temporal evolution of r_h in PIC simulations

We examine the electron heating in four PIC simulations with negligible guide field as introduced in Chapter 5. The results are listed in Table 6.1. For each simulation, the electron heating is analyzed at two time slices: the peak reconnection rate, and 8 ω_{ci}^{-1} later. As shown in Figure 6-1a, the $T_{e,exhaust}$ is taken as the average over the exhaust region. In PIC simulations with open boundary conditions, although the magnetic flux and particles are continuously injected into the system, the total flux and energy in the reconnection system still gradually vary with time, usually decreasing [*Daughton et al.*, 2006]. For the simulations we use, upstream conditions present clear changes for runs 1 and 2 (m_i/m_e=400) at the times after the peak reconnection rate. In both cases, the asymptotic magnetic field and lobe densities decrease by a factor of 30%. Therefore, the heating coefficients normalized by both initial upstream $m_i v_{Ai}^2$ (r_{h0}) and by the same quantity at the same time to that $T_{e,exhaust}$ (r_{ht}) is measured are presented in Table 6.1. The uncertainties of r_h come from

Run NO.	$t\omega_{ci}$	r_{h0}	$\delta r_{h0}/r_{h0}$	r_{ht}
1	18	1.2%±0.1%		1.1%±0.1%
1	26	1.8%±0.4%	50%	2.6%±0.5%
2	19	1.5%±0.2%		1.5%±0.2%
2	27	2.8%±0.4%	87%	4.2%±0.6%
Average		1.8%		1.2%±2.4%
3	15	2.8%±0.3%		2.5%±0.3%
3	23	3.6%±0.9%	29%	3.4%±0.9%
4	16	2.5%±0.5%		2.3%±0.5%
4	24	3.7%±1.0%	48%	3.5%±0.9%
Average		3.2%		1.2%±0.1%

Table 6.1: Electron heating coefficients in PIC simulations. Simulation numbers are the same as those used in Chapter 5. r_{h0} is calculated with the average electron temperature in the exhaust region ($T_{e,exhaust}$) normalized by $m_i v_{Ai}^2$ based on the initial asymptotic magnetic field B_0 and the lobe density n_b. Its uncertainty is from the standard deviation of $T_{e,exhaust}$. $\delta r_{h0}/r_{h0}$ is the fractional increase of r_{h0} between two examined times for each run. r_{ht} has similar definitions with r_{h0}, except that v_{Ai} is based on B_0 and n_b at the instant times with $T_{e,exhaust}$.

the standard deviation of T_e in the exhaust region.

It is clear that for the examined cases, r_h lies in the range of 1%-4%. The average r_h for runs 1 and 2 is ∼2% and that for runs 3 and 4 is ∼3%. The difference between these two sets of simulations might be due to the difference in the mass ratio [*Shay et al.*, 2014] and the initial lobe densities. One noticeable result is that r_h increases with time. As listed in Table 6.1, r_{h0} increases by a factor of 30%-90% in 8 ω_{ci}^{-1} for the four runs.

6.4 Electron bulk heating in the magnetotail reconnection observations

We perform a statistical study of the electron bulk heating for 13 magnetotail reconnection events observed by the Cluster spacecraft, which will be presented in this section.

6.4.1 A case study with the electron heating coefficient calculation

The estimation of r_h requires the determinations of the exhaust T_e, upstream asymptotic magnetic field in the lobe (B_0), and the upstream lobe density (n_b). In this section, we present a magnetotail reconnection event on 21 August, 2002, and illustrate how we estimate r_h.

Figure 6-2 illustrates how we determine the exhaust parameters. The electron temperature data ($T_{e,int}$ in Figure 6-2a) are obtained from the integration of the pitch angle distributions as introduced in Chapter 2. We need to select the exhaust intervals to take T_e data, using the election energy spectrogram, ion velocity, magnetic field, plasma β, and electron VDFs. The C1 measurements show features of three typical regions. The reconnection exhaust intervals are between each pair of the black and red vertical lines; the interval before the first black vertical line is the ambient plasma sheet; 08:17-08:18 UT, after 08:23 UT, and other intervals that are not mentioned are at the plasma sheet boundary layer or reconnection separatrix region. The reconnection exhaust region is identified based on five criteria. (1) The electron energy spectrogram (Figure 6-2b) exhibits enhancements at energies higher than ~1 keV. The spectrogram shows enhancements in the intermediate energy ranges when the spacecraft crossed the separatrix region, as shown in the purple oval in Figure 6-2b, where T_e gradually increases. Here we only need the exhaust T_e, so that such transition layers are avoided. (2) The magnetic field Bx has smaller values than those near the boundary layer (Figure 6-2c). (3) H^+ velocity (Figure 6-2d) presents large v_x compared with both ambient plasma sheet and boundary layers. (4) Plasma β is typically greater than 1 in the plasma sheet and between 0.1 and 1 in the boundary layer [e.g., *Ueno et al.*, 2002]. Thus, plasma β, which is dominated by the ion β (Figure 6-2e) including the H^+ and O^+ contributions, is required to be greater than unity for the reconnection exhaust. (5) The electron VDFs are typically non-Maxwellian in the reconnection exhaust,

as analyzed in Chapter 5, while VDFs are quasi-Maxwellian in the ambient plasma sheet. Thus, a non-Maxwellian VDF is required to distinguish between the reconnection exhaust and the ambient plasma sheet.

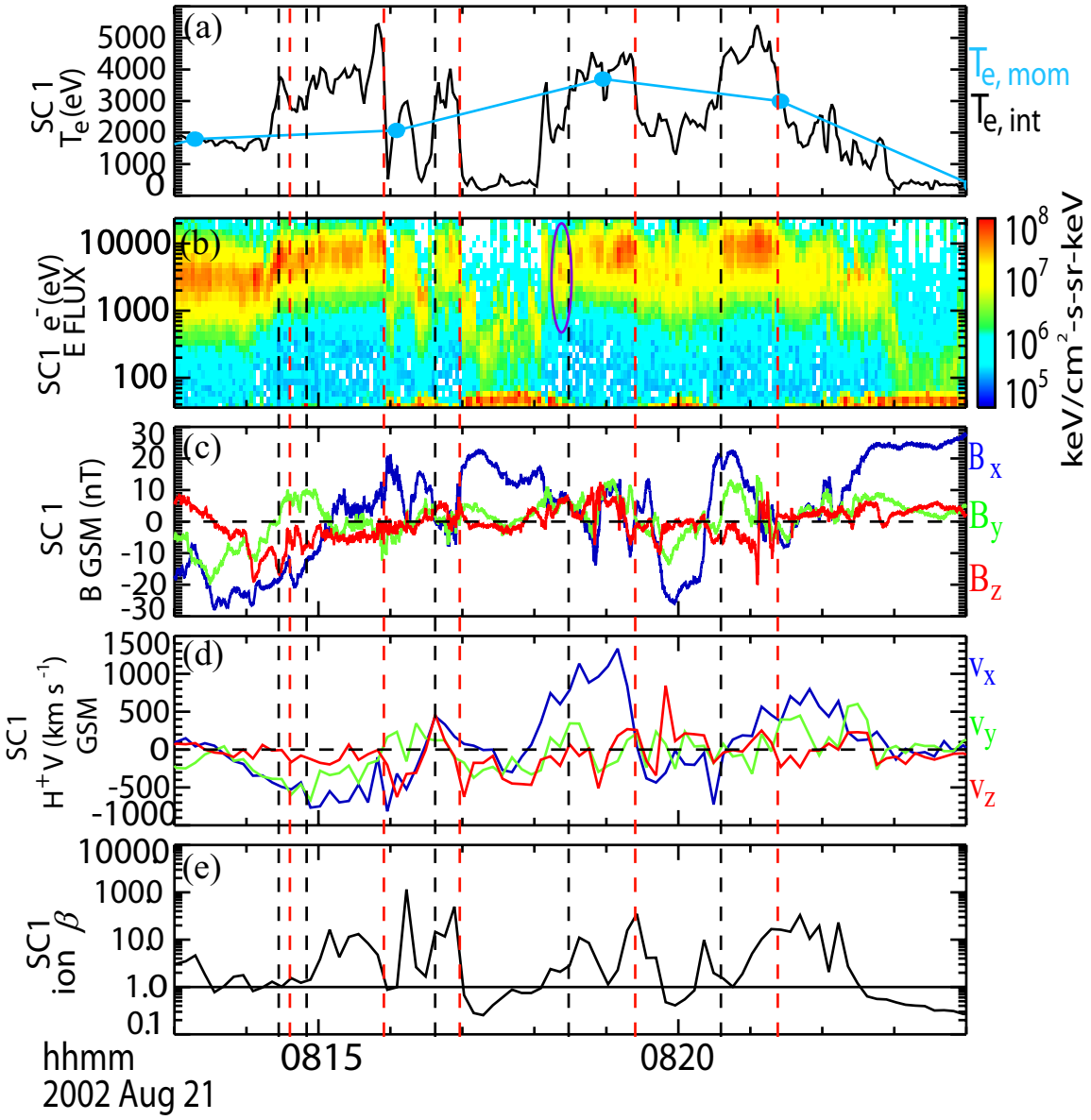

Figure 6-2: Magnetotail reconnection on 21 August, 2002 with data from C1. (a)) T_e. The black lines are calculated from the integration of the pitch-angle distribution, and the blue lines are from PEACE moments data. (b) e^- spectrogram. (c) magnetic field in GSM. (d) H^+ velocity in GSM. (e) Ion plasma β including the contribution of H^+ and O^+. Vertical lines mark the exhaust intervals to take T_e. In each interval, the starting (end) time is marked by the black (red) line. The purple oval in (d) marks a region close to the separatrix, which is not selected to evaluate the electron heating.

With the selected exhaust intervals for all four spacecraft, we use the average T_e to represent the exhaust temperature, and the standard deviation as its uncertainty. The uncertainties may come from both the spatial and temporal variations of T_e. For this event, the exhaust T_e is 3783±622 eV. Since the upstream lobe T_e is below 100 eV, which can be seen from Figure 6-2a in the boundary layer intervals, it is negligible compared with the exhaust T_e. Thus, the exhaust T_e is used as ΔT_e from inflow to exhaust regions.

Figure 6-3 shows how we determine the upstream parameters for this event with C4 measurements. The interval between two black vertical dashed lines in Figures 6-3a-6-3f (08:14-08:21 UT) is the time when other spacecraft encounter the reconnection exhaust. C4 is closer to the lobe in the same interval, as can be seen from the plasma spectrograms (Figures 6-3a-6-3c) that show reduced fluxes at higher energies and peaked fluxes at lower energies.

An inflow interval is selected to determine the inflow density n_b. For this event, it is between the red vertical lines (08:17:00-08:17:40 UT). During this interval, H^+ and O^+ energy spectrograms (Figure 6-3g-6-3h) exhibit narrow peaks around 200 eV and 2 keV, respectively. The lack of the higher energy populations indicates that the spacecraft is far from the current sheet mid-plane. In addition, the H^+ velocity (Figure 6-3i) shows a v_z around -200 km/s, which is likely to be the superposition of the inflow velocity and the magnetotail flapping motion. Such a convection velocity lifts the energies of the lobe cold ions up to their peaked values, so that they can be measured by CODIF. Therefore, this interval is identified as the inflow region, with parameters representing the upstream lobe. The average density from the spacecraft potential (Figure 6-3i, black line) of 0.60 cm^{-3}, which is close to the sum of H^+ and O^+ density of 0.58 cm^{-3} (not shown), is used as n_b. In general, the selection of the inflow interval for n_b requires (1) the lack of high-energy plasma sheet ions and electrons, and (2) the dominance of the magnetic pressure to the

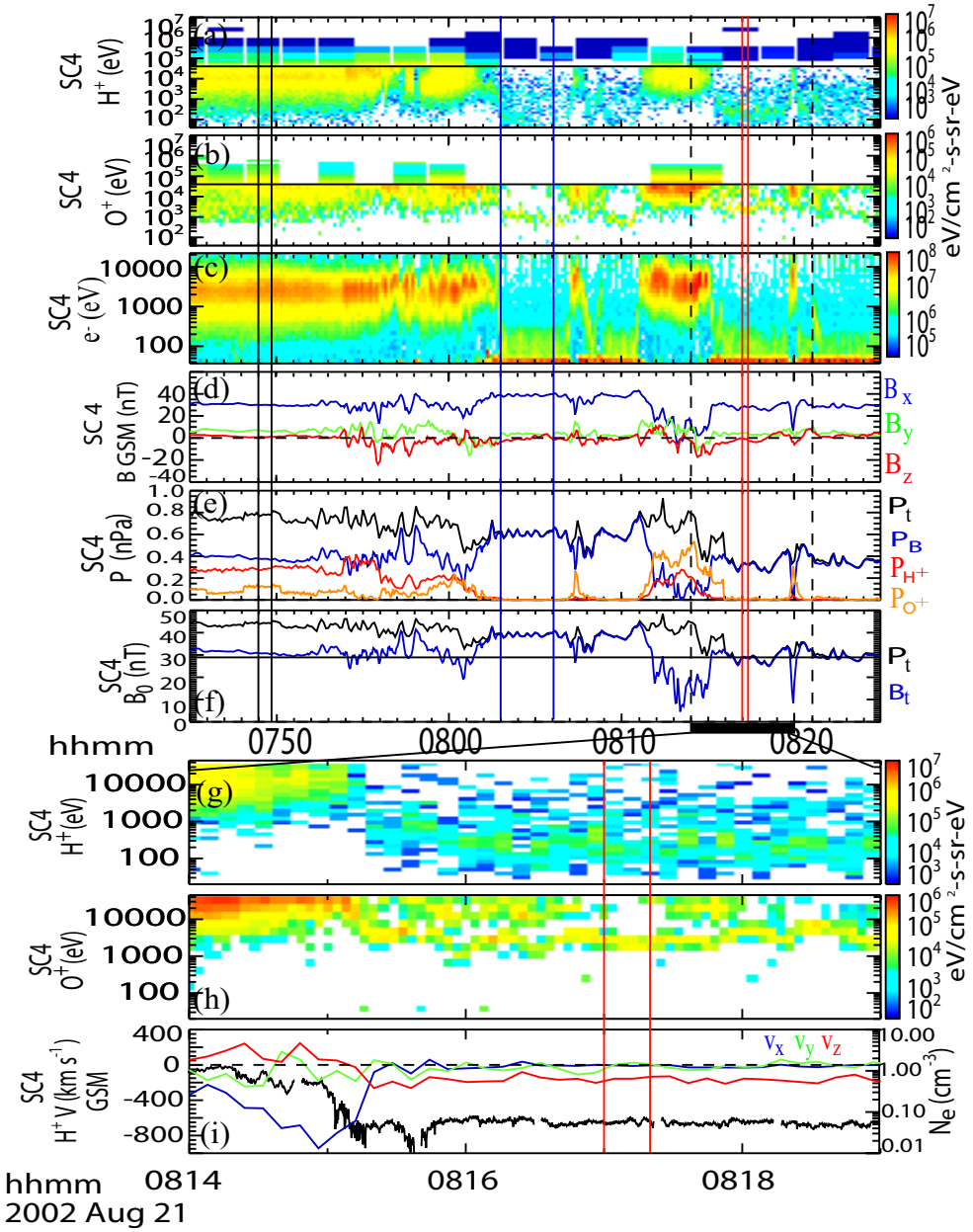

Figure 6-3: Inflow parameters of the reconnection on 21 August, 2002 from C4. (a), (b) H^+ and O^+ spectrogram combining CODIF and RAPID measurements. (c) e^- spectrogram. (d) magnetic field. (e) total pressure (P_t) (black), magnetic pressure (blue), H^+ (red), and O^+ (orange) perpendicular pressure. (f) asymptotic upstream magnetic field (B_0) derived from P_t (black) and local B_t (blue). The black horizontal line in (f) marks the average B_0 in the inflow region (within red vertical lines). Black (blue) vertical lines represent the interval with maximum asymptotic B_0 from P_t (B_t). Black dashed vertical lines mark the interval within which other spacecraft encounter the exhaust region. (g)-(i) are the zoom-in plots of H^+ and O^+ CODIF spectrograms, H^+ velocity and electron density. Red vertical lines mark the inflow interval, same with those in (a)-(f).

plasma pressure. (3) The narrow-energy band ions with a bulk v_z as shown in this event may or may not be clear.

The determination of the B_0 requires more detailed analysis, due to the temporal and spatial variations of the magnetic field. The average B_x in the above inflow interval is 29 nT (Figure 6-3d). However, a few minutes earlier, around 08:10 UT, when C4 encountered the inflow region another time, B_x is close to 40 nT. The decrease of lobe B_x from 08:10 UT to 08:17 UT is likely to be caused by the pressure release of the magnetotail during the substorm unloading phase. Therefore, the B_0 that corresponds to the reconnection exhaust features observed at 08:14-08:21 UT may change with time, with larger amplitude than in simulations.

In order to determine how B_0 varies with time when the spacecraft is in the plasma sheet or reconnection exhaust region, we apply the pressure balance assumption to derive B_0 from the total pressure [*Hoshino et al.*, 2001b; *Liu et al.*, 2013]

$$P_t = \frac{B_0^2}{2\mu_0} = \frac{B_t^2}{2\mu 0} + P_\perp \tag{6.7}$$

where B_t is the local total magnetic field, and $P_\perp$ is the perpendicular plasma pressure. The typical ion-to-electron temperature ratio (T_i/T_e) in the plasma sheet is around 7 [*Baumjohann et al.*, 1989]. Therefore, we use the ion pressure including the contribution of both H^+ and O^+ to calculate $P_\perp$.

The perpendicular particle pressure, $P_\perp$, is determined with both CODIF and RPAID instruments. The interpolated energy flux is shown at the gap energy channels (right above the horizontal lines) of the energy spectrograms in Figures 6-3a and 6-3b. The resulting P_t and the contribution from different pressure components are shown in Figure 6-3e. B_0 derived from P_t with eq. (6.7) and local measurements of B_t are shown in Figure 6-3f. It is clear that B_0 exhibits a continuous trend of decrease from 07:50 UT to 08:20 UT, especially

after 08:10 UT. The range of B_0 variations is used as its error bar. Its maximum is taken when the total pressure starts to unload (between solid black vertical lines in Figure 6-3), which is 45.4 nT. Its minimum is the minimum B_0 by the end of the reconnection exhaust encounters by all spacecraft. For this event, it is from the same time as the inflow interval (between the red vertical lines) with a value of 29.0 nT. Considering the uncertainties in the pressure balance method, we also determine the B_0 range only according to the measured B_t every time when the spacecraft crossed to the inflow/lobe region, where P_B dominates the pressure. Its maximum (between blue vertical lines) is 38.9 nT and its minimum (between red vertical lines) is 28.7 nT.

With $T_{e,exhaust}$=3783 eV, and upstream conditions in the inflow interval between red vertical lines in Figure 6-3 (n_b=0.06 cm^{-3} and B_0=29.0 nT), r_h is 5.5%. Considering the uncertainties in $T_{e,exhaust}$ and B_0, r_h ranges between 2.0% and 6.3%. Such a range includes the spatial variation of T_e, the temporal evolution of the reconnection, and the uncertainties in data analysis.

6.4.2 Statistical results

Using the same procedure for the above example event, we estimate the electron heating in the magnetotail reconnection region for 13 events. The results are shown in Figure 6-4.

In Figure 6-4a, B_0 used to calculate v_{Ai} is from P_t. The location of each point on the x axis uses the average B_0 in the inflow interval, where n_b is taken. In most cases, it is close to the minimum B_0. Except for two events marked as the green points, the other 11 events are well linearly correlated with an r_h (slope between $T_{e,exhaut}$ and $m_i v_{Ai}^2$) of 2.6%. r_h calculated in this way is close to the definition of r_{ht} in the PIC simulations (Table 6.1). The uncertainties of the points are large, especially on the x axis, indicating the large temporal variations of B_0 that changes the available energy for reconnection.

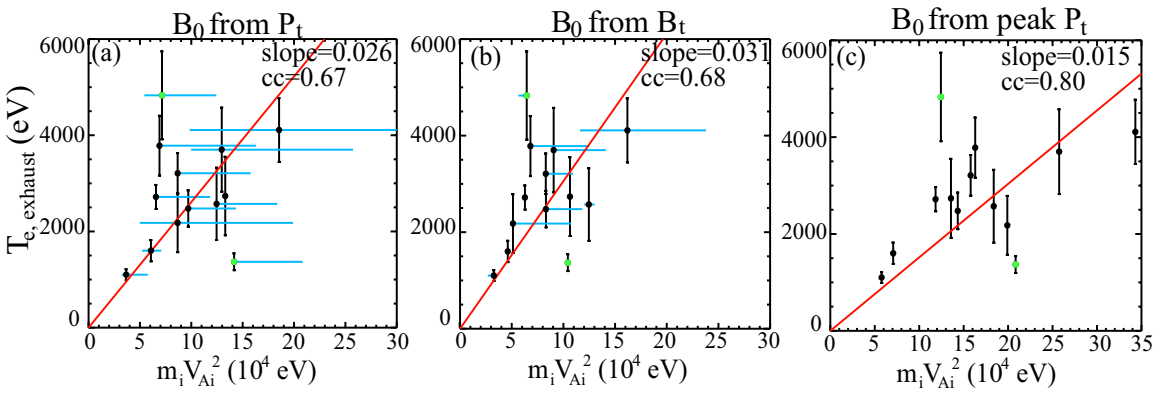

Figure 6-4: Statistical results of e^- heating in the magnetotail reconnection. $T_{e,xhaust}$ is the average T_e in the selected exhaust intervals, and their standard deviations are used as error bars. The lobe density is used for calculating v_{Ai}. In (a), v_{Ai} is calculated with B_0 derived from P_t. In (b), v_{Ai} is calculated with B_t in the intervals where the plasmas pressure is negligible. In (a) and (b), the locations on the x axis of the points correspond to upstream conditions taken in the inflow intervals close to when the spacecraft encountered the exhaust regions. In (c), v_{Ai} is calculated with the maximum B_0 when the magnetotail pressure starts to release pressure.

The statistical results with v_{Ai} calculated from B_t when the spacecraft crossed close to the lobe are shown in Figure 6-4b. It exhibits a statistical r_h of 3.1% after excluding the two extreme cases. It is close to the 2.6% found using the pressure balance calculations, showing that the results are insensitive to the specific data analysis process. The uncertainty in the x axis is much smaller than that in Figure 6-4a, since the spacecraft only stayed close to the lobe for a limited time when B_t can be taken as B_0.

Finally, we calculate r_h with v_{Ai} according to B_0 from the peak P_t (Figure 6-4c). Since reconnection occurs with varying upstream conditions, the correct upstream condition corresponding to the measured T_e in the exhaust for each event might be anywhere within the $m_i v_{Ai}^2$ uncertainty. r_h from the peak B_0 represents the heating coefficient based on the maximum initial available magnetic energy for reconnection. The r_h calculated in this way has the same definition with r_{h0} in PIC simulations (Table 6.1). It is the lower limit of r_h, which is 1.5% excluding the two extreme cases (Figure 6-4c).

The significant deviation of r_h for the two extreme events might be caused by the limita-

tion of the observation data. For these two events, the measured upstream conditions in the inflow intervals are similar, but they have very different in $T_{e,exhaust}$. As shown in Figure 6-4a, the event with largest r_h (upper left) would become closer to other points if the real upstream B_0 is at the maximum limit. This also suggests the importance of the upstream condition variations during magnetotail reconnection. In the event with the smallest r_h (lower right in Figure 6-4a), the crossing of the reconnection region was very brief. Considering the temporal and spatial variations of T_e, it is possible that the spacecraft did not encounter the time and the region with maximum electron heating for this reconnection event.

In summary, 11/13 of the magnetotail reconnection events in this study show statistically consistent electron r_h. The rate of r_{ht} is around 2.6% using the local inflow parameters, and has a lower limit of r_{h0}=1.5% normalized by the maximum B_0 when the magnetotail pressure starts to release.

6.5 Summary

In this study, we extract a simplified electron VDF model based on the real electron distributions in the EDR in the PIC simulation, to calculate the electron heating coefficient r_h. The electron temperatures calculated from the VDF model agree with those from the PIC simulation data at the same locations; in the simulation, the temperatures inside the EDR at the selected points are close to the average temperature over the whole reconnection exhaust. Therefore, the r_h calculated from the model can be used to evaluate the electron bulk heating in the whole reconnection. In fact, the r_h derived from the model agrees with that calculated from the average simulation exhaust temperature within 20% of the uncertainty. With the simplified model, r_h is related to the bulk acceleration, and the maximum speed an electron can obtain from the reconnection electric field in the EDR

during the meandering motion. It demonstrates the important role of the EDR energization in determining the electron acceleration and thermalization.

The electron bulk heating is examined using four PIC simulations with r_h around 2%-3%, and we find that r_h increases with time by a fraction of ∼30-90% in 8 ω_{ci}^{-1}. We also perform a statistical study of the electron heating in the Earth's magnetotail reconnection using Cluster observations. Using the inflow parameters during the time when the spacecraft crossed the reconnection exhaust regions, the electron r_h is 2.6%. The continuous decrease of the magnetotail pressure during reconnection is considerable. The lower limit of the electron r_h, using the maximum initial upstream parameters, is 1.5%.

Chapter 7

Summary and future work

We have investigated the motions of magnetospheric hot O^+ and cold ions in the magnetopause reconnection, the dependence of the magnetopause reconnection rate on local parameters, and the electron heating in magnetotail reconnection. Our results are summarized in this chapter. Remaining open questions related to the kinetic processes in reconnection that deserve to be studied in future will also be discussed.

7.1 The Dynamics of ions and electrons in reconnection, and the impact of their behavior

The reason to distinguish motions of different ion and electron species is that they have different characteristic Larmor radii and can be demagnetized in different scales. Thus, one question is whether particles with large Larmor radii compared to the scale of the current sheet, such as heavy ions, can still be affected by the reconnection electromagnetic fields near the current sheet mid-plane, and participate in the reconnection outflow; or they may freely move between two sides of the current sheet without being deflected by the fields near the center. Another question is whether particles with small enough Larmor radii, such as magnetospheric cold ions, are always magnetized when going through the reconnection structure.

Our studies use the observed velocity distribution functions (VDFs) at dayside magnetopause reconnection to support that all species, including heavy ions and cold ions, are affected by the reconnection fields and join the reconnection outflow. Their behavior, instead of completely depending on the species, depends on the locations where they enter the reconnection region. The conventional Hall reconnection diffusion region is two-folded with ion and electron diffusion regions. With the existence of more distinct populations in the plasma, the diffusion region becomes multi-layered: heavy ions form a larger scale of the diffusion region, and cold ions can only be demagnetized at a scale smaller than that for the hotter ions.

If the population enters its own diffusion region, particles in this population become demagnetized, perform the meandering and cyclotron motions, and get accelerated to the outflow direction. The observed magnetospheric hot O^+ VDFs with a clear velocity shift and cutoff in the outflow direction, and the non-adiabatic signatures in the VDFs of cold ions, indicate such demagnetization-pickup process. The electron VDFs in the electron diffusion region (EDR) from the particle-in-cell (PIC) simulation evolving from a semi-circle in the outflow direction to a full circle in the plane perpendicular to the reconnected magnetic field, and the test-particle trajectories, illustrate the same type of motions for electrons as well. We also find with PIC simulations that the electron temperature in the EDR is representative for the whole reconnection exhaust, which indicates the important role of the diffusion region energization in the electron bulk heating.

If the population enters the reconnection current sheet through direct crossing of the separatrix downstream of its own diffusion region, except for being demagnetized by the electric field parallel to the magnetic field mainly near the separatrix region, particles in this population roughly keep convecting with the magnetic field in a quasi-adiabatic way, and catch up with the reconnection outflow with the $\vec{E} \times \vec{B}$ drift. Such an adiabatic motion

downstream of the diffusion region is also demonstrated with the cold ion VDFs observed in the magnetopause reconnection.

One difference between the ion and electron motions is that electrons have much higher thermal velocities, so that they can rapidly bounce along the magnetic field lines in the reconnection exhaust after being re-magnetized. Every time when an electron crosses the mid-plane, it can be further accelerated from the curvature and/or gradient-B drift velocities opposite to the electric field, which is shown with test-particle results in our study.

Since all plasma populations that enter the reconnection region participate in the reconnection, the mass loading contribution from all of them should be included when calculating the reconnection rate. Our results show that the measured dayside magnetopause reconnection rate does correlate with the fluid-based Cassak-Shay prediction including all hot and cold populations in the magnetosphere and the magnetosheath inflow regions. However, the correlation is slightly better if only the mass loading from the magnetosheath population is included in the reconnection rate calculation. This suggests imperfect coupling of the different populations in the reconnection region. Although the behavior of each species can be similarly categorized into pick-up and adiabatic motions depending on whether the population enters its own diffusion region, their behaviors can be different at the same location, e.g., inside the diffusion region of one population but outside the diffusion region of another. This may cause imperfect coupling among them. In addition, the structure, such as the aspect ratio, of the diffusion region for different populations may be different. The overall reconnection structure might also be distorted by the density, temperature and the magnetic field asymmetries between two sides, and guide field strength, etc., although our results have not shown clear dependence of the aspect ratio on the O^+ abundance or other factors, with the uncertainties in the analysis.

Above all, the analysis of the single particle motions helps understand the dynamics of

ions and electrons in reconnection. The kinetic effects resulting from the imperfect coupling between the different populations, due to their different scales of the diffusion region, are indicated to exist and affect the reconnection rate.

7.2 Future work

Knowing that the kinetic process is a key to understanding reconnection, there are still related open questions to answer.

(1) The effect of O^+ on the reconnection rate. Although we do not find a clear dependence of the diffusion region aspect ratio on the O^+ abundance in the magnetopause reconnection observations, this may be because the O^+ mass density is usually negligible compared to the magnetosheath ions. Because there is no dense plasma entering the reconnection region in the magnetotail, the relative O^+ abundance is higher in the storm-time magnetotail. Therefore, the effect of O^+ on the reconnection rate may be better examined in the magnetotail reconnection observations.

(2) More detailed comparisons of the VDFs between observations and simulations. Comprehensive examinations of the ion and electron VDFs have been conducted in this thesis and previous studies, where the relationship between the VDF features and the locations in the reconnection region is built up with simulation results, and the explanations for why the highly structured VDFs are formed, are proposed. Some types of VDFs, particularly those in the exhaust downstream of the diffusion region, have been observed in the in situ measurements. However, those inside the EDR have not been reported with the observation data. With the upcoming Magnetospheric MultiScale (MMS) spacecraft data, the distributions in the electron scale are expected to be better observed, so that the plasma dynamics can be better analyzed with real space measurements.

(3) Coupling between different plasma species. We have examined the dynamics of

ions and electrons separately, and it is suggested that imperfect coupling between different plasma species may exist to alter the reconnection structure. How exactly the difference in the ion and electron motions may change the field structure and impact the dynamics of other species needs to be carried out.

(4) Coupling between different energization mechanisms. In the electron heating study, we distinguish the dominant energization mechanisms at different locations for electrons in different populations of the VDFs. The energization in the diffusion region is found to be important for the electron heating. More quantitative analysis can be investigated to figure out up to how much energy electrons can obtain from each mechanism, and how different mechanisms work together to determine the overall acceleration and thermalization. Similar studies can also be applied to ions. In addition, the effects of asymmetry, guide field, waves and turbulence on the particle energization and VDFs, which are barely included in this thesis, can be further studied.

Appendix

Derivations of the electron acceleration formulas in section 5.4.1

From eq. (5.1)

$$\frac{dU}{dt} = -e\vec{E}\cdot\vec{v}$$

and eq. (5.2)

$$\vec{v} = v_{\parallel}\hat{b} + \vec{v}_{d,E\times B} + \vec{v}_{d,curv} + \vec{v}_{d,gradB} + \Delta\vec{v}_{\perp}$$

we can get

$$\begin{aligned}\frac{dU}{dt} &= -e\vec{E}\cdot\left(v_{\parallel}\hat{b} + \vec{v}_{d,E\times B} + \vec{v}_{d,curv} + \vec{v}_{d,gradB} + \Delta\vec{v}_{\perp}\right)\\ &= -eE_{\parallel}v_{\parallel} - e\vec{E}_{\perp}\cdot(\vec{v}_{d,E\times B} + \vec{v}_{d,curv} + \vec{v}_{d,gradB} + \Delta\vec{v}_{\perp})\end{aligned} \tag{1}$$

$\vec{E}_{\perp} = \hat{b}\times\left(\vec{E}_{\perp}\times\hat{b}\right)$, so that

$$\begin{aligned}\frac{dU}{dt} &= -eE_{\parallel}v_{\parallel} - eB\frac{\hat{b}\times\left(\vec{E}_{\perp}\times\hat{b}\right)}{B}\cdot(\vec{v}_{d,E\times B} + \vec{v}_{d,curv} + \vec{v}_{d,gradB} + \Delta\vec{v}_{\perp})\\ &= eE_{\parallel}v_{\parallel} - -eB\left(\hat{b}\times\vec{v}_{d,E\times B}\right)\cdot(\vec{v}_{d,curv} + \vec{v}_{d,gradB} + \Delta\vec{v}_{\perp})\\ &= -eE_{\parallel}v_{\parallel} + eB\left(\vec{v}_{d,curv}\times\vec{v}_{d,E\times B}\right)\cdot\hat{b} + eB\left(\vec{v}_{d,gradB}\times\vec{v}_{d,E\times B}\right)\cdot\hat{b}\\ &\qquad + eB\left(\Delta\vec{v}_{\perp}\times\vec{v}_{d,E\times B}\right)\cdot\hat{b}\end{aligned} \tag{2}$$

which is eq. (5.3).

From eq. (5.8)

$$\frac{dU_{\parallel}}{dt} = v_{\parallel}m\left(\hat{b}\cdot\frac{d\vec{v}}{dt} + \vec{v}\cdot\frac{d\hat{b}}{dt}\right)$$

and eq. (5.9)

$$m\vec{v}\cdot\frac{d\hat{b}}{dt} = m\vec{v}\cdot\left(\vec{v}_{\parallel}\cdot\nabla\hat{b} + \vec{v}_{\perp}\cdot\nabla\hat{b}\right)$$

we can get

$$\frac{dU_{\parallel}}{dt} = mv_{\parallel}\left[\hat{b}\cdot\frac{d\vec{v}}{dt} + \vec{v}\cdot\left(v_{\parallel}\hat{b}\cdot\nabla\hat{b} + \vec{v}_{\perp}\cdot\nabla\hat{b}\right)\right] \tag{3}$$

$m\hat{b}\cdot\frac{d\vec{v}}{dt}=-e\hat{b}\cdot\left(\vec{E}+\vec{v}\times\vec{B}\right)=-eE_{\parallel}$, so that

$$\begin{aligned}\frac{dU_{\parallel}}{dt}&=-eE_{\parallel}v_{\parallel}+m|v_{\parallel}|^2\vec{v}.\left(\hat{b}\cdot\nabla\hat{b}\right)+mv_{\parallel}\vec{v}\cdot\left(\vec{v}_{\perp}\cdot\nabla\hat{b}\right)\\&=-eE_{\parallel}v_{\parallel}+m|v_{\parallel}|^2\left(v_{\parallel}\hat{b}+\vec{v}_{d,E\times B}+\vec{v}_{d,curv}+\vec{v}_{d,gradB}+\Delta\vec{v}_{\perp}\right)\cdot\left(\hat{b}\cdot\nabla\hat{b}\right)\\&\qquad+mv_{\parallel}\vec{v}\cdot\left(\vec{v}_{\perp}\cdot\nabla\hat{b}\right)\end{aligned}\tag{4}$$

where the second term on the right-hand side is $F_{curv}\left(\vec{v}\cdot\hat{b}\right)$, and its sign depends on the dot product between the velocity and the magnetic field curvature.

With $\hat{b}\cdot\nabla\hat{b}=\hat{b}\times\left[(\hat{b}\cdot\nabla\hat{b})\times\hat{b}\right]$, the second term on the right-hand side of eq. (4) becomes

$$\begin{aligned}\frac{dW_{curv,\parallel}}{dt}&=F_{curv}\left(\vec{v}\cdot\hat{b}\right)\\&=\left\{\hat{b}\times\left[m|v_{\parallel}|^2(\hat{b}\cdot\nabla\hat{b})\times\hat{b}\right]\right\}\cdot\left(v_{\parallel}\hat{b}+\vec{v}_{d,E\times B}+\vec{v}_{d,curv}+\vec{v}_{d,gradB}+\Delta\vec{v}_{\perp}\right)\\&=eB\left(\hat{b}\times\vec{v}_{d,curv}\right)\cdot\left(v_{\parallel}\hat{b}+\vec{v}_{d,E\times B}+\vec{v}_{d,curv}+\vec{v}_{d,gradB}+\Delta\vec{v}_{\perp}\right)\\&=eB\left(\vec{v}_{d,curv}\times\vec{v}_{d,E\times B}\right)\cdot\hat{b}-eB\left(\vec{v}_{d,gradB}\times\vec{v}_{d,curv}\right)-eB\left(\Delta\vec{v}_{\perp}\times\vec{v}_{d,curv}\right)\end{aligned}\tag{5}$$

which is eq. (5.11)

The last term in eq. (4) is $F_{mirror}\left(\vec{v}\cdot\hat{b}\right)$. Assume that the magnetic field is mainly in the z direction in an arbitrary xyz coordinate system, and it has variations along all directions.$\nabla\hat{b}=\nabla\left(\frac{1}{B}\vec{B}\right)=-\frac{1}{B^2}\nabla B\vec{B}+\frac{1}{B}\nabla\vec{B}$, and hence

$$\begin{aligned}\vec{v}\cdot\left(\vec{v}_{\perp}\cdot\nabla\hat{b}\right)&=\vec{v}\cdot\left[-\frac{1}{B^2}\left(\vec{v}_{\perp}\cdot\nabla B\right)\vec{B}+\frac{1}{B}\vec{v}_{\perp}\cdot\nabla\vec{B}\right]\\&=-\frac{v_{\parallel}}{B}\left(\vec{v}_{\perp}\cdot\nabla B\right)+\frac{1}{B}\vec{v}_{\parallel}\cdot\left(\vec{v}_{\perp}\cdot\nabla\right)\vec{B}+\frac{1}{B}\vec{v}_{\perp}\cdot\left(\vec{v}_{\perp}\cdot\nabla\right)\vec{B}\end{aligned}\tag{6}$$

Since $\nabla B=\frac{\partial}{\partial x_j}B=\frac{B_i}{B}\frac{\partial}{\partial x_j}B_i=b_i\frac{\partial}{\partial x_j}B_i$ (sum over all i=x, y, z components), we have

$$v_{\parallel}\left(\vec{v}_{\perp}\cdot\nabla B\right)=v_{\parallel}\left(v_{\perp j}b_i\frac{\partial}{\partial x_j}B_i\right)=v_{\parallel}b_i\left(v_{\perp j}\frac{\partial}{\partial x_j}\right)B_i=\vec{v}_{\parallel}\cdot\left(\vec{v}_{\perp}\cdot\nabla\right)\vec{B}$$

Therefore, the first two terms in eq. (6) are cancelled, and we get eq. (5.12):

$$\frac{dW_{mirror,\parallel}}{dt}=F_{mirror}\left(\vec{v}\cdot\hat{b}\right)=\frac{mv_{\parallel}}{B}\vec{v}_{\perp}\cdot\left(\vec{v}_{\perp}\cdot\nabla\right)\vec{B}\tag{7}$$

For a magnetized electron, $\vec{v}_{\perp}=\vec{v}_d+\Delta\vec{v}_{\perp}$, where $\vec{v}_d$ is the sum of all drift velocities, and $\Delta\vec{v}_{\perp}$ is the gyro-velocity with a constant amplitude. Here we show how eq. (7) is related to the regular form of the mirror force in the limit that the drift velocity is much smaller than the gyro-velocity, e.g., $\vec{v}_{\perp}\sim\Delta\vec{v}_{\perp}$.

$$\vec{v}_{\perp}\cdot\left(\vec{v}_{\perp}\cdot\nabla\right)\vec{B}=v_xv_x\frac{\partial B_x}{\partial x}+v_yv_y\frac{\partial B_y}{\partial y}+v_xv_y\left(\frac{\partial B_x}{\partial y}+\frac{\partial B_y}{\partial x}\right)\tag{8}$$

Averaging over a gyro-period, $< v_x v_x >= 1/2|v_\perp|^2$, $< v_y v_y >= 1/2|v_\perp|^2$, and $< v_x v_y >= 0$. Assuming that $\partial B_i/\partial x_j$ (i, j=x, y) is constant within a gyro-period, and applying $\nabla \cdot \vec{B} = \frac{\partial B_x}{\partial x} + \frac{\partial B_y}{\partial y} + \frac{\partial B_z}{\partial z} = 0$, eq. (8) becomes

$$\vec{v}_\perp \cdot (\vec{v}_\perp \cdot \nabla)\, \vec{B} = -v_\perp^2 \frac{\partial B_z}{\partial z}$$

Using $\partial B_z/\partial z \sim dB/dz$, eq. (7) becomes

$$\frac{dW_{mirror,\parallel}}{dt} = F_{mirror}\left(\vec{v} \cdot \hat{b}\right) = -\frac{m v_\parallel v_\perp^2}{B} \nabla_\parallel B = -v_\parallel \mu \nabla_\parallel B \tag{9}$$

which is related to the regular form of the mirror force.

Bibliography

André, M., and C. M. Cully (2012), Low-energy ions: A previously hidden solar system particle population, *Geophys. Res. Lett.*, *39*(L03101), doi:10.1029/ 2011GL050242.

Argall, M., L.-J. Chen, R. B. Torbert, W. Daughton, J. S. Yoo, and M. Yamada (2014), Inferring proximity to the reconnection site via structural changes to the magnetopause caused by asymmetric reconnection, in *AGU fall meeting*, AGU, San Francisco, CA, USA.

Asano, Y., R. Nakamura, I. Shinohara, M. Fujimoto, T. Takada, W. Baumjohann, C. J. Owen, A. N. Fazakerley, A. Runov, T. Nagai, and E. A. L. andH. Rème (2008), Electron flat-top distributions around the magnetic reconnection region, *J. Geophys. Res.*, *113*(A01207), doi:10.1029/2007JA012461.

Axford, W. I. (1984), Magnetic reconnection, in *Magnetic reconnection in space and laboratory plasmas, Geophys. Monogr. Ser.*, vol. 30, edited by J. E. W. Hones, p. 1, AGU, Washington, D.C.

Balogh, A., C. M. Carr, M. H. Acuna, M. W. Dunlop, T. J. Beek, P. Brown, K. H. Fornacon, E. Georgescu, K. H. Glassmeier, J. Harris, G. Musmann, T. Oddy, and K. Schwingenschuh (2001), The cluster magnetic field investigation: overview of in-flight performance and initial results, *Ann. Geophys.*, *19*, 1207–1217.

Baumjohann, W., G. Paschmann, and C. A. Cattell (1989), Average plasma properties in the central plasma sheet, *J. Geophys. Res.*, *94*(A6), 6597–6606, doi: 10.1029/JA094iA06p06597.

Belle-Hamer, A. L. L., A. Otto, and L. C. Lee (1995), Magnetic reconnection in the presence of sheared flow and density asymmetry: Applications to the earth's magnetopause, *J. Geophys. Res.*, *100*(A7), 11,875–11,889.

Bessho, N., L.-J. Chen, J. R. Shuster, and S. Wang (2014), Electron distribution functions in the electron diffusion region of magnetic reconnection: Physics behind the fine structures, *Geophys. Res. Lett.*, *41*(24), 8688–8695, doi:10.1002/2014GL062034.

Birdsall, C. K., and A. B. Langdon (1991), Chapter 15: Electromagnetic programs in two and three dimensions, in *Plasma physics via computer simulation*, pp. 383–388, Adam Hilger, Bristol, Philadelphia and New York.

Birn, J., and E. Priest (2007), *Reconnection of magnetic fields*, Cambridge University Press, Cambridge.

Birn, J., J. F. Drake, M. A. Shay, B. N. Rogers, R. E. Denton, M. Hesse, M. Kuznetsova, Z. W. Ma, A. Bhattacharjee, A. Otto, and P. L. Pritchett (2001), Geospace environmental modeling (gem) magnetic reconnection challenge, *J. Geophys. Res.*, *106*(A3), 3715–3719, doi:10.1029/1999JA900449.

Birn, J., J. E. Borovsky, M. Hesse, and K. Schindler (2010), Scaling of asymmetric reconnection in compressible plasmas, *Phys. Plasmas*, *17*(052108), doi:10.1063/1.3429676.

Biskamp, D. (1986), Magnetic reconnection via current sheets, *Phys. Fluids*, *29*(1520), doi: 10.1063/1.865670.

Boris, V. S. (2006), Chapter 5: Motion of a charged particle in given fields, in *Plasma astrophysics part I: fundamentals and practice*, pp. 79–91, Springer, New York.

Borovsky, J. E., and J. Birn (2014), The solar wind electric field does not control the dayside reconnection rate, *J. Geophys. Res.*, *119*, 751–760, doi:10.1002/2013JA019193.

Borovsky, J. E., and M. Hesse (2007), The reconnection of magnetic fields between plasmas with different densities: scaling relations, *Phys. Plasmas*, *14*(102309), doi: 10.1063/1.2772619.

Borovsky, J. E., M. Hesse, J. Birn, and M. M. Kuznetsova (2008), What determines the reconnection rate at the dayside magnetosphere?, *J. Geophys. Res.*, *113*(A07210), doi: 10.1029/2007JA012645.

Borovsky, J. E., M. H. Denton, R. E. Denton, V. K. Jordanova, and J. Krall (2013), Estimating the effects of ionospheric plasma on solar wind/magnetosphere coupling via mass loading of dayside reconnection: Ion-plasma-sheet oxygen, plasmaspheric drainage plumes, and the plasma cloak, *J. Geophys. Res.*, *118*, 5695–5719, doi:10.1002/jgra.50527.

Bouhram, M., B. Klecker, G. Paschmann, S. Haaland, H. Hasegawa, A. Blagau, H. Réme, J.-A. Sauvaud, L. M. Kistler, and A. Balogh (2005), Survey of energetic o+ ions near the dayside mid-latitude magnetopause with cluster, *Ann. Geophys.*, *23*, 1281–1294, doi: 10.5194/angeo-23-1281-2005.

Bowers, K. J., B. J. Albright, L. Yin, B. Bergen, and T. J. T. Kwan (2008), Ultrahigh performance three-dimensional electromagnetic relativistic kinetic plasma simulation, *Phys. Plasmas*, *15*(055703), doi:10.1063/1.2840133.

Cassak, P. A., and A. Otto (2011), Scaling of the magnetic reconnection rate with symmetric shear flow, *Phys. Plasmas*, *18*(074501), doi:10.1063/1.3609771.

Cassak, P. A., and M. A. Shay (2007), Scaling of asymmetric magnetic reconnection: General theory and collisional simulations, *Phys. Plasmas*, *14*(102), 114.

Cassak, P. A., and M. A. Shay (2008), Scaling of asymmetric hall magnetic reconnection, *Geophys. Res. Lett.*, *35*(L19102), doi:10.1029/2008GL035268.

Cassak, P. A., M. A. Shay, and J. F. Drake (2005), Catastrophe model for fast magnetic reconnection onset, *Phys. Rev. Lett.*, *95*(235002), doi:10.1103/PhysRevLett.95.235002.

Christon, S. P., D. J. Williams, D. G. Mitchell, L. A. Frank, and C. Y. Huang (1989), Spectral characteristics of plasma sheet ion and electron populations during undisturbed geomagnetic conditions, *J. Geophys. Res.*, *94*(A10), 13,409–13,424, doi: 10.1029/JA094iA10p13409.

Cowley, S. W. H. (1982), The causes of convection in the earth's magnetosphere: a review of developments during the ims, *Rev. Geophys.*, *20*(3), 531–565, doi: 10.1029/RG020i003p00531.

Dahlin, J. T., J. F. Drake, and M. Swisdak (2014), The mechanisms of electron heating and acceleration during magnetic reconnection, *Phys. Plasmas*, *21*(092304), doi: 10.1063/1.4894484.

Daughton, W., J. Scudder, and H. Karimabadi (2006), Fully kinetic simulations of undriven magnetic reconnection with open boundary conditions, *Phys. Plasmas*, *13*(072101), doi: 10.1063/1.2218817.

Décréau, P. M. E., P. Fergeau, V. Krannosels'kikh, M. Lévéque, P. Martin, O. Randriamboarison, F. X. Sené, J. G. Trotignon, P. Canu, and P. B. Mögensen (1997), Whisper, a resonance sounder and wave analyser : performances and perspectives for the cluster mission, *Space Sci. Rev.*, *79*, 157–193.

deHoffmann, F., and E. Teller (1950), Magneto-hydrodynamic shocks, *Phys. Rev.*, *80*, 692.

Drake, J. F., M. Swisdak, C. Cattell, M. A. Shay, B. N. Rogers, and A. Zeiler (2003), Formation of electron holes and particle energization during magnetic reconnection, *Science*, *299*.

Drake, J. F., M. Swisdak, H. Che, and M. A. Shay (2006), Electron acceleration from contracting magnetic islands during reconnection, *Nature*, *443*, doi:10.1038/nature05116.

Drake, J. F., M. A. Shay, and M. Swisdak (2008), The hall fields and fast magnetic reconnection, *Phys. Plasmas*, *15*(042306), doi:10.1063/1.2901194.

Drake, J. F., P. A. Cassaka, M. A. Shay, M. Swisdak, and E. Quataert (2009a), A magnetic reconnection mechanism for ion acceleration and abundance enhancements in impulsive flares, *Astrophys. J.*, *700*, 16–20, doi:10.1088/0004-637X.

Drake, J. F., M. Swisdak, T. D. Phan, P. A. Cassak, M. A. Shay, S. T. Lepri, R. P. Lin, E. Quataert, and T. H. Zurbuchen (2009b), Ion heating resulting from pickup in magnetic reconnection exhausts, *J. Geophys. Res.*, *114*(A5), doi:10.1029/2008JA013701.

Dungey, J. W. (1961), Interplanetary magnetic field and the auroral zones, *Phys. Rev. Lett.*, *6*(2), 47–48.

Dungey, J. W. (1963), The structure of the exosphere or adventures in velocity, in *Geophysics, The Earth's Environment*, edited by C. DeWitt, J. Hieblot, and L. LeBeau, pp. 503–550, Gordon and Breach, New York.

Dunlop, M. W., Q.-H. Zhang, C.-J. Xiao, J.-S. He, Z. Pu, R. C. Fear, C. Shen, and C. P. Escoubet (2009), Reconnection at high latitudes: Antiparallel merging, *Phys. Rev. Lett.*, *102*(075005), doi:10.1103/PhysRevLett.102.075005.

Eastman, T. E., and L. A. Frank (1982), Observations of high-speed plasma flow near the earth's magnetopause: Evidence for reconnection?, *J. Geophys. Res.*, *87*(A4), 2187–2201, doi:10.1029/JA087iA04p02187.

Egedal, J., A. Le, N. Katz, L.-J. Chen, B. Lefebvre, W. Daughton, and A. Fazakerley (2010), Cluster observations of bidirectional beams caused by electron trapping during antiparallel reconnection, *J. Geophys. Res.*, *115*(A03214), doi:10.1029/2009JA014650.

Egedal, J., W. Daughton, and A. Le (2012), Large-scale electron acceleration by parallel elecric fields during magnetic reconnection, *Nature Physics*, *8*, 321–324, doi:10.1038/nphys2249.

Escoubet, C. P., M. Fehringer, and M. Goldstein (2001), The cluster mission, *Ann. Geophys.*, *19*, 1197–1200, doi:10.5194/angeo-19-1197-2001.

Escoubet, C. P., M. G. G. T. Taylor, A. Masson, H. Laakso, J. Volpp, M. Hapgood, and M. L. Goldstein (2013), Dynamical processes in space: Cluster results, *Ann. Geophys.*, *31*, 1045–1059, doi:10.5194/angeo-31-1045-2013.

Fazakerley, A. N. (2014), User guideto the peace measurements in hte cluster active archive (caa), *CAA-EST-UG-PEA*.

Fisher, R. A. (1921), On the 'probable error' of a coefficient of correlation deduced from a small sample, *Metron*, *1*, 3–32.

Fuselier, S. A., H. U. Frey, K. J. Trattner, S. B. Mende, and J. L. Burch (2002), Cusp aurora dependence on interplanetary magnetic field bz, *J. Geophys. Res.*, *107*(A7), doi:10.1029/2001JA900165.

Fuselier, S. A., K. J. Trattner, S. M. Petrinec, C. J. Owen, and H. Rème (2005), Computing the reconnection rate at the earth's magnetopause using two spacecraft observations, *J. Geophys. Res.*, *110*(A06212), doi:10.1029/2004JA010805.

Fuselier, S. A., K. J. Trattner, and S. M. Petrinec (2011), Antiparallel and component reconnection at the dayside magnetopause, *J. Geophys. Res.*, *116*(A10227), doi:10.1029/2011JA016888.

Genestreti, K. (2012), *The role and dynamics of oxygen of ionospheric origin in magnetopause reconnection*, B.S. thesis, University of New Hampshire, Durham, New Hampshire.

Germaschewski, K., W. Fox, N. Ahmadi, L. Wang, S. Abbott, H. Ruhl, and A. Bhattacharjee (2013), The plasma simulation code: A modern particle-in-cell code with load-balancing and gpu support, *J. Comput. Phys.*, doi:arXiv:1310.7866.

Giovanelli, R. G. (1946), A theory of chromospheric flares, *Nature*, *158*, 81–82.

Guo, R.-L., L.-J. Chen, Z.-Y. Pu, S. Wang, J. R. Shuster, G.-L. Li, N. Bessho, R. B. Torbert, S.-Y. Fu, and W. Daughton (2014), Electron distribution functions in the separatrix layer inside the diffusion region, in *AGU fall meeting*, AGU, San Francisco, CA, USA.

Gustafsson, G., R. Boström, B. Holback, G. Holmgren, A. Lundgren, K. Stasiewicz, L. Åhlén, F. S. Mozer, D. Pankow, P. Harvey, P. Berg, R. Ulrich, A. Pedersen, R. Schmidt, A. Butler, A. W. C. Fransen, D. Klinge, M. Thomsen, C.-G. Fälthammar, P.-A. Lindqvist, S. Christenson, J. Holtet, B. Lybekk, T. A. Sten, P. Tanskanen, K. Lappalainen, and J. Wygant (1997), The electric field and wave experiment for the cluster mission, *Space Sci. Rev.*, *79*, 137–156.

Hesse, M., and K. Schindler (1988), A theoretical foundation of general magnetic reconnection, *J. Geophys. Res.*, *93*(A6), 5559–5567, doi:10.1029/JA093iA06p05559.

Hesse, M., N. Aunai, S. Zenitani, M. Kuznetsova, and J. Birn (2013), Aspects of collisionless magnetic reconnection in asymmetric systems, *Phys. Plasmas*, *20*(061210), doi: 10.1063/1.4811467.

Hoshino, M., K. Hiraide, and T. Mukai (2001a), Strong electron heating and non-maxwellian behavior in magnetic reconnection, *Earth Planets Space*, *53*, 627–634.

Hoshino, M., T. Mukai, T. Terasawa, and I. Shinohara (2001b), Suprathermal electron acceleration in magnetic reconnection, *J. Geophys. Res.*, *106*(A11), 25,979–25,997, doi: 10.1029/2001JA900052.

Hughes, W. J. (1995), Chapter 9: The magnetopause, magnetotail, and magnetic reconnection, in *Introduction to space physics*, edited by M. G. Kivelson and C. T. Russell, pp. 246–247, Cambridge University Press, New York, NY, USA.

Johnstone, A. D., C. Alsop, S. Burge, P. J. Carter, A. J. Coates, A. J. Coker, A. N. Fazakerley, M. Grande, R. A. Gowen, C. Gurgiolo, B. K. Hancock, B. Narheim, A. Preece, P. H. Sheather, J. D. Winningham, and R. D. Woodliffe (1997), Peace: A plasma electron and current experiment, *Space Sci. Rev.*, *79*(1-2), 351–398, doi:10.1023/A:1004938001388.

Karimabadi, H., V. Roytershteyn, C. G. Mouikis, L. M. Kistler, and W. Daughton (2011), Flushing effect in reconnection: Effects of minority species of oxygen ions, *Planetary and Space Science*, *59*(7), doi:10.1016/j.pss.2010.07.014.

Kasahara, S., H. Hasegawa, K. Keika, Y. Miyashita, M. N. Nishino, T. Sotirelis, Y. Saito, and T. Mukai (2008), Escape of high-energy oxygen ions through magnetopause reconnection under northward imf, *Ann. Geophys.*, *26*, 3955–3966.

Khrabrov, A. V., and B. U. Ö. Sonnerup (1998), Orientation and motion of current layers: Minimization of the faradary residue, *Geophys. Res. Lett.*, *25*(13), 2373, doi: 10.1029/98GL51784.

Komar, C. M., R. L. Fermo, and P. A. Cassak (2015), Comparative analysis of dayside magnetic reconnection models in global magnetosphere simulations, *J. Geophys. Res.*, *120*, 276–294, doi:10.1002/2014JA020587.

Kronberg, E. A., and P. W. Daly (2015), Calibration report of the rapid measurements in the cluster science archive (csa), *CAA-EST-CR-RAP*.

Le, A., J. Egedal, W. Daughton, W. Fox, and N. Katz (2009), Equations of state for collisionless guide-field reconnection, *Phys. Rev. Lett.*, *102*(085001), doi: 10.1103/PhysRevLett.102.085001.

Lee, S. H., H. Zhang, Q.-G. Zong, A. Otto, D. G. Sibeck, Y. Wang, K.-H. Glassmeier, P. W. Daly, and H. Rème (2014), Plasma and energetic particle behaviors during asymmetric magnetic reconnection at the magnetopause, *J. Geophys. Res.*, *119*, 1658–1672, doi:10.1002/2013JA019168.

Lindstedt, T., V. Khotyaintsev, A. Vaivads, M. André, R. C. Fear, B. Lavraud, S. Haaland, and C. J. Owen (2009), Separatrix regions of magnetic reconnection at the magnetopause, *Ann. Geophys.*, *27*, 4039–4056, doi:10.5194/angeo-27-4039-2009.

Liu, Y., L. M. Kistler, C. G. Mouikis, B. Klecker, and I. Dandouras (2013), Heavy ion effects on substorm loading and unloading in the earth's magnetotail, *J. Geophys. Res.*, *118*, 2101–2112, doi:10.1002/jgra.50240.

Liu, Y. H., C. G. Mouikis, L. M. Kistler, S. Wang, V. Roytershteyn, and H. Karimabadi (2015), The heavy ion diffusion region in magnetic reconnection in the earth's magnetotail, *J. Geophys. Res.*, doi:10.1002/2015JA020982.

Longcope, D. W., D. Mckenzie, J. Cirtain, and J. Scott (2005), Observations of separator reconnection to an emerging active region, *Astrophys. J.*, *630*, 596–614.

Lybekk, B., A. Pedersen, S. Haaland, K. Svenes, A. N. Fazakerley, A. Masson, M. G. G. T. Taylor, and J.-G. Trotignon (2012), Solar cycle variations of the cluster spacecraft potential and its use for electron density estimations, *J. Geophys. Res.*, *117*(A01217), doi:10.1029/2011JA016969.

Malakit, K., M. A. Shay, P. A. Cassak, and C. Bard (2010), Scaling of asymmetric magnetic reconnection: Kinetic particle-in-cell simulations, *J. Geophys. Res.*, *115*(A10223), doi: 10.1029/2010JA015452.

Malakit, K., M. A. Shay, P. A. Cassak, and D. Ruffolo (2013), New electric field in asymmetric magnetic reconnection, *Phys. Rev. Lett.*, *111*(135001), doi: 10.1103/PhysRevLett.111.135001.

Mandt, M. E., R. E. Denton, and J. F. Drake (1994), Transition to whistler mediated magnetic reconnection, *Geophys. Res. Lett.*, *21*(1), 73–76, doi:10.1029/93GL03382.

Marcucci, M. F., M. B. B. Cattaneo, E. A. G. Pallocchia and, R. Bruno, A. M. D. Lellis, V. Formisano, H. Rème, J. M. Bosqued, I. Dandouras, J.-A. Sauvaud, L. M. Kistler, E. Moebius, B. Klecker, C. W. Carlson, G. K. Parks, M. McCarthy, A. Korth, R. Lundin, and A. Balogh (2004), Energetic magnetospheric oxygen in the magnetosheath and its response to imf orientation: Cluster observations, *J. Geophys. Res.*, *109*(A07203), doi: 10.1029/2003JA010312.

Möbius, E., L. M. Kistler, M. A. Popecki, K. N. Crocker, M. Granoff, Y. Jiang, E. Sartori, V. Ye, H. Rème, J. A. Sauvaud, A. Cros, C. Aoustin, T. Camus, J.-L. Médale, J. Rouzaud, C. W. Carlson, J. P. Mcfadden, D. Curtis, H. Heetderks, J. Croyle, C. Ingraham, B. Klecker, D. Hovestadt, M. Ertl, F. Eberl, H. Kästle, E. Künneth, P. Laeverenz, E. Seidenschwang4, E. G. Shelley, D. M. Klumpar, E. Hertzberg, G. K. Parks, M. McCarthy, A. Korth, H. Rosenbauer, B. Gräve, L. Eliasson, S. Olsen, H. Balsiger, U. Schwab, and M. Steinacher (1998), The 3-d plasma distribution function analyzers with time-of-flight mass discrimination for cluster, fast and equator-s, in *Measurement Techniques in Space Plasmas: Particles*, edited by R. F. Pfaff, J. E. Borovsky, and D. T. Young, AGU, Washington D. C., doi:10.1029/GM102p0243.

Morse, R. L., and C. W. Nielson (1971), Numerical simulation of the weibel instability in one and two dimensions, *Phys. Fluids*, *14*(830), doi:http://dx.doi.org/10.1063/1.1693518.

Mouikis, C. G., L. M. Kistler, Y. H. Liu, B. Klecker, A. Korth, and I. Dandouras (2010), h^+ and o^+ content of the plasma sheet at 15-19 re as a function of geomagnetic and solar activity, *J. Geophys. Res.*, *115*(A00J16), doi:10.1029/2010JA015978.

Mozer, F. S., and A. Retinò (2007), Quantitative estimates of magnetic field reconnection properties from electric and magnetic field measurements, *J. Geophys. Res.*, *112*(A10206), doi:10.1029/2007JA012406.

Mozer, F. S., S. D. Bale, and T. D. Phan (2002), Evidence of diffusion regions at a subsolar magnetopause crossing, *Phys. Rev. Lett.*, *89*(1), doi:10.1103/PhysRevLett.89.015002.

Nagai, T., M. Fujimoto, Y. Saito, S. Machida, T. Terasawa, R. Nakamura, T. Yamamoto, T. Mukai, A. Nishida, and S. Kokubun (1998), Structure and dynamics of magnetic reconnection for substorm onsets with geotail observations, *J. Geophys. Res.*, *103*(A3), 4419–4440.

Nagai, T., I. Shinohara, M. Fujimoto, M. Hoshino, Y. Saito, S. Machida, and T. Mukai (2001), Geotail observations of the hall current system: Evidence of magnetic reconnection in the magnetotail, *2001*, *106*(A11), 25,929–25,949, doi:10.1029/2001JA900038.

Nagai, T., S. Zenitani, I. Shinohara, R. Nakamura, M. Fujimoto, Y. Saito, and T. Mukai (2013), Ion and electron dynamics in the ion-electron decoupling region of magnetic reconnection with geotail observations, *2013*, *118*, 7703–7713, doi:10.1002/2013JA019135.

Ng, J., J. Egedal, A. Le, and W. Daughton (2012), Phase space structure of the electron diffusion region in reconnection with weak guide fields, *Phys. Plasmas*, *19*(112108), doi:10.1063/1.4766895.

Ouellette, J. E., J. G. Lyon, and B. N. Rogers (2014), A study of asymmetric reconnection scaling in the lyon-fedder-mobarry code, *J. Geophys. Res.*, *119*, 1673–1682, doi:10.1002/2013JA019366.

Parker, E. N. (1957), Sweet's mechanism for merging magnetic fields in conducting fluids, *J. Geophys. Res.*, *62*(4), 509–520.

Paschmann, G., B. U. Ö. Sonnerup, I. Papamastorakis, N. Sckopke, G. Haerendel, S. J. Bame, J. R.Asbridge, J. T. Gosling, C. T. Russell, and R. C. Elphic (1979), Plasma acceleration at the earth's magnetopause: evidence for reconnection, *Nature*, *282*(5736).

Pedersen, A., B. Lybekk, M. André, A. Eriksson, A. Masson, F. S. Mozer, P.-A. Lindqvist, P. M. E. Décréau, I. Dandouras, J.-A. Sauvaud, A. Fazakerley, M. Taylor, G. Paschmann, K. R. Svenes, K. Torkar, and E. Whipple (2008), Electron density estimations derived from spacecraft potential measurements on cluster in tenuous plasma regions, *J. Geophys. Res.*, *113*(A07S33), doi:10.1029/2007JA012636.

Petschek, H. E. (1964), Magnetic field annihilation, in *AAS/NASA Symposium on the physics of solar flares*, edited by W. N. Hess, pp. 425–439, Government Priting Office, Washington, D.C.

Phan, T., H. U. Frey, S. Frey, L. Peticolas, S. Fuselier, C. Carlson, H. Rème, J.-A. Sauvaud, S. Mende, J. McFadden, G. Parks, E. Moebius, B. Klecker, G. Paschmann, M. Fujimoto, S. Petrinec, M. F. Marcucci, A. Korth, and R. Lundin (2003), Simultaneous cluster and image observations of cusp reconnection and auroral proton spot for northward imf, *Geophys. Res. Lett.*, *30*(10), doi:10.1029/2003GL016885.

Phan, T. D., B. U. Ö. Sonnerup, and R. P. Lin (2001), Fluid and kinetics signatures of reconnection at the dawn tail magnetopause: Wind observations, *J. Geophys. Res.*, *106*(A11), 25,489–25,501, doi:10.1029/2001JA900054.

Phan, T. D., M. Dunlop, G. Paschmann, B. Klecker, J. M. Bosqued, H. Rème, A. Balogh, C. Twitty, F. S. Mozer, C. W. Carlson, C. Mouikis, and L. M. Kistler (2004), Cluster observations of continuous reconnection at the magnetopause under steady interplanetary magnetic field conditions, *Ann. Geophys.*, *22*, 2355–2367, doi:10.5194/angeo-22-2355-2004.

Phan, T. D., M. A. Shay, J. T. Gosling, M. Fujimoto, J. F. Drake, G. Paschmann, M. Oieroset, J. P. Eastwood, and V. Angelopoulos (2013), Electron bulk heating in magnetic reconnection at earth's magnetopause: Dependence on the inflow alfvén speed and magnetic shear, *Geophys. Res. Lett.*, *40*, 4475–4480, doi:10.1002/grl.50917.

Phan, T. D., J. F. Drake, M. A. Shay, J. T. Gosling, G. Paschmann, J. P. Eastwood, M. Oieroset, M. Fujimoto, and V. Angelopoulos (2014), Ion bulk heating in magnetic reconnection exhausts at earth's magnetopause: Dependence on the inflow alfvn speed and magnetic shear angle, *Geophys. Res. Lett.*, *41*, 7002–7010, doi:10.1002/2014GL061547.

Priest, E. R., and V. S. Titov (1996), Magnetic reconnection at three-dimensional null points, *Phil. Trans. R. Soc.*, *354*, 2951–2992.

Rème, H., C. Aoustin, J. M. Bosqued, I. Dandouras, B. Lavraud, J. A. Sauvaud, A. Barthe, J. Bouyssou, T. Camus, O. Coeur-Joly, A. Cros, J. Cuvilo, F. Ducay, Y. Garbarowitz, J. L. Medale, E. Penou, H. Perrier, D. Romefort, J. Rouzaud, C. Vallat, D. Alcaydé, C. Jacquey, C. Mazelle, C. d'Uston, E. Möbius, L. M. Kistler, K. Crocker, M. Granoff, C. Mouikis, M. Popecki, M. Vosbury, B. Klecker, D. Hovestadt, H. Kucharek, E. Kuenneth, G. Paschmann, M. Scholer, N. Sckopke, E. Seidenschwang, C. W. Carlson, D. W. Curtis, C. Ingraham, R. P. Lin, J. P. McFadden, G. K. Parks, T. Phan, V. Formisano, E. Amata, M. B. Bavassano-Cattaneo, P. Baldetti, R. Bruno, G. Chionchio, A. D. Lellis, M. F. Marcucci, G. Pallocchia, A. Korth, P. W. Daly, B. Graeve, H. Rosenbauer, V. Vasyliunas, M. McCarthy, M. Wilber, L. Eliasson, R. Lundin, S. Olsen, E. G. Shelley, S. Fuselier, A. G. Ghielmetti, W. Lennartsson, C. P. Escoubet, H. Balsiger, R. Friedel, J. B. Cao, R. A. Kovrazhkin, I. Papamastorakis, R. Pellat, J. Scudder, and B. Sonnerup (2001), First multispacecraft ion measurements in and near the earth's magnetosphere with the identical cluster ion spectrometry (cis) experiment, *Ann. Geophys.*, *19*, 1303–1354, doi:10.5194/angeo-19-1303-2001.

Rosenqvist, L., A. Vaivads, A. Retinò, T. Phan, H. J. Opgenoorth, I. Dandouras, and S. Buchert (2008), Modulated reconnection rate and energy conversion at the magnetopause under steady imf conditions, *Geophys. Res. Lett.*, *35*(L08104), doi:10.1029/2007GL032868.

Runov, A., V. A. Sergeev, R. Nakamura, W. Baumjohann, T. L. Zhang, Y. Asano, M. Volwerk, and H. R. Z. Vörös, A. Balogh (2005), Reconstruction of the magnetotail current sheet structure using multi-point cluster measurements, *Planet. Space Sci.*, *53*(1-3), 237–243, doi:10.1016/j.pss.2004.09.049.

Schindler, K., M. Hesse, and J. Birn (1988), General magnetic reconnection, parallel electric fields, and helicity, *J. Geophys. Res.*, *93*(A6), 5547–5557, doi:10.1029/JA093iA06p05547.

Shay, M. A., and M. Swisdak (2004), Three species collisionless reconnection: Effect of o^+ on magnetotail reconnection, *Phys. Rev. Lett.*, *93*(17), doi:10.1103/PhysRevLett.93.175001.

Shay, M. A., J. F. Drake, B. N. Rogers, and R. E. Denton (1999), The scaling of collisionless, magnetic reconnection for large systems, *Geophys. Res. Lett.*, *26*(14), 2163–2166, doi:10.1029/1999GL900481.

Shay, M. A., J. F. Drake, B. N. Rogers, and R. E. Denton (2001), Alfvénic collisionless magnetic reconnection and the hall term, *J. Geophys. Res.*, *106*(A3), 3759–3772, doi:10.1029/1999JA001007.

Shay, M. A., C. C. Haggerty, T. Phan, J. F. Drake, P. A.Cassak, P. Wu, M. Oieroset, M. Swisdak, and K. Malakit (2014), Electron heating during magnetic reconnection: A simulation scaling study, *Phys. Plasmas*, *21*(122902), doi:10.1063/1.4904203.

Shuster, J. R., L.-J. Chen, W. S. Daughton, L. C. Lee, K. H. Lee, N. Bessho, R. B. Torbert, G. Li, and M. R. Argall (2014), Highly structured electron anisotropy in collisionless reconnection exhausts, *Geophys. Res. Lett.*, *41*, 5389–5395, doi:10.1002/2014GL060608.

Shuster, J. R., L.-J. Chen, M. Hesse, M. R. Argall1, W. Daughton, R. B. Rorbert, and N. Bessho (2015), Spatiotemporal evolution of electron characteristics in the electron diffusion region of magnetic reconnection: Implications for acceleration and heating, *Geophys. Res. Lett.*, *42*(8), 2586–2593, doi:10.1002/2015GL063601.

Sibeck, D. G., R. W. McEntire, A. T. Y. Lui, R. E. Lopez, S. M. Krimigis, R. B. Decker, L. J. Zanetti, and T. A. Potemra (1987), Energetic magnetospheric ions at the dayside magnetopause: Leakage or merging?, *J. Geophys. Res.*, *92*(A11), 12,097–12,114, doi:10.1029/JA092iA11p12097.

Smets, R., D. Delcourt, and D. Fontaine (1998), Ion and electron distribution functions in the distant magnetotail: modeling of geotail observations, *J. Geophys. Res.*, *103*(A9), 20,407–20,417, doi:10.1029/98JA01369.

Sonnerup, B. U. Ö. (1974), Magnetopause reconnection rate, *J. Geophys. Res.*, *79*(10), 1546–1549.

Sonnerup, B. U. Ö., and L. J. Cahill Jr. (1967), Magnetopause structure and attitude from explorer 12 observations, *J. Geophys. Res.*, *72*(1), 171–183, doi:10.1029/JZ072i001p00171.

Sonnerup, B. U. Ö., G. Paschmann, I. Papamastorakis, N. Sckopke, G. Haerendel, S. J. Bame, J. R. Asbridge, J. T. Gosling, and C. T. Russell (1981), Evidence for magnetic field reconnection at the earth's magnetopause, *J. Geophys. Res.*, *86*(A12), 10,049–10,067, doi:10.1029/JA086iA12p10049.

Sonnerup, B. U. Ö., I. Papamastorakis, G. Paschmann, and H. Lühr (1987), Magnetopause properties from ampte/irm observations of the convection electric field: Method development, *J. Geophys. Res.*, *92*(A11), 12,137–12,159, doi:10.1029/JA092iA11p12137.

Sonnerup, B. U. Ö., R. E. Denton, H. Hasegawa, and M. Swisdak (2013), Axis and velocity determination for quasi two-dimensional plasma/field structures from faraday's law: A second look, *J. Geophys. Res.*, *118*, 2073–2086, doi:10.1002/jgra.50211.

Speiser, T. W. (1965), Particle trajectories in model current sheets: 1. analytical solutions, *J. Geophys. Res.*, *70*(17), 4219–4226, doi:10.1029/JZ070i017p04219.

Su, Y.-J., J. E. Borovsky, M. F. T. adn R. C. Elphic, and D. J. McComas (2000), Plasmaspheric material at the reconnecting magnetopause, *J. Geophys. Res.*, *105*(A4), 7591–7600, doi:10.1029/1999JA000266.

Su, Y.-J., M. F. Thomsen, J. E. Borovsky, and D. J. Lawrence (2001), A comprehensive survey of plasmasphere refilling at geosynchronous orbit, *J. Geophys. Res.*, *106*(25), 615.

Sweet, P. (1958), The production of high energy particles in solar flares, *Il Nuovo Cimento*, *8*, 188–196.

Swisdak, M., and J. F. Drake (2007), Orientation of the reconnection x-line, *Geophys. Res. Lett.*, *34*(L11106), doi:10.1029/2007GL029815.

Taylor, J. R. (1997), Chapter 9: Covariance and correlation, in *An introduction to error analysis*, pp. 209–220, University Science Books, Sausalito, California.

Trattner, K. J., J. S. Mulcock, S. M. Petrinec, and S. A. Fuselier (2007), Probing the boundary between antiparallel and component reconnection during southward interplanetary magnetic field conditions, *J. Geophys. Res.*, *112*(A08210), doi:10.1029/2007JA012270.

Trattner, K. J., S. M. Petrinec, S. A. Fuselier, and T. D. Phan (2012), The location of reconnection at the magnetopause: Testing the maximum magnetic shear model with themis observations, *J. Geophys. Res.*, *117*(A01201), doi:10.1029/2011JA016959.

Ueno, G., S. Ohtani, Y. Saito, and T. Mukai (2002), Field-aligned currents in the outermost plasma sheet boundary layer with geotail observation, *J. Geophys. Res.*, *107*, 1399, doi:10.1029/2002JA009367.

Vaivads, A., Y. Khotyaintsev, M. André, A. Retinò, S. C. Buchert, B. N. Rogers, P. Décréau, G. Paschmann, and T. D. Phan (2004), Structure of the magnetic reconnection diffusion region from four-spacecraft observations, *Phys. Rev. Lett.*, *93*(10), doi:10.1103/PhysRevLett.93.105001.

Vasyliunas, V. M. (1975), Theoretical models of magnetic field line merging, 1., *Rev. Geophys. Space Phys*, *13*, 303–336.

Walén, C. (1944), On the theory of sunspots, *Ark. Mat. Astron. Fys.*, *30A*(15), 1–87.

Walsh, B. M., T. D. Phan, D. G. Sibeck, and V. M. Souza (2014), The plasmaspheric plume and magnetopause reconnection, *Geophys. Res. Lett.*, *41*, 223–228, doi:10.1002/2013GL058802.

Wang, R., Q. Lu, M. V. Y. V. Khotyaintsev and, A. Du, R. Nakamura, W. D. Gonzalez, X. Sun, W. Baumjohann, X. Li, T. Zhang, A. N. Fazakerley, C. Huang, and M. Wu (2014), Observation of double layer in the separatrix region during magnetic reconnection, *Geophys. Res. Lett.*, *41*(14), 4851–4858, doi:10.1002/2014GL061157.

Wilken, B., W. I. Axford, I. Daglis, P. Daly, W. GüTTLER, W. H. Ip, A. Korth, G. Kremser, S. Livi, V. M. Vasyliunas, J. Woch, D. Baker, R. D. Belian, J. B. Blake, J. F. Fennell,

L. R. Lyons, H. Borg, T. A. Fritz, F. Gliem, R. Rathje, M. Grande, D. Hall, K. KecsuemÉTY, S. Mckenna-LAWLOR, K. Mursula, P. Tanskanen, Z. Pu, I. Sandahl, E. T. Sarris, M. Scholer, M. Schulz, F. SØRASS, and S. Ullaland (1997), Rapid: The imaging energetic particle spectrometer on cluster, *Space Sci. Rev.*, *79*, 399–473.

Wygant, J. R., C. A. Cattell, R. Lysak, Y. Song, J. Dombeck, J. McFadden, F. S. Mozer, C. W. Carlson, G. Parks, E. A. Lucek, A. Balogh, M. Andre, H. Reme, M. Hesse, and C. Mouikis (2005), Cluster observations of an intense normal component of the electric field at a thin reconnecting current sheet in the tail and its role in the shock-like acceleration of the ion fluid into the separatrix region, *J. Geophys. Res.*, *110*(A9), doi: 10.1029/2004JA010708.

Yamada, M. (1999), Review of controlled laboratory experiments on physics of magnetic reconnection, *J. Geophys. Res.*, *104*(A7), 14,529–14,541.

Zong, Q.-G., and B. Wilken (1998), Layered structure of energetic oxygen ions in the dayside magnetosheath, *Geophys. Res. Lett.*, *25*(22), 4121–4124, doi:10.1029/1998GL900110.

Zong, Q.-G., and B. Wilken (1999), Bursty energetic oxygen events in the dayside magnetosheath: Geotail observations, *Geophys. Res. Lett.*, *26*(22), 3349–3352, doi: 10.1029/1999GL003634.

Zong, Q.-G., B. Wilken, S. Y. Fu, T. A. Fritz, A. Korth, N. Hasebe, D. J. Williams, and Z.-Y. Pu (2001), Ring current oxygen ions escaping into the magnetosheath, *J. Geophys. Res.*, *106*(A11), 25,541–25,556, doi:10.1029/2000JA000127.